BINDING SERVICES
Tel +44 (0)29 2087 4949
Fax.+44 (0)29 2037 1921
E-Mail Bindery@Cardiff.ac.uk

CARDIFF UNIVERSITY
PRIFYSGOL CAERDYDD

Structure and reactivity of model oxides related to automobile exhaust catalysis

Federico Grillo

Ph.D. Thesis

Cardiff University, 2007

ProQuest LLC
789 East Eisenhower Parkway
P.O. Box 1346
Ann Arbor, MI 48106-1346

Ai miei genitori

Acknowledgments

First, I would like to thank Professor Mike Bowker for giving me the opportunity and good advice to realise this work. Then Dr. Phil Davies and Dr. Albert Carley for their support in the everyday laboratory practice. I also thank the European Union for its financial support under the contract HPRN-CT-2002-191 and all the people belonging to the different institutions involved in the project.
I associate, in those acknowledgments, my work colleagues, in particular Dr. Sandy McDowall, and Dr. David Morgan whose help was essential in resolving the various problems I encountered with the different equipments used in Cardiff. Dr. Elodie Fourré for all the good and the bad moments we spent together and making me realize that, although we can try to plan it, life has to be taken as it comes; I will never forget. Surin Saipanya and Emma Richards who shared the difficult task of working with such a big and complicated equipment. Dr. Roger Nix, Dr. Jörn Erichsen and Alexandra Tsami, form Queen Mary, University of London, for the possibility of setting up good collaborations. Dr. Chris Morgan, Matt House and Monica Gonzalez-Herrera: with them I shared many conversations and complaints about work and life and also moments of fun. Then, all the rest of the Bowker's group.
I thank the workshop guys, especially Gerald, Alun and Jon, who repaired some of the equipments essential to my work, and Gary from stores.

On the family side, I give a special thank to my mum Francesca and my sister Linda for moral support and believing in me, and to my dad Gabriele for pushing me to complete my degree first and advising me to do what I really liked and trying to be happy after.

Finally, I will never forget the warmth and cosiness of the city of Cardiff.

A tutti grazie.

Abstract

In this thesis, different ceria and barium oxide based model systems, related to automobile exhaust catalysis, are studied, with the aim of characterizing their structure and reactivity.

Chapter 1 is an introduction to the relevance of surface science studies and its cross links with heterogeneous catalysis. The knowledge of a process at atomic scale, which can ultimately be achieved through surface science, can help to improve the design and performance of a material. A description of the techniques used is presented in Chapter 2. The studies of ceria based systems are described in Chapter 3. An introduction to the ceria and oxygen storage capacity (OSC) in ceria containing materials is given. Oxygen adsorption investigations on a $CeO_2(111)$ single crystal are presented in the second part. Finally, the preparation and characterisation of CeO_{2-x} layers on a Cu(111) single crystal and, how preparation conditions dictate the ceria overlayer structure and oxidation state, is presented. Chapter 4 concerns the study of oxidised barium layers related to NSR (NO_x Storage and Reduction). This involves the preparation of BaO_x layers on a Pt(111) single crystal and BaO(100) layers on a Cu(111) single crystal. These layers were exposed to both *in situ* mixed NO and O_2 gases and premixed NO and O_2 gases. In the case of BaO(100)/Cu(111), during the latter experiments, nitrite groups could be observed to form on the surface. The preparation of NSR model systems [$Pt/BaO^*/\alpha-Al_2O_3(0001)$ and $BaO^*/Pt/\alpha-Al_2O_3(0001)$] using traditional, wet chemistry, methods is described in Chapter 5. The model systems were characterised using XPS and air AFM. Finally, the same techniques were used to evaluate NO_x storage capabilities of those model systems. Chapter 6 summarises the conclusions.

Contents

Chapter 1

Introduction

1.1. Surface Science and Heterogeneous Catalysis

The work presented in this thesis relates to the investigation of the reactivity of gaseous molecules with well-defined metal and metal-oxide surfaces.

Chemical reactions play an important role in our everyday life. All the processes occurring inside our body, nearly all the gadgets we normally use, all drugs that help to fight diseases are ultimately the result of chemical reactions. Chemical reactions can be accelerated by means of catalysts. A substance that can be introduced in a chemical process, affects the kinetics of a reaction without having effects on its equilibrium, lowering the activation energy level $\Delta E_{nc}^{\ddagger}$, i.e. without modification of its energy of reaction ΔE_r, and is regenerated at the end of the process is called catalyst. An energy vs reaction path diagram for the same reaction without and with a catalyst is shown in figure 1.1.

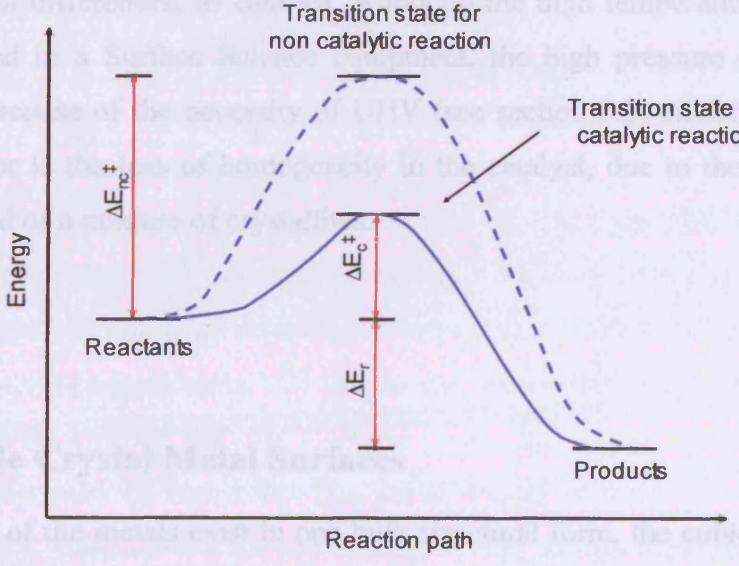

Fig. 1.1: The effect of the catalyst is to lower the reaction activation energy from $\Delta E_{nc}^{\ddagger}$ to $\Delta E_c^{\ddagger}$. The reaction will then follow a more favourable pathway.

The vast majority of industrial synthesis, starting from oil refining, to drug production, are chemical processes using metals and metal-oxides as catalysts. The reactants and

the products are normally in the gas or liquid phase, whereas the catalyst is in a solid phase. As the reactions are occurring at the interface between the two, or three, phases present in the system, the system itself is called "heterogeneous". More precisely the reactions take place at the surface of the catalyst, not in the bulk, the surface being the portion of the catalyst exposed and in contact with the reactants. In almost all the industrial applications, metals and metal oxides are used in a finely divided form, as for supported metal catalysts, or in a massive, polycrystalline form, as for mechanical fabrications. However, they can be regarded as a collection of small single crystal particles, at the microscopic level. The chemistry of the material is therefore dependent upon the nature and type of surfaces exposed. Understanding the surface properties of any single crystal particle can integrate the information acquired via heterogeneous catalysis method, helping to understand catalytic processes at atomic scale and in particular at surfaces. The knowledge of a process at atomic scale can help to improve catalyst design and performances. Nevertheless, the transfer of knowledge from Surface Science to industrial world is complicated because of the different conditions in which Heterogeneous catalysis and respectively Surface Science work. Industrial processes are carried out at high temperatures and high pressures and with a mixture of crystallites, which can present a variety of morphological differences, as catalyst. Although the high temperature condition can be reproduced in a Surface Science equipment, the high pressure condition is not achievable because of the necessity of UHV (see section 2.3) environment. Another limiting factor is the loss of homogeneity in the catalyst, due to the use of a single crystal instead of a mixture of crystallites.

1.2. Single Crystal Metal Surfaces

The majority of the metals exist in one bulk structural form, the cubic one. The most common metallic crystal structures are presented in figure 1.2. For each of these crystal systems, there are in principle an infinite number of possible surfaces which can be exposed. However, for thermodynamics reasons (minimisation of the surface energy, γ), only a small number of planes exist in any significant amount, the so called "low-index" surfaces.

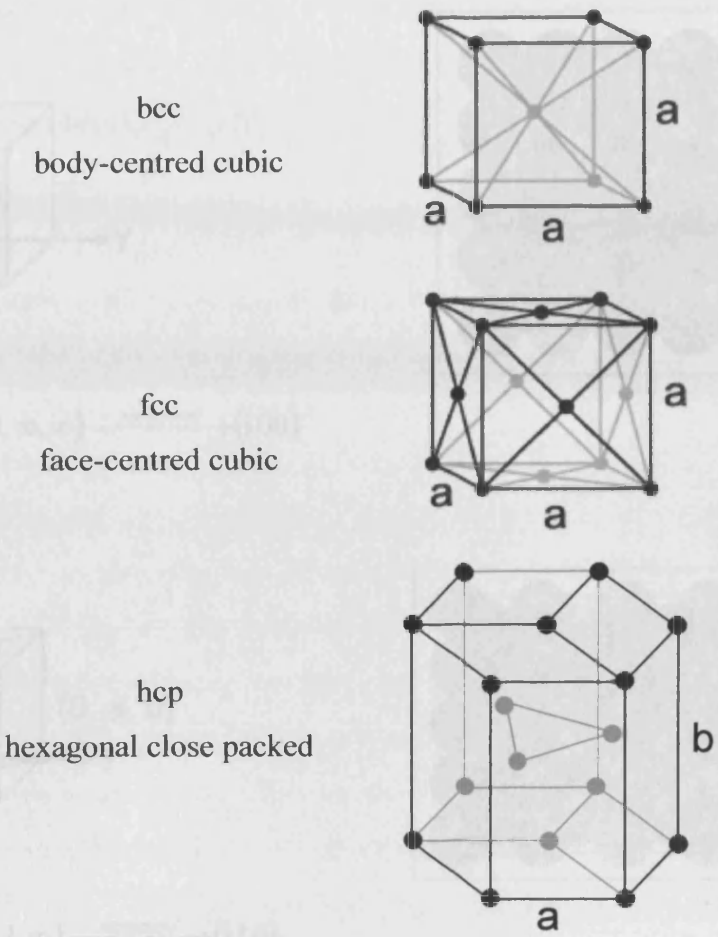

Fig. 1.2: A representation of the bcc, fcc and hcp structures.

A Single Crystal Metal Surface is the result of the cleavage of a bulk solid metal along a particular crystallographic plane, to expose a well-defined crystal plane. The cleavage is normally achieved orienting the crystal using X-ray diffraction techniques and cutting via spark erosion. To define the exposed plane, Miller indices are commonly used. Miller indices describe how the plane intersects the main crystallographic axes of the solid. The metal crystal is then described as M(hkl), where M is the chemical symbol and (hkl) a ternary of numbers which quantify the intercepts and therefore identifies unequivocally the plane or surface. In the present work different single metal crystals such as Pt(111) and Cu(111) have been used. As an example, copper is a fcc metal with unit cell a = 0.36nm. Let's consider the crystal plane that intercepts the x axis at a = (a, 0, 0) and is parallel to y and z axis.

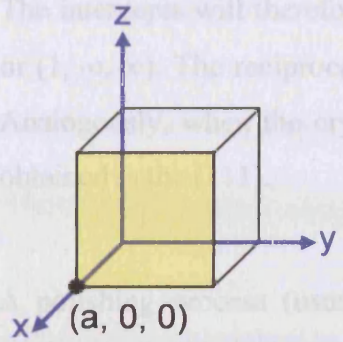

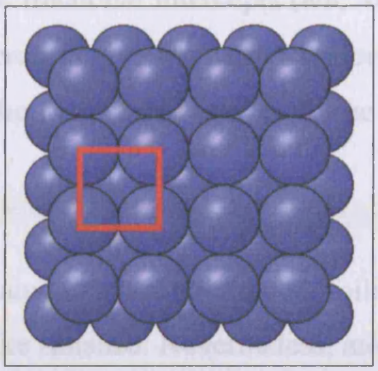

$$\left(\frac{a}{x},\frac{\infty}{y},\frac{\infty}{z}\right)\rightarrow(1,\infty,\infty)\xrightarrow{reciprocal}(100)$$

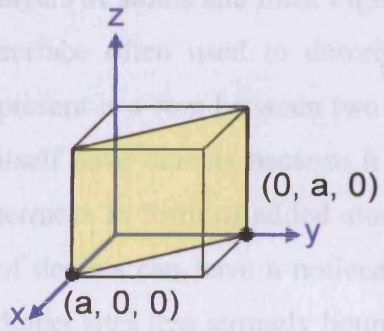

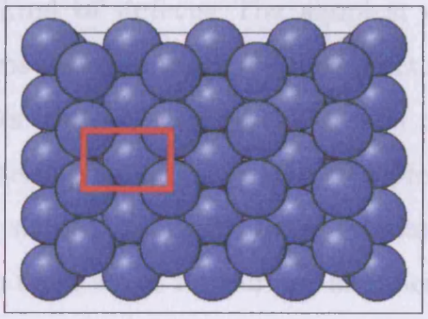

$$\left(\frac{a}{x},\frac{a}{y},\frac{\infty}{z}\right)\rightarrow(1,1,\infty)\xrightarrow{reciprocal}(110)$$

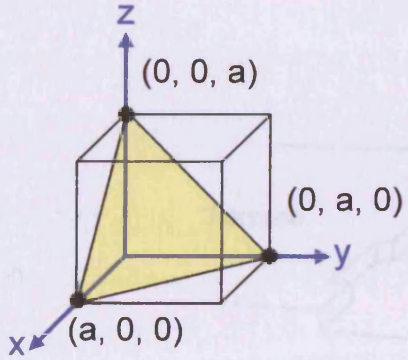

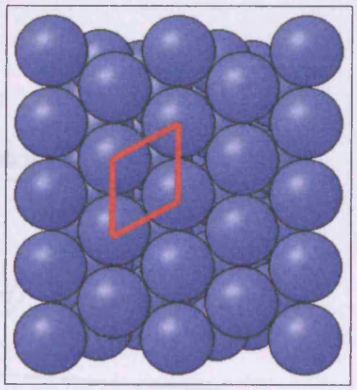

$$\left(\frac{a}{x},\frac{a}{y},\frac{a}{z}\right)\rightarrow(1,1,1)\xrightarrow{reciprocal}(111)$$

Fig. 1.3: Identification of the low-index crystal lattice planes for an fcc crystal lattice using Miller indices. From top to bottom, on the left end side the (100), (110) and (111) face are in yellow. On the right side a representation of the surface, with the unit cell in red (figure on the right were generated using the applet Surface Explorer [1]).

The intercepts will therefore be (a, ∞, ∞) and the fractional intercepts (a/a, ∞/a, ∞/a) or (1, ∞, ∞). The reciprocal of the fractional intercepts give the Miller Indices (100). Analogously, when the crystal plane intersects the three axis at (a, a, a), the surface obtained is the (111).

A polishing process (usually abrasion using diamond paste) normally follows the cutting procedure and leaves the surface mirror-like finished. Nevertheless, atomically smooth crystal surfaces are in practice impossible to achieve, because defective structures are always present. These defects are usually comprised of incomplete layers of atoms and ions. Figure 1.4 shows the Terrace-Step-Kink (TSK) model of the surface often used to describe the different kind of defects. The simplest defect present is a step between two flat layers of atoms called terraces. A step defect might itself have defects because it may contain kinks. Defects can also be present on the terraces in form of added atoms (adatom) or missing atoms (vacancy). The presence of defects can have a noticeable effect on the surface reactivity, being the atoms at defect sites less strongly bound to the bulk than those at the flat surface and therefore more reactive. These so called low-coordination atoms may provide an initial reaction site for the adsorption of gaseous molecules and they are called "active sites".

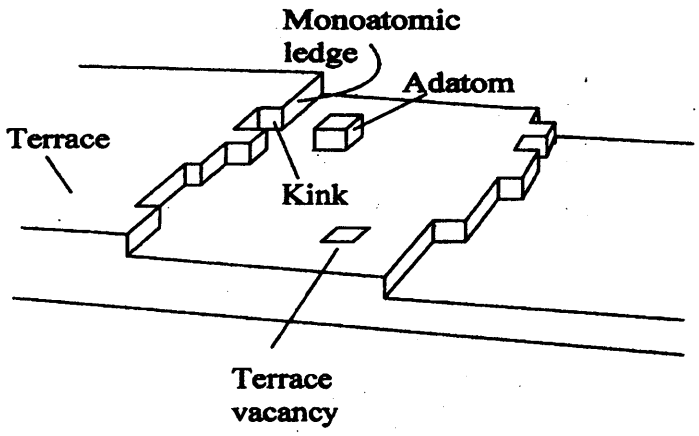

Fig. 1.4: The Terrace-Step-Kink (TSK) showing different defects on the surface [2].

1.3. Reactions at Surfaces

When a gaseous molecule comes in contact with a surface, a number of processes can occur. Any reaction can be reduced to a series of events such as adsorption of gas molecules (reactants) on the surface, diffusion, bond breaking, making, rearranging, desorption of products. If the surface appears unchanged at the end of the process and favours the reaction, it acts as a catalyst for the reaction. If figure 1.5 the above processes are exemplified for the theoretical oxidation of CO to CO_2 on a supported metal nanoparticle catalyst [3].

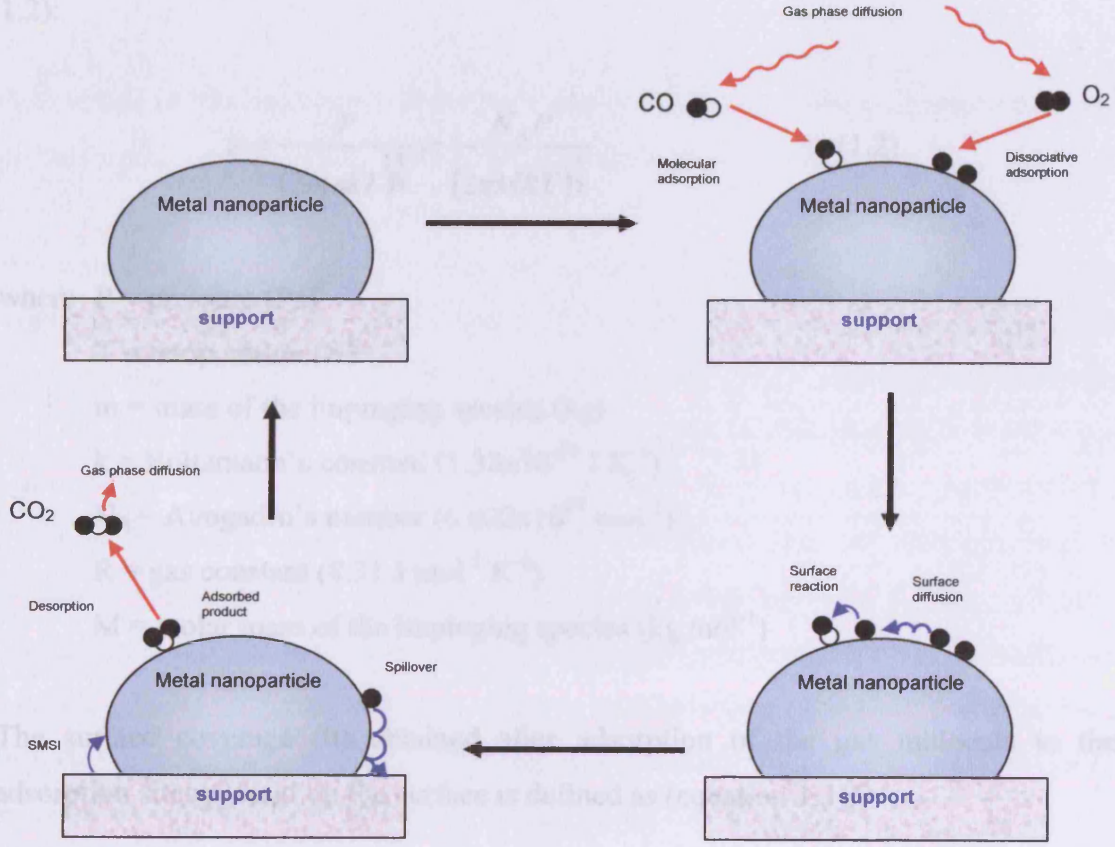

Fig. 1.5: Different events occurring on the interface surface-gas phase. Adapted from [3].

1.3.1. Adsorption Process

Adsorption is the process by which a molecule due to a collision to it, sticks on a surface. A measure of the fraction of gas molecules that can adsorb on a surface is called sticking probability (S) and it is defined as (equation 1.1):

$$S = \frac{\text{Adosorption rate}}{\text{Surface collision rate}} = \frac{R_A}{z} \qquad \ldots(1.1)$$

S varies from 0, when no adsorption occurs to 1, when total adsorption on the surface occurs. In general it is $0 < S < 1$, because part of the molecules colliding on the surface can be "reflected", as a result of elastic (collision without energy loss) or inelastic scattering (collision with loss of energy). Other parameters influencing the sticking probability are the temperature of the system, the crystal face, presence of already adsorbed species.

The surface collision rate (z) is given by the Hertz-Kundsen equation [4] (equation 1.2):

$$z = \frac{P}{(2m\pi kT)^{\frac{1}{2}}} = \frac{N_A P}{(2\pi MRT)^{\frac{1}{2}}} \qquad \ldots(1.2)$$

where P = pressure (Pa)

T = temperature (K)

m = mass of the impinging species (kg)

k = Boltzmann's constant (1.38×10^{-23} J K^{-1})

N_A = Avogadro's number (6.022×10^{23} mol^{-1})

R = gas constant (8.31 J mol^{-1} K^{-1})

M = molar mass of the impinging species (kg mol^{-1})

The surface coverage (θ) obtained after adsorption of the gas molecule to the adsorption sites present on the surface is defined as (equation 1.3):

$$\theta = \frac{\text{Adsorbed species number}}{\text{Total adsorption sites number}} = \frac{N_{ads}}{N_S} \qquad \ldots(1.3)$$

For the adsorption to be thermodynamically favourable, from the thermodynamic equation (1.4), the variation of free energy (ΔG) of the system has to be negative:

$$\Delta G = \Delta H - T\Delta S \qquad \ldots(1.4)$$

where ΔG = variation of free energy (kJ mol^{-1})

ΔH = variation of enthalpy (kJ mol^{-1})

T = temperature (K)

ΔS = variation of entropy (J mol^{-1} K^{-1})

Adsorption is usually also accompanied by an entropy decrease, as the translational freedom of the gas molecule is reduced due to adsorption. So, being $\Delta G < 0$ and $\Delta S < 0$, the adsorption process must be exothermic ($\Delta H < 0$).

Adsorption of gas molecules on surfaces can occur in two modes, physisorption and chemisorption, which can be distinguished by their heats of adsorption.

Physisorption is the interaction of a gas molecule with the surface due to van der Waals forces. This dipole induced forces are weak ($E_a \sim 40$ kJ mol^{-1}) and they result in weak, long range bonding. The electron density of the two species, the molecule and the surface, remains separate with no exchange of electrons between the gas molecule and the surface, therefore no chemical bond is present. Although the molecule remains unbroken, due to the interaction with the surface some geometrical distortion can occur. The surface can adsorb the small amount of energy released during physisorption as vibrations of the lattice (phonons) and dissipate the energy as thermal motion. The molecule in the physisorbed state occupies a temperature dependent equilibrium position, oscillating in a potential well. The potential energy vs reaction coordinate diagram in figure 1.6 illustrates this situation.

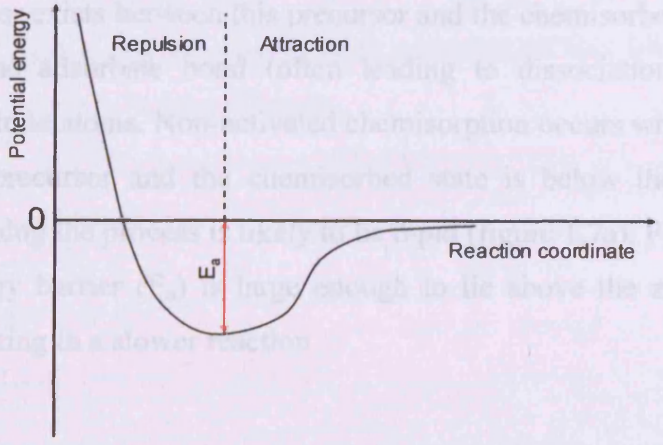

Fig. 1.6: Potential energy vs reaction coordinate diagram for physisorption process.

No energy barrier exists so the incoming molecule can enter the physisorption well making the process very fast. The depth of the physisorption well is equal to the heat of adsorption (E_a), and therefore the molecule will require this same energy to desorb from the surface i.e. $E_a = E_d$, being E_d the energy required for desorption.

The vibrational energy of the physisorbed molecule depends primarily upon the surface temperature; increases in temperature can increase the vibrational energy above the desorption energy (E_d) allowing the molecule to desorb from the surface. The Frenkel equation (equation 1.5) describes the residence time (τ) of the physisorbed molecule on the surface and its dependence on surface temperature.

$$\tau = \tau_0 \exp\left(\frac{-E_d}{kT}\right) \qquad \ldots 1.5$$

where τ_0 = period of oscillation of the molecule at the surface (seconds)

E_d = desorption energy (kJ mol^{-1})

k = Boltzmann's constant (1.38×10^{-23} J K^{-1})

T = temperature (K)

Chemisorption occurs when the magnitude of the heat of adsorption is large ($E_a \sim 40 - 1000$ kJ mol^{-1}), and a chemical bond (usually covalent) forms between the gas molecule and the surface. The potential energy vs reaction coordinate diagram for chemisorption (see figure 1.7) shows a potential well for the chemisorbed state much deeper than the one for the physisorbed state. As the molecule approaches the surface it becomes physisorbed into a chemisorption precursor state. A potential energy barrier exists between this precursor and the chemisorbed state due to the deformation of the adsorbate bond (often leading to dissociation) and rearrangement of the substrate atoms. Non-activated chemisorption occurs when the energy barrier between the precursor and the chemisorbed state is below the energy zero reference axis meaning the process is likely to be rapid (figure 1.7a). For activated chemisorption the energy barrier (E_a) is large enough to lie above the zero energy axis (figure 1.7b) resulting in a slower reaction.

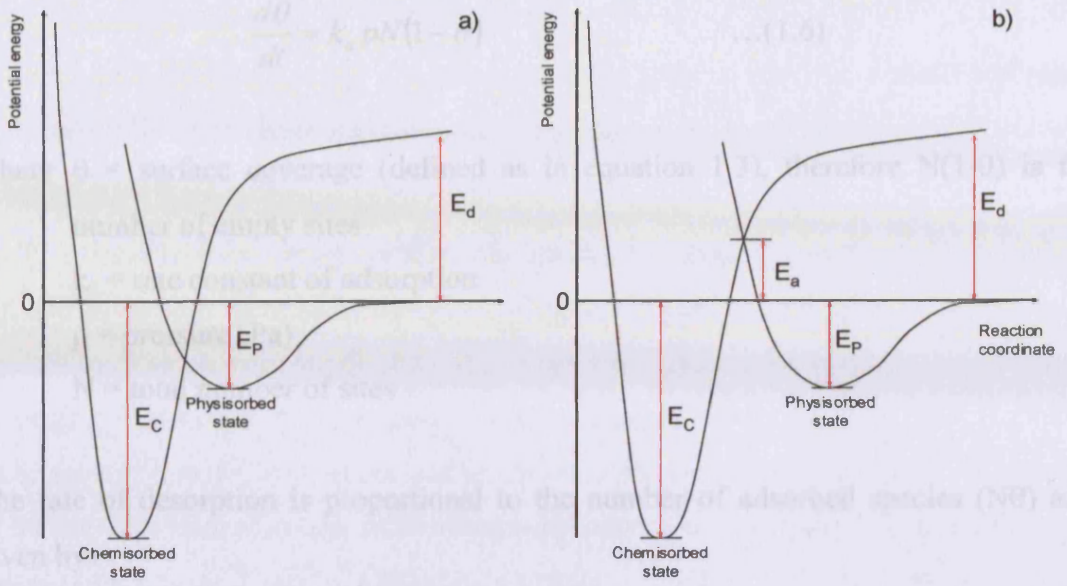

Fig. 1.7: Potential energy vs reaction coordinate diagrams for a) non-activated chemisorption and b) activated chemisorption processes.

1.3.2. Adsorption Isotherms [5]

Adsorption isotherms describe the relationship between the amounts of gas adsorbed on a surface as a function of pressure at a given temperature. One of the models that can be used to for this purpose is the one derived by Langmuir. The model is based on several assumptions:

- all the adsorption sites present on the surface are considered equal to each other, so there are no preferred adsorption sites;
- the adsorption of a molecule is not influenced by the state (full or empty) of the adjacent site;
- all molecules adsorb with unit sticking probability and there is no activation energy for the process;
- adsorption terminates when the maximum coverage (a complete monolayer) is reached.

For the Langmuir isotherm, the rate of change of surface coverage due to the adsorption process is given by:

$$\frac{d\theta}{dt} = k_a pN(1-\theta) \qquad \ldots(1.6)$$

where θ = surface coverage (defined as in equation 1.3), therefore $N(1-\theta)$ is the number of empty sites

k_a = rate constant of adsorption

p = pressure (Pa)

N = total number of sites

The rate of desorption is proportional to the number of adsorbed species ($N\theta$) and given by:

$$\frac{d\theta}{dt} = -k_d N\theta \qquad \ldots(1.7)$$

where k_d = rate constant of desorption.

At equilibrium, adsorption and desorption rate must be equal, therefore, resolving for θ, gives the Langmuir isotherm equation:

$$\theta = \frac{Kp}{1+Kp} \qquad \ldots(1.8)$$

where $K=k_a/k_d$.

Other isotherm methods have been developed to overcome some of the Langmuir assumptions and present a model more close to reality. For example the Brunauer-Emmett-Teller (BET) model takes into account the possibility that an adsorbed monolayer may allow further physical adsorption, and the Temkin and Freundlich accounts for the non-equivalence of the adsorption sites.

1.4. Surface Sensitive Techniques

In order to fully characterise a surface, Surface Science requires a multi-technique approach in which a range of surface-sensitive probes are used in conjunction in order to provide complementary information.

Surface sensitivity is a major problem in Surface Science. The surface of a sample is defined as the top layer of it; therefore, a surface sensitive analytical technique must be able to detect a very small amount of matter and discriminate between the signals belonging to the surface of the sample and the signals belonging to its bulk. A classic example to illustrate how important to discriminate between surface and bulk atoms of a sample is quantification of the atoms belonging to each other [5]. Considering a cubic block of side 1 cm^2 of Pt (lattice constant a = 3.92Å [6]), oriented in the (111) direction. From figure 1.8, using some geometrical consideration, the area (A) of each primitive unit cell will be:

$$A = \frac{a^2\sqrt{3}}{4} = 6.65\ \text{Å}^2 = 6.65\text{x}10^{-16}\ \text{cm}^2 \qquad \ldots(1.9)$$

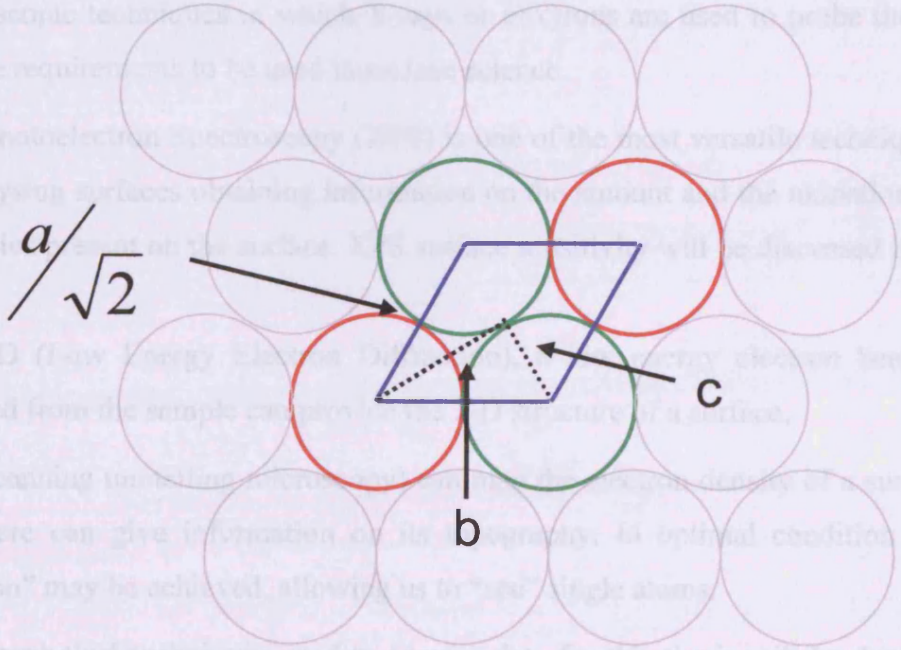

Fig. 1.8: to calculate the theoretical area of a unit cell notice that $b = \frac{a\sqrt{3}}{2\sqrt{2}}$ and $c = \frac{a}{2\sqrt{2}}$.

Since only one atom is contained in the unit cell, the total number of unit cells in 1 cm^2 and therefore the total number of atom in 1 cm^2, is:

$$\frac{1\,cm^2}{6.65\times10^{-16}\,cm^2}=1.50\times10^{15} \qquad ...(1.10)$$

This could appear to be a very large number, but in term of moles it will be only ~ $2.5x10^{-9}$ mol cm^{-2}. The typical area analysed by a surface sensitive technique such as XPS is of the order of magnitude of 5 mm^2 or less, lowering the detection limit by another 20 orders of magnitude.

The volume occupied by one atom of Pt is $11.28x10^{-24}$ cm^3, the radius being 1.39 Å [6] or $1.39x10^{-8}$ cm; therefore in a cube of a 1 cm^3 volume, $8.89x10^{22}$ atoms are present. Thus, if we consider only the surface of interest, the surface atoms to bulk atoms ratio is ~ $1:10^8$.

Spectroscopic techniques in which X-rays or electrons are used to probe the surface meet the requirements to be used in surface science.

X-ray Photoelectron Spectroscopy (XPS) is one of the most versatile techniques used for analysing surfaces obtaining information on the amount and the oxidation state of the species present on the surface. XPS surface sensitivity will be discussed in section 2.4.5.1.

In LEED (Low Energy Electron Diffraction), a low energy electron beam being diffracted from the sample can provide the 2-D structure of a surface.

STM (scanning tunnelling microscopy) can map the electron density of a surface and from there can give information on its topography. In optimal condition "atomic resolution" may be achieved, allowing us to "see" single atoms.

All the analytical techniques used to acquire data for this thesis will be described in Chapter 2.

1.5. Oxygen storage on CeO_2 [7]

The surface science of metal oxides is a relatively young field that benefits from a rapidly increasing interest. This is motivated by the desire to contribute to the numerous applications where oxide surfaces play a role; after all, most metals are oxidised immediately when exposed to the ambient.

Rare-earth oxides have been widely investigated as structural and electronic promoters to improve the activity, selectivity and thermal stability of catalysts. The most significant of the oxides of rare-earth elements in industrial catalysis is certainly CeO_2. Its use in catalysis has attracted considerable attention in recent years, especially for those applications, such as treatment of emissions, where ceria has shown great potential mainly for its Oxygen Storage Capacity (OSC). The increasing number of scientific articles and patents that have appeared on this topic in the last few years confirms it.

The catalyst formulation for the treatment of exhaust gases from spark-ignited internal combustion engines consists primarily of noble metals such as Rh, Pd and Pt and metal oxides impregnated either on the surface of γ-Al_2O_3 pellets or an alumina washcoat anchored to a monolithic ceramic substrate (see figure 1.9).

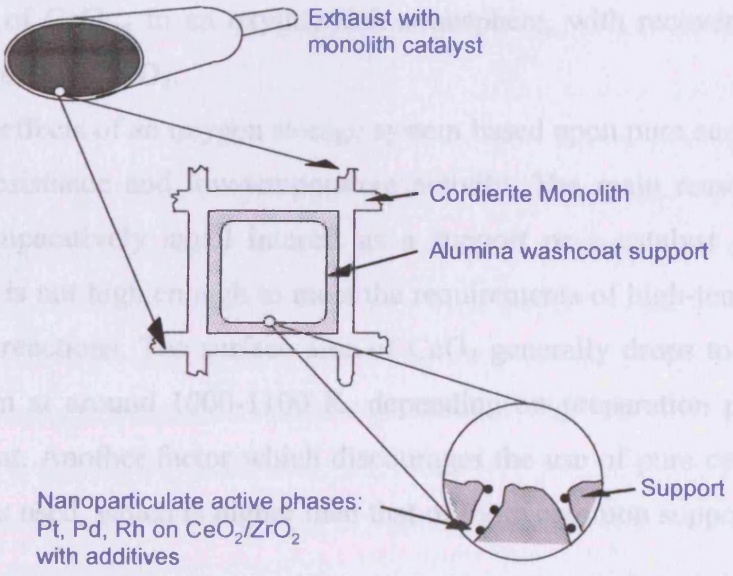

Fig. 1.9: Schematic representation of an exhaust catalyst. Adapted from [3].

CeO_2 is present in the ceramic substrate and acts as oxygen storage component. It is well-known that the main role of ceria in this complex mixture is to provide oxygen buffering during the rich/lean oscillation of exhaust gases. Highest conversion of the pollutants is attained close to the stoichiometric conditions, while excursion to fuel-rich (net reducing) or fuel-poor (net oxidising) air-to-fuel (A/F) ratios severely decrease the efficiency of the Three-Way-Catalysts (TWCs). The so called Oxygen Store Capacity is related to the amount of a reducing gas (H_2, CO), which is oxidised after passing through an oxygen pre-saturated catalyst. Thus, it is related to the most reactive oxygen species and the most readily available oxygen atoms.

If the atmospheric environment in which CeO_2 operates changes continuously from a net oxidising to a net reducing composition, the oxidation state of cerium correspondingly shifts from +IV to +III. As it will be shown in Chapter 3, this enhances the conversion of CO and HC during rich conditions and of NO during lean conditions. This characteristic of ceria derives from the possibility for CeO_2 to be easily and reversibly reduced to several CeO_{2-x} sub-stoichiometries when exposed to O_2 deficient atmospheres. Even after loss of oxygen from its lattice and the consequent formation of a large number of oxygen vacancies, CeO_2 retains its fluorite crystal structure. This also facilitates rapid and complete refilling of oxygen vacancies upon exposure of CeO_{2-x} to an oxygen rich atmosphere, with recovery of the fully oxidised stoichiometry CeO_2.

The major side effects of an oxygen storage system based upon pure ceria is related to poor thermal resistance and low-temperature activity. The main reason why CeO_2 alone is of comparatively small interest as a support or a catalyst is its textural stability, which is not high enough to meet the requirements of high-temperature gas-phase catalytic reactions. The surface area of CeO_2 generally drops to a few square meters per gram at around 1000-1100 K, depending on preparation procedure and type of treatment. Another factor which discourages the use of pure ceria is its cost, nevertheless it is used, which is higher than that of more common supports like Al_2O_3 and SiO_2.

In this work, ceria oxygen storage capacity has been firstly studied using a $CeO_2(111)$ single crystal with the aim of quantifying via XPS the amount of oxygen that can be stored/de-stored and verifying the presence of defects in the form of Ce(III) and oxygen radicals, under different oxidising/reducing environments. STM attempts to image the surface were unsuccessful, mainly due to the well known difficulties in

creating enough conductivity through the crystal. Several films of CeO_2 were then grown on a Cu(111) single crystal. The use of a metallic substrate minimises charging effects in XPS measurements and offers the possibility of being able to create better conduction in the insulating ceria layer allowing improving STM measurements. This work will be described in detail in Chapter 3.

1.6. NSR: NO_x Storage and Reduction

Nowadays, there is an increasing concern in the world about environmental preservation. A good step toward environmental preservation is the sensible use of starting products for chemical synthesis, crude oil to start with, and a very well targeted recycling policy. One of the major problems we have to face is dictated by global warming, which in turn, is mainly related to the ozone layer depletion and to the large amounts of CO_2 discarded by factories, houses and automotive vehicles.

TWCs have been introduced in automotive pollution control, with the aim of degrading exhaust gases to less pollutant ones, i.e. the NO_x to N_2, the CO to CO_2, and the hydrocarbons to CO_2 and H_2O.

Moreover, the demand to improve engines efficiency has led to the introduction of lean-burn engine technology, where the engine is operated in the presence of excess oxygen. Unfortunately, the presence of excess oxygen under lean-burn conditions renders the catalytic reduction of NO_x difficult, and a variety of strategies are currently being investigated to rectify the problem. One solution involves the use of a NO_x Storage and Reduction (NSR) catalyst in combination with mixed-lean engine operation. This has been introduced by Toyota during the mid 1990s [8, 9, 10]. On a ceramic support, NSR catalysts contain a noble metal (e.g. platinum), and a component that is used to store the NO_x gases (e.g. barium oxide) while the engine is running under lean conditions. When the storage component is full, the engine switches to running under rich conditions, resulting in unburnt hydrocarbons being released into the exhaust. These unburnt hydrocarbons reduce the platinum and help NO_x decomposition, which is then reduced by the platinum to form N_2. With the storage component regenerated, the engine switches back to running under lean conditions, and the cycle begins again.

It has also been shown that the presence of a particular transition metal into the system has an effect on its NO_x storage capacity.

Chapter 4 will illustrate the experiments undertaken to improve the knowledge about NSR catalysts with data collected in the Omicron Multiprobe ® Surface Science System (described in Chapter 2) on BaO_x/Pt(111) systems. Moreover, results of gas mixtures dosing experiments performed in collaboration with Queen Mary, University of London, on BaO/Cu(111) will also be presented.

1.7. High Pressure Study of NSR Model Catalysts

The purpose of this set of experiments is to decrease in a certain way the gap between Heterogeneous Catalysis and Surface Science investigating a NSR system at atmospheric conditions. This has been done preparing the BaO^*/Pt/α-Al_2O_3(0001) and Pt/BaO^*/α-Al_2O_3(0001) systems in a similar way to that the real catalyst is prepared, without therefore any cleaning process typical of Surface Science. BaO^* is preferred to BaO because the barium compound actually prepared is a mixture of BaO, $BaCO_3$ and probably $BaHCO_3$. Because of their insulating characteristics, the systems have been structurally characterized via Tapping Mode Atomic Force Microscopy (TM-AFM) and chemically characterized using a Kratos Axis Ultra XP Spectrometer. After characterization the systems have been tested for reactivity in an AFM environmental cell allowing high temperature – high pressure scanning conditions and by means of the Kratos XP Spectrometer. Chapter 5 will show the results about these experiments, whereas the analytical techniques utilised are described in Chapter 2.

1.8. Thesis Synopsis

This research work deals with the preparation of model systems related to automotive catalysis. The aim is to prepare these model systems, characterize their structure and quantify their reactivity mainly via a traditional Surface Science approach using UHV conditions. This first chapter has provided background information on the general topic that will be developed in the following chapters. Chapter 2 describes the

different apparatuses and techniques used to obtain the experimental data. Chapter 3 will show results related to oxygen storage in ceria-based material. Chapter 4 will describe the results obtained studying the BaO_x/Pt(111) and the BaO_x/Cu(111) systems. Chapter 5 is an attempt to obtain information about a NSR model catalyst, from a non-traditional Surface Science point of view, i.e. using non UHV techniques. Finally, chapter 6 will summarize the results of Chapters 3 to 5.

The project was supported by the European Union [11] and is introduced in a European context of Human Mobility involving several universities: Uppsala University, (Sweden), Queen Mary University of London (UK), Otto-von-Guericke University in Magdeburg (Germany), University College in Cork (Ireland), Linköping University (Sweden), The University of Liverpool (UK) and finally Cardiff University (UK).

For this purpose, part of the data have been acquired in collaboration with Young Researchers (PhD students and Post Docs) within the group and belonging to other universities. Notice of this will be given where appropriate.

1.9. References

1. http://w3.rz-berlin.mpg.de/~rammer/surfexp_prod
2. P. W. Atkins, *Physical Chemistry 4th edition,* Oxford University Press, 1990
3. M. Bowker, *The Basis and Applications of Heterogeneous Catalysis*, Oxford University Press Inc., New York, 1998
4. A. Chambers, R.K. Fitch, B.S. Halliday, *Basic Vacuum Technology*, 2nd Ed, IoP Publishing, 1998
5. G. Attard, C. Barnes, *Surfaces*, Oxford University Press Inc., New York, 1998
6. Chemistry online database in www.webelements.com
7. A. Trovarelli, *Catalysis by Ceria and Related Materials*, Imperial College Press Ed. Catalytic Science, ed. G.J. Hutchings, 2001
8. D. James, E. Fourré, M. Ishii, M. Bowker, *App. Cat. B.* 45, 2003, 147
9. N. Miyoshini, S. Matsumoto, K. Katoh, T. Tanaka, J. Harada, N. Takahashi, K. Yokota, M. Sugiura, K. Kasahara, SAE *Technical Paper Series*, 950809, 1995
10. S. Matsumoto, *CatTech* 4 2, 2000, 102

11. http://www.teoroo.mkem.uu.se/EU-surface/

Chapter 2
Experimental

2.1. Introduction

A general overview on an Ultra High Vacuum (UHV) system and the importance of using UHV condition for surface science studies is given. The attention is pointed to the UHV system used, presenting a general overview of it. Single components as well as the different experimental techniques used during the experimental sessions are presented with their relevant characteristics.

2.2. The system [1]

All the experimental data have been collected using a custom designed Multiprobe ® Surface Science System supplied by Omicron Vakuumphysik GmbH. The system consists of three UHV chambers equipped with facilities allowing surface preparation and analysis. Typical surface preparation methods include sputtering, annealing and evaporation coating. The samples prepared using the methods reported above can then be analyzed using different techniques present on the system, such as Scanning Probe Microscopy (SPM), Raman Spectroscopy, Low Energy Electron Diffraction (LEED), X-Ray Photoelectron Spectroscopy (XPS), Ultraviolet Photoelectron Spectroscopy (UPS), Ion Scattering Spectroscopy (ISS) and Electron Paramagnetic Resonance (EPR).

Only some of these techniques have been used and they will be extensively described, nevertheless the other techniques will be briefly mentioned. Figure 2.1 shows a picture of the system.

The preparation (P) chamber consists of a fast entry lock, a sputtering gun, a gas inlet, and some metal dispensers. The SPM chamber is connected to the P chamber far end and isolated from it by means of a gate valve.

The Surface Raman and some more metal evaporators are set on the central (C) chamber.

The analysis (A) chamber hosts different analytical techniques such as LEED, XPS, UPS, ISS, EPR, other than a sputtering gun and a gas inlet.

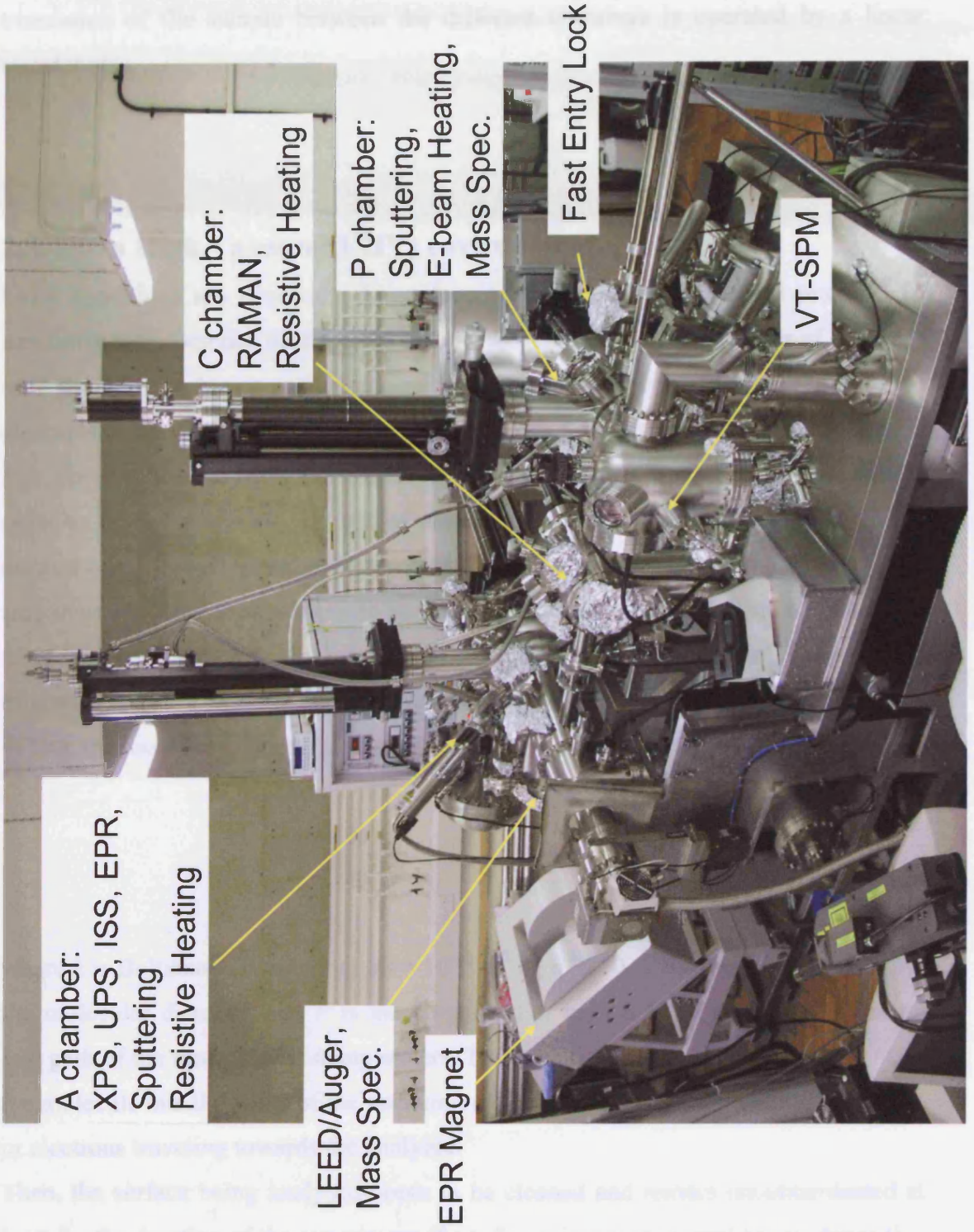

Fig. 2.1: The Omicron Multiprobe ® Surface Science System.

Each chamber is equipped with one horizontal (C), or one horizontal and one vertical (P and A) manipulators to move the sample in the different area needed. The translation of the sample between the different chambers is operated by a linear transfer arm.

2.3. Ultra High Vacuum (UHV) environment

UHV conditions are necessary for surface science studies for several reasons. To maximise the efficiency of the spectroscopic techniques used, the number of electrons used should be as big as possible, therefore it is necessary to minimise the hurdles the electrons can find, thus increase the mean free path for electrons, ions and photons. In fact, photons emitted from the sources should encounter as few hurdles as possible in order to reach the sample, as well as electrons emitted from the surface, in order to reach the analyser. Gas molecules present in the chamber can scatter the electrons and stop them reaching the analyser. In this way a poor result (low counting and high s/n) would be obtained. For this purpose a base pressure of 10^{-6} mbar[1] is enough to minimise the interaction of the electrons with residual gas molecules in the chamber. In fact, the mean free path of gaseous molecules (l) is given by:

$$\lambda = \frac{kT}{\sqrt{2}\pi d^2 P} \qquad \ldots(2.1)$$

where k is Boltzmann constant (1.38×10^{-23} m^2 kg s^{-2} K^{-1}), T the temperature (K), d is the molecular diameter and P is the pressure. For typical UHV pressures the mean free path of the molecules is many meters. This means that it is much more likely that the molecule hits the walls of the vacuum vessel or the pumps than another molecule, or electrons traveling towards the analyzer.

Then, the surface being analysed needs to be cleaned and remain uncontaminated at least for the duration of the experiment (from few minutes to several hours, depending

[1] The pressure SI unit is the pascal (Pa), but millibar (mbar) and Torr are commonly used in the laboratory practice. The conversion between these units is: 100Pa = 1 mbar = 0.76 Torr. The pressure will always be expressed in mbar unless otherwise stated.

upon the type of experiment performed). The frequency (Z) of gas molecules colliding to the surface in a time dt is given by:

$$Z = \frac{dN}{dt} = \frac{P}{\sqrt{2\pi mkT}} \quad \text{cm}^{-2}\text{s}^{-1} \qquad \ldots(2.2)$$

where P is the pressure, m the molecular mass of the gas, k is Boltzmann constant, T the temperature (K). Giving all the values to the constants, the 2.3 became:

$$Z = \frac{1.52 \cdot 10^{21} P(mbar)}{\sqrt{m}} \text{ cm}^{-2}\text{s}^{-1} \qquad \ldots(2.3)$$

At P = 1x10^{-6} mbar and T = 300K, typical numbers of molecules hitting the surface are as in table 2.1:

molecule	m /u	Z /cm^{-2}s^{-1}
H_2	2	1.1x10^{15}
H_2O	18	3.6x10^{14}
CO	28	2.9 x10^{14}
O_2	32	2.7 x10^{14}
CO_2	44	2.3 x10^{14}

Table 2.1: frequency of collision for selected gas molecules at P = 1x10^{-6} mbar and T = 300K

Let's take into consideration CO, a typical gaseous contaminant and a surface with atomic density of 10^{15} atoms × cm^{-2}. This means that the rate of surface contamination, if the sticking probability of the gas is 1 (all the molecules stick to the surface with 100% of efficiency) would be:

$$\frac{2.9 \cdot 10^{14} cm^{-2} s^{-1}}{10^{15} cm^{-2} ML^{-1}} = 0.29 MLs^{-1} \qquad \ldots(2.4)$$

Thus in 3.4 seconds the surface would be completely covered by CO. At P = 1x10^{-10} mbar and T = 300 K, the surface would be completely covered within ~34 800 seconds (~ 9.6 hours) instead.

From the calculations exposed above, to keep the surface clean for one working day, a base pressure of at least 10^{-10} mbar is necessary.

Another issue equally important is that all the spectroscopic techniques used have in their in-vacuum electric components some pins carrying high voltages. UHV conditions prevent electrical arcing and high voltage breakdown, because of the vacuum capacitance high value.

According to the magnitude of the pressure, the following degrees of vacuum are defined [2] as in table 2.2:

Definition	Pressure range
Low Vacuum	Atmospheric pressure to 1 mbar
Medium Vacuum	1 mbar to 10^{-3} mbar
High Vacuum (HV)	10^{-3} mbar to 10^{-8} mbar
Ultra-High Vacuum (UHV)	10^{-8} mbar to 10^{-12} mbar
Extreme high Vacuum (XHV)	Less than 10^{-12} mbar

Table 2.2: Definition of the different magnitude of vacuum.

This classification is somewhat arbitrary, nevertheless it is usually accepted. The more important difference is associated with the mechanism of gas flow. How gas behaves depends upon its state as determined by the Knudsen number (Kn):

$$Kn = \frac{\lambda}{D} \qquad \ldots(2.5)$$

where λ is the mean free path of the gaseous molecules and D a characteristic dimension of its container. When $\lambda << D$, thus $Kn << 1$, molecule – molecule collisions are the most likely way the gaseous molecules interact and the gas behave as a fluid. Gas in this state can physically be pumped out of the chamber, the same way water is sucked out of a vessel. When $\lambda >> D$, thus $Kn >> 1$, molecule – surface wall collisions are more likely to occur and the gas will behave as molecular. Now molecules are not following a proper trajectory behaving randomly inside the vessel, travelling from wall to wall without colliding to each other. This means that the gas can not be pumped in the traditional sense: gas is removed from the vacuum vessel when its molecules collide to the pump and are then trapped on it. From equation 2.1,

it is possible to derive the mean free path of gaseous molecules at the pressure present in the chamber and make a comparison between it and the diameter of the pipes and the vacuum vessels. For description purposes, the following thumb rule can be applied:

$$\lambda = \frac{0.007}{P} \text{ cm} \qquad \ldots(2.6)$$

where P is the pressure expressed in mbar. It appears clear that the Knudsen number depends upon the gas pressure and the size of the vacuum vessels. Typical external diameters of the flanges and pipes for the chambers used in UHV applications are 34, 70, 114, 152, 203 mm nominal [3]. We can refer to them, although the internal diameters can vary from manufacturer to manufacturer and the difference would not be so significant. The mean free path, λ, is greater than the smaller diameter reported, when $P < 2x10^{-2}$ mbar and the gaseous molecules will enter in molecular flow.

2.3.1. Obtaining UHV conditions

In order to obtain UHV condition a certain number of vacuum pumps are necessary, being each one able to create only a specific magnitude of vacuum. The typical vacuum pumps assembly for one of the vacuum vessels used is comprised of:

- Rotary mechanical pump (rotary vane pump) (figure 2.2): it can create a vacuum of 10^{-2} mbar, starting from atmospheric pressure. It is also used as backing pump for the turbomolecular pumps. The rotary pump physically removes gases from the system.
- Turbomolecular pump (figure 2.3): it consists of a rotor fitted with blades that spins at the same order of magnitude than the gas molecules move in the chamber. The gas molecules collide with the rotor and are then directed in the direction of the backing pump. The turbomolecular pump allows reaching vacuums of 10^{-9} mbar, pumping directly from atmospheric pressure. Nevertheless, best performances are usually obtained when it operates in a pressure range where molecular flow prevails. The turbomolecular pump physically removes gases from the system.

Fig. 2.2: One of the rotary pumps used in the system.

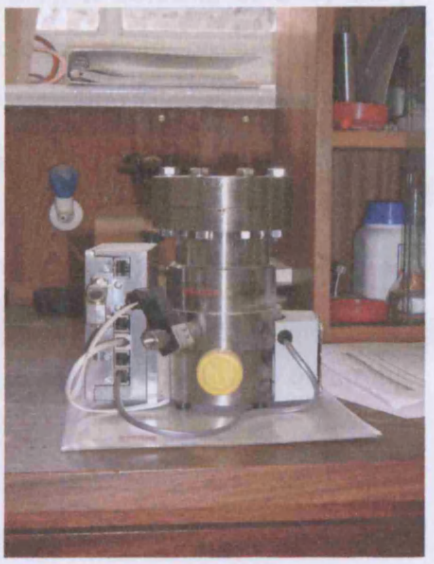

Fig. 2.3 (on the right): A turbo molecular pump.

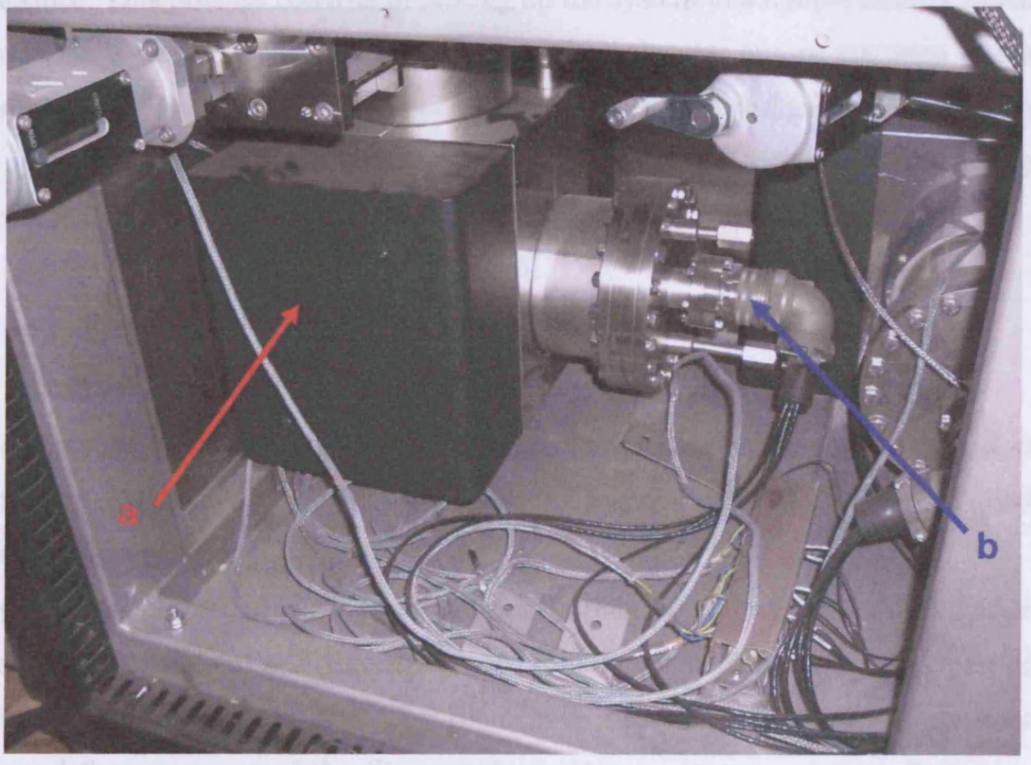

Fig. 2.4: One of the four Ion pumps present in the system is indicated by the red arrow (a); the titanium sublimation pump is indicated by the blue arrow (b).

- Ionic pump (a in figure 2.4): it consists of a chamber with two ionizing plates kept at 7 kV. The gases present in the pump are ionized by a plasma discharge due to the high voltage between anode and cathode. The ionization is enhanced by the presence of a magnetic field. The ionic pump does not remove gas from the system, it simply trap it.

- Titanium Sublimation Pump (TSP) (b in figure 2.4): it consists of a Ti-alloy filament from where Ti ions are sublimated in the chamber by passing a current through the filament. When gas molecules hit the Titanium filament they can be buried in it or react with it. Moreover, as the TSP is held inside the ion pump, sublimated Ti ions can react with the residual gases and hence increases the pumping effect. The ion pump and the TSP do not remove gas from the system. They only trap it such that it can not contribute to the pressure any more. The combination between ion pump and Titanium sublimation pump allows obtaining pressures of $10^{-11} - 10^{-12}$ mbar.

To help the pumps reaching UHV range pressure, bakeout of the system is necessary after the first installation and every time the system has been brought to air for maintenance. This process consists in heating up the system to a temperature between 100 and 120 °C for several hours, while only turbomolecular pumps are open to the vacuum vessels. The increase in temperature increases also the gaseous molecules mean speed, thus a bigger amount of gas can be removed. Degassing the ionizing filaments is usually performed after bakeout.

2.3.2. Measuring the pressure

There are several equipments allowing the measure the pressure; the ones present in the Omicron Multiprobe ® Surface Science System are Pirani gauges and Thermoionic Ion gauges.

Pirani gauges are employed in the backing lines for the turbo pumps. The Pirani gauge measures the resistance of a W filament placed into the vacuum line and being part of a Wheatstone bridge (figure 2.5). The filament is heated by supplying a constant voltage and the resistance of the filament depends upon its temperature. Collisions with gas molecules changes the temperature of the filament and hence its resistance. The Pirani gauge measures the out of balance current produced in the Wheatstone bridge and gives a pressure reading because the resistance of the filament can be calibrated as function of the pressure. Pirani gauges work from atmospheric pressure to 10^{-3} mbar.

The lower measuring limit is reached when the molecules are not enough to produce a further change in the temperature of the filament.

Fig. 2.5: A Pirani gauge.

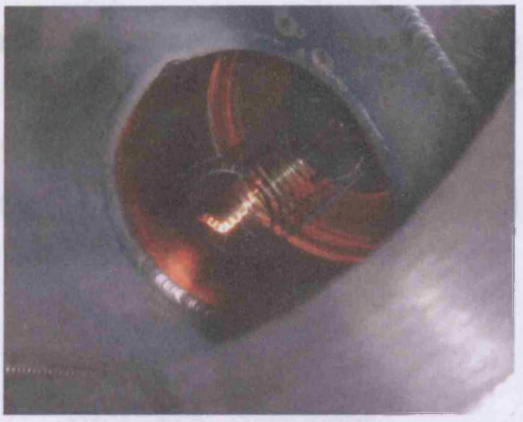

Fig. 2.6: An ion gauge retracted under working conditions inside a UHV chamber.

Thermoionic Ion gauges are used in order to measure pressures down to $10^{-11} - 10^{-12}$ mbar and they are located in the main vacuum vessels. The apparatus (figure 2.6) consists of a filament emitting electrons, by thermoionic effect. The electrons generated are accelerated inside the cage. Electrons collide on the gas molecules present in the cage and ionise them. These ions hit the central W filament, the collector, and produce a current directly proportional to the pressure of the gas molecules in the gas phase. When the number of gaseous molecules become to low, the ion gauge reaches its limit because the ions produced are not enough to generate a current on the collector filament.

A side effect using ion gauges is represented by desorption of residual gases, such as H_2, CO and CO_2, from the filament [3]. This factor can be minimised by degassing the filament before use. This is a practice common to all the ionising filaments present in the system. It consist in gradually increasing the current passing through the filament from the minimum value, to the maximum (usually the operating current), thus inducing thermal desorption of gaseous molecules adsorbed on it.

2.3.3. Residual gas analysis

Residual gas analysis is a technique commonly used in order to know the composition of the residual atmosphere in the chamber. It is usually performed using a Quadrupolar Mass Spectrometer. This instrument permits also to measure the pressure, determine the purity of gases prior or during experiments, leak detection and with the proper setup Temperature Programmed Desorption (TPD) experiments.

A description of the Mass Spectrometer with Quadrupolar analyser is presented in figure 2.7.

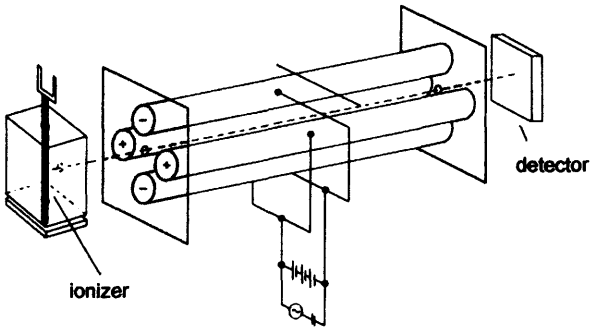

Fig. 2.7: A schematic representation of a quadrupolar mass spectrometer.

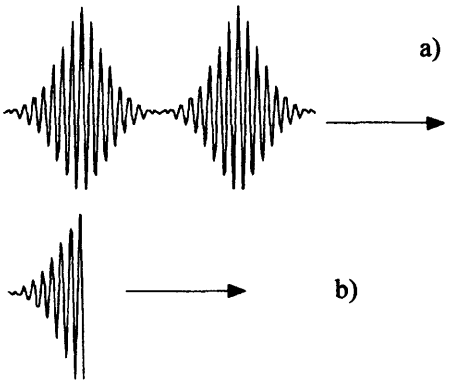

Fig. 2.8: Resonant (a) and not resonant (b) pathways of the electrons inside the quadrupole rods; the arrow indicates the direction parallel to the rods .

The Quadrupolar Mass analyser consists of four conducting rods parallel among themselves. Two opposite bars are connected to the positive pole of a variable DC generator, while the other two are connected to the negative pole. An AC RF voltage, out of phase of 180°, is also applied to each couple of bars. This setting allows adjacent bars to have the same tension in modulus $|U+V\cos(\omega t)|$, but opposite in sign and to invert their polarity every 2ω. The result is the production of a complex magnetic field between the bars. The gas molecules arriving into the ionisation region (a W filament) are ionised and accelerated inside the quadrupole region. Here the interaction of the charged ions with the magnetic field results in complex trajectories for the ions (figure 2.8, shows a plot of resonant and not resonant pathways in one direction, x or y, for the electrons inside the quadrupole region; the arrow indicates the direction of the quadrupole length, z). Varying opportunely the DC potential U and the AC potential V from minimum to maximum, ions with different mass can describe a

stable pathway inside the analyser and be detected by the electron multiplier positioned at the end of it. The ions describing an instable pathway collide to the analyser bar, are converted to neutral molecules and pumped away.

The system is equipped with two Quadrupolar Mass Spectrometers, one on the P and the other on the A chamber, from MKS Instruments, allowing to measure 200 amu (being 1 amu the mass of one atom of hydrogen).

2.3.4. Sample cleaning

Obtaining a clean surface is the first step for all surfaces science studies. This is normally achieved by cycles of sputtering and annealing. Sputtering consists of the physical removal of surface material by bombardment of the surface with a beam of high-energy argon ions (100 – 3000 eV typically). The collision of argon ions causes surface atoms to break their bonds with the substrate and desorb into the vacuum. Because of the violent nature of the process, sputtering leaves a damaged and rough surface. It is necessary to perform an annealing procedure of the substrate both to facilitate surface diffusion (and hence the removal of defects sites so that a flat and clean surface can be produced), and also to desorb argon atoms embedded in the substrate itself. The temperatures of annealing are usually below or close to the melting point of the crystal. As annealing may lead to segregation of impurities from the bulk of the sample to the surface, sputtering needs to be repeated several times. Periods of between several hours and several days of sputtering and annealing cycles may be necessary to obtain a surface enough clean to perform experiments.

Once cleaned, the surface should be kept clean at least over the period of an experiment (several minutes to hours). The rate of contamination depends upon the rate at which gaseous molecules collide with the surface and upon their sticking probability. As from consideration of the kinetic theory of gases, the rate of surface bombardment by molecules directly depends upon the ambient pressure, the UHV is necessary to reduce the amount of collision to as small as possible.

2.3.5. Sample mounting

The system allows mounting the sample in different ways, according to the range of temperature in which the experiments will be performed. The preferred way consisted in mounting the single crystal being studied by clamping it onto a stainless steel sample plate using two tantalum strips spot welded on the sample plate (figure 2.9). This allows a good heat transfer between the heating source via the use of an electronic bombardment heater (E-beam) and the sample, and a wide free sample area where to perform experiments.

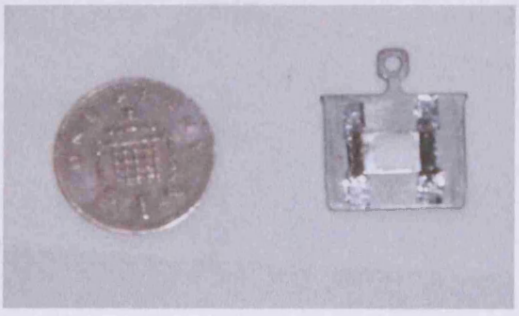

Fig. 2.9: On the right, the Pt(111) single crystal mounted on a stainless steel sample plate. On the left, a 1p coin as a size reference.

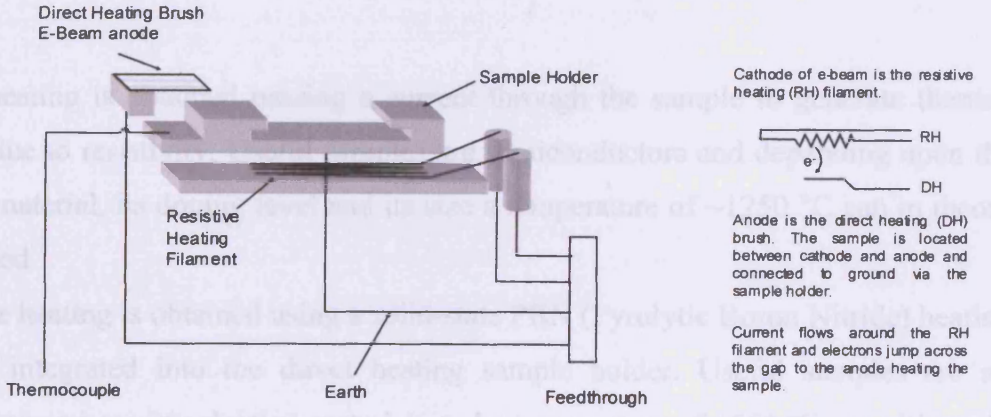

Fig. 2.10: A schematic representation of the different annealing options available.

The E-beam heater (figure 2.10) consists of a cathode represented by a Thoria-coated Ir filament emitting electrons. As a high voltage (~650 V) is applied between the cathode and the anode, the electrons flowing through the filament are accelerated towards the anode and their collision with the sample located between cathode and anode produces heat. It allows reaching ~1250 °C within a very short time.

Despite the fact that the sample can be annealed to very high temperatures, it can not be cooled to low temperatures (liquid nitrogen, or liquid helium), using this setup. Other ways to mount the sample are using the appropriate holder to allow reaching high temperatures or low temperatures. High temperatures can be reached using a VT (variable temperature) Sample Plate Direct Current Heating or a VT Sample Plate Resistive Current Heating (figure 2.11).

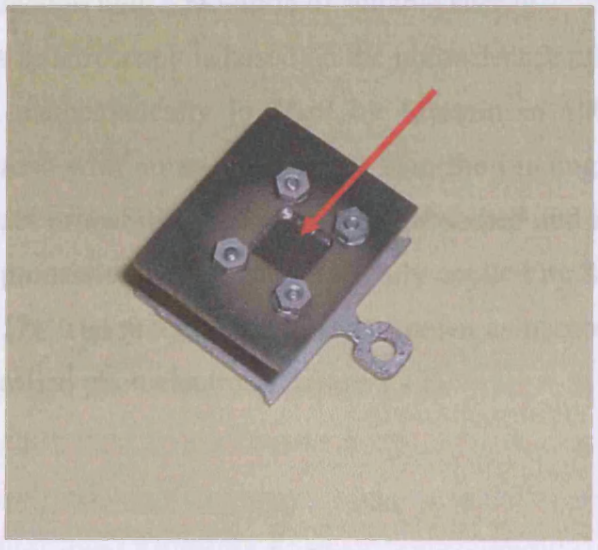

Fig. 2.11: The Pt(111) single crystal, indicated by the arrow, mounted on a Resistive Heating Sample Holder.

Direct heating is obtained passing a current through the sample to generate thermal energy due to resistivity. Useful samples are semiconductors and depending upon the sample material, its doping level and its size a temperature of ~1250 °C can in theory be reached.

Resistive heating is obtained using a solid-state PBN (Pyrolytic Boron Nitride) heating element integrated into the direct heating sample holder. Useful samples are all conducting and semiconducting materials and a temperature of ~550 °C can ultimately be reached. Low temperature experiments can be performed using a VT Sample Cooling Plate.

2.4. X-Ray Photoelectron Spectroscopy (XPS)

X-Ray Photoelectron Spectroscopy, also known as Electron Spectroscopy for Chemical Analysis (ESCA), allows both quantitative and qualitative analysis of the surface of solid samples. By XPS it is possible to determine the elementary composition and the chemical state of the different species present on the surface sample by measuring the Kinetic Energy of the photoelectrons emitted after the interaction with a radiation of suitable energy.

This spectroscopy is based on the photoelectric effect discovered by Hertz in 1887 [5] and mathematically justified by Einstein in 1905 [6]: when a material is hit by photons with an energy greater than the binding energy of the electrons, there is a certain probability that a photon is absorbed and an electron expelled. The physics of the process was then technologically applied by Siegbhan and co-workers in the mid-'60 [7]. The process is generally known as photoemission and the expelled electrons are called photoelectrons (figure 2.12).

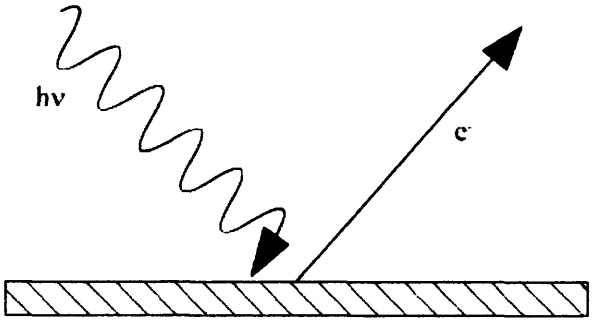

Fig. 2.12: Schematic representation of the photoelectric effect.

In other words, the photoelectric effect is the observation that a minimum of energy (or frequency of light) is needed to remove any electron. This minimum energy corresponds to the work function (ϕ) of the material. Work functions of bulk materials are always less than the first ionization energy of the element. This is due to relaxation effects in the bulk material. Work functions can be altered by changes in the chemistry and composition of the surface of a material. For metals, work functions also depend on the lattice plane.

2.4.1. Koopmans' theorem

According to Koopmans' theorem the binding energy of an ejected photoelectron is equal in energy to the orbital from which the electron is ejected. This is true under the assumption that the orbital from where the photoelectron is ejected leaves does not interact in anyway with the cloud of the remaining electrons in the solid within the timescale of photoemission, i.e. that the spatial distribution of the electrons after the photoemission remains the same as before. However, the relaxation of the electron cloud occurs in the ion in order to minimize the effect of the positively charged core hole created during the ionization. The effect of the electron relaxation is a lowering in binding energy values than are actually seen and are attributed to differences between the initial and final states, which results in higher observed kinetic energy. In any case, the entity of this shift is not more than few eV and allows the identification of the orbital from which the electron has been generated.

2.4.2. The excitation process

In the mono-electronic approximation, the energetic balance of the excitation process is represented by the Einstein equation:

$$h\nu = BE + KE \qquad \ldots(2.7)$$

where $h\nu$ is the energy of the incident photon, BE the binding energy of the electron, referred to the vacuum level, and KE the kinetic energy of the expelled electron. A schematic description of the process is reported in figure 2.13. As already noted, in gas-phase spectroscopy BE is equal to the ionisation energy, whereas in solid-phase it is more convenient to refer to the Fermi level and the energetic balance became:

$$h\nu = BE + KE + \phi \qquad \ldots(2.8)$$

where ϕ is a correcting factor representing the work function. In this case the work function takes into account not only the energy necessary to remove an electron from the highest occupied energy level in the solid (the "Fermi level"), to the "vacuum level" but also the electrostatic environment in which the electron is generated and measured and some instrumental correction factors.

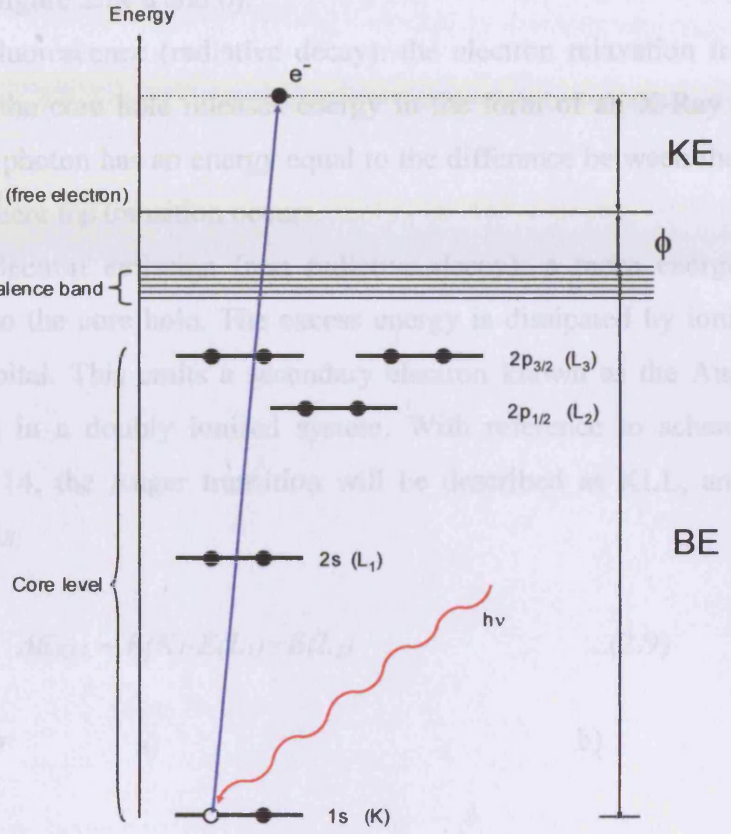

Fig. 2.13: Schematic representation of the ejection of an electron induced by a photon in relation to the energetics of the process.

The work function dependence on the spectrometer implies some important consideration. First of all, for a proper detection, it is necessary that sample and detector are at the same potential. This is typically obtained connecting both sample and detector to ground. Then, it is important to have a very well know value of radiation to irradiate the sample and stimulate electronic emission. This is usually achieved using a monochromatic X-Ray source. Moreover, the detector work function should be accurately known, as the BE calculation depends upon it.

2.4.3. Relaxation of excited system

The photoelectric excitation leaves the system in an excited state, with a negative charge missing, i.e. a core hole. The system stays in this excited state for a very short time ($\Delta E_n \sim 10^{-15} - 10^{-16}$ sec), then relaxes to rearrange the charge distribution by

filling the core hole with an electron from an outer shell. This can happen in two different ways (figure 2.14 a and b):

1) X-Ray fluorescence (radiative decay): the electron relaxation from an outer shell to the core hole releases energy in the form of an X-Ray photon. The released photon has an energy equal to the difference between the two energy levels where the transition occurs.
2) Auger electron emission (non radiative decay): a more energetic electron relaxes to the core hole. The excess energy is dissipated by ionisation of an outer orbital. This emits a secondary electron known as the Auger electron, resulting in a doubly ionised system. With reference to scheme shown in figure 2.14, the Auger transition will be described as KLL, and its energy balance is:

$$\Delta E_{KLL} \sim E(K)-E(L_1)+E(L_2) \qquad ...(2.9)$$

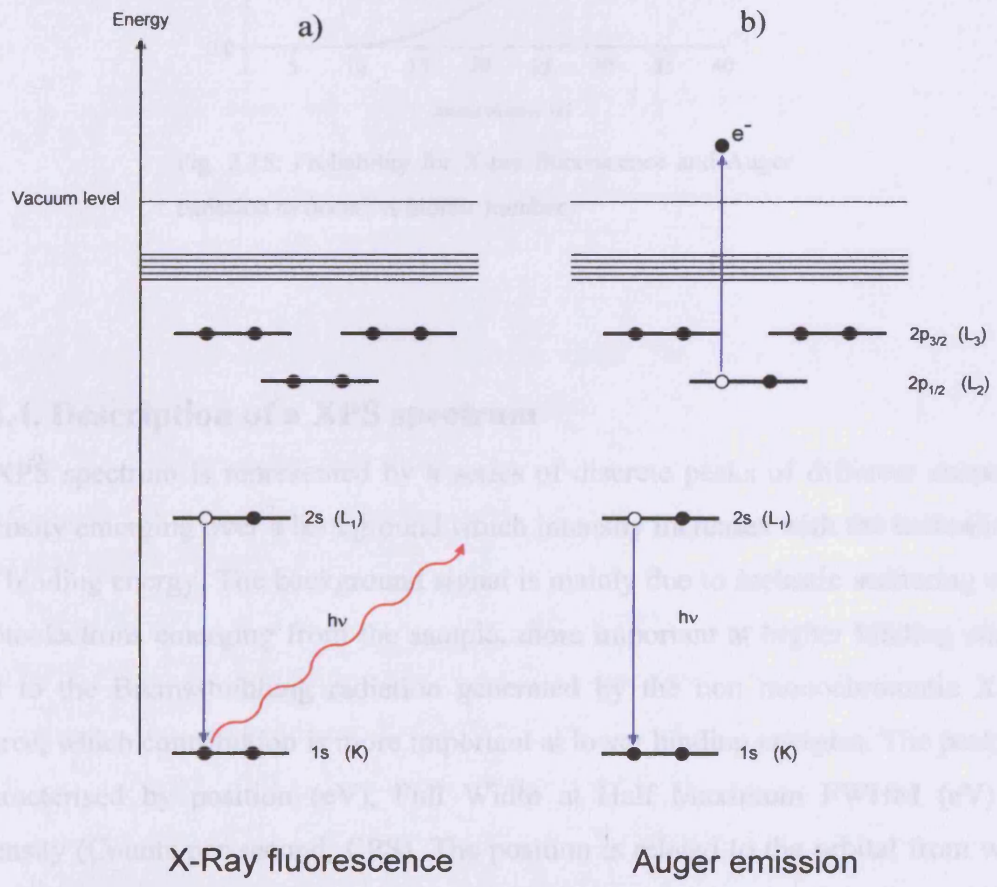

Fig. 2.14: a) X-ray fluorescence energy diagram and b) Auger emission energy diagram.

Auger emission and X-Ray fluorescence are competitive processes. Auger electrons are analysed along with the photoelectrons, via the same analyser, giving contributions on an XP spectrum. However, Auger electrons are distinguishable from photoelectrons because of the independence of their kinetic energy upon the photon energy. Both decay processes are very rapid, resulting in extremely short lived core holes and are dependent on atomic number (Z). Auger decay dominates the low atomic number region (Z<20) whereas X-Ray fluorescence becomes more important as the atomic number increases (figure 2.15).

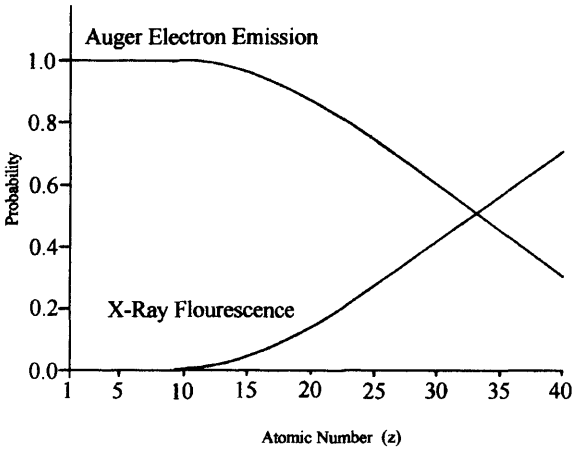

Fig. 2.15: Probability for X-ray fluorescence and Auger emission to occur, vs atomic number.

2.4.4. Description of a XPS spectrum

A XPS spectrum is represented by a series of discrete peaks of different shape and intensity emerging over a background which intensity increases with the increasing of the binding energy. The background signal is mainly due to inelastic scattering of the photoelectrons emerging from the sample, more important at higher binding energy, and to the Bremsstrahlung radiation generated by the non monochromatic X-Ray source, which contribution is more important at lower binding energies. The peaks are characterised by position (eV), Full Width at Half Maximum FWHM (eV) and intensity (Counts per second, CPS). The position is related to the orbital from which the photoelectrons are generated, the FWHM is related to a contribution of different

parameters (see below) and the intensity is mainly correlated to the amount of material analysed and to the cross-section of the ions.

In figure 2.16 the survey XP spectrum of a clean Cu(111) single crystal obtained using a Mg excitation source is presented.

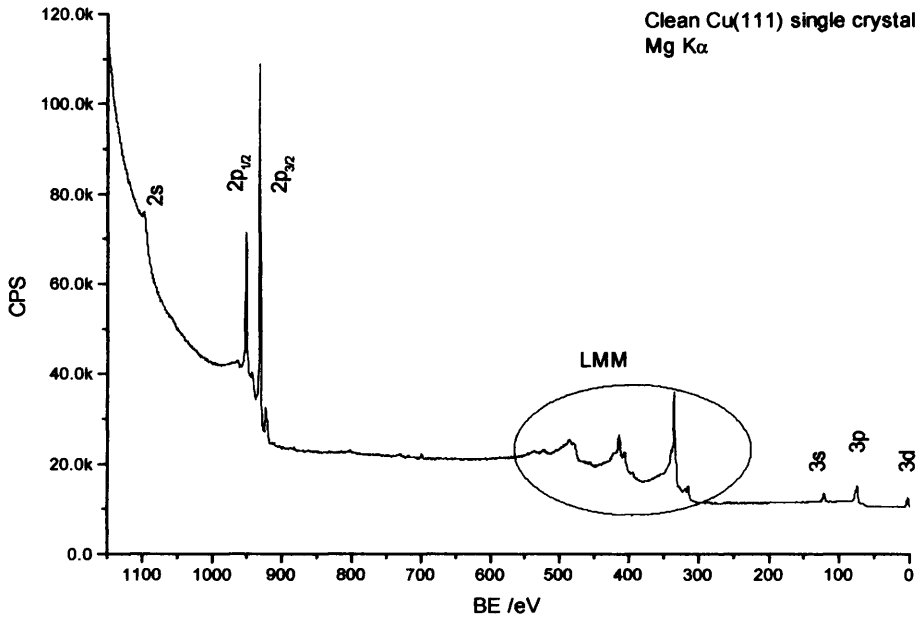

Fig. 2.16: Survey XP spectrum collected using a Mg excitation source.

The XP peaks are indicated taking into account the following notation: to the principal quantum number n follows the symbol s, p, d, f, ..., depending upon the value of the angular quantum number l (0, 1, 2, 3, ...), with subscript the value of the total angular momentum J, (usually omitted for the s shell). The Auger peaks are indicated using the following notation: three letters indicating respectively the shell where the initial core hole was localised, the outer shell from which the electron relaxes to fill the hole in the inner shell and the shell from where the ejected electron is generated. The letter used are K, L, M, ..., corresponding to the quantum number n (0, 1, 2, ...). On the subscript a number related to the spin multiplicity is added.

2.4.4.1. Spin-orbit splitting

When l>0, the magnetic coupling between the spin of an unpaired core electron with its angular momentum induces splitting known as spin-orbit splitting. Following

photo-ionisation an unpaired electron remains which can have its spin vector (s = 1/2) parallel or anti-parallel to its orbital angular momentum vector (l). For a one-hole configuration this resolves the degenerate hole state into two components, where the total orbital quantum number, $J = L \pm S$. For the Cu (2p) spectrum, l = 1 and s =1/2. This give raise to two components indicated as Cu ($2p_{3/2}$) for the anti parallel configuration and Cu ($2p_{1/2}$) for the parallel configuration. The respective intensities of these final states are given by (2J + 1), resulting in a Cu ($2p_{3/2}$): Cu ($2p_{1/2}$) intensity ratio of 2:1.

2.4.4.2. Multiplet splitting

Multiplet splitting (also known as spin-spin interaction) of the photoelectron peak occurs when an unpaired valence electron interacts with the unpaired core hole electron. This results in two final states, which are dependent upon the alignment of the spin vector (s) of the electrons, either parallel or anti-parallel, resulting into a multi-component asymmetrical splitting of the XP lines or as binding energy shift. It is usually less important than spin-orbit splitting.

2.4.4.3. Shake Up and Shake Off Processes

Shake Up and Shake Off Processes are due to the transfer of energy from the photoelectrons to valence electrons, followed by relaxation processes. They will appear as satellite features at the low kinetic energy side of the main peak.

Shake Up processes arise when a valence electron is excited simultaneously with the photo-ionisation event to a higher, unoccupied state. These satellite features are sometimes useful for the identification of the chemical state of an element.

Shake Off processes occur when a valence electron is expelled off the atom resulting in a doubly ionised state and a very broad XP feature. Shake Off processes do not offer spectroscopic information and the signals tend to be lost into the background of inelastically scattered electrons.

2.4.4.4. Plasmon Loss Effect

With certain conducting materials, there is the possibility that some of the kinetic energy of the ejected photoelectron may induce oscillations in the conduction band as it passes through the solid. These oscillations are known as Plasmons Losses and appear normally at binding energies 20-25 eV higher that the parent peak.

2.4.4.5. X-Ray Satellite and Ghost Peaks

Non monochromatic X-Ray radiation presents satellite lines at lower binding energies, with intensity and spacing characteristic of the X-Ray anode material, generated from less probable transitions. This gives rise to additional features in the XP spectrum. The pattern of these additional lines is presented in the following table (2.3):

Emission peak	$\alpha_{1,2}$	α_3	α_4	α_5	α_6	β
Mg displacement /eV	0	8.4	10.1	17.6	20.6	48.7
Relative height /%	100	8.0	4.1	0.6	0.5	0.5
Al displacement /eV	0	9.8	11.8	20.1	23.4	69.7
Relative height /%	100	6.4	3.2	0.4	0.3	0.6

Table 2.3: X-Ray satellites displacements and relative heights for the Mg and Al excitation anodes.

Ghost peaks are due to X-radiation from an element other than the X-Ray source anode exciting the sample. This generates peaks corresponding to the most intense XP peaks, but displaced by a characteristic amount of energy related to the difference in energy between the two X emitters. Occasionally anode contamination occurs, i.e. Mg impurities on the Al anode, or vice versa, or Cu migration from the anode base structure, generating unattended XP lines.

2.4.4.6. Peak widths

The XP lines are expected to be Dirac's delta functions with zero width, but each peak is characterised by a finite FWHM quantified as:

$$\Delta E_{FWHM} = (\Delta E_a^2 + \Delta E_f^2 + \Delta E_n^2)^{1/2} \qquad \ldots(2.10)$$

where ΔE_a is the analyser resolution (see below), ΔE_f is the width of the X radiation used and ΔE_n is directly correlated to the lifetime broadening. ΔE_a for the analyser used is ~ 0.8 – 1.0 eV and ΔE_f is respectively 0.7 eV for the Mg anode and 0.85 eV for the Al anode. Being $\Delta t \sim 10^{-15} - 10^{-16}$ sec the lifetime of the photoelectron from when it has been emitted to the time it needs to reach the detector and be recorded, from Heisenberg's Uncertainty Principle, an estimation of $\Delta E_n \sim 0.33$ eV. Thus, ΔE_{FWHM} is in theory ~1.11 – 1.35 eV. However, the peaks are usually not that narrow,

because of all the other phenomena previously described that contribute to the generation of the XP spectrum.

2.4.5 Qualitative and quantitative analysis

XPS allows quantitative and qualitative analysis to be performed on the sample being analysed. The identification of the elements present in the XP spectrum can be obtained assigning the lines to the respective element, by comparison with a database [8, 9, 10]. Chemical state identification and quantification can be performed only after appropriate data collection (narrow scans) and correction for static charging, if present.

2.4.5.1. Surface sensitivity in XPS

XPS is known to be a surface specific spectroscopic technique due to the escape depth of the emitted photoelectron. Although X-Rays can penetrate the sample for several mm, the measured photoelectron signal originates from a surface depth not more than ~50Å, due to the inelastic scattering of the emitted electrons within the sample. The so called inelastic mean free path (IMFP, λ) is a measure of the average distance travelled by an electron through a solid before it is inelastically scattered.

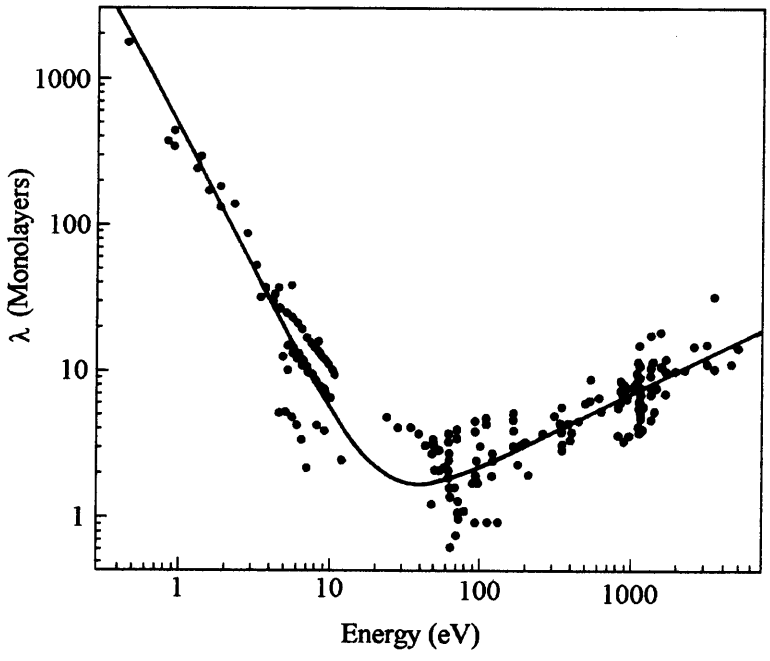

Fig. 2.17: The so called universal curve.

The electron IMFP for a material is dependent upon the photoelectron kinetic energy, this dependence being known as the "universal" curve (figure 2.17) [11]. If electrons with kinetic energies between 10 - 1500 eV are measured, their escape depths will be less than 20 Å, thus electrons can be considered to come from the surface region (Appendix A describes some mathematical models to derive the IMFP). Only photoelectrons that escape from the solid without suffering a reduction in energy contribute to the primary photoelectron signal. For an electron path length (d) through a thin film of material the resulting photoelectron flux will be given by,

$$I = I_0 \exp\left(\frac{-d}{\lambda}\right) \qquad \ldots(2.11)$$

Since I represents the detected electron flux originating from below a depth (d), for emission from a solid surface, the photoelectron flux originating *within* this depth is given by (figure 2.18),

$$I' = I_0\left[1 - \exp\left(\frac{-d}{\lambda}\right)\right] \qquad \ldots(2.12)$$

Fig. 2.18: The detected photoelectron flux passing through a thin film (thickness d), and originating from within a surface depth (d).

2.4.5.2. Angle Resolved XPS

For increased sensitivity towards the outer atomic layers of the surface, it is possible to vary the collection angle (ϕ) between the analyser and the surface. Reducing ϕ photoelectrons collected from a depth (d) will have further to travel through the material before reaching the detector. Since the maximum path length of the detected

photoelectron (d^1) must remain constant, only photoelectrons from the outermost layers will escape without losing energy. Equation 2.11 must now be rewritten to take into account the effect of the detection angle (ϕ), which will affect the flux of photoelectrons detected. The effective path length (d') is given by:

$$d' = d/\cos\phi \qquad ...(2.13)$$

The equation for the photoelectron flux now becomes,

$$I = I_0 \exp\left(\frac{-d}{\lambda \cos\phi}\right) \qquad ...(2.14)$$

Equation 2.14 can be used to calculate the thickness of a substrate deposited onto the sample (figure 2.19).

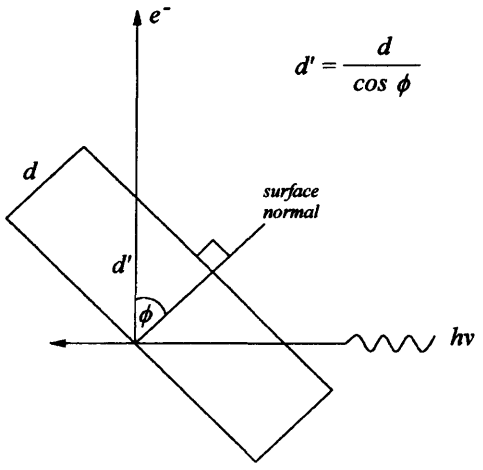

Fig. 2.19: Off-normal photoelectron detection angle

2.4.5.3. Qualitative analysis and chemical shift

The identification of the chemical species present on a sample is usually done by assigning the peaks present in the XP spectrum, by comparison of the line positions with a reference database [8, 9, 10]. Another analytical feature of XPS is the chemical shift, the measurable binding energy difference between two or more non-equivalent chemical environments of the same element. The variation on chemical environment

of an atom causes a variation in its electron density, originating changes in the chemical shift. For example, the N(1s) binding energy of a nitrite group is around 404 eV, whereas it is around 407-408 eV for the nitrate group. For an electron tightly held in a positively charged species, the binding energy will be higher. On the same way, if the positive charge in the system increases, also the binding energy will increase, as more energy is required to remove the electron from an already positively charged atom.

2.4.5.4. Quantitative analysis

The relative concentrations of the different constituents of a sample can be determined via quantitative analysis. For a homogeneous sample, the number of photoelectrons per second (I) in a specific spectrum is given by

$$I = nf\sigma\theta y\lambda AT \qquad \ldots(2.15)$$

where n is the number of atoms of the element per cm^3 of the sample, f is the X-Ray flux in photons cm^{-2} sec^{-1}, σ is the photoelectric cross-section for the atomic orbital considered in cm^2, θ is an angular efficiency factor based upon the angle between the X-Ray gun and the detector, y is the efficiency of photoelectron formation, λ is the IMFP of the photoelectron within the sample, A is the area of the sample from where photoelectrons are collected and T is the transmission coefficient of the detector.
Rearranging the previous:

$$n = I/f\sigma\theta y\lambda AT \qquad \ldots(2.16)$$

and the denominator can be defined as the atomic sensitivity factor S, therefore:

$$n = I/S \qquad \ldots(2.17)$$

The composition of a sample of n elements can be calculated by:

$$C_x = \frac{n_x}{\sum_1^n n_i} = \frac{I_x/S_x}{\sum_1^n I_i/S_i} \qquad \ldots(2.18)$$

where C_x is the concentration of the element x, I_x is the amount of photoelectrons generated by element x and S_x the atomic sensitivity factor of the element x. Matrix correction factors are neglected.

2.4.5.5. Charging

During XP analysis, insulating samples tend to accumulate positive electrostatic charge due to the electron emission process. This can create ambiguities in the peak assignment process as the amount of charging can reach several eV and shift the spectrum toward higher binding energies. A way to avoid the problem is to use a charge neutraliser gun that should emit electrons towards the sample and neutralise the electrostatic charge. Otherwise, charge correction methods can be applied during data manipulation. For example the spectrum can be calibrated measuring the C(1s) peak and assigning the value of 284.5 eV to it. The rest of the spectrum will be corrected accordingly. Working with pure metals, it is possible to calibrate the spectrum to the XP lines of the metal (this is at the base of the instrument calibration process, using for example, alone or in combination, gold, silver and copper).

2.4.6. Description of components of the Omicron XPS

A X-ray Photoelectron Spectroscopy facility is present in the A chamber of the Omicron Multiprobe ® Surface Science System. Figure 2.20 shows the inside of the vacuum vessel, taken from the horizontal manipulator flange, where the samples can be loaded. The different components can be identified as follows: starting from the top right corner the X-ray gun is visible (a), then proceeding clockwise, the Inelastic Scattering Spectroscopy gun (b), the UV-lamp (c), the electronic analyser entrance (d), the charge neutralizer (e), one of the metal evaporators (f), a Mass Spectrometer (not on focus, in the background, g) and the vertical manipulator probe (h), for EPR measurements.

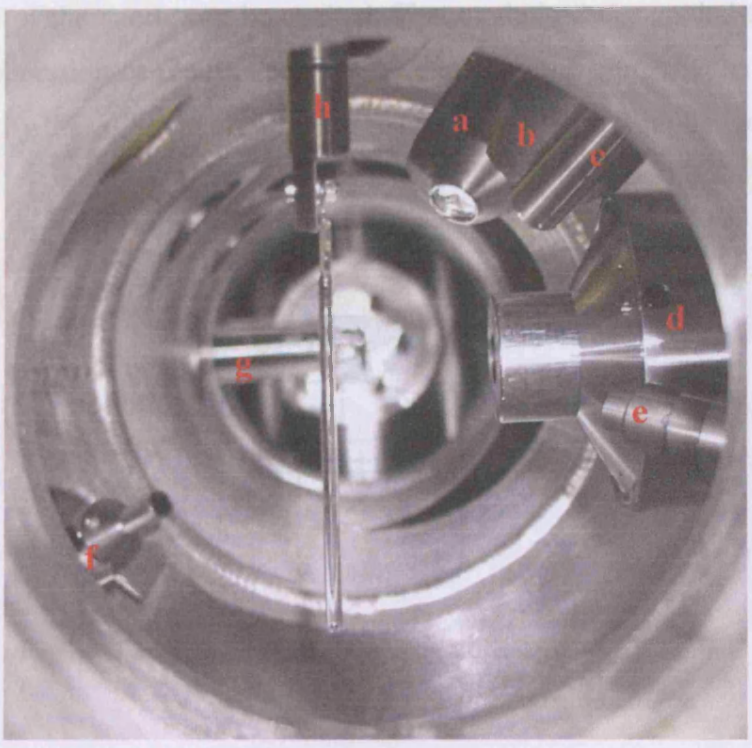

Fig. 2.20: The inside of the analysis chamber. The letters refer to the different components present. See text for description.

2.4.6.1. The X-Ray gun

The X-Ray gun is a twin anode DAR 400 X-Ray Source, allowing either Mg Kα (1253.6 eV) or Al Kα (1486.6 eV) radiation to be selected [12]. The advantage of a twin anode source is represented by the possibility to switch between sources to resolve any interference, which can occur between the photoelectron and the Auger electron signals. Auger electrons kinetic energy is independent of the photoelectron energy, therefore only the photoelectron signal is affected by changing the anodes. Thus, on a kinetic energy scale, photoelectron peaks will be shifted by 233 eV, being 233 eV the difference in energy between the two anode sources. On a binding energy scale, Auger peaks will by shifted by the same amount.

The operating principles of the X-ray source are shown in the schematic in figure 2.21. A heated ThO_2-Ir filament, kept at ground potential, bombards the selected anode, at a high positive potential. The high potential difference between the filament and the anode is necessary to accelerate the electrons. By switching the filament used,

the other face of the anode can be excited. The anode is water cooled to prevent Mg and/or Al evaporation or melting of the Cu support in the worst of the cases. X-rays are generated by the collision of the electrons with the selected anode face.

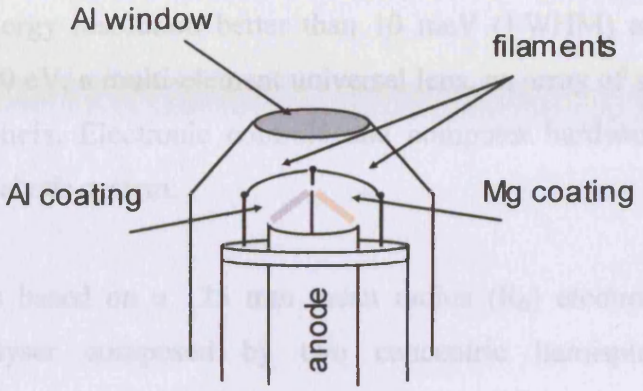

Fig. 2.21: X-ray gun schematic representation.

A thin aluminium foil window (2 μm thick) is placed in front of the X-Ray source. The Al window forms a sort of vacuum barrier between the X-Ray source and the sample, allowing the source to be differentially pumped. The Al window also shields the sample from stray electrons, heating effects and contamination originating in the source region. The window also blocks approx the 80% of Bremsstrahlung radiation - a broad continuous energy background caused by other electronic transitions within the source (figure 2.22).

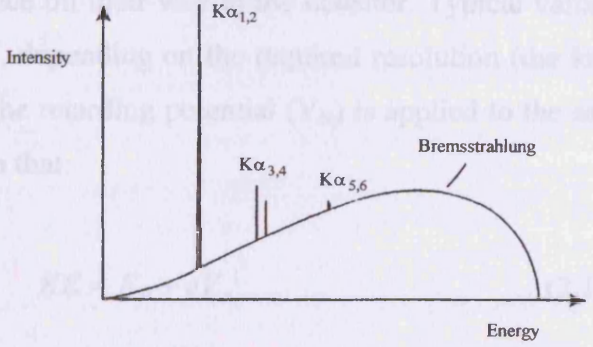

Fig. 2.22: X-ray emission spectrum. Main transitions ($K\alpha_i$) are superimposed on the rising Bremsstrahlung background. Note that the transitions $K\alpha_i$ are responsible for the X-Ray induced satellite structure described in section 2.4.4.5.

2.4.6.2. The EA125 Energy Analyser [13]

The EA 125 Energy Analyser assembly consists of a hemispherical electrostatic analyser allowing the measurement of the kinetic energies of the electrons generated during photo-emission experiments and ions from ion-scattering spectroscopy, featuring an energy resolution better than 10 meV (FWHM) and a kinetic energy range up to 2000 eV, a multi-element universal lens, an array of seven Channeltron ® electron multipliers. Electronic controls and computer hardware-software package complete the analysis system.

The EA 125 is based on a 125 mm mean radius (R_0) electrostatic hemispherical deflection analyser composed by two concentric hemispheres. To the two hemispherical surfaces of radii R_1 (inner sphere) and R_2 (outer sphere), a potential difference (V) is applied in the way that the inner is positive and the outer is negative. These potentials act producing an area of zero potential (V_0) at the same distance from each hemisphere at radius R_0, where

$$R_0 = \frac{R_1 + R_2}{2} \qquad \ldots(2.18)$$

When electrons enter the analyser they encounter an applied retarding potential (V_R) between the hemispheres, which decrease the electrons to a constant kinetic energy, known as the analyser pass energy (E_P). Only electrons travelling in the R_0 orbit with this pass energy will pass through the analyser without colliding with either hemispheric surface on their way to the detector. Typical values of pass energies are 20, 50 or 100 eV, depending on the required resolution (the lower the E_P, the higher the resolution). The retarding potential (V_R) is applied to the sample to decelerate the photoelectrons, so that:

$$KE = E_P + eV_R \qquad \ldots(2.19)$$

where KE = Photoelectron kinetic energy, E_P = Analyser pass energy, e = electron charge, V_R = retarding potential. The equation relating pass energy and the applied retarding potential is shown in Equation 2.20:

$$eV_R = E_P\left[\frac{R_2}{R_1} - \frac{R_1}{R_2}\right] \qquad \ldots(2.20)$$

The reciprocal of the term in brackets is known as the Hemispherical Constant. Changing the retarding potential it is possible to vary the kinetic energies of the photoelectrons passing through the analyser to the detector. Normally the retarding potential is linearly ramped so that the electrons of decreasing kinetic energy are analysed.

A diagram of the Concentric Hemispherical Analyzer is shown in figure 2.23. The analyser entrance and exit are fitted with slit mechanisms. The slits can be operated independently resulting in a large combination of aperture sizes (entrance) and filters (exit), reflecting on the analyser resolution. At the analyser entrance a universal lens assembly collects the electrons generated from the sample, focuses them onto the entrance slit and simultaneously adjusts their kinetic energy to match the pass energy of the analyser. In particular, the first lens selects the analysis area and angular acceptance and the second retards or accelerates the electrons to match the E_P.
The analyser acts as a band–pass energy filter for electrons at a specific energy E_P and has a finite energy resolution ΔE dependant upon the specific operating conditions given by:

$$\Delta E + E_P\left(\frac{d}{2R_0} + \alpha^2\right) \qquad \ldots(2.21)$$

where d = slit width, R_0 = mean radius of hemispheres and α = half angle of electron entering the analyser (at entrance slit; in radiant units) (figure 2.24).

The detector is represented by an array of seven Channeltron ® electron multipliers, placed across the exit plain of the analyser. A Channeltron ® consists of a coiled tube of semi conducting glass, coated on the inside with a high secondary electron coefficient material (lead oxide), a material that easily produces electrons when excited by photoelectrons (figure 2.25 a and b)

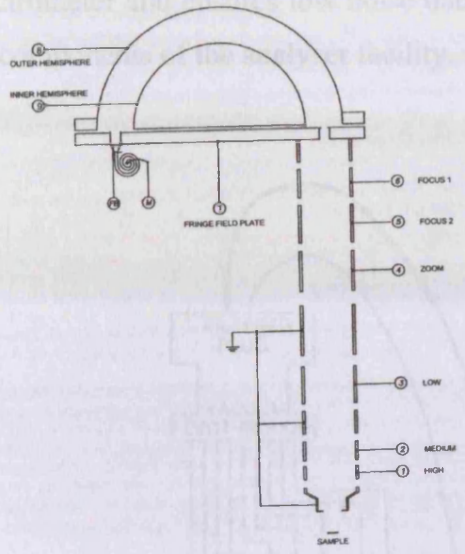

Fig. 2.23: A diagram of the Concentric Hemispherical Analyser [13].

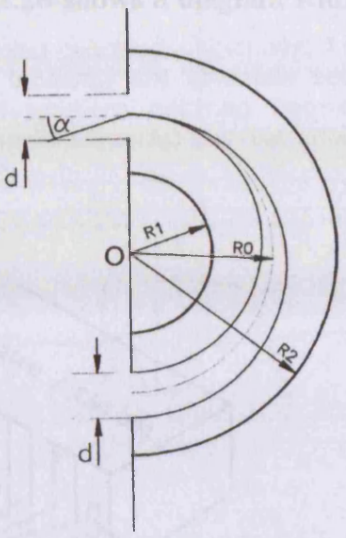

Fig. 2.24: Principle of operation of the Concentric Hemispherical Analyser.

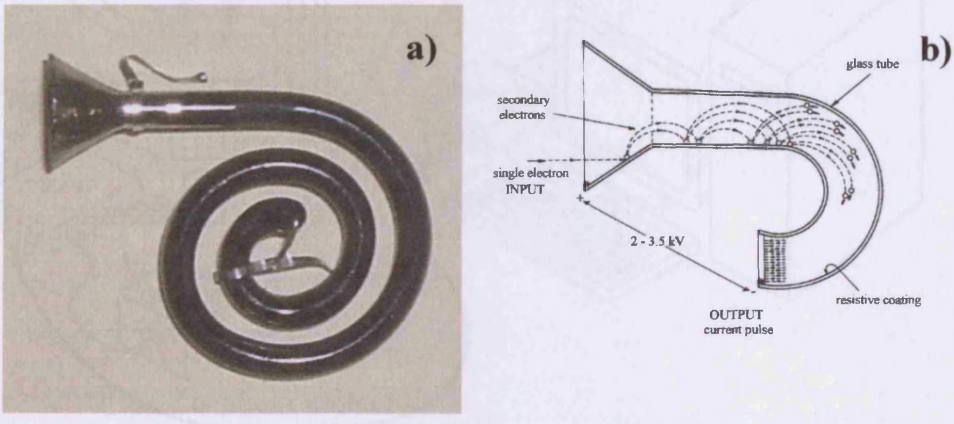

Fig. 2.25: a) A picture of a Channeltron ® electron multiplier and b) a scheme with the principle of its operation.

In order to drain the electrons a positive voltage bias (+2.3 - 2.8 V) is applied to the Channeltron ®. The small electron current (10^{-16} to 10^{-13} A) emerging from the analyser magnetic sector is amplified by a factor of 10^7 - 10^8 by the Channeltron ® and directed to a preamplifier that filters off the system noise using a high speed threshold circuit comparator. From the preamplifier, the electric signal is converted to optical signal which is transmitted to the receiver unit via optic fibre link. The optical receiver converts back the optical signal into electric signal and pass it to a computer counter. The use of optical link isolates the pulse counting system from the

spectrometer and ensures low noise data level. Figure 2.26 shows a diagram with all the components of the analyser facility.

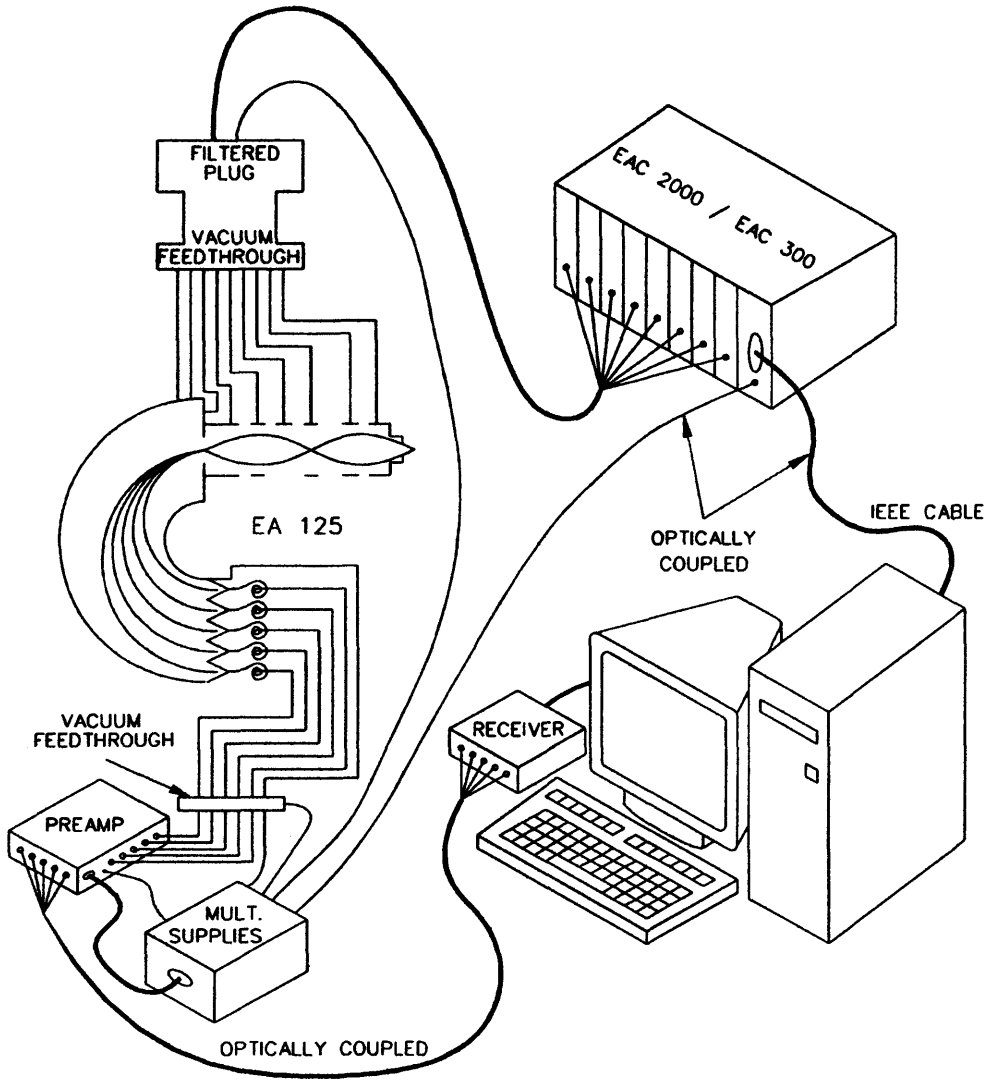

Fig. 2.26: Overview of the different parts of the analyser [13].

2.4.6.3. Charge neutralizer [14]

A NU-05 Charge Neutraliser is present into the system. It is designed to deliver a high current density of 1 to 10 eV electrons to insulating or semi-conducting samples that can be affected by charging problems during XP analysis. The electron source is a BaO_2 cathode that can supply a current density up to 400 nA/mm^2. The charge neutralizer has not been used during the XP data collection.

2.5. Low Energy Electron Diffraction (LEED) [15]

Low Energy Electron Diffraction was discovered by Davisson and Kunsman during study of electron emission from a Ni crystal in 1924 and set up as a proper technique by Davisson and Germer in 1927.

In LEED (Low Energy Electron Diffraction), incident electrons, elastically back scattered (without energy loss) from a surface, are analysed in the energy range 20-200 eV. Electrons in this energy range are excellent probes of surface structure because they possess de Broglie wavelengths of the same order of magnitude as the interatomic spacing between atoms at surfaces.

De Broglie wavelength λ for an electron is given by:

$$\lambda = \frac{h}{p} = \frac{h}{\sqrt{2m_e eV_0}} \qquad \ldots(2.22)$$

where λ is the wavelength, p the momentum and h Planck's constant, m_e the mass of one electron, e the elementary charge and V_0 the electron beam energy.

The dependence of λ from V_0 (expressed in eV) can be obtained substituting the numerical values:

$$\lambda = \frac{1.23}{\sqrt{V_0}} \text{ nm} \qquad \ldots(2.23)$$

Thus, for V_o = 20 eV, λ = 0.27 nm and for V_o = 200 eV, λ = 0.087 nm. These wavelengths are of the same order of magnitude than the interatomic space of atoms on a surface. When the beam of electrons interacts with an ordered surface array, discrete back scattered electron beams will emerge from the substrate obeying a Braggs' like law. The situation is explained for a one-dimensional array of atoms with separation d in the scheme in figure 2.26. The electron beam is incident perpendicular to the array of atoms. The electrons will be backscattered from two adjacent atoms at a well-defined angle, θ, to the surface normal. There is a "path length difference", Δ_{pl}, in the distance the electrons have to travel from the scattering centres, the atoms, to the detector. From trigonometric considerations, the path length difference is equal to $d \sin\theta$. Thus:

$$\Delta_{pl} = d \sin\theta \qquad \ldots(2.24)$$

For constructive interference to occur when the scattered electron beams join the detector, the path length difference has also to be equal to an integer number of wavelengths. Thus:

$$\Delta_{pl} = n\lambda \qquad \text{with } n = 0, \pm 1, \pm 2, \ldots \qquad \ldots(2.25)$$

Combining the two equations a Braggs' like law equation is obtained:

$$n\lambda = d \sin\theta \qquad \ldots(2.26)$$

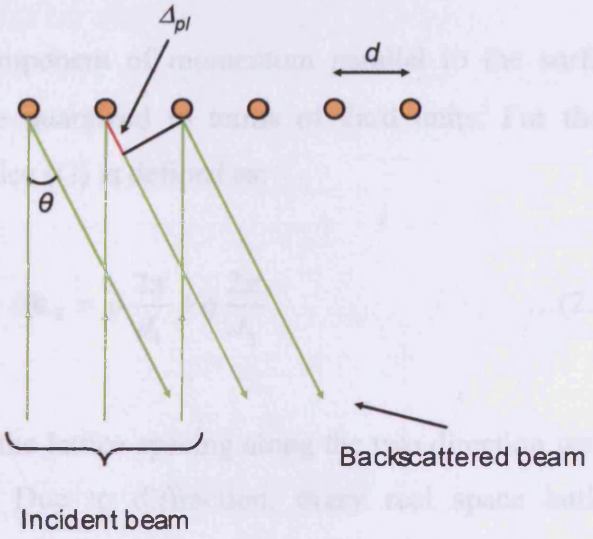

Fig. 2.26: Electrons scattering due to a 1D array of atoms of separation d [adapted from 16].

Important considerations can be driven out of it:

- $\sin\theta$ is proportional to $1/d$, thus the diffraction angle gets bigger as d becomes smaller;
- $\sin\theta$ is proportional to $1/\sqrt{V_0}$, hence, the diffraction angle becomes bigger as electron energy becomes smaller;
- the diffraction has the same probability with n = 1 and n = -1 hence, the diffraction pattern is symmetric.

All the considerations reported above can be extended to the two - dimensional case, typical of surface studies. To illustrate the 2D case it is convenient to represent the condition of diffraction as in equation 2.26 in terms of "reciprocal lattice vector" $\mathbf{k_0}$ [17] defined as:

$$|\mathbf{k}_0| = \frac{2\pi}{\lambda} \qquad \ldots(2.27)$$

For the 1D case, substitution of equation 2.26 into 2.27 and eliminating λ, gives:

$$|\mathbf{k}_0| \sin\theta = \left(\frac{2\pi}{d}\right) n = \Delta\mathbf{k}_{//} \qquad \ldots(2.28)$$

where $\mathbf{k}_{//}$ is the component of momentum parallel to the surface of the incident electron and can be quantized in terms of $2\pi/d$ units. For the 2D case, the 2D reciprocal vector lattice (G) is defined as:

$$\mathbf{G} = \Delta\mathbf{k}_{//} = p\frac{2\pi}{d_1} + q\frac{2\pi}{d_2} \qquad \ldots(2.29)$$

where d_1 and d_2 are the lattice spacing along the two direction we consider and p and q integer numbers. Due to diffraction, every real space lattice will produce a reciprocal lattice according to the following rules:

$$G = p\mathbf{d_1}^* + q\mathbf{d_2}^* \qquad \text{(with p and q integers)} \qquad \ldots(2.30)$$

$$|\mathbf{d}_1^*| = \frac{2\pi}{|\mathbf{d}_1|} \quad \text{and} \quad |\mathbf{d}_2^*| = \frac{2\pi}{|\mathbf{d}_2|} \qquad \ldots(2.31)$$

where $\mathbf{d_1}$ and $\mathbf{d_2}$ are the elementary vectors of the surface 2D unit cell and $\mathbf{d_1}^*$ and $\mathbf{d_2}^*$ are the elementary vectors of the associated reciprocal lattice. The reciprocal space vectors are related to the real space vectors by the scalar product relations:

$$\mathbf{d}_1 \cdot \mathbf{d}_2^* = \mathbf{d}_2 \cdot \mathbf{d}_1^* = 0 \quad \text{and} \quad \mathbf{d}_1 \cdot \mathbf{d}_1^* = \mathbf{d}_2 \cdot \mathbf{d}_2^* = 1 \qquad \ldots(2.32)$$

In mathematical terms, these equations mean that a large distance in real space is a short distance in reciprocal space and vice-versa.

The use of LEED as a surface sensitive technique arises from the fact that electrons penetrate only the first monolayers of the surface. In summary, all surface diffraction patterns show a symmetry reflecting the symmetry of the surface from where they are generated. The patterns are centrally symmetric, and there is an inverse relationship to both the square root of the electron energy and the size of the surface unit cell.

A range of information is available from a LEED pattern:

- from the position of the diffracted beams, the two-dimensional periodicity of the surface unit cell may be deduced;
- from the variation of spot intensities with beam energy, the complete surface geometry can be obtained, including bond lengths and angles (I-V curves).

A typical LEED set up is shown in figure 2.27:

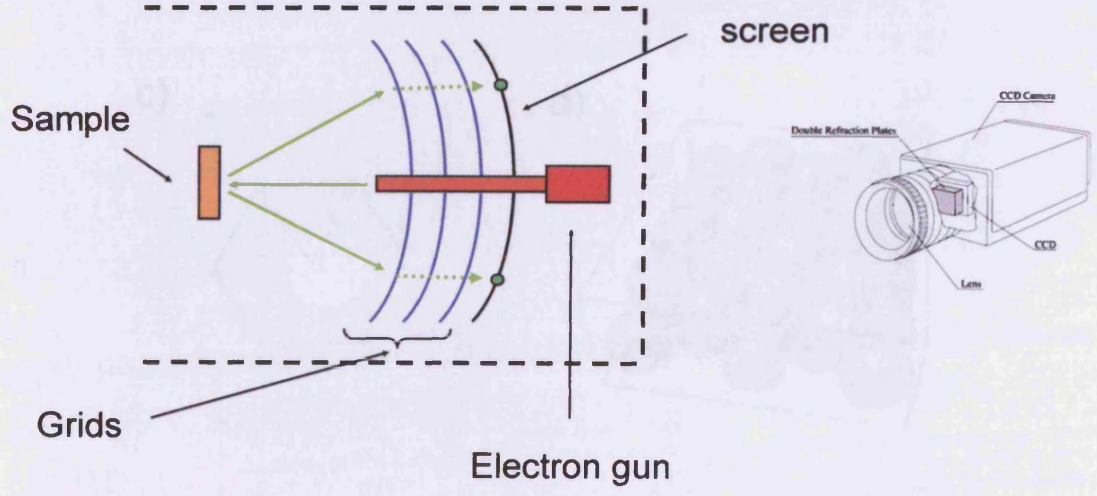

Fig. 2.27: A typical LEED experiment set up. The image is generated on the phosphorus screen and collected using a CCD camera. The dashed line is the vacuum limit [adapted from 16].

Experimentally, the electron beam emitted from a LaB_6 crystal in the electron gun, hits the sample and is backscattered towards the screen, passing through a set of electrostatic grids. The voltages applied to the grids in front of the screen can be varied to filter the scattered electrons and tune them, to ensure only elastically scattered electrons can reach the screen. The screen itself is biased to accelerate the electrons.

LEED is sensitive of areas of around $100Å^2$ and the higher the degree of ordered the surface, the sharper the spots will be. Highly ordered surfaces will also give good contrast between the spots and the background. If the ordering is poor the background will be much lighter. Some examples of a Pt(111) single crystal LEED patterns as well as a scheme of the surface are shown in figure 2.28.

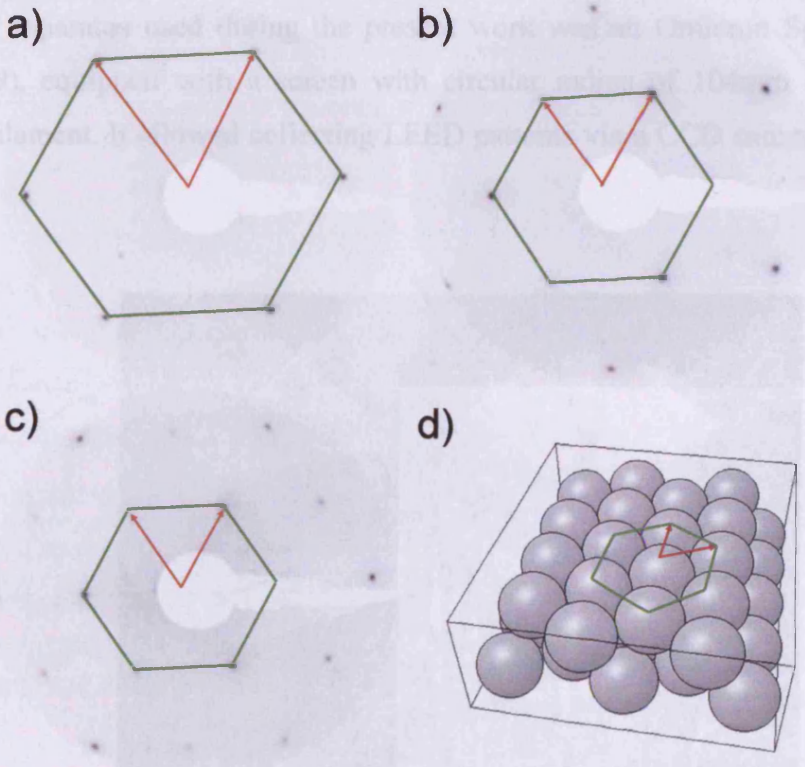

Fig. 2.28: three LEED patterns of Pt(111) collected at a) 65eV, b) 138 eV and c) 185eV respectively. Note that increasing the electron energy the lattice vector decreases showing more diffracted points. d) (111) plane of an fcc lattice [18].

LEED can be used prior to carrying out experiments to control if the substrate to be used is clean and has large and ordered domains. It can also provide an extremely

quick method allowing establishing if an ordered structure has been produced before carrying out more time consuming experiments such as STM.

When looking at an ordered adsorbate overlayer, depending on the level of coverage, the overlayer spots may be seen in conjunction with the substrate spots or may obscure them completely. If the adsorbate layer is disordered or the domains are ordered, but too small, then the spots will become more diffuse or will not be seen at all. If an ordered LEED pattern is recorded then, the geometry and spacing of the overlayer spots with respect to those of the substrate can be useful in determining the overlayer unit cell parameters.

The LEED apparatus used during the present work was an Omicron SpectraLEED (figure 2.29), equipped with a screen with circular radius of 104mm and a LaB_6 excitation filament. It allowed collecting LEED patterns via a CCD camera as well as I-V curves.

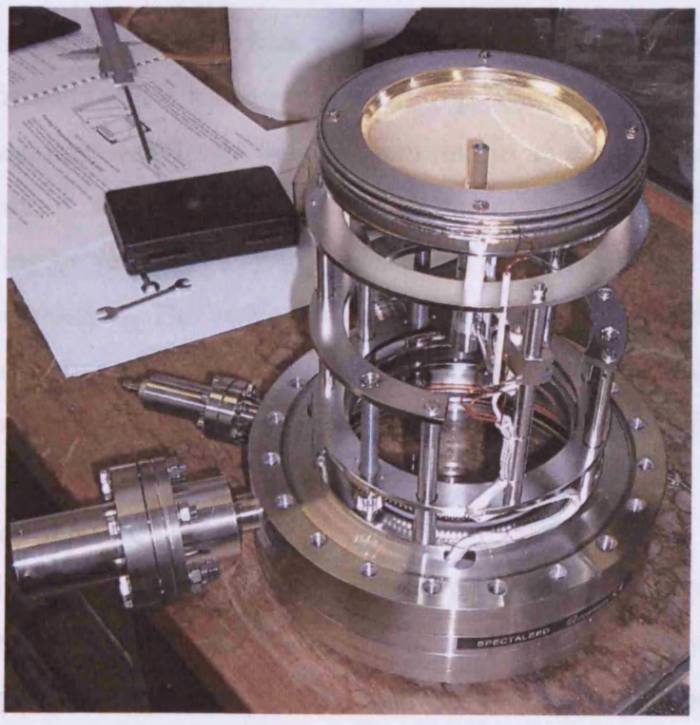

Fig. 2.29: The Omicron SpectraLEED outside the UHV system.

2.6. Surface Probe Microscopy (SPM)

All the analytical techniques allow various information to be obtained, such as topography, electron density and chemical composition, on a surface by means of sharp probes scanning the surface and monitoring the probe – surface interaction, go under the Surface Probe Microscopy definition. Two are of primary importance in Surface Science: Scanning Tunnelling Microscopy and Atomic Force Microscopy.

2.6.1 Scanning Tunnelling Microscopy (STM)

STM (Scanning Tunnelling Microscopy) was invented in 1982 by Binning, Rohrer, Gerber, and Weibel at IBM research labs in Zurich, Switzerland` [19]. Binning and Rohrer won the Nobel Prize in Physics for this invention in 1986. The technique is based on the fact that the tunnelling current between a conductive tip and sample is exponentially dependent on their separation. This can be represented by the equation:

$$I \approx Ve^{-cd} \qquad \ldots(2.33)$$

where I is the tunnelling current, V the bias voltage between tip and sample, d the tip-sample separation distance and c a constant. As the tip scans the sample surface, it encounters sample features of different heights, resulting in an exponential change in the tunnelling current. A feedback loop is used to maintain a constant tunnelling current during scanning by vertically moving the scanner at each (x, y) data point until a "setpoint" current is reached. The vertical position of the scanner at each (x, y) data point is stored by the computer to form the topographic image of the sample surface. This technique is typically limited to conductive and semi-conducting surfaces.

2.6.1.1. The electron tunnelling effect

In classical mechanics an electron is considered as a particle with proper finite size and volume. Electrons are bound within a sample and to extract them from the sample a minimum of energy has to be supplied to the system. This energy is the Ionization energy or the so-called work function (ϕ) of the sample and it is defined as the minimum energy required to remove one electron from the highest occupied energy level (the Fermi level) and bring it to infinite distance (the vacuum level). Even if two

conductors are very close together, without touching each other, the electron cannot penetrate into the vacuum gap (a potential barrier) if its energy E is smaller than the work function within the barrier (figure 2.30 a).

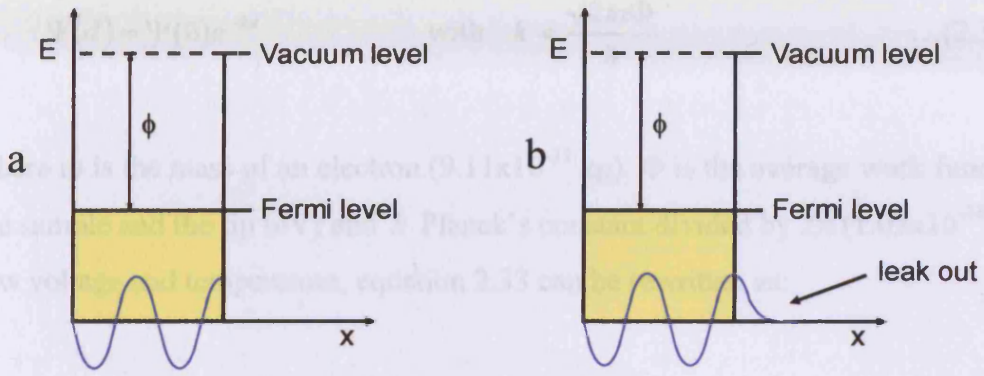

Fig. 2.30: a, classical view: the electron is confined in the box; b, quantum mechanical view: the electron can escape and the wave function leaks out the box.

From a quantum mechanic point of view, the electron is treated both as a particle and as a wave. For an oscillating electron i.e. an oscillating wavefunction, quantum mechanics predicts the possibility to escape from the sample even if its energy is not bigger than the work function; therefore the wavefunction can leak-out into the vacuum (fig 2.30 b). When two conductors are very close to each other, but not touching, the oscillating wavefunction can escape from one conductor, penetrate the vacuum gap, with an exponential decaying solution for the electron wave function in the barrier, and reappear on the other conductor, where it will oscillate again (figure 2.31).

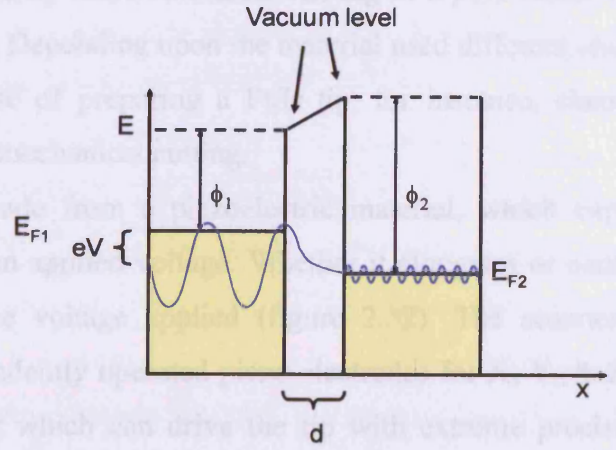

Fig. 2.31: Quantum tunnelling through a barrier d thick.

The penetration into the vacuum barrier is the so-called "tunnel" effect, and the current associated with the process is the "tunnelling current". The solution for the electron wave function has the form:

$$\Psi(d) = \Psi(0)e^{-kd} \qquad \text{with} \quad k = \frac{\sqrt{2m\Phi}}{\hbar} \qquad \ldots(2.34)$$

where m is the mass of an electron (9.11×10^{-31} kg), Φ is the average work function for the sample and the tip (eV) and $\hbar$ Planck's constant divided by 2π (1.05×10^{-34} J s). At low voltage and temperature, equation 2.33 can be rewritten as:

$$I \propto e^{-2kd} \qquad \ldots(2.35)$$

Where I is the tunnelling current (mA), k is defined as in equation 2.34 and d is the thickness of the barrier i.e. the distance between the two conductors (in this case the tip and the sample) (Å).

Equation 2.35 states an important concept related to the sensitivity of the technique: if the distance is increased by 1 Å, the current will decrease by one order of magnitude; therefore the vertical sensitivity is very high.

2.6.1.2. Scanning

Experimentally, an atomically sharp tip is mounted on a scanner drive. The tip is essentially prepared by electrochemical etching of a pure metal wire, for example W or alloys as W/Re. Depending upon the material used different etching procedures can be applied. In case of preparing a Pt/Ir tip, for instance, chemical etching is not required, but only mechanical cutting.

The scanner is made from a piezoelectric material, which expands and contracts proportionally to an applied voltage. Whether it elongates or contracts depends upon the polarity of the voltage applied (figure 2.32). The scanner is constructed by combining independently operated piezo electrodes for X, Y, & Z into a single tube, forming a scanner which can drive the tip with extreme precision in all the three directions (figure 2.33).

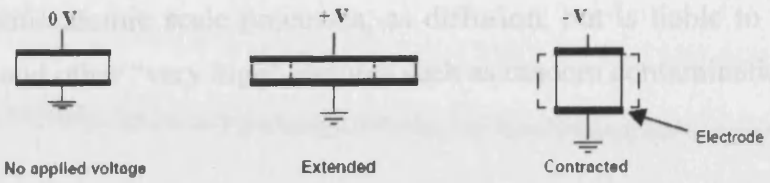

Fig. 2.32: Deformation of the piezo scanner depending upon the voltage bias applied.

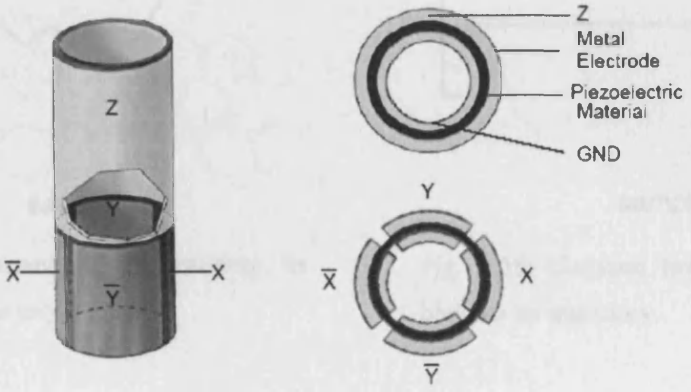

Fig. 2.33: A schematic diagram of a single tube piezo scanner [adapted from 20].

The surface rastering process is controlled by a computer. This allows the generation of a map of the electron density, dependent upon nature of the sample and magnitude and sign of the tunnelling current, not an image showing the position of the atoms present on a given surface.

There are essentially two different scanning modes: constant current and constant height. In constant current mode (figure 2.34) a feedback loop continuously adjusts the tip height during scanning, in the way that there is a constant tunnelling current between the tip and the sample. This scanning mode is ideal for rough surfaces as tip-surface crashes are avoided. Another advantage is the possibility to obtain height measurements of the features scanned. A disadvantage might be represented by the slow response in time of the feedback loop which can limit the scan speed and therefore increase the acquisition time. A way to overcome this limitation is the constant height scanning mode (figure 2.35). In this scanning mode, the change in the tunnelling current, due to the change of the distance between tip and surface, will construct the electronic map of the surface. Such imaging may give the opportunity to

observe dynamic atomic scale processes, as diffusion, but is liable to tip crashes at surface steps and other "very high" features such as random contamination.

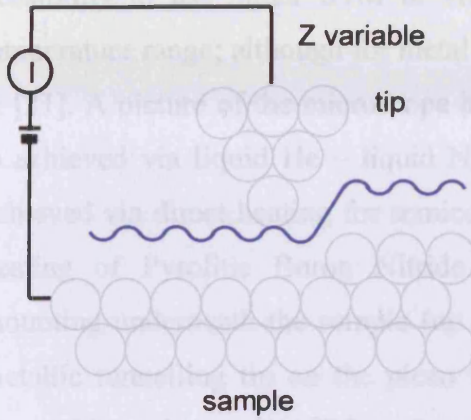

Fig. 2.34: Constant current scanning. In blue the tip trajectory.

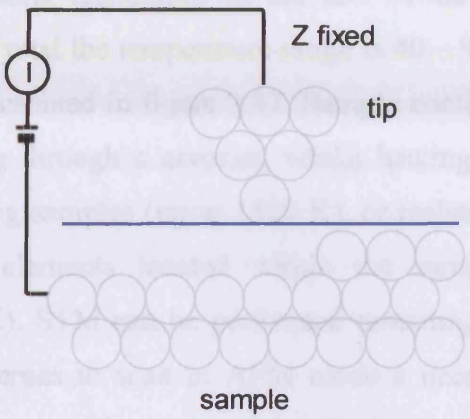

Fig. 2.35: Constant height scanning. In blue the tip trajectory.

Another important tunnelling technique is the so called Scanning Tunnelling Spectroscopy (STS), also called single point spectroscopy, by means of the ohmic behaviour of a sample can be determined. The tunneling current (I) is measured from the variation in the bias voltage (V) between the tip and the sample at the measurement point. As a result, the $I(V)$ curves give information on the cunducting or semicounductiong character of the sample (figure 2.36).

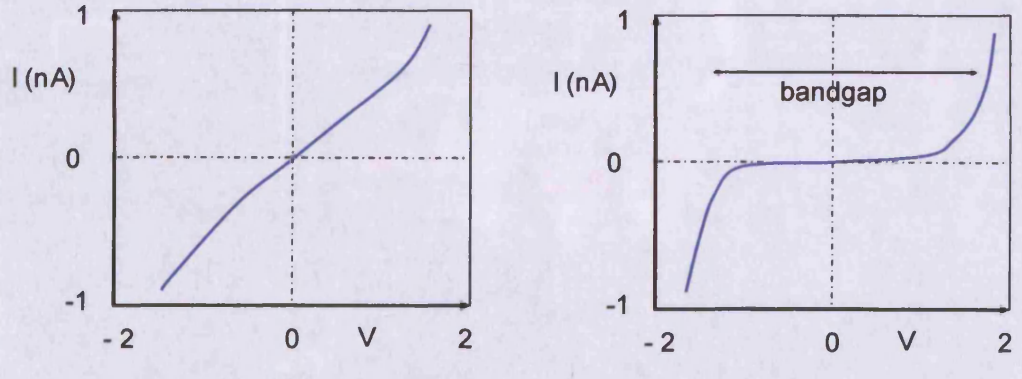

Fig 2.36: Theoretical STS curves for conducting samples (left) and semiconductors (right). In semiconductors STS can give a rough estimation of the bandgap.

2.6.1.3. The SPM in the system

An Omicron Variable Temperature Surface Probe Microscope (VT-SPM) is mounted on the Omicron Multiprobe ® Surface Science System. The VT-SPM offers the possibility to use either STM or AFM scanning techniques in the 25 – 1400 K temperature range; although for metal single crystal the temperature range is 40 – 800 K [21]. A picture of the microscope head is presented in figure 2.37. Sample cooling is achieved via liquid He – liquid N_2 flowing through a cryostat, whilst heating is achieved via direct heating for semicounducting samples (up to 1400 K), or resistive heating of Pyrolitic Boron Nitride (PBN) elements located within the sample mounting underneath the sample (up to 800 K). STM can be performed mounting a metallic tunnelling tip on the piezo tube, whereas to scan in AFM mode a needle sensor has to be used (AFM mode will be illustrated in section 2.6.1.3). A carousel present on the side of the scanning head gives the possibility to store up to 12 between samples, tunnelling tips and needle sensors.

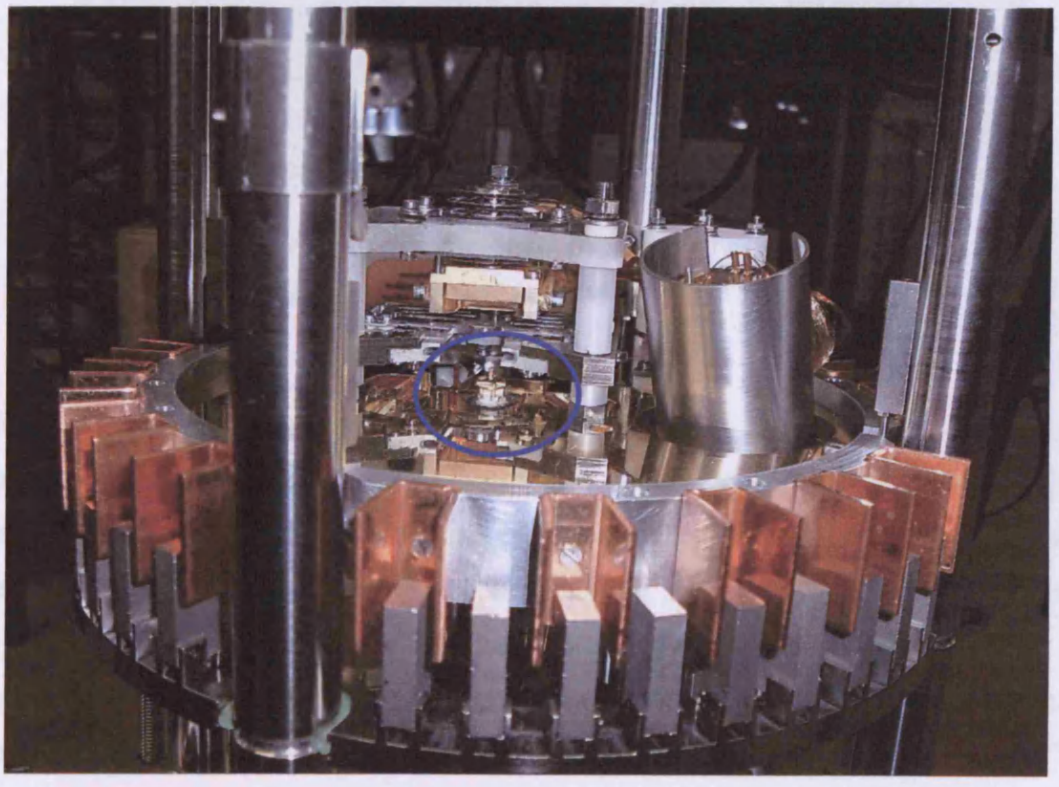

Fig. 2.37: The VT-SPM. In the blue circle the tip.

2.6.1.4. In vacuum Atomic Force Microscopy [22]

As already mentioned, the Omicron VT-SPM also allows doing Atomic Force Microscopy. The theory of the technique will be illustrated in section 2.8.4. Here the attention is directed towards the way a needle sensor works. The needle sensor is made of a quartz resonator (figure 2.38 a) which is made to oscillate far away from the sample with fixed amplitude and frequency. Since it is a piezoelectric material, the oscillation generates a small AC current, phase-coupled to the mechanical oscillation, which is recorded as a reference. In the presence of a force applied to the needle i.e. due to the interaction between the needle sensor and the sample, the oscillation is shifted with respect to the reference frequency. The phase shift is a measure of the interaction between tip and surface and it is used as feedback signal for the height regulation. The oscillation difference gives information correlated to the topography. This technique was not used during the experimental work.

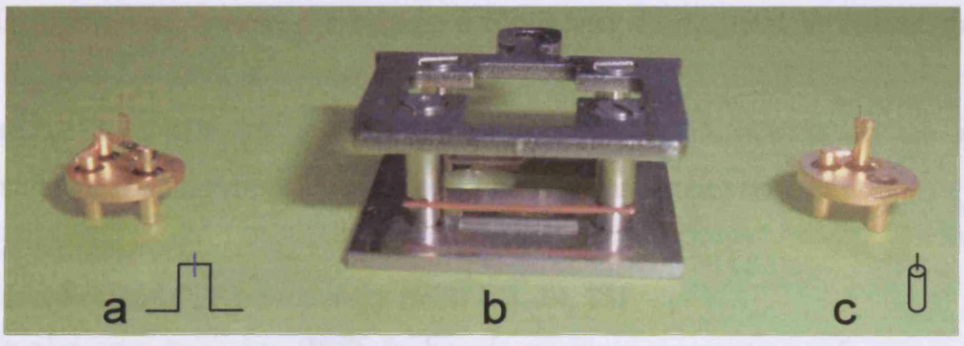

Fig. 2.38: a) the needle sensor (the quartz resonator is represented in blue in the model), b) the needle and tip holder and c) the tunnelling tip.

2.6.1.4. Vibrational damping

Isolation from external sources of noise is a major concern in as SPM system. Electrical noise is minimized because of the Faraday cage effect produce by the stainless steel chamber where UHV conditions are achieved. Mechanical noise can arise from any vibration transmitted from the surroundings to the SPM, leading to degradation of the image quality or collision of the tip with the surface. To ensure isolation from external vibrations the SPM head is suspended on four soft springs. To minimize the vibration of the springs an additional magnetic dampening mechanism is present. This consists of a ring of copper plates mounted on the SPM head and a ring of magnets mounted on the support of the springs as a counterpart called "Eddy-current damping".

2.7. Other techniques

The following section will briefly describe analytical techniques present in the Omicron Multiprobe ® Surface Science System but not used during experimental work.

2.7.1. A Chamber

2.7.1.1 Ultraviolet Photoelectron Spectroscopy (UPS) [16, 17, 23]

Along with XPS, UPS is a kind of Photoelectron Spectroscopy utilized in order to obtain information on the composition and electronic state of the surface of a sample. It uses a vacuum UV (10-45 eV) radiation generated by a noble gas discharge lamp to examine valence levels. These radiations can excite electrons from the valence levels of the atoms. The electrons are then analysed via an electrostatic electronic analyser. The advantage of using such UV radiation over X-Rays is the very narrow line width of the UV radiation, resulting in enhanced resolution if compared to X-Ray source and the high flux of photons available from the discharge source. UPS provides a way to determine the electronic structure of solids, obtain information on the work function and allows studying the adsorption of simple molecules on metals.

2.7.1.2. Ion Scattering Spectroscopy (ISS) [13, 24, 25]

Ion scattering spectroscopy (ISS) is based on the conservation of energy and momentum during the collision of ions with individual surface atoms. If the initial and final energies and momenta of the projectile are known, the mass of the surface atom from which the ion has been inelastically scattered can be calculated.

Since the de Broglie wavelength of a helium atom is of the order of 0.05 nm depending on temperature, elastic collisions are expected to give rise to diffraction phenomena. Therefore He atom diffraction can be used for structural determination of single crystal surfaces. The sizes of the unit cell can be determined from the angular position of the diffractions peaks, whilst the arrangement of atoms in the unit cell and the resulting surface electronic structure determine their relative intensities.

2.7.1.3. Electron Paramagnetic Resonance (EPR) [25]

Electron Paramagnetic Resonance (EPR), also called Electron Spin Resonance (ESR), is a type of spectroscopy in which electromagnetic radiation in the microwave-

frequency region is absorbed by samples in form of molecules, ions, or atoms possessing electrons with unpaired spins, i.e. possessing total electronic spin $S > 0$. The unpaired electron, which gives the EPR spectrum, is very sensitive to its local surroundings, represented in general by the nuclei. The interaction between the electron and the nuclei gives us a wealth of information about the sample such as the identity and number of atoms which make up a molecule or complex as well as their distances from the unpaired electron.

2.7.2. C chamber

2.7.2.1. Surface-Raman Spectroscopy

Raman spectroscopy is the measurement of the wavelength and intensity of inelastically scattered light from molecules. The mechanism of Raman scattering is different from that of infrared absorption (see section 2.8.1), and Raman and IR spectra provide complementary information. The Raman scattering effect is due to the polarizability of the electronic cloud of a molecule which happens when a photon impinges upon the molecule interacting with its electronic structure. The amount of the polarizability of the bond will determine the intensity and frequency of the Raman shift. The molecule must be symmetric to observe the Raman shift. The photon excites one of the electrons into a higher energy state. When the photon is released the molecule relaxes back into vibrational energy state. Typical applications are in structure determination, multicomponent qualitative analysis, and quantitative analysis.

2.8. Other techniques used

2.8.1. Reflectance Absorption Infrared Spectroscopy (RAIRS) [16]

Chemical bonds have specific frequencies at which they can vibrate if excited. The vibrational frequencies are dependent upon the shape of the molecular Lennard-Jones potential surfaces and the masses of the atoms. As a general selection rule, in order for a vibrational mode in a molecule to be IR active, it must be associated with changes in the permanent dipole moment.

In traditional IR Spectroscopy a beam of infrared light is passed through the sample, and the amount of energy absorbed at each wavelength is recorded. This may be done by scanning through the spectrum with a monochromatic beam, which changes in wavelength over time, or by using a Fourier Transform instrument to measure all wavelengths at once. From this, a Transmittance (Absorbance) vs wavenumber spectrum may be plotted, which shows at which wavelengths the sample absorbs the IR radiation, and allows an interpretation of which bonds are present.

A way of identification of molecules adsorbed on a surface is provided by Reflection-Absorption IR Spectroscopy (RAIRS). In this IR technique, the IR beam is specularly reflected from a highly-reflective sample, such as a metal single crystal surface, to the IR detector. Figure 2.39 shows the experimental setup.

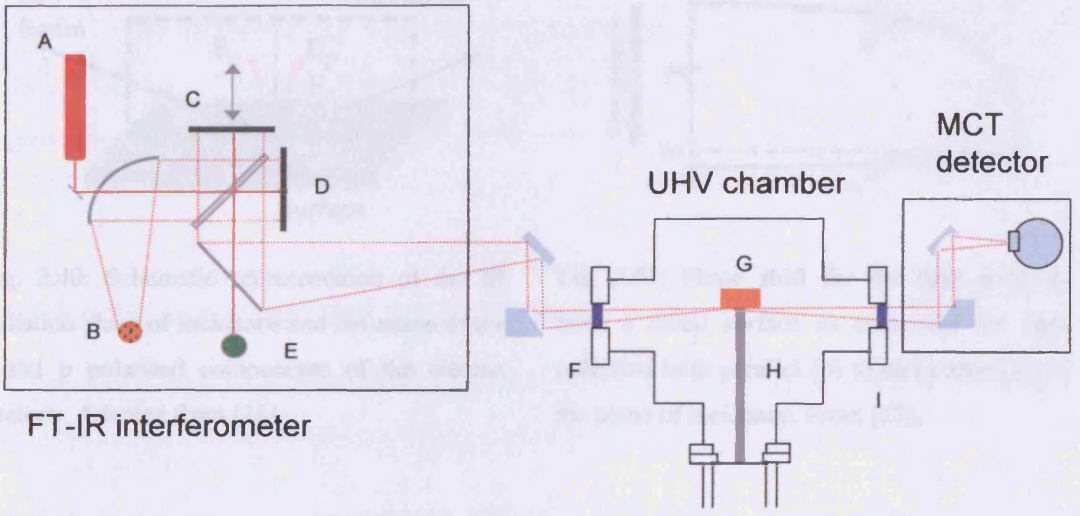

Fig. 2.39: RAIRS experimental setup at Queen Mary, University of London. A: reference LASER source, B: IR source, C: moving mirror, D: fixed mirror, E: LASER detector, F and I: KBr windows, G: sample, H: manipulator.

The IR technique is not surface specific, however, because of the reflectance operation mode, there is no signal originated from the bulk of the sample and the surface signal is easily distinguishable form the one of the gas molecules adsorbed using polarization effects. Greenler [27] demonstrated that the absorption of IR radiation by the overlayer is enhanced at high angles of incidence and involves only one polarisation of the incident IR beam. Figure 2.40 shows the s (normal) and p

(parallel) polarised components, with respect to the plane of incidence, of the incident and reflected electric vectors. At the point of contact with the surface, the p-polarised radiation has an overall combined amplitude which is almost double that of the incident radiation because of the sum of the E_P and E_P' vectors. The s-polarised radiation will however be suppressed because the incident and reflected electric vectors E_S and E_S' undergo a 180° phase-shift with respect to each other. This gives zero overall amplitude of the IR radiation parallel to the surface plane. This means that only the p-polarised radiation can interact with the surface and that the only active vibration that may be observed in RAIRS must have a component of the dipole moment polarised in the direction normal to the surface.

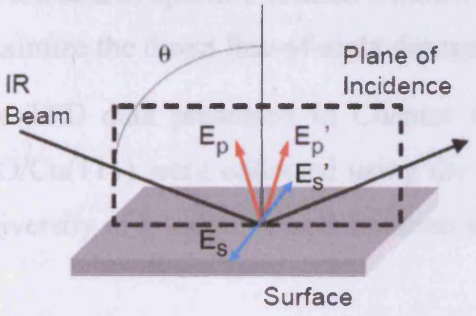

Fig. 2.40: Schematic representation of the IR radiation plane of incidence and definition of the s and p polarised components of the electric vectors. Adapted from [28].

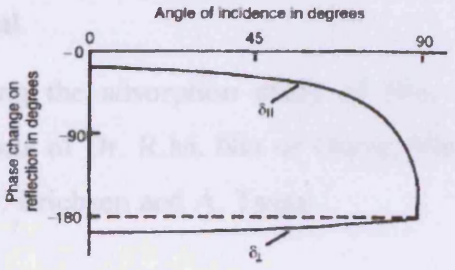

Fig. 2.41: Phase shift for the light reflected from a metal surface as calculated for light polarised both parallel (p) to and normal (s) to the plane of incidence. From [27].

This represent the so-called surface selection rule: only the vibrational modes which give rise to an oscillating dipole perpendicular (normal) to the surface are IR active and generate an absorption band.

Low frequency vibrational modes (<600 cm^{-1}) are not generally observable and in this case it is not normally possible to see the vibration of the metal-adsorbate bond. The intrinsic vibrations of the adsorbate species in the range 600 – 3600 cm^{-1} are instead detected. The IR data presented in Chapter 4 regarding the adsorption study of NO_x on BaO/Cu(111) were collected using the equipments of Dr. R.M. Nix of Queen Mary, University of Landon, in collaboration with Dr. J. Erichsen and A. Tsami.

2.8.2. Temperature Programmed Desorption (TPD) [16, 17]

During Temperature Programmed Desorption, the residual gas present in the UHV chamber is analysed by means of a Quadrupolar Mass Spectrometer (see section 2.3.3), while the sample is heated up. As the temperature rises, the thermal energy given to the system will stimulate the desorption of absorbed species that will be detected as an increase in partial pressure for a certain mass. This results in a peak in the pressure versus time plot. The temperature of the peak maximum provides information on the binding energy of the bound species. The peak area gives an indication on the amount of species desorbed.

TPD measurements are normally acquired in a multiple ion monitoring mode and with the ion source aperture located within a few millimetres of the crystal surface, so as to maximize the direct line-of-sight desorption signal.

The TPD data presented in Chapter 4 regarding the adsorption study of NO_x on BaO/Cu(111) were collected using the equipments of Dr. R.M. Nix of Queen Mary, University of Landon, in collaboration with Dr. J. Erichsen and A. Tsami.

2.8.3. Kratos Axis Ultra DLD XP Spectrometer [28]

The theory behind XPS was described in section 2.4. Here a description of the Kratos Axis Ultra is given, highlighting its important features.

The Kratos Axis Ultra is a high-resolution XPS system allowing chemical analysis and imaging, equipped with a monochromatic Al X-ray source, dual anode Mg/Al X-ray source and a charge neutralization system. A particular feature of the spectrometer is the way the emitted electrons are collected and then analysed. A Kratos patented magnetic immersion lens system, situated below the sample, focuses the vast majority of the electrons directly onto the concentric hemispherical analyser entrance slit (figure 2.42). The hemispherical analyser provides both high energy resolution and high sensitivity. The combination of the electrostatic lenses and the magnetic immersion lens system gives small spot area capabilities. In imaging mode photoelectrons are transferred to a spherical mirror analyser which produces real time chemical state images with better than 3μm spatial resolution.

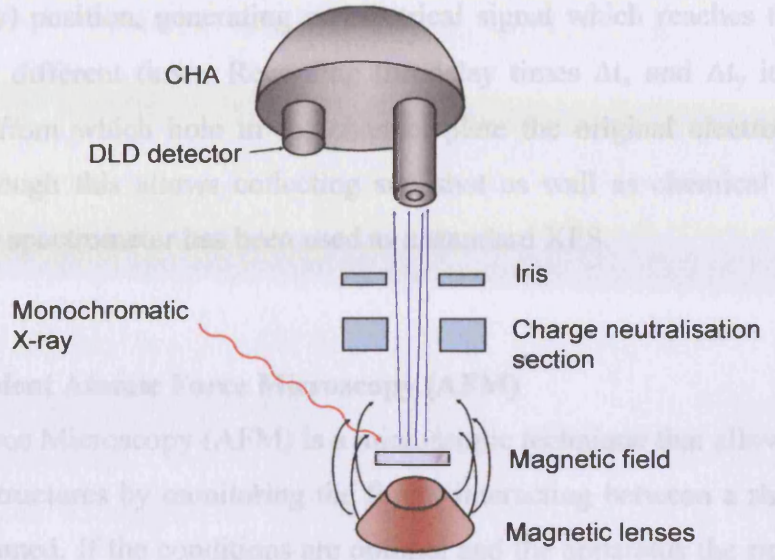

Fig. 2.42: representation of the Kratos Axis Ultra XPS components.

In both spectroscopy and imaging modes a Delay-Line Detector (DLD) (figure 2.43), made of multi-channel plates is used for photoelectron detection allowing a dramatic reduction in the scanning time.

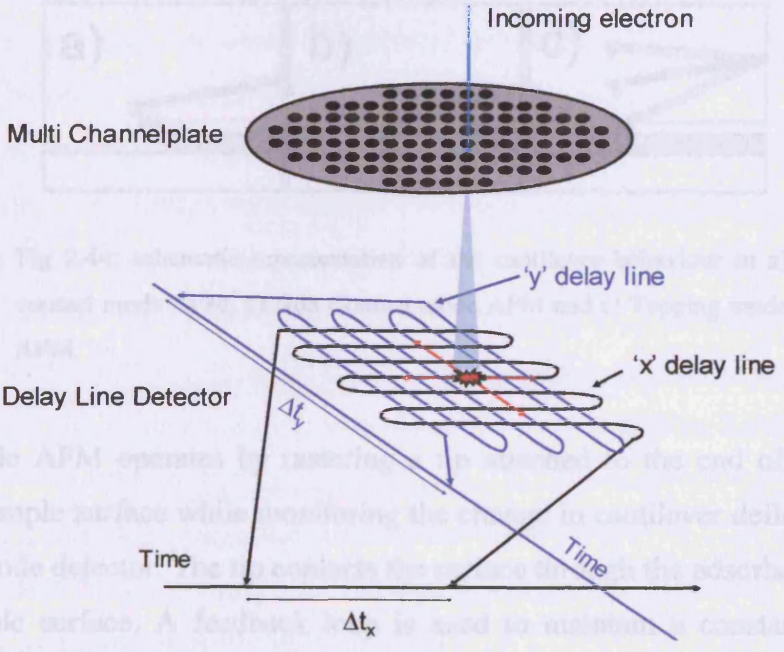

Fig. 2.43: Delay Line Detector (DLD) operation principles. See text for details.

The electron arriving from the CHA impinges upon a stack of three channel plates and is amplified. The electrons generated in this way impinge upon the delay line winding

in the (x, y) position, generating an electrical signal which reaches the ends of the winding in different times. Recording the delay times Δt_x and Δt_y it is possible to determine from which hole in the channel plate the original electron was coming form. Although this allows collecting snapshot as wall as chemical images of the sample, the spectrometer has been used as a standard XPS.

2.8.4. Ambient Atomic Force Microscopy (AFM)

Atomic Force Microscopy (AFM) is a microscopic technique that allows image micro and nano-structures by monitoring the forces interacting between a sharp tip and the surface scanned. If the conditions are optimal and the apparatus the right one, atomic resolution could be achieved.

The operating modes for AFM are usually divided in three categories: contact, non contact and tapping (figure 2.44). Among them, lots of other microscopies can be performed, each one involving the measurement of a different kind of force interacting between the probe and the sample.

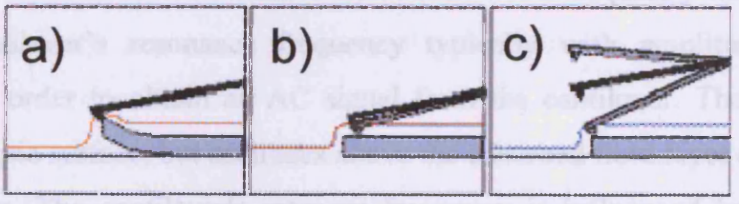

Fig 2.44: schematic representation of the cantilever behaviour in a) contact mode AFM, b) Non Contact mode AFM and c) Tapping mode AFM.

Contact mode AFM operates by rastering a tip attached to the end of a cantilever across the sample surface while monitoring the change in cantilever deflection with a split photodiode detector. The tip contacts the surface through the adsorbed fluid layer on the sample surface. A feedback loop is used to maintain a constant deflection between the cantilever and the sample by vertically moving the scanner at each (x,y) data point to maintain a "setpoint" deflection. By maintaining a constant cantilever deflection, the force between the tip and the sample remains constant. The force is calculated from Hooke's Law (equation 2.36):

$$F = -k (x - x_0) \qquad \ldots(2.36)$$

where F is the force (N), k the cantilever spring constant (N/m) and $(x - x_0)$ the cantilever deformation (m). The distance the scanner moves vertically at each (x,y) data point is stored by the computer to form the topographic image of the sample surface.

Advantages of contact mode AFM are:

- High scan speeds (throughput).
- Contact mode AFM is the only AFM technique which can obtain "atomic resolution" images.
- Rough samples with extreme changes in vertical topography can sometimes be scanned more easily in contact mode.

The main disadvantage is represented by the fact that the tip is actually in contact with the sample and can damage it if the sum of the forces (vertical, z, and lateral, x & y) applied is too high or the sample itself is too rough.

In non contact mode AFM, the cantilever is oscillated at a frequency which is slightly above the cantilever's resonance frequency typically with amplitude of a few nanometers, in order to obtain an AC signal from the cantilever. The tip does not contact the sample surface, but oscillates above the adsorbed fluid layer on the surface during scanning. The cantilever's resonant frequency is influenced by the van der Waals forces interacting between cantilever and sample. A feedback loop is used to maintain a constant oscillation amplitude (or frequency) by vertically moving the scanner at each (x,y) data point until a "setpoint" amplitude (or frequency) is reached. The distance the scanner moves vertically at each (x,y) data point is recorded and used to obtain the topographic image of the surface.

The main advantage of non-contact AFM is very little force is exerted on the sample surface; this lead to less damage of the surface. Thus the technique results good especially for soft samples, as biological systems.

Disadvantages are:

- Lower lateral resolution, limited by the tip-sample separation.
- Slower scan speed than tapping mode and contact mode to avoid contacting the adsorbed fluid layer which results in the tip getting stuck.

- Non-contact usually only works on extremely hydrophobic samples, where the adsorbed fluid layer is at a minimum. If the fluid layer is too thick, the tip becomes trapped in the adsorbed fluid layer causing unstable feedback and scraping of the sample.

Tapping mode AFM operates by scanning with a tip attached to the end of an oscillating cantilever across the sample surface. The tip constantly taps the surface and in effect is in contact with it for very few instants. A feedback loop maintains a constant oscillation amplitude by maintaining a constant RMS of the oscillation signal acquired by the split photodiode detector. The vertical position of the scanner at each (x,y) data point in order to maintain a constant "setpoint" amplitude is recorded and used to form the topographic image of the surface. By maintaining a constant oscillation amplitude, a constant tip-sample interaction is maintained during imaging.
Advantages of tapping mode AFM are:

- Higher lateral resolution on most samples (1 nm to 5 nm).
- Lower forces and less damage to soft samples imaged in air.
- Lateral forces are virtually eliminated, so there is no scraping.

The main disadvantage is represented by a slightly slower scan speed than contact mode AFM.

2.8.4.1 The Veeco NanoscopeIII Multimode SPM [20]

A Veeco NanoscopeIII Multimode SPM has been used to collect the data presented in Chapter 5. The Multimode SPM allows performing mainly NonContact-AFM (NC-AFM) and TappingMde-AFM (TM-AFM). With a heated scanner element, in conjunction with the AFM Air Cell, also called Environmental Cell and a silicon collar, in an environmentally conditioned atmosphere scanning at temperatures up to 250°C may be performed. The air cell allows scanning in dry conditions, for example in flux of dry air or N_2, or reactive atmosphere.
Moreover, whit the appropriate electronic extenders, lateral force measurement phase detection and electrochemical STM can also be performed.
In all the AFM mode cases, the cantilever oscillation is monitored by a LASER beam and recorded by a split photodiode (figure 2.45).

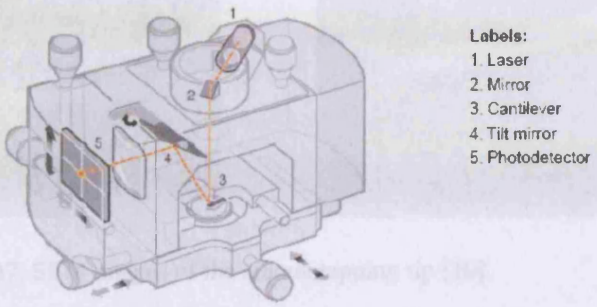

Fig. 2.45: The head of the SPM. The tips are mounted in it. In orange, the pathway of the LASER beam is shown [20].

The scanner itself is represented by a piezoelectric device similar to the one previously described for STM. In some instruments (the present case) the scanner tube moves the sample relative to a stationary tip, whereas in other models the sample is stationary while the scanner moves the tip.

Depending upon the scanning mode, different types of tip are used. For contact mode AFM imaging, it is necessary to have a cantilever which is soft enough to be deflected by very small forces and has a high enough resonant frequency to not be susceptible to vibrational instabilities. This is accomplished by making the cantilever short, to provide a high resonant frequency, and thin, to provide a small force constant. These tips are made of silicon nitride and they have 4 cantilevers with different geometries attached to each substrate, resulting in 4 different spring constants (figure 2.46). Silicon probes are used primarily for tapping mode applications. The tip and cantilever are an integrated assembly of single crystal silicon, produced by etching techniques. Only one cantilever and tip are integrated with each substrate. These probes can be much stiffer than the silicon nitride probes, resulting in larger force constants and resonant frequencies (figure 2.47).

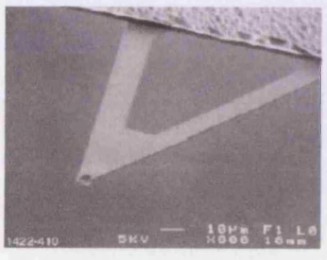

Fig. 2.46: SEM image of the silicon nitride contact tip; each tip holds four cantilevers. On the right the force constant (N/m) is reported next to each cantilever [20].

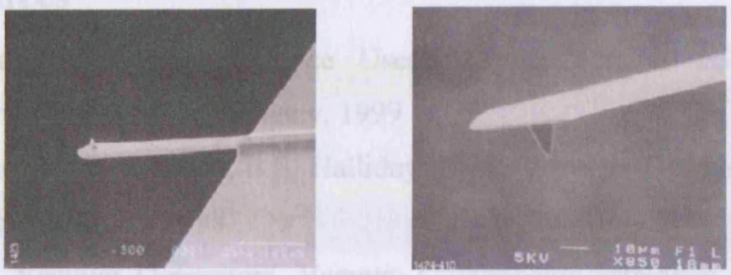

Fig. 2.47: SEM images of the silicon tapping tip [20].

2.8.4.2. The environmental cell [30]

The environmental cell is an accessory studied for the purpose of allowing to scan at temperatures different from ambient and in inert / reactive atmosphere. The cell is made of fuse silica and used in combination with a silicon collar gives a sealed scanning environment. In figure 2.48 a diagram of the environmental cell and a picture if it are showed.

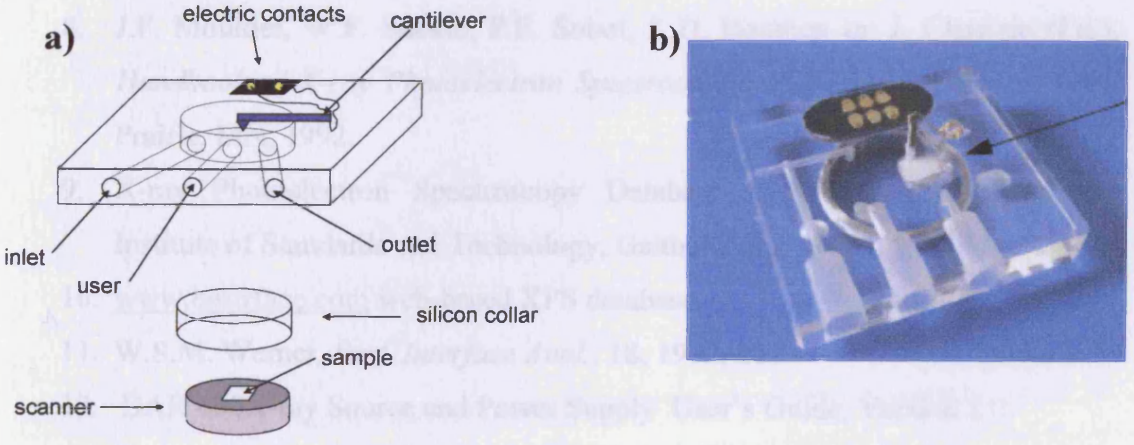

Fig. 2.48: a) Diagram describing the environmental cell. The silicon collar ensures a sealed scanning environment; temperature can be controlled using a particularly designed scanner and heating and cooling systems; gases can be introduce via the inlet nozzle and collected through the outlet nozzle; the user nozzle con be customised to be inlet, outlet or blanked. b) a picture of the cell, the arrow indicate the groove where the cantilever is inserted. from [30].

2.9. References

1. Multiprobe ® Surface Science User's Guide, version 1.5.1, Omicron Vakuumphysik GmbH, Germany, 1999
2. A. Chambers, R.K. Fitch, B.S. Halliday, Basic Vacuum Technology, 2nd Ed, IOP Publishing Ltd, 1998
3. Thermo Vacuum Generators, Vacuum Components catalogue and products description no. 37
4. Omicron Manipulator with E-Beam Heater manual, version 1.0, Omicron Vakuumphysik GmbH, Germany, 2003
5. H. Hertz, *Ann. Physik*, 31, 1887, 983
6. A. Einstein, *Ann. Physik*, 17, 1905,132
7. K. Siegbahn, C. Nordling, A. Fahlman, R. Nordberg, K. Hamrin, J. Hedman, G. Johansson, T. Bergmark, S.E. Karlsson, I. Lindgren, and B. Lindberg, ESCA - Atomic, Molecu lar and Solid State Structure Studied by Means of Electron Spectroscopy, *Nova Acta Regiae Soc. Sci. Upsaliensis*, Ser. IV, Vol. 20 (1967)
8. J.F. Moulder, W.F. Stickle, P.E. Sobol, K.D. Bomben in: J. Chastain (Ed.), *Handbook of X-ray Photoelectron Spectroscopy*, Physical Electronics, Eden Prairie, MN, 1992.
9. X-ray Photoelectron Spectroscopy Database 20, Version 3.0, National Institute of Standards and Technology, Gaithersburg, MD.
10. www.lasurface.com web-based XPS database.
11. W.S.M. Werner, *Surf. Interface Anal.*, 18, 1992, 217
12. DAR 400X-ray Source and Power Supply User's Guide, Version 2.0, Omicron Vakuumphysik GmbH, Germany, 2000
13. EA 125 Energy Analyser User's Guide, Version 2.1, Omicron Vakuumphysik GmbH, Germany, 2002
14. NU-05 Charge Neutraliser User's Guide, Version 1.0, Omicron Vakuumphysik GmbH, Germany, 2003
15. SpectraLEED Optics and Electron Gun, User's Guide, Version 4.1, Omicron Vakuumphysik GmbH, Germany, 2002
16. R.M. Nix, *An Introduction to Surface Chemistry*, Queen Mary, University of London, London, UK; www.chem.qmul.ac.uk/surfaces/scc/

17. G. Attard, C. Barnes, *Surfaces*, Oxford University Press, 1998
18. Model was made using the on-line applet Surface Explorer, Version 2, developed by Klaus Hermann, Fritrz Haber Institue, Berlin, Germany; http://w3.rz-berlin.mpg.de/~rammer/surfexp_prod/SXinput.html
19. R. Wiesendager in *Scanning Probe Microscopy and Spectroscopy,* Cambridge University Press, 1994
20. SPM Training Notebook, Rev E, Veeco Instruments Inc., Santa Barbara, 2003
21. VT SPM User's Guide, Version 1.7, Omicron Vakuumphysik GmbH, Germany, 2002
22. Needle Sensor AFM Supplement, Version 1.2, Omicron Vakuumphysik GmbH, Germany, 1999
23. HIS 13 VUV User's Guide, Version 1, Omicron Vakuumphysik GmbH, Germany, 2001
24. ISS User's Guide for EA 125, Version 1.0, Omicron Vakuumphysik GmbH, Germany, 1999
25. ISE 100 Fine Focus Ion Gun User's Guide, Version 1.2, Omicron Vakuumphysik GmbH, Germany, 1997
26. EMX User's Manual, Version 2.0, Bruker Instruments, Inc. Billerica, MA 01821 USA, 1998
27. R.G. Greenler, *J. Chem. Phys.*, 1966, 44, 310.
28. M.E. Pemble in *Surface Analysis: The Principle Techniques*, Ed. J.C. Vickerman, J. Wiley and Sons, 1997
29. www.kratos.com/Axis/AXISUltra.html
30. Support Note 392, Rev. C, Veeco Instruments Inc., Santa Barbara, 2004

Chapter 3

Oxygen Storage in Ceria Based Systems

This chapter deals with studies related to oxygen adsorption on ceria based systems. Ceria based materials are of primary importance as components of oxidation catalysts because of their characteristic rapid oxygen exchange with the atmosphere. They can release oxygen when in low oxygen concentration environment and in this way they act as oxidants; when in oxygen rich environment, however, they can adsorb oxygen from the surrounding, acting as reducing agents. An overview on the relevant literature about the so called Oxygen Storage Capacity (OSC) for ceria is firstly given, followed by the description of the experiments undertaken using a $CeO_2(111)$ single crystal as a substrate. Finally, the preparation of ordered ceria layers on a Cu(111) single crystal will be shown.

3.1. Introduction

Cerium dioxide is a promising material in several distinctly different application areas. It has commonly been used as an additive or support material in oxidation catalysts because of the ability to act as intermediate oxygen storage media. It favours noble metal dispersion, acts as a temperature stabiliser, and has the capability/capacity to dissolve a large number of divalent and trivalent rare earth metals into its lattice [1]. In more detail, it has been used in a variety of industrial applications such as catalysis, fuel cells and oxygen sensing, thanks to its high oxygen transport and storage capacities. Ceria shows unique activities for various reactions such as [2]:

- oxidation of CO;
- removal of SO_x from fluid catalytic cracking (FCC) flue gases;
- oxidative coupling of methane;
- water gas shift reaction;
- three way catalysts (TWC) for automobile exhaust gas treatments;
- chemical/mechanical polishing (CMP).

3.1.1. Ceria structure [1, 2, 3, 4]

Pure stoichiometric CeO_2 has a cubic fluorite (CaF_2) structure (figure 3.1) over the whole range of temperatures from room temperature to the melting point (2750 K), with a lattice constant of 0.541nm. Each Ce^{4+} cation is surrounded by equivalent six O^{2-} anions, which form the corners of a cube, and each O^{2-} anion is surrounded by four cations in a tetrahedron. Ce^{4+} cations occupy fcc-type positions in the unit cell. CeO_2 is an electrically insulating f-transition metal oxide at its stoichiometric composition with empty localized electronic Ce $4f^0$ states in its wide bandgap of ~ 6eV. Oxygen deficiencies lead to the reduction of Ce^{4+} to Ce^{3+} and to the occupation of the electronic Ce $4f^1$ states in the bandgap. Thus CeO_{2-x} becomes conductive to some extent by creating oxygen vacancies in the bulk.

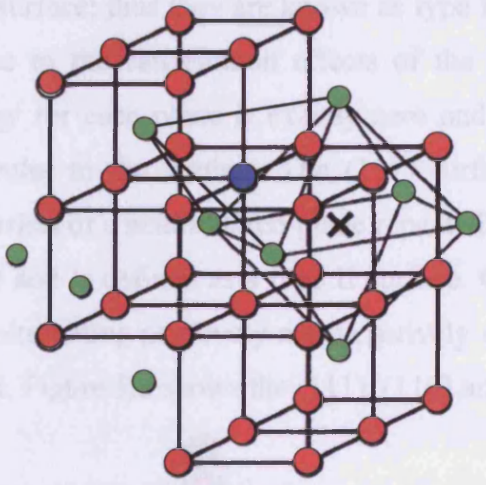

Fig. 3.1: The perfect fluorite structure of ceria. Cations (green circles) occupy each second interstitial site of the cubes of oxygen ions (red and blue circles). The cationic sublattice forms tetrahedral and octahedral sites. The centres (blue) of the tetrahedral sites coincide with the vertices of the oxygen cubes, while those of the octahedral sites (marked by a cross) coincide with centres of the oxygen cubes. All the tetrahedral sites are filled by oxygen ions, and all the octahedral sites are empty. Adapted from [4].

Pure ceria is pale yellow in colour probably due to Ce(IV)-O(-II) UV charge transfer extending to ~450nm. The ceria structure is known to tolerate a considerable reduction without phase change, especially at elevated temperatures. Such CeO_{2-x} is blue and turns almost black when it is grossly under-stoichiometric. The colour of

ceria is also sensitive to the presence of other lanthanides, for example a small content as 0.02% of Pr results in a brownish-yellow colour.

3.1.2. Surface structure

In order to understand the reactivity of ceria and its interaction with metal particles or adsorbates, it is fundamental to know its surface structure and the extent or type of defects present.

The surface structure has been largely considered by theoretical calculations. Sayle *et al.* [5] modelled the (110), (310) and (111) surfaces of CeO_2. The (110) and the (310) surfaces are neutrally charged with stoichiometric proportions of anions and cations in each plane parallel to the surface; thus they are known as type I surfaces according to Tasker definition [6]. Due to the cancellation effects of the positive and negative charges, the surface energy for each plane is exactly zero and moreover there is no dipole moment perpendicular to the surface. The (111) surface terminates with a single anion plane and consists of a neutral three-plane repeated unit; this surface does not have a dipole moment and is defined as a type II surface. On the other hand, the (100) surface consists of alternating positively and negatively charged planes, which introduce a dipole moment. Figure 3.2 shows the (111), (110) and (100) surfaces.

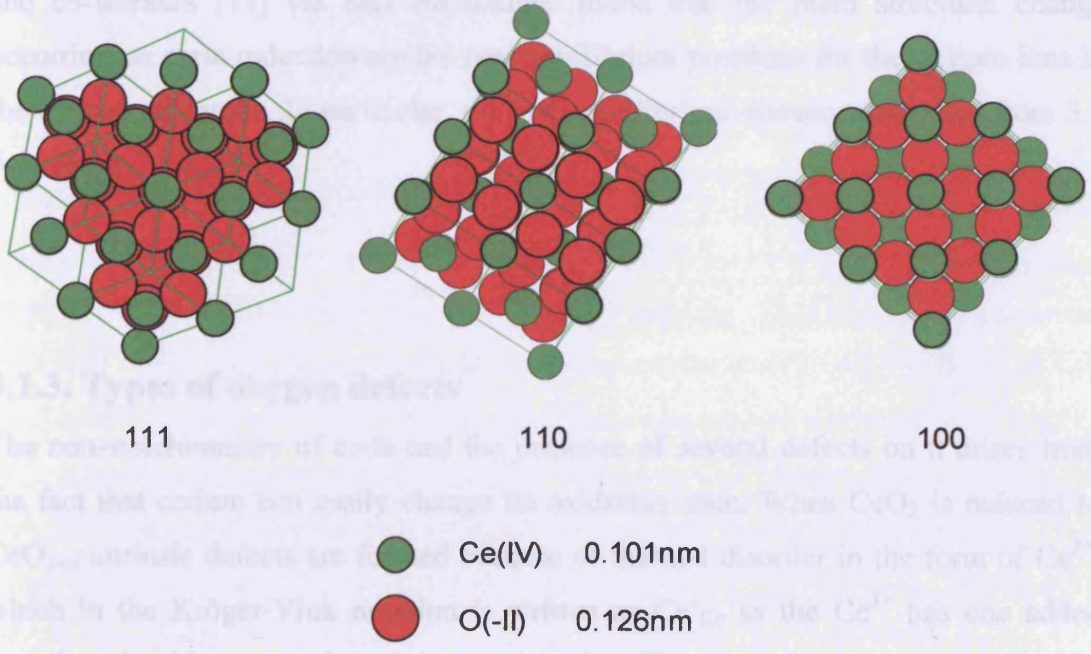

Fig. 3.2: (111), (110) and (100) surface terminations for ceria.

Conesa [7], in a computer simulated study of the surfaces and the defects, found that the most compact surface, the oxygen-terminated (111), is lowest in energy and (110) comes next. Surface (211), not excluded by the electric dipole rule, seems able to restructure spontaneously into a stepped configuration with (111) terraces. Based on surface energy criteria, the relative stability of the considered surfaces is in the order (111) > (110) > (310) after relaxation process simulation. Other surfaces such as the (210) and the (310) are much less stable. Less energy is required to form an anion vacancy on (110) than on (111). For the latter, surface generation of vacancies does not seem more favourable than full reduction of the CeO_2 phase to Ce_2O_3. This suggests that the presence and extent of one or other surface type might be discerned via appropriate reduction/oxidation experiments. Once formed, anion vacancies show tendency to associate in more complex structures on (111) surface, but not on (110). Baudin *et al.* [8] considered the three low index surfaces (111), (011) and (001). Using molecular dynamics simulation on a 20-30 Å slab, they found that the more stable surface is the (111) in which the ionic motion mainly due to the oxygen anions is smaller than for the (011) and the less stable (001). They confirmed the previous results performing also DFT calculations [9]. In a later publication [10], the same group suggested that the oxygen mobility is stronger into the bulk than on the surfaces. Oxygen vacancies are favourable in the surface layer for the (110) and subsurface for the (111), in particular from the second O-atomic layer. For the (011) surface, Gotte and co-workers [11] via MD simulations found that the main structural change occurring on ceria reduction are the new equilibrium positions for the oxygen ions in the oxygen sublattice. In particular, the O-O equilibrium distance decreases from 3.8 Å to about 3.3 Å.

3.1.3. Types of oxygen defects

The non-stoichiometry of ceria and the presence of several defects on it arises from the fact that cerium can easily change its oxidation state. When CeO_2 is reduced to CeO_{2-x}, intrinsic defects are formed because of thermal disorder in the form of Ce^{3+}, which in the Kröger-Vink notation is written as Ce'_{Ce} as the Ce^{3+} has one added negative charge compared to the normal lattice. There are three possible thermally

generated intrinsic disorder reactions in ceria. These defects are of Schottky and Frenkel type:

$$Ce_{Ce} + 2O_2 \leftrightarrow V_{Ce}^{''''} + 2V_{\ddot{o}} + CeO_2 \qquad \Delta E = 3.53 \text{ eV} \qquad ...(3.1)$$

$$Ce_{Ce} \leftrightarrow Ce_i^{\bullet\bullet\bullet\bullet} + V_{Ce}^{''''} \qquad \Delta E = 11.11 \text{ eV} \qquad ...(3.2)$$

$$O_O \leftrightarrow O_i'' + V_{\ddot{o}} \qquad \Delta E = 3.2 \text{ eV} \qquad ...(3.3)$$

where O_O and Ce_{Ce} represent oxygen and cerium at their respective lattice sites, $V_{\ddot{o}}$ and $V_{Ce}^{''''}$ indicate respectively an oxygen and cerium vacancy, and $Ce_i^{\bullet\bullet\bullet\bullet}$ and O_i'' a cerium and oxygen ion in interstitial position. The effective charge (i.e. the charge expressed in terms of the charge normally present in the same position in the host lattice) is indicated by a dot (•) for each positive charge and prime (′) for each negative charge.

It is generally agreed that the main compensating defects in CeO_{2-x} are oxygen vacancies.

The process of ceria reduction may be written as:

$$O_O + 2Ce_{Ce} = \frac{1}{2}O_{2(gas)} + V_O^{\bullet\bullet} + 2Ce_{Ce}' \qquad ...(3.4)$$

Extrinsic defects present as oxide vacancies may be introduced by doping CeO_2 with oxides of metals with lower valences (CaO or Gd_2O_3 for example). Oxide vacancies may be removed by doping with oxides of higher valences (Nb_2O_5 as an example).

Reaction (3.4) may also take place in doped ceria, and doping will affect the equilibrium of the reaction by changing the concentrations of oxide vacancies and of Ce_{Ce}. Assuming no interaction between the various defects (assumption valid only for very low concentrations) the law of mass action is valid and applied on reaction (3.4) gives:

$$[V_O^{\cdot\cdot}]\cdot[Ce'_{Ce}]^2 P_{O_2}{}^{1/2} = \text{constant} \qquad \ldots(3.5)$$

as the concentrations of O_O and Ce_{Ce} are about constant. In the case of undoped ceria $[V_O^{\cdot\cdot}] = x$ and $[Ce'_{Ce}] = 2x$. Substitution in reaction (3.5) and rearrangement gives:

$$x = \text{constant} P_{O_2}{}^{-1/6} \qquad \ldots(3.6)$$

For doped ceria the concentration of vacancies may also be regarded as constant, and thus the result is:

$$x = \text{constant} P_{O_2}{}^{-1/4} \qquad \ldots(3.7)$$

where x is defined by $2x = [Ce'_{Ce}]$.

The concentration of vacancies can directly be correlated to the oxygen partial pressure, in other words to the interactions between the solid and its surrounding atmosphere. Jiang and co-workers [12] reported the following stability after relaxation: (111) > (110) > (210) > (211) > (100) > (310) and they found that the (111) surface is the more stable at all the oxygen partial pressures and temperatures considered. At 300 K, the (111) surface has the lowest free energy for a wide range of oxygen partial pressures up to 1 atm, and, only in UHV conditions, the Ce-terminated (111) surface does becomes the most stable one. The transition point for the Ce-terminated (111) surfaces moves to higher oxygen partial pressures when temperature increases, but even at T = 1200 K, the transition point still occurs at a very low oxygen partial pressure ($\ln P_{O_2} = -80$). In reality, as defects can form on those surfaces and can lower the surface energies, especially at higher temperatures, the transition from the stoichiometric (111) surface to the (111) Ce-terminated occurs gradually with the presence of many intermediate defective surface structures.

The formation of lattice oxygen vacancies in ceria is associated with the reduction of Ce(IV) to Ce(III). This enables the reversible addition and removal of oxygen atoms; this in turn allows cerium dioxide to act as an oxygen storage material in oxidation

reactions. From ΔE values in equations (3.1), (3.2) and (3.3), the predominant defect category is the anion-Frenkel type, which leads to the formation of oxygen in interstitial positions (ΔE ~ 3.2 eV) and pairs of oxygen vacancies (ΔE ~ 3.53 eV). Generally these defects are present in low concentration and do not produce any change in the stoichiometry. In ceria, however, a high concentration of defects can be formed by exposure to reducing gases. Upon reduction, ceria has excess metal compared to its anion content.

There are, in principle, two ways in which CeO_2 can accommodate its variation in composition. In the first case, oxygen vacancies are assumed to compensate the holes formed on reduction. If oxygen is removed, the crystal will end up with an overall positive charge and in order to keep electroneutrality, introduction of two electrons for each of the oxygen ions would be needed. These electrons derive from two cerium atoms that change oxidation state, from Ce^{4+} to Ce^{3+}. The process is generally represented as

$$CeO_2 \leftrightarrow CeO_{2-x} + \frac{x}{2}O_2 \qquad \ldots(3.8)$$

Interstitial cations provide an alternative way to create positively charged defects. These interstitials may be formed by transfer of cerium cations located on the surface to an interstitial position and by the removal of two anions to the gas phase for each cerium interstitial formed. The process can be described as

$$(1+y)CeO_2 \leftrightarrow Ce_{1+y}O_2 + yO_2 \qquad \ldots(3.9)$$

Those two processes can be pictured as in figure 3.3. As a support for figure 3.3 a), Nolan and co-workers [13] calculated the charge density of the oxygen deficient (111) surface and found that the electronic states are localised on the two Ce^{3+} ions neighbouring the oxygen vacancy site.

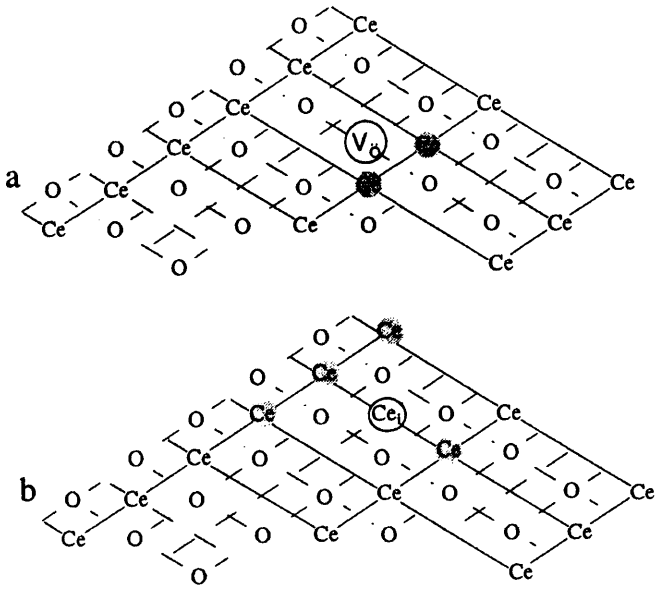

Fig. 3.3: Schematic representation of (a) an oxygen vacancy ($V_{\ddot{O}}$) and b) a quadruply ionised cerium interstitial (Ce_i) in an idealised reduced CeO_2 surface. Ce^{3+} cations are shaded [13].

3.1.4. Oxygen Storage Capacity [14]

Oxygen diffusion as well as other transport properties of oxides such as electrical conduction are mainly determined by the presence, concentration and mobility of lattice defects and are believed to play a key role in catalysis [2]. However, oxygen vacancies in the bulk are normally not directly involved in catalytic reactions that take place on the surface. The formation of lattice oxygen vacancies is usually associated with the presence of the ion Ce(III); this process is generally expressed as in equation (3.4). The process described by reaction (3.4) is created by the insertion of a bi- or tri-valent cation according to the following reactions:

$$MO \xrightarrow{CeO_2} M'_{Ce} + V''_O + \tfrac{1}{2}O_2 \qquad \ldots(3.10)$$

for the bi-valent cation, and

$$M_2O_3 \xrightarrow{CeO_2} 2M'_{Ce} + 2O^x_O + V''_O + \tfrac{1}{2}O_2 \qquad \ldots(3.11)$$

for the trivalent one.

The main feature of ceria is its capacity to act as an oxygen buffer, being able to release or store the oxygen in certain appropriate conditions. The so called Oxygen Storage Capacity (OSC) is related to the amount of a reducing gas (H_2, CO), which is oxidised after passing through an oxygen presaturated catalyst. Thus it is related to the most reactive oxygen species and the most readily available oxygen atoms. Experimental values for OSC on pure ceria, and for $Ce_{0.5}Zr_{0.5}O_2$ as comparison, are showed in table 3.1 and reported to be dependent upon the annealing treatments that decreases ceria surface area [4].

compound	Sintering temp /°C	OSC measured in CO TPR up to 700 °C, /moles(O_2) g^{-1}	Surface area /m^2g^{-1}
CeO_2	500	186	75
CeO_2	700	186	50
CeO_2	750	217	38
CeO_2	800	62	37
$Ce_{0.5}Zr_{0.5}O_2$	500	534	26
$Ce_{0.5}Zr_{0.5}O_2$	850	558	10

Table 3.1: Oxygen Storage Capacity and the Surface Area of selected ceria and ceria-zirconia samples [4].

The OSC was studied mainly via $^{18}O/^{16}O$ isotopic exchange on oxide-supported metals and FT-IR Spectroscopy, in order to determine the mechanism of the process [14]. Referring to figure 3.4, different steps could be well distinguished:

1. dissociative adsorption of $^{18}O_2$ on the metal particle;
2. transfer of ^{18}O atoms from the metal to the support;
3. surface migration of ^{18}O atoms on the support;
4. exchange of ^{18}O atoms with ^{16}O atoms on the surface;
5. to every step corresponds the reverse route for the exchanged species.

Depending on reaction temperature, two other steps may be involved:

6. internal (bulk) migration and exchange of ^{18}O with ^{16}O atoms of the support;
7. direct exchange of $^{18}O_2(g)$ with oxygen atoms of the support.

Assuming no bulk diffusion and no direct exchange, two types of exchange can occur:

1. homoexchange, also denoted as "equilibrium", when the adsorption-desorption on the metal particle is rate determining. This exchange corresponds to an equilibration of the two oxygen isotopes at the catalyst surface. The reaction is usually much more rapid on the metal than on the oxide and can give useful information about the oxygen activation process at the surface of metallic particles;
2. heteroexchange, denoted as "isotopic exchange". It can provide information about the oxygen surface migration kinetics. To get reliable data three conditions must be fulfilled: exchange must occur via the metal particle; surface migration must be the rate-determining step and exchange must exclusively occur with surface atoms.

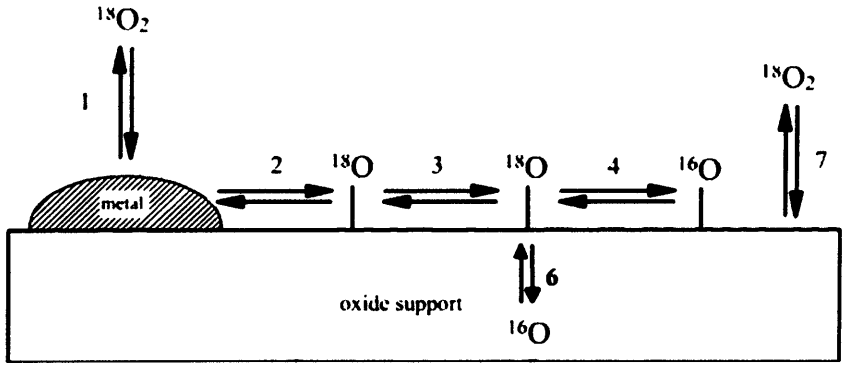

Fig. 3.4: Schematic representation of $^{18}O/^{16}O$ exchange on oxide-supported metal (adapted from [14]).

3.1.5. Main ceria application: Three Way Catalyst (TWC)

Cerium oxides are used to carry out several catalytic reactions. However, the most important application is in the field of Three Way Catalysts (TWC) for automobile exhaust gas treatments [15 - 18].

Since the beginning of the 1980s, the use of CeO_2 in the automotive pollution control has become so broad that it represents today the most important application of rare earth oxides. The development of the TWCs was dictated by the need to convert

simultaneously the hydrocarbons (HC), CO and NO_x present in the automotive exhaust to H_2O, CO_2 and N_2.

The catalyst formulation for the treatment of exhaust gases from spark-ignited internal combustion engines consists primarily of noble metals such as Rh, Pd and Pt and metal oxides impregnated either on the surface of γ-Al_2O_3 pellets or an alumina washcoat anchored to a monolithic ceramic substrate. A diagram of an exhaust catalyst was presented figure 1.9 [19]. CeO_2 acts as oxygen storage component. It is well-known that the main role of ceria in this complex mixture is to provide oxygen buffering during the rich/lean oscillation of exhaust gases. Highest conversion of the pollutants is attained close to the stoichiometric conditions, while excursion to fuel-rich (net reducing) or fuel-poor (net oxidising) air-to-fuel (A/F) ratios severely decrease the efficiency of the TWCs.

The catalytic activity of ceria in TWC involving its OSC capacity can be summarised as follow: CeO_2 acting as oxidant transfers oxygen and reduces to CeO_{2-x} (equations 3.12-3.14)

$$CeO_2 + xCO \rightarrow CeO_{2-x} + xCO_2 \quad \ldots(3.12)$$

$$CeO_2 + HC \rightarrow CeO_{2-x} + (H_2O, CO_2, CO, H_2) \quad \ldots(3.13)$$

$$CeO_2 + xH_2 \rightarrow CeO_{2-x} + xH_2O \quad \ldots(3.14)$$

By reaction with an oxidant CeO_{2-x} acts as a reducent and re-oxidises to CeO_2 (equations 3.15 and 3.16):

$$CeO_{2-x} + xNO \rightarrow CeO_2 + \tfrac{1}{2}xN_2 \quad \ldots(3.15)$$

$$CeO_{2-x} + xH_2O \rightarrow CeO_2 + xH_2 \quad \ldots(3.16)$$

Oxygen defective ceria can also regain the full oxygen stoichiometry by reaction with oxygen (equation 3.17)

$$CeO_{2-x} + \tfrac{1}{2}xO_2 \rightarrow CeO_2 \quad \ldots(3.17)$$

Under working conditions, the catalyst is in fact exposed to feedstream compositions going alternatively from rich exhaust stoichiometry (deficient O_2) to lean stoichiometry (excess of O_2). In this environment ceria has the ability to donate its oxygen for the removal of CO and HC during the oxygen-deficient portion of the cycle (reactions 3.12-3.14) while adsorbing and storing oxygen from O_2, NO and water during excursion into the lean part of the cycle (reactions 3.15-3.17). These reactions positively affect the conversion of the three major pollutants (CO, HC and NO) under conditions typically encountered in the normal operation of a TWC. Such excursion may represent a serious limitation for a TWC since the A/F significantly oscillates around the stoichiometric value.

If the atmospheric environment in which CeO_2 operates changes continuously from a net oxidising to a net reducing composition, the oxidation state of cerium correspondingly shifts from +IV to +III, enhancing the conversion of CO and HC during rich oscillations and NO during lean oscillations. This unique feature of ceria derives from the ability of CeO_2 to be easily and reversibly reduced to several CeO_{2-x} stoichiometries when exposed to O_2 deficient atmospheres. Removal of oxygen from ceria at high temperatures in fact leads to the formation of a continuum of O-deficient nonstoichiometric compositions of the type CeO_{2-x} (α phase $0 < x < 0.178$). Even after loss of oxygen from its lattice and the consequent formation of a large number of oxygen vacancies, CeO_2 retains its fluorite crystal structure. This also facilitates rapid and complete refilling of oxygen vacancies upon exposure of CeO_{2-x} to oxygen, with recovery of CeO_2.

The major drawbacks of an oxygen storage system based on pure ceria are related to thermal resistance and low-temperature activity. The main reason why CeO_2 alone is of comparatively little interest as a support or a catalyst is its textural stability, which is not high enough to meet the requirements of high-temperature gas-phase catalytic reactions. The surface area of CeO_2 generally drops to a few square meters per gram at around 1000-1100 K, depending on preparation procedure and type of treatment. Another factor which discourages the use of pure ceria is its cost, which is higher than that of more common supports like Al_2O_3 and SiO_2.

Much effort has therefore been directed in recent years to find catalyst formulations which can enhance the thermal stability of ceria without diminishing its special features, such as its redox properties and its high oxygen mobility.

In summary, ceria plays several roles in TWC; it was suggested to:

- promote the noble metal (NM) dispersion;
- increase the thermal stability of the alumina support;
- promote the water gas shift (WGS) reaction;
- favours catalytic activity at the interfacial metal-support site;
- promote CO removal through oxidation employing a lattice oxygen;
- enhance the NO_x reduction capability of rhodium;
- store and release oxygen under, respectively, lean and rich conditions.

There is a common point in all the properties listed above which is related to the ability of NM/CeO_2 system to promote migration/exchange of oxygen species in the reaction. Furthermore alumina tends to sinter and lose its large surface area under high temperature conditions. The addition of ceria can limit this reaction. Kašpar *et al.* [20] reported that the thermal ageing leads to loss of NM/CeO_2 interactions and noted that the consequent deactivation seems to be related to two different phenomena:

1. sintering on the noble metal particles leading to a loss of metal surface area;
2. loss of CeO_2 surface area leading to a loss of the OSC.

It appears that whether or not, the promoting effects of ceria on the TWCs are exact, they are noticeable as long as high surface area compounds are present in the CeO_2-based catalysts. The research focused on the improvement of the surface stability in the ceria promoter found that ZrO_2 was the most effective thermal stabiliser of CeO_2, mainly when it formed a mixed oxide with ceria, in fact a ceria-zirconia compound, usually called ceria stabilized zirconia, is used in exhaust catalytic converters. From this considerations, many studies are dedicated to ceria-zirconia solid solutions as systems with high thermal stability and rather high bulk and surface oxygen mobility [15, 20 - 22].

Thermal stabilisation could also be obtained with cation doping: for example cations with ionic radii smaller than that of Ce^{4+}, e.g. Th^{4+}, Si^{4+}, La^{3+}, Y^{3+}, Sc^{3+}, Al^{3+}, Ca^{2+}, have been found to stabilise the CeO_2 against sintering [15]. It appears that the common mechanism of the stabilisation of surface area with the tri-valent dopants is a surface M^{3+} enrichment that impedes ceria crystallite growth under oxidising conditions. Segregation at the surface of low-valent cations together with oxygen

vacancies is energetically favoured and may represent the driving force for this surface area stabilisation [23].

3.1.6. Surface Science techniques

Common surface science techniques can be used to study ceria based systems, providing the peculiarities of the material are taken into account; among them, the insulating character of cerium dioxide is one of the major factors. In fact, this creates difficulties in working with microscopic techniques such as STM and can lead to charging effects during XPS analysis.

3.1.6.1. Scanning Probe Microscopy

One of the requirements to be able to perform STM measurements is that the sample has to be conductive, or at least it has to be possible to induce conductivity on it using different strategies. Ceria is known to be an insulator with a ~6 eV energy band gap between the valence band and the conduction band. Figure 3.5 shows the partial and total density of states of bulk CeO_2 [10].

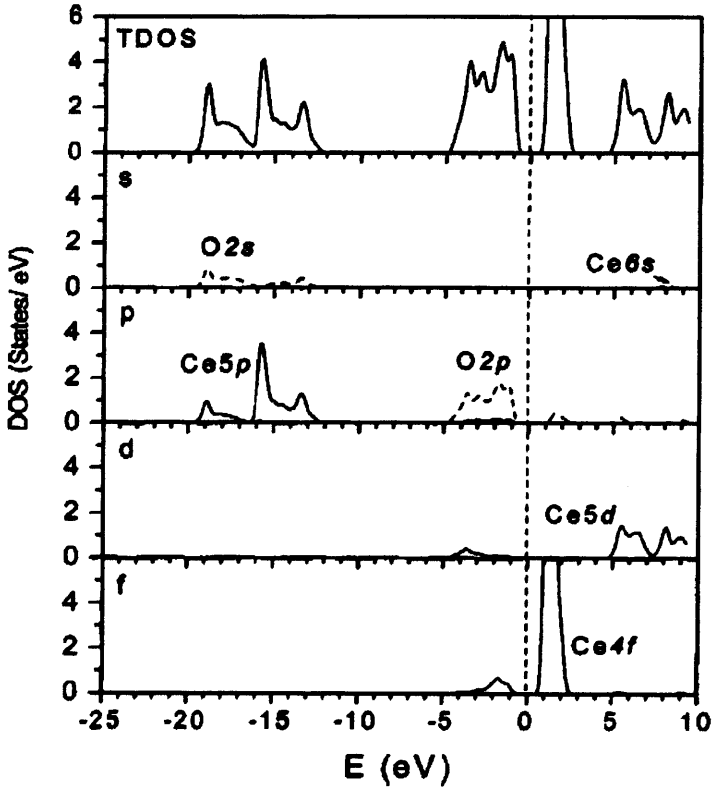

Fig. 3.5: Partial and total density of states of bulk CeO_2. The dashed line at 0eV represents the Fermi level [10].

The highest occupied valence band state exhibits a marked O 2p character, whereas the conduction band is the result of a contribution from mainly Ce 5d and less of Ce 6s states. The narrow band situated just above the Fermi level is essentially made of Ce 4f empty states.

Nörenberg and Briggs [24, 25] published the first atomically resolved STM pictures of $CeO_2(111)$. They have been able to induce a small but effective degree of conductivity to a ceria (111) single crystal and they have been able to image it using very low tunnelling currents (10 - 20 pA) and a commercial Pt-Ir tip, at room temperature. They claimed that the small conductivity was probably due to the presence of CaO contamination on the surface, as revealed by AES and they increased it annealing in UHV conditions at 1000 °C for few minutes [26]. Since annealing had the effect of removing oxygen, from conductivity measurements they estimated a slight understoichiometric oxide such as CeO_{2-x} with $x=0.01 \pm 0.005$. Using negative bias (-2 V to -3.5 V) they recorded a hexagonal array of atoms, which they said to be oxygen atoms and the tunnelling was from the tip to the oxygen 2p states. They also manage to characterise the defects present on the surface (figure 3.6 a). These are triangular and or linear oxygen vacancies, as shown in the model in figure 3.6 b.

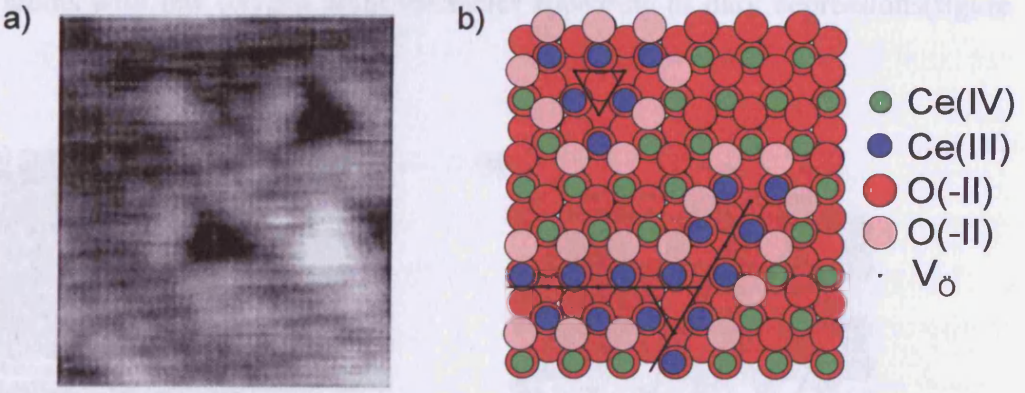

Fig. 3.6: a): STM image of triangular defects present on non-stoichiometric $CeO_2(111)$ showing enhanced brightness at the defect edges, image size 35 Å x 40 Å, U_{bias} - 2.5 V, I_T - 10 pA, RT. b): model of non-stoichiometric $CeO_2(111)$ showing the (1x1) terminated surface with triangular defects (upper left corner) and line defects (lower right corner); the edge of the oxygen vacancies are shown in a lighter shade [adapted from 25].

In a further publication they showed the evolution of the triangular defects with the annealing temperature [27]. Triangular clusters firstly form and then lines of missing oxygen appear. Branches are then appearing in the linear defects and finally, additional triangular effects appear at the points of intersection of linear defects, creating a rather regular pattern of triangular defects on the surface. Oxygen defects were usually accompanied by enhanced brightness of the surrounding oxygen atoms. This was explained as delocalization of the electron density, formerly on the oxygen now missing, to the surrounding oxygen atoms. Although able to tunnel on the sample, they tried to obtain atomic resolution on the (110) face without success [27].

Nörenberg and Harding [28] obtained atomic resolution also on the (001) face, which should be polar, a type III surface according to Tasker definition [6], but rapidly undergoes oxygen reconstruction. Oxygen vacancies created by annealing showed a $\sqrt{2}/2(3\times2)R45$ reconstruction and after exposure to air and UHV cleaning they observed a $c(3\times3)$ reconstruction.

The (111) surface has also been studied by NonContact Atomic Force Microscopy (NC-AFM). Fukui and co-workers [29, 30] prepared a ceria (111) single crystal as Nörenberg [24] suggested and obtained atomic resolution using NC-AFM. After annealing at 1173 K for 1 minute, as expected they obtain a hexagonal array of oxygen atoms with few oxygen point vacancies appearing as dark depressions(figure 3.7).

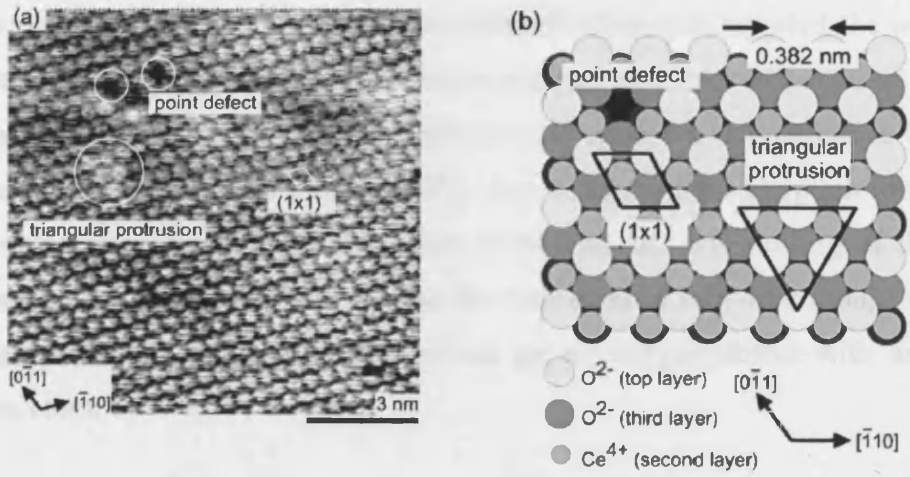

Fig 3.7: (a) Atom-resolved NC-AFM image of nearly stoichiometric $CeO_2(111)$ surface, $\Delta f \sim 149$ Hz; (b) model of bulk-terminated structure of $CeO_2(111)$ with oxygen layer termination [30].

They also observed some triangular protrusion which had an apparent topography higher than other surface oxygen atoms by 0.03-0.05 nm and a slight distortion in the in plane oxygen atoms. They interpreted the distortion as reflection of the surface stress induced by the formation of oxygen vacancies After a longer annealing (3 minutes), they reported the increase of oxygen defects, appearing now as triangular and linear. The linear defect were formed by removal of oxygen atoms along the (111) plane main directions. Moreover they reported a slight change in position of the oxygen atoms surrounding the defect which appear to move towards the defect (figure 3.8).

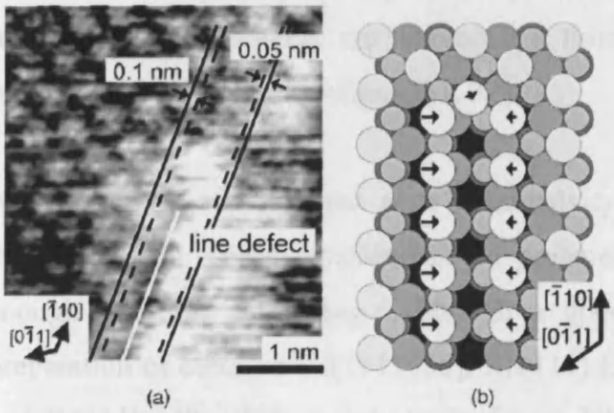

Fig 3.8: NC-AFM image at a line defect observed on a surface annealing at 1137 K for 2 minutes, $\Delta f \sim 228$ Hz. (b) tentative model showing displacement of oxygen atoms surrounding the line defect observed in (a) [30].

They also showed that oxygen vacancies can be healed by O_2 exposure at room temperature [31, 32]. By exposing the surface to methanol they concluded that they are the reactive sites on the surface, because methoxy groups could adsorb only where single point and triangular defects were present. They also reported the presence of hopping surface oxygen atoms at room temperature and they estimated an activation energy barrier of 30 kJ mol^{-1} for this process. By exposure of a defective $CeO_2(111)$ surface to NO_2 at room temperature [33], they observed the adsorption of the gas on the oxygen vacancies, with dissociation of NO_2 to NO and healing of the surface vacancy. A minor parallel process was the formation of NO_3-like groups tentatively interpreted as oxidation of NO_2 adsorbed on an oxygen defect with an adjacent oxygen atom.

Recently Esch and co-workers [34] published large scale (~14×14 nm) high resolution STM pictures of CeO_2(111) after annealing at 900 °C, imaged at 300 °C. This allowed the evaluation of defects distribution on the surface. On a slightly reduced surface obtained after 1 minute of annealing, two types of single oxygen vacancies prevail. One appears as a depression surrounded by three paired lobes and was assigned to surface oxygen vacancies by comparison with simulated images. The other type appears as a triple protrusion in a filled-state image and as a single vacancy in an empty-state image. These defects count for the 1.3% of the surface atoms. On a more reduced surface prepared by annealing at 900°C for 5 minutes, the linear defects represent the 92% of the total and they count for the 2.2% - 3.0% of surface atoms. All the defects find explanation by comparison with DFT calculation. Moreover they reported that the defects are stable on a time scale of minutes, in contrast with previous NC-AFM observations [31, 32].

As a way to overcome the poor conductivity of ceria, CeO_2(111) thin films on different metal single crystals can be prepared; such ceria layers should be thin enough to allow tunnelling. Although a good number of publication cover the preparation of ceria on Pd(111) [35], Rh(111) [36 - 38], Ru(0001) and Ni(111) [39], and Pt(111) [40 - 44], mainly, only few publications reported atomically resolved STM images.

In particular, Eck and co-workers [37] prepared ultrathin (less than 6 monolayers equivalent) ceria films on Rh(111). The ceria appeared to grow in form of ordered arrays of randomly shaped particles in a Volmer-Weber island growth mode (figure 3.9). The islands have a CeO_2(111) orientation, with their edges parallel to the Rh(111) main directions. Annealing in vacuum at ~ 600 °C promotes the self organization of the ceria layer and the particles became flatter and hexagonal. They obtained atomic resolution on these islands where it was possible to identify several oxygen vacancies evenly distributed in an hexagonal arrangement. Annealing at temperature higher than 800 °C caused the decomposition of the ceria layer and the formation of a Ce-Rh alloy.

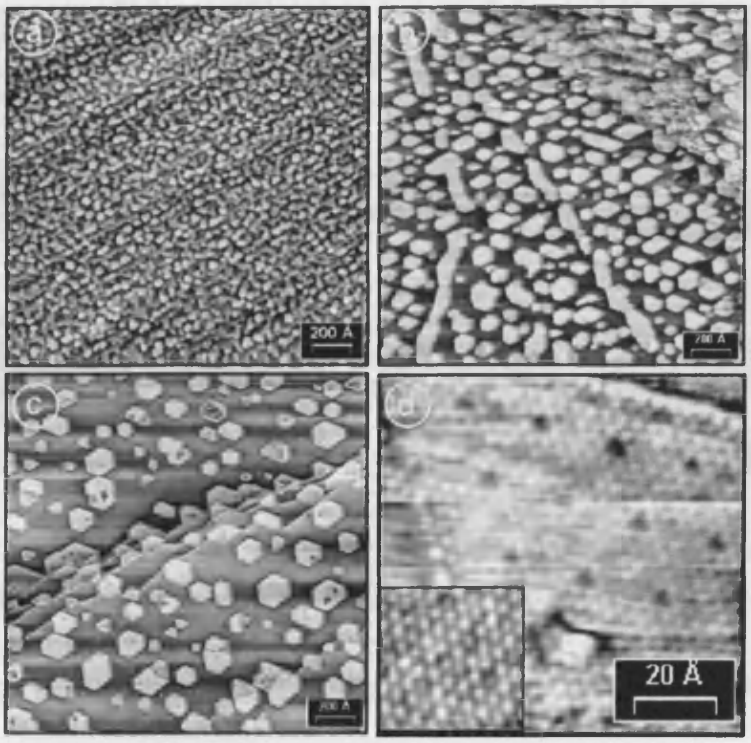

Fig. 3.9: STM images of 0.9 MLE ceria/Rh(111) after annealing to: (a) 475 °C, 2 V, 0.96 nA; (b) 585 °C, 1.98 V, 1.03 nA; (c) 700 °C, 0.73 V, 1.18 nA; (d) 700 °C, 0.98 V, 1.02 nA; high-resolution image of the surface of a ceria island as in (c). Note the dark patches due to oxygen vacancy defects. The insert in (d) is a magnified atomic-resolution image (0.75 V, 1.07 nA) of the ceria surface [37].

Berner and Schierbaum [42, 43] prepared a Ce-Pt alloy by depositing metallic cerium on a Pt(111) single crystal at 1000 K, resulting in well ordered two-dimensional overlayers (figure 3.10a). They obtain atomically resolved STM images of these layers compatible with the presence of Pt_5Ce superstructures. Preparing the same system annealing at 900 K a structure thought to be a precursor of the Ce-Pt alloy was formed. By oxidation at 1000 K, the Pt_5Ce islands reconstruct into several layers of defective $CeO_2(111)$. Atomically resolved STM pictures showed the ceria lattice with some oxygen vacancies (figure 3.10b). The ceria islands reverse back to Pt-Ce alloy passing through a structure that was tentatively attribute to $Ce_2O_3(0001)$.

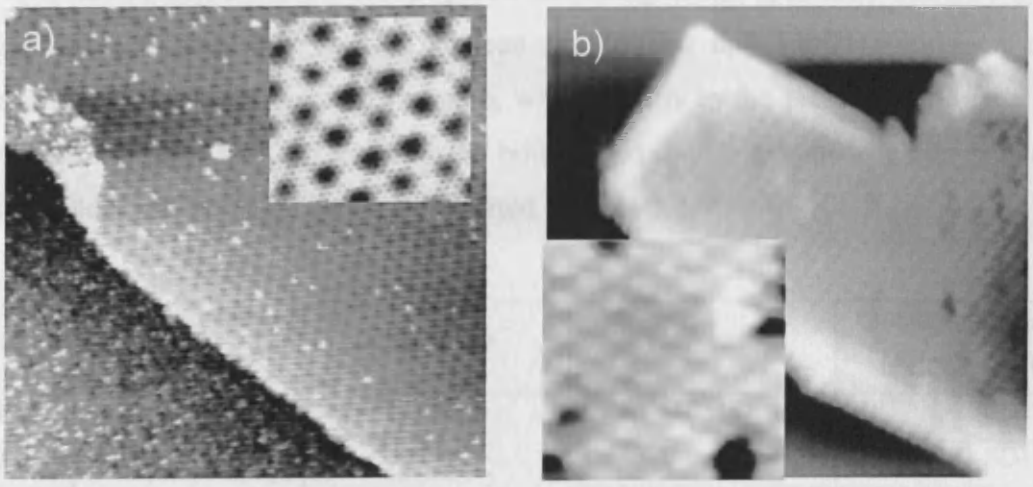

Fig. 3.10: a) Constant-current STM image (455×455 Å) of the Ce-dosed Pt(111) surface after heating in UHV at 1000 K (0.07 V, 0.57 nA). Insert image: 67×67 Å close-up (0.14 V, 0.69 nA). b) STM constant-current topography of a CeO_2 island (230×230 Å, -3.1 V, 0.115 nA). The inset (29×29 Å, -3.1 V, 0.108 nA) displays atomic resolution. a) from [42], b) from [43].

3.1.6.2. X-ray Photoelectron Spectroscopy

The identification of the Ce oxidation state is a complex and controversial matter to the extent that in several publications Ce(3d) spectra are only presented, without any other peak identification than the $3d_{5/2}$ (V) and the U''' feature at 916.8 eV. Moreover, also a clear estimation of the relative amount of the different oxidation states of the cation results very difficult [41, 46, 47]. On the other hand, there are a number of publications agreeing in the identification of the peaks [45, 48 - 52] and trying to propose a way to analyze them. The 3d peak of metallic cerium shows a doublet with the $3d_{5/2}$ set at 883.8 eV and a J splitting of 18.1 eV [53]. For an oxidised metal a shift of the 3d band toward higher binding energies is normally expected, but for Ce(IV) a position of ~ 882 eV is reported [52]. For Ce(III) the $3d_{5/2}$ (V^0) is expected at ~881 eV. Because of the finite probability of different final occupation states following the excitation process, a series of *satellite* peaks is generated. These peaks are attributed by different authors [49, 51] to photoelectron energy gain (*shake-down, SD*) as well as photoelectron energy loss (*shake-up, SU*) processes. For stoichiometric, defect-free CeO_2, a spectrum containing six peaks consisting in three J doublets, having approximately the same spin-orbit separation of 18.4 – 18.6 eV, is expected, whereas

Ce_2O_3 shows only a pattern of four peaks consisting in two spin-orbit doublets (figure 3.11). CeO_2 can easily switch between the Ce(IV) and Ce(III) oxidation states depending upon the O_2 partial pressure, which results in the presence of a pattern of 10 peaks related to the Ce cation in both its oxidation states. The ten peaks are classified according to the scheme reported in table 3.2.

BE /eV	J	Oxidation state	Initial state	Final state	Notation [47]	Type [49]
917.0	3/2	IV	$Ce\ 3d^{10}\ O\ 2p^6\ Ce\ 4f^0$	$Ce\ 3d^9\ O\ 2p^6\ Ce\ 4f^0$	U'''	SD2
906.3				$Ce\ 3d^9\ O\ 2p^5\ Ce\ 4f^1$	U''	SD1
900.6				$Ce\ 3d^9\ O\ 2p^4\ Ce\ 4f^2$	U	M
898.5	5/2			$Ce\ 3d^9\ O\ 2p^6\ Ce\ 4f^0$	V'''	SD2
888.8				$Ce\ 3d^9\ O\ 2p^5\ Ce\ 4f^1$	V''	SD1
882.5				$Ce\ 3d^9\ O\ 2p^4\ Ce\ 4f^2$	V	M
900.2	3/2	III	$Ce\ 3d^{10}\ O\ 2p^6\ Ce\ 4f^1$	$Ce\ 3d^9\ O\ 2p^6\ Ce\ 4f^1$	U^0	M
904.8				$Ce\ 3d^9\ O\ 2p^5\ Ce\ 4f^2$	U'	SU
881.7	5/2			$Ce\ 3d^9\ O\ 2p^6\ Ce\ 4f^1$	V^0	M
886.3				$Ce\ 3d^9\ O\ 2p^5\ Ce\ 4f^2$	V'	SU

Table 3.2: attribution of the Ce(3d) peaks on CeO_2; BE values +/- 0.5eV. M = main peak, SD = shake down, SU = shake up.

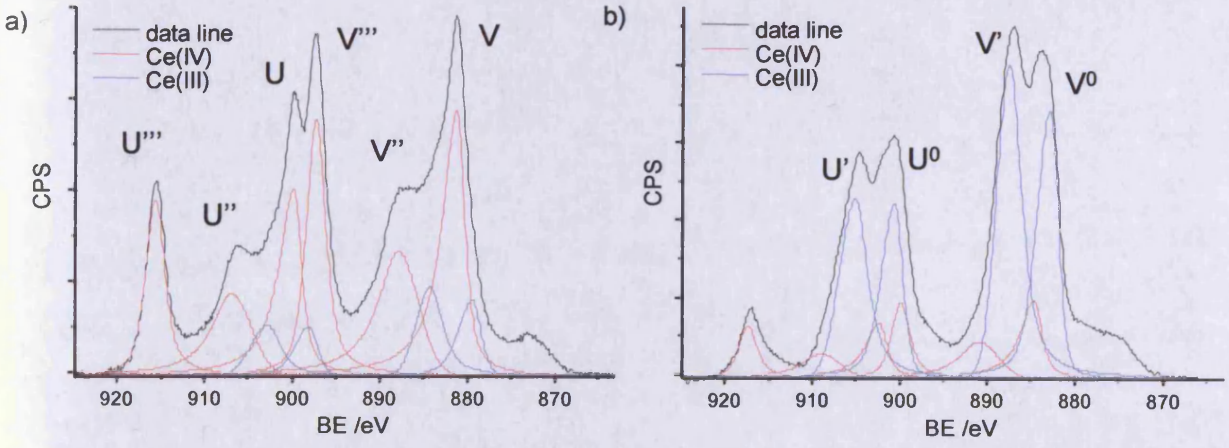

Fig. 3.11: Ce(3d) XP spectrum deconvolution [54]. a) Ce(IV) ~80% (red lines), Ce(III) ~20% (blue lines). b) Ce(IV) ~20% (red lines), Ce(III) ~80% (blue lines).

Since the Ce(3d) spectrum is in general composed of a series of 10 overlapping peaks, if Gaussian or Gaussian-Lorentian functions are used to fit the spectrum, there are at

least three parameters for each peak that have to be taken into account: peak position, Full Width at Half Maximum (FWHM) and peak intensity. This means a total of 30 parameters. Statistical routines can handle the problem, but there is a chance that the results will be not unique and/or not reproducible, or even produce a pattern of peaks that fit the experimental data but does not have chemical meaning. This could happen, for example, if the mathematical fitting will only minimise the residuum, in order to find the best fit, without taking into consideration chemical restriction. These are dictated by the type of element and its oxidation state and reflects on the number of peaks that have to be present, their width, their areas and the distance in energy between each other. Taking into account these restrictions, it is possible to simplify the fitting procedure. For a fully oxidised specimen, after subtracting a Shirley-type background, 6 peaks can be unambiguously identified. The U''' peak, easily recognized at ~ 917 eV because normally well separated from the rest of the spectrum, is typical of Ce(IV). However, a broad feature roughly at this binding energy is also present for Ce(III) and should correspond to the satellites of the U' and U^0 peaks due to the $K\alpha_3$ and $K\alpha_4$ of X-ray source (see section 2.4.4.5). The U''' can be distinguished by the satellite feature because it is considerably narrower, in fact it has a FWHM ~ 2.2 eV, whereas the satellite structure can extend for 4-5 eV. Using a J splitting of ~18.5 eV it is possible to identify V''' and from here to estimate a more precise value of J. Unfortunately the spin-orbit splitting is reported from many authors to be different for the different components. Nevertheless, since the difference is only of few tenth of eV, there is the possibility to estimate it with a good accuracy. In this way three different values of J are obtained. Imposing approximately the same FWHM and the area ratios 3:2 to the three couple of peaks, the pattern of 6 peaks belonging to Ce(IV) is obtained. For a fully reduced sample the procedure is similar but the peaks to be identified are only 4. For a specimen with the majority of cerium atoms in (IV) oxidation state, subtracting from the experimental data the peaks belonging to Ce(IV), a pattern of 4 peaks should result and therefore an estimation of the amount of Ce(III) can be made. Sometimes also in this simplified scenario it is difficult to obtain a result consistent with the experiments as an inaccuracy > 10% has been recorded for small degrees of reduction [51].

3.2. Experimental setup

All the experimental work was performed on the Omicron Multiprobe ® Surface Science System described in Chapter 2. The UHV chamber had a typical base pressure of ~ 3×10^{-10} mbar, which increased to ~ 1×10^{-9} mbar during XPS and LEED analysis. The base pressure during STM, with the STM chamber closed off from the rest of the system, was ~ 9×10^{-11} mbar.

The XPS analysis were performed using both a Mg Kα x-ray source (1253.6 eV) and an Al Kα x-ray source (1486.6eV) depending upon the case. A pass energy of 100 eV was used to collect the survey spectra, whilst a pass energy of 50 eV was used to collect detailed spectra. Binding energies were calibrated with respect to the C(1s) (BE = 284.5 eV) feature corresponding to the presence of adventitious carbon. When carbon was not present the calibration was done according to the Ce($3d_{3/2}$), U''', peak at 916.8 eV for the CeO_2(111) single crystal and according to the Cu($2p_{3/2}$) at 932.6 eV for the CeO_2(111)/Cu(111) system. The value for the U''' peak was derived taking the average values reported in [48 - 52, 56 - 59]. All the data were recorded at RT. All STM measurements were acquired using a W tip obtained by electrochemical etch of a W wire (99.995% purity, 0.39 mm Ø).

XPS data analysis and interpretation was done using CasaXPS [60] software, STM and AFM images were analysed using WSxM package [61], or Nanoscope [62].

3.3. Results

3.3.1. Oxygen adsorption studies on CeO_2(111) single crystal

3.3.1.1. Crystal cleaning

The ceria (111) single crystal used was previously used in a variable temperature Oxford Instruments STM, in the attempt to atomically resolve its structure and image the oxygen storage process.

To clean the crystal without damaging the surface and create enough conductivity on it in order to obtain tunnelling current the procedure elaborated and performed by Nörenberg and Briggs [24 - 27], was used. The crystal was cleaned by repeated cycles of Ar^+ sputtering, followed by annealing under 1×10^{-6} mbar of O_2 at 723 K and

subsequent flashing at 1023 K without oxygen. The STM could tunnel on the sample and image steps and terraces, but atomic resolution was not achieved. In order to create more conductivity, the sample was flashed gradually to higher temperature. The last experiments carried out to obtain a tunnelling current involved flashing at 1173 K and 1273 K. It was, unfortunately, not possible to obtain a decent tunnelling current after annealing treatment at low temperature. Due to annealing to very high temperatures, the crystal had lost its flat and smooth surface presenting a cleaved surface with a small hole in the middle (likely the effect of tip crashes). Cracks on the surface could be imaged using contact mode air AFM. Figure 3.12 a) and b) show two different areas of the crystal.

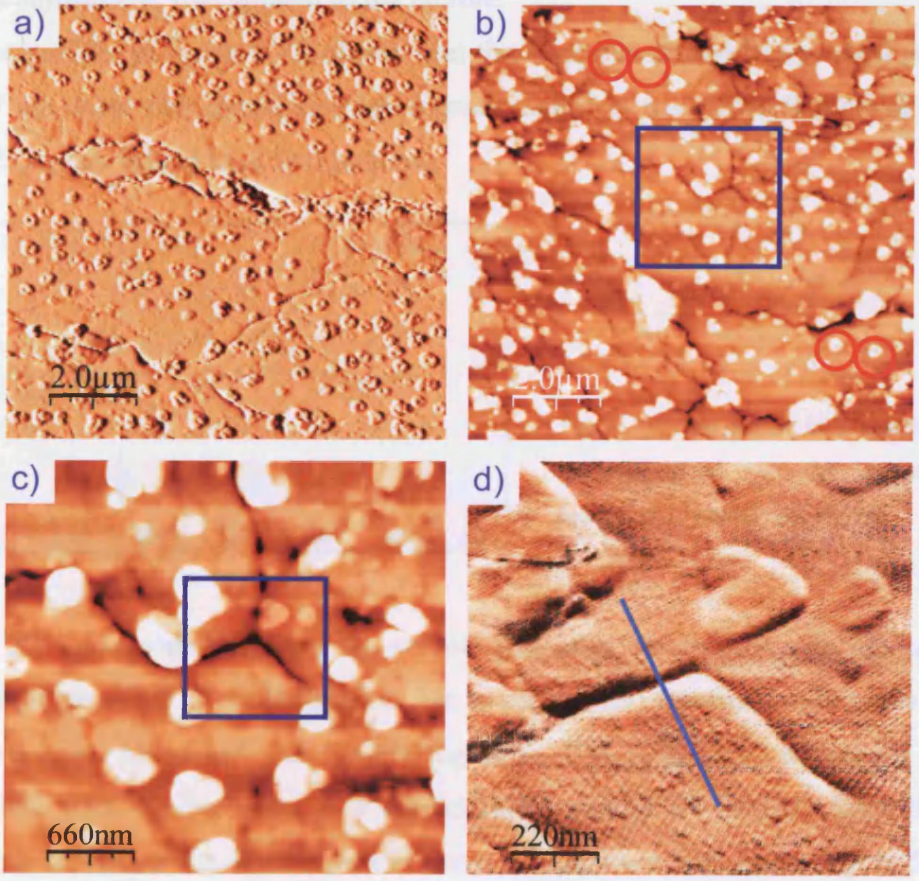

Fig. 3.12: Contact mode AFM images of the CeO_2(111) single crystal before use. a) friction image (image size 10×10 µm); b) topography on a different area than a) (image size 10×10 µm); c) topography of the blue square area in b) (image size 3.3×3.3 µm); d) friction image of the blue square area in c) (image size 1.1×1.1 µm).

On a flat background several fracture lines are evident. The presence of particles was also recorded. These could have been due to contaminants on the surface. However, the contamination level may not be as important as it might appear. In fact, a tip artefact could be responsible for additional repeated particles (see particle in red circles in figure 3.12 b), although not all the particles appeared repeated. Also the unusual "ring" appearance of the particles, visible in figure 3.13 a), can be attributed to a tip artefact. While scanning in contact mode, this could derive from accumulation of mobile debris on the apex of the tip. The ring shape may derive by the convolution of the signal recorded by the tip with the one recorded from the debris. Since the debris is mobile, the particles appear normally elongated and inhomogeneous in size. The ring shape effect is less visible in figure 3.12 b) because a equalization filter, contrast adjustment, was applied to the picture.

The line profile, in figure 3.13, shows that the fractures are typically ~100 nm wide and ~ 7 nm deep. The crystal also had a crack visible at naked eye that could diffract the LEED beam into at least two patterns.

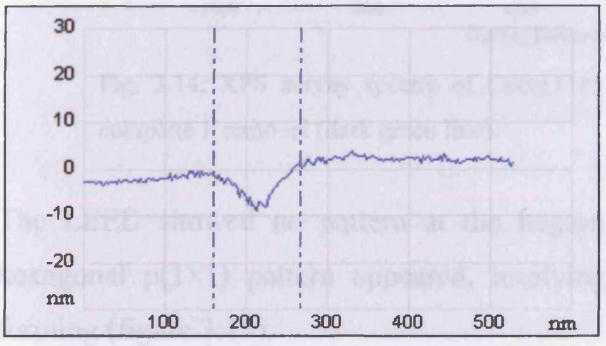

Fig. 3.13: Line profile as in figure 3.12 d), but measured on the corresponding topographic image, not shown.

Survey XP spectra collected on the sample just after inserting it into the chamber showed the presence of contamination due to carbon and fluorine compounds (figure 3.14, red line). Moreover, the Ce(3d) region (~ 870 – 920 eV) showed a pattern compatible with the presence of a considerable amount of Ce(III). After the first sputtering treatment for 10 minutes at room temperature and annealing at 500 °C, carbon removal was achieved (no signal at XPS around 285 eV). On the contrary, the F was still present after two weeks of cleaning (figure 3.14, dark green line), but the signal of the F(1s) peak at ~ 685 eV was progressively losing intensity. Although it was not possible to remove it completely, the amount of F present was decreased during the cleaning cycles to less than 1% of the surface concentration. The Ce(3d)

region showed now the pattern typical of cerium in the +4 oxidation state. Moreover it is interesting to notice that also the Ce(4d) at ~110 eV changed in shape after cleaning. The Ce(5p) now appears on the spectrum.

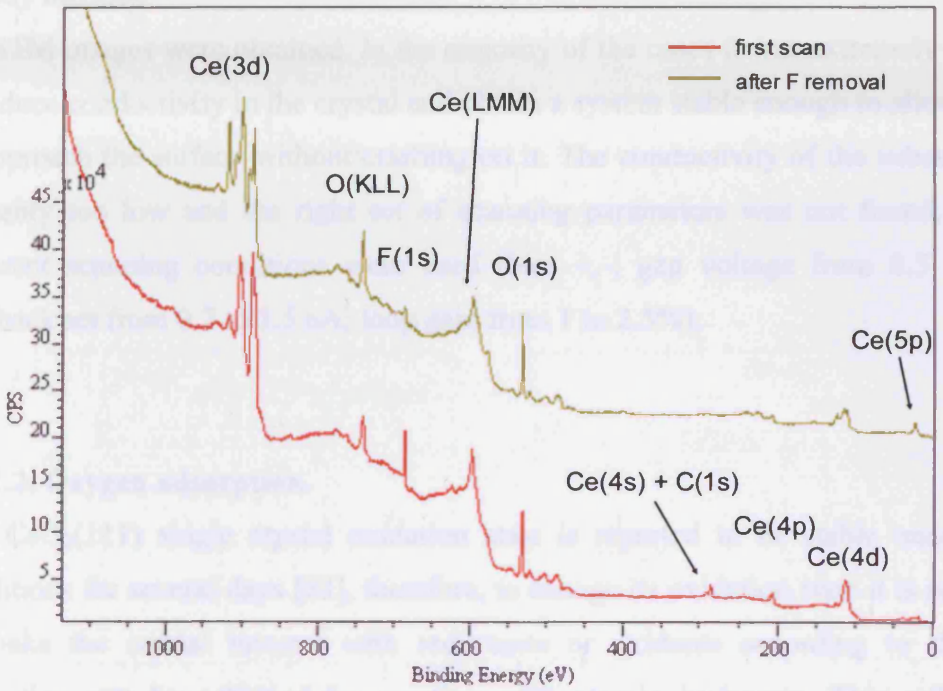

Fig. 3.14: XPS survey spectra of CeO_2(111) before (red line) and after nearly complete F removal (dark green line).

The LEED showed no pattern at the beginning. After a couple of days, a faint hexagonal p(1×1) pattern appeared, implying that a fairly ordered structure was forming (figure 3.15).

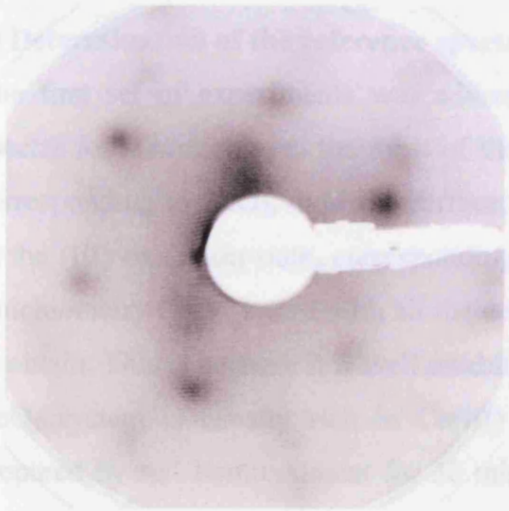

Fig. 3.15: LEED pattern of CeO_2, recorded at 48 eV. Although the overall quality is not good, the hexagonal pattern confirms that the surface under study is the (111).

After two weeks the LEED pattern was significantly improved, but still with poor sharpness of the spots as well as poor contrast with the background. This effect was likely caused by the presence of fluorine and of several fractures on the surface, as already mention.

No STM images were obtained. In the majority of the cases it was extremely difficult to induce conductivity in the crystal and obtain a system stable enough to allow the tip to approach the surface without crashing on it. The conductivity of the substrate was probably too low and the right set of scanning parameters was not found, even if different scanning conditions were used (bias +,-; gap voltage from 0.5 to 4 V; feedback set from 0.7 to 1.5 nA; loop gain from 1 to 2.5%).

3.3.1.2. Oxygen adsorption.

The $CeO_2(111)$ single crystal oxidation state is reported to be stable under UHV conditions for several days [63], therefore, to change its oxidation state it is necessary to make the crystal interact with reductants or oxidants according to the case. Reduction can be achieved by reaction with atomic hydrogen. This will create hydroxyl-species which will combine and desorb as water [49]. Simply annealing at high temperature induces oxygen desorption and hence surface reduction. Oxidation can be induced by exposing the ceria crystal to an oxygen rich environment.

Oxygen adsorption on $CeO_2(111)$ was studied with the aim of identifying the active oxygen species present and to obtain quantitative information about its OSC.

a) Determination of the reference spectra.

The first set of experiments was addressed to the determination of the reference spectra for a surface with the most of the cerium cations in the (IV) oxidation state, corresponding to CeO_2, oxidised surface, and a surface where the cerium cations are in the (III) oxidation state, corresponding to Ce_2O_3, reduced surface. A surface with stoichiometry CeO_2, hence with all the cerium ions in (IV) oxidation state, is difficult to obtain. This is because it is well established [35, 37, 40] that the very top layer of a CeO_2 system is usually rich in Ce(III) cations. Starting from a reduced surface, prepared by Ar^+ bombardment for 30 minutes at room temperature, the ceria crystal

was firstly flashed to 800 °C, allowed to cool to 300 °C in vacuum, then exposed to $1x10^{-7}$ mbar of oxygen for 30 minutes, at 300 °C. The heating was stopped and the sample allowed to cool to room temperature in oxygen. This was necessary to ensure that no oxygen desorption may occur; this becomes even more important when the temperature at which the experiments are carried out increases. XPS was collected and then a second oxygen treatment was made in the same way as exposed above. Ce(3d) and O(1s) XP spectra illustrating this experiments are showed in figure 3.16. In figure 3.17 the fittings of the Ce(3d) region before and after the first oxygen exposure are shown.

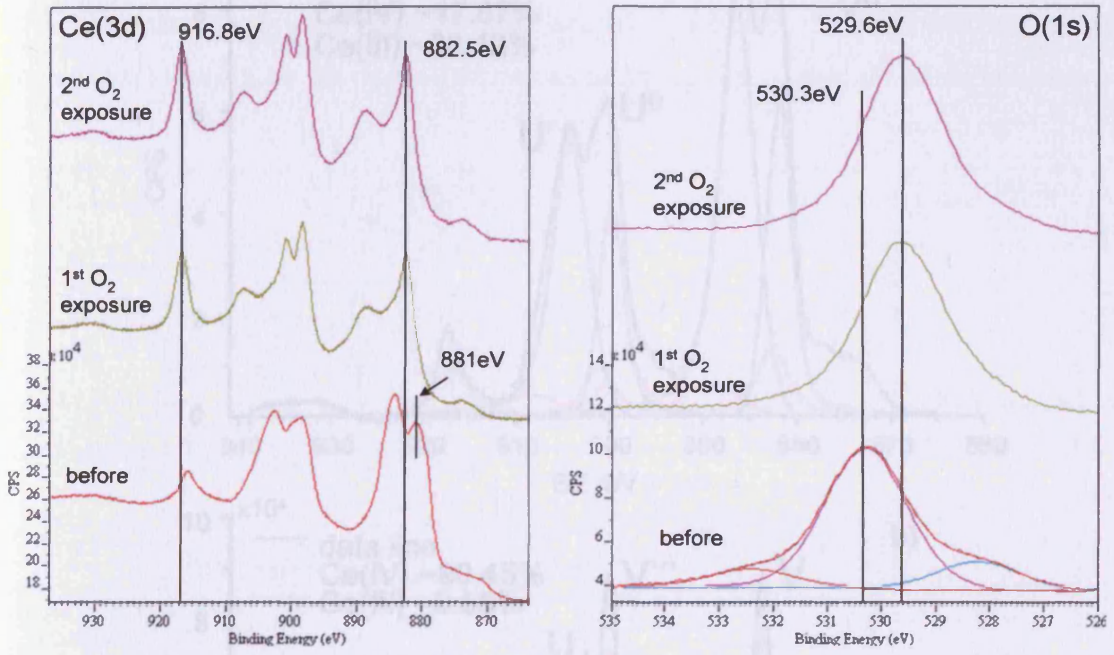

Fig. 3.16: XP spectra relative to the set of experiment to determine the Ce(3d) XP spectrum for the surface with the maximum degree of oxidation. Ce(3d) region on the left, O(1s) region and fitting on the right.

As expected, the Ce(3d) shows that starting from a reduced surface (Ce(III) > 76%, O/Ce integral ratio ~1.60), the majority of the cerium cations were oxidised to Ce(IV) due to the first oxidising treatment; the relative amount of Ce(IV) did not change after the second oxygen exposure. This Ce(3d) pattern was assumed to represent the surface with maximum degree of oxidation (Ce(IV) ~ 92% after the first exposure and ~91% after the second exposure, with O/Ce integral ratio ~1.96. The $Ce(3d_{5/2})$ component was recorded at 882.5 eV for Ce(IV) and at 881.0 eV for Ce(III). The

O(1s) XP spectra varied accordingly; the spectrum recorded after sputtering but before the high temperature flashing showed at least three components, one at ~528.4 eV and one at ~532.4 eV other than the one at ~530.3 eV, attributed to the oxide which increased by 18% approximately after the first exposure and increased of a further 1% after the second. After oxidation a single oxygen peak at ~529.6 eV was present.

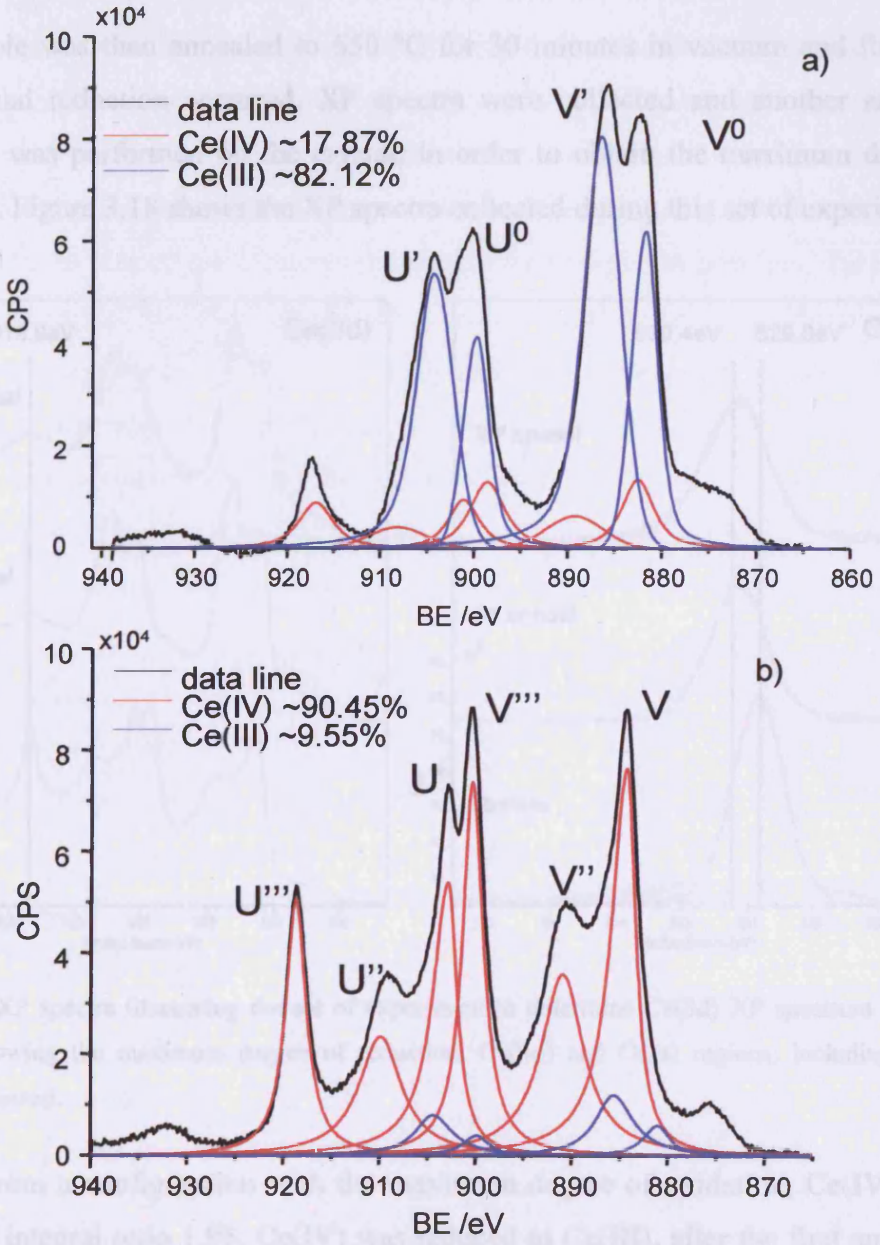

Fig. 3.17: Ce(3d) XP spectra before (a) and after the first oxygen treatment (b). Peak fitting components are shown.

The component formerly at ~532.4 eV disappeared after oxidation. This peak is linked to the presence of Ce(III) as will be clarified later (see section 3.4.4.). The O(1s) component at ~528.4 eV may represent a lattice oxygen species with a more "ionic" character in respect of the normal one [64]. A very low binding energy oxygen feature will also be recorded in a following set of experiments. The relative amount of Ce(III) and Ce(IV) was calculated by fitting the Ce(3d) region as illustrated in section 3.1.6.2.

The sample was then annealed to 650 °C for 30 minutes in vacuum and flashed to 800 °C and reduction occurred. XP spectra were collected and another annealing treatment was performed on the crystal, in order to obtain the maximum degree of reduction. Figure 3.18 shows the XP spectra collected during this set of experiments.

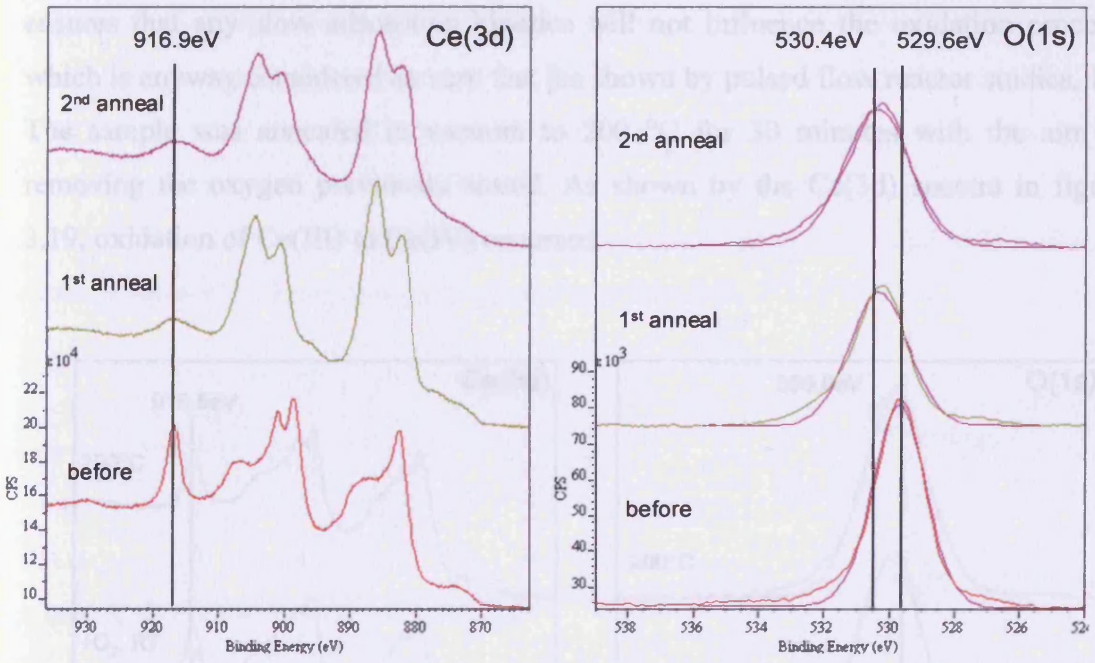

Fig. 3.18: XP spectra illustrating the set of experiment to determine Ce(3d) XP spectrum for the surface showing the maximum degree of reduction. Ce(3d) and O(1s) regions, including peak fittings, showed.

Starting from a configuration with the maximum degree of oxidation, Ce(IV) ~91% and O/Ce integral ratio 1.95, Ce(IV) was reduced to Ce(III), after the first annealing. After the annealing, the amount of Ce(III) was estimated in ~74.4%, and the O/Ce integral ratio 1.62. The O(1s) XP peak decreased by 19.2% and shifted from 529.6 eV

to 530.4 eV. Both Ce(3d) and O(1s) peaks do not show any further change after the second heating treatment. In particular, the O(1s) region did not show any feature other than the oxide peak. The final Ce(3d) pattern was taken as a reference for the system having the maximum degree of reduction.

b) Oxidation/reduction experiments

Oxidation/reduction experiments were performed in an interval of temperature generally lower than the operating temperature of an exhaust catalyst. Starting from the reduced surface prepared as previously explained, the crystal was exposed to $1x10^{-7}$ mbar of O_2 for 30 minutes at room temperature, the gas was evacuated and the XPS collected. A very long time of exposure corresponding of ~2350 Langmuirs was chosen with the aim of inducing as higher oxidation degree as possible. This, in turn, ensures that any slow adsorption kinetics will not influence the oxidation process, which is anyway considered as very fast [as shown by pulsed flow reactor studies, 14]. The sample was annealed in vacuum to 200 °C for 30 minutes with the aim of removing the oxygen previously stored. As shown by the Ce(3d) spectra in figure 3.19, oxidation of Ce(III) to Ce(IV) occurred.

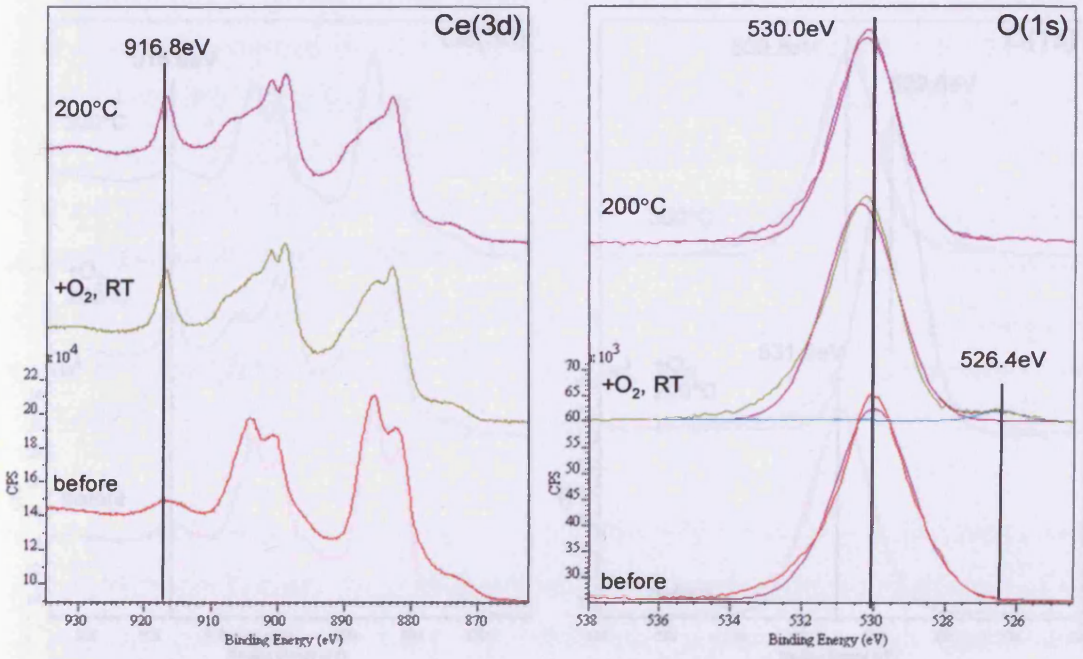

Fig. 3.19: Ce(3d) XP spectra and O(1s) XP spectra and peak fittings for the surface showing mainly Ce(III) (>80.5%), after oxygen exposure at room temperature and after annealing at 200 °C.

The relative amount of Ce(IV), initially ~19.5% with O/Ce ~1.57, was calculated as ~57%, with O/Ce ~1.77, after oxidation and ~54%, with O/Ce ~1.76, after annealing at 200 °C. The O(1s) XP spectrum showed a moderate shift from 530.0 eV to 530.3 eV, in contrast with the trend observed before, consisting in a decrease of O(1s) binding energies with an increase of the oxidation level. A second feature, at 526.4 eV, was present after oxygen exposure and disappeared after annealing. Even if the nature of this feature is not really clear, it is tentatively attributed to lattice oxygen [64]. Another attribution could be a very negatively charged oxygen species weakly bound on the surface, which disappears as a mild annealing effect, although weakly adsorbed species usually show a signal in the ~ 531-533 eV binding energy range [65]. The sample was then reduced by annealing in vacuum to 650 °C for 30 minutes and flashing to 800 °C. XP spectra revealed that the maximum degree of reduction was achieved, being Ce(IV) ~19.7% and O/Ce ~1.58. This procedure will be called reduction procedure in the rest of the section. After reduction, the sample was subsequently exposed to $1x10^{-7}$ mbar of O_2 for 30 minutes at 200 °C and allowed to cool to room temperature in oxygen. This gives a total exposure bigger than the ~2350 Langmuirs mentioned above. XPS was collected, then the sample annealed at 300 °C in vacuum for 30 minutes allowed to cool to room temperature and XPS collected again. Figure 3.20 shows the results of the experiments.

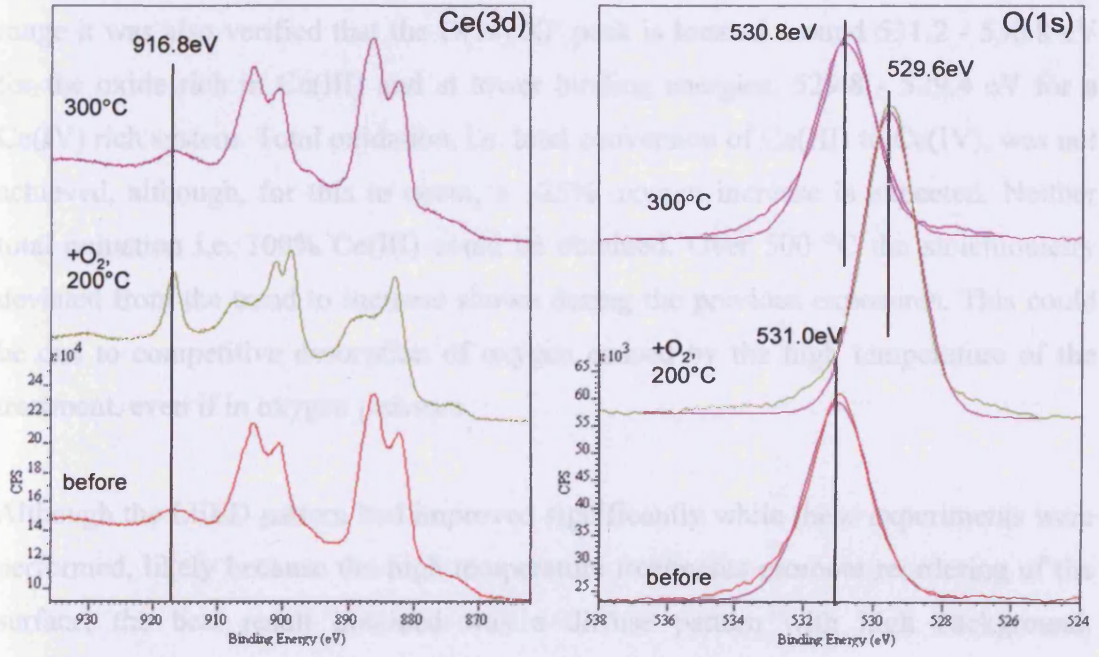

Fig. 3.20: Ce(3d) XP spectra and O(1s) XP spectra and peak fittings for the Ce(III) rich surface, after oxygen exposure at 200 °C and after annealing at 300 °C.

The amount of Ce(IV) from ~19% (O/Ce ~1.56) went up to ~66% (O/Ce ~1.82) after oxygen exposure and down again to ~17% (O/Ce ~1.54) after annealing. The oxygen peak at ~ 531.0 eV before exposure showed an increase of ~36% and a shift to 529.6 eV after exposure. As a consequence of the annealing, it shifted to 530.8 eV and decreased by a ~28%. Similar experiments were repeated for the following temperatures 300 °C, 400 °C, 500 °C and 600 °C. After each exposure to oxygen, the system was annealed for 30 minutes to a temperature 100 degrees higher than that of exposure, i.e. exposure at 300 °C in oxygen, annealing at 400 °C in vacuum. XP spectra were collected before and after each exposure to oxygen and after the reduction procedure, allowing the time necessary for the sample to reach room temperature in oxygen pressure after oxidation and in vacuum after reduction. The relative amount of Ce(III) and Ce(IV) was calculated fitting the Ce(3d) XP spectrum and is affected by an error of +/-5%. The variation of the amount of oxygen was calculated by integration of the O(1s) XP peak. Results are summarised in table 3.3.
From these data it appears that the oxidation / reduction process is enhanced above 300 °C and the same amount of oxygen can be firstly stored and then removed. At lower temperature oxygen migration from the gas phase to the bulk may not be efficient enough to fully oxidise the bulk and then saturate the surface. Moreover, the maximum stoichiometry achieved was $CeO_{1.92}$, for a system containing the 86% of Ce(IV), meaning a certain amount of Ce(III) was still present. In this temperature range it was also verified that the O(1s) XP peak is located around 531.2 - 530.8 eV for the oxide rich in Ce(III) and at lower binding energies, 529.8 - 529.4 eV for a Ce(IV) rich system. Total oxidation, i.e. total conversion of Ce(III) to Ce(IV), was not achieved, although, for this to occur, a ~25% oxygen increase is expected. Neither total reduction i.e. 100% Ce(III) could be obtained. Over 500 °C the stoichiometry deviated from the trend to increase shown during the previous exposures. This could be due to competitive desorption of oxygen caused by the high temperature of the treatment, even if in oxygen pressure.

Although the LEED pattern had improved significantly while these experiments were performed, likely because the high temperature treatments promote reordering of the surface, the best result obtained was a diffuse pattern with high background. Moreover, STM images could not be recorded because of lack of conductivity, even if

the crystal was far away from the bulk CeO_2 stoichiometry, thus supposed more conductive than stoichiometric ceria.

Temp /°C	Ce(III)/Ce(IV) BO	Ce(III)/Ce(IV) AO	Ce(III)/Ce(IV) AR	ΔO(1s) /% AO	ΔO(1s) /% AR	O/Ce BO	O/Ce AO	O/Ce AR
RT	80.5/19.5	43/57	46/54	+10.1	-07.4	1.57	1.77	1.74
200	81/19	34/66	83/17	+36.1	-28.0	1.56	1.82	1.54
300	80/20	28/72	81/19	+24.3	-25.1	1.58	1.85	1.55
400	83/17	22/78	81/20	+23.5	-22.6	1.54	1.87	1.57
500	82/18	14/86	81/19	+28.4	-23.1	1.55	1.92	1.56
600	81/19	32/68	82/18	+25.8	-24.5	1.56	1.78	1.54

Table 3.3: Results of oxygen adsorption/ desorption experiments at different temperatures, see text for details (BO, before oxidation at temperature T; AO, after oxidation at temperature T+100°; AR after reduction at temperature T+200°; O/Ce is the XP integral ratio).

3.3.2. Oxygen adsorption studies on CeO_{2-x}(111)/Cu(111)

This work was undertaken at Cardiff University, in part in collaboration with Dr. Jörn Erichsen from Queen Mary University of London. The experimental setup was already described in section 3.2.

3.3.2.1. Clean Cu(111) single crystal

In figure 3.21 two XP spectra of the Cu(111) crystal are shown. A scan on a surface which had not been cleaned (black line) has been recorded. It showed that the Cu peaks were small, due to a high level of contaminants containing carbon (~ 285 eV) and oxygen (~ 530 eV). After the appropriate cleaning procedure (involving several cycles of sputtering with Ar^+ at 0.6 keV for 20 minutes, annealing in vacuum at 600 °C for 30 minutes, then heating to 820 °C) it was possible to obtain a clean crystal surface (red line).

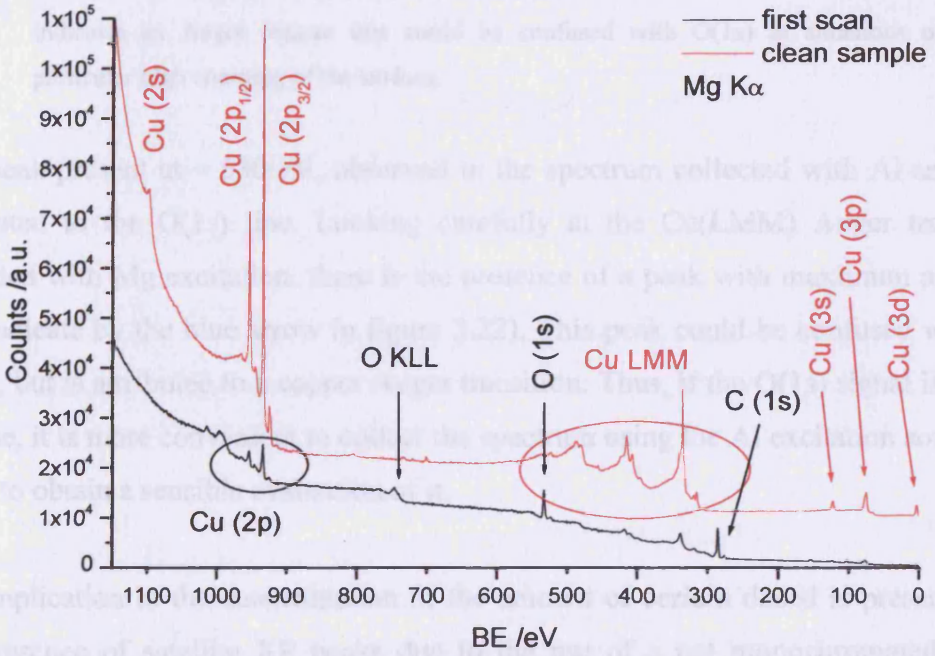

Fig. 3.21: XPS spectra of Cu(111) single crystal recorded with Mg Kα excitation, before (black line) and after cleaning (red line)

Since the copper XPS structure recorded with the Mg anode comprises several Auger transitions in the range of 300 – 550 eV binding energies, it was necessary to use the Al anode in order to obtain a clear evaluation of the O(1s) peak. In figure 3.22 XP

spectra of the Auger Cu(LMM) transitions, collected using both Mg (black line) and Al Kα (red line) excitation are shown.

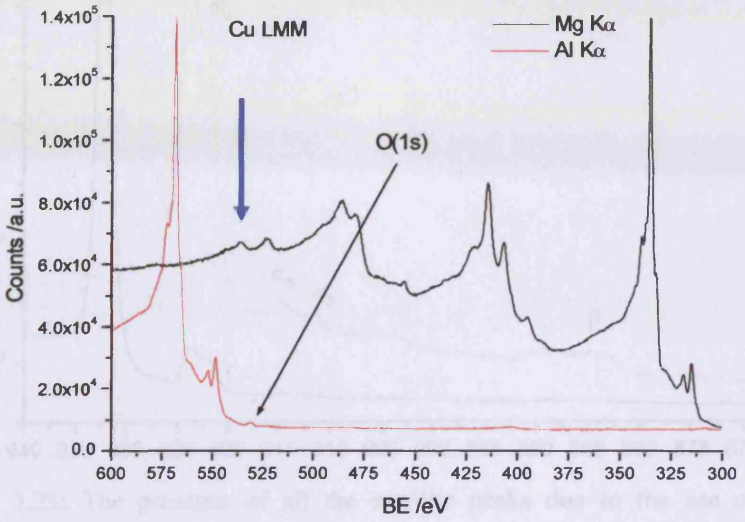

Fig. 3.22: The Cu LMM transition recorded with Mg excitation (black line) and Al excitation (red line.). The presence of the O (1s) is also indicated. The blue arrow indicates an Auger feature that could be confused with O(1s) in situations of particular high charging of the surface.

The peak present at ~ 530 eV, observed in the spectrum collected with Al anode, is attributed to the O(1s) line. Looking carefully at the Cu(LMM) Auger transition recorded with Mg excitation, there is the presence of a peak with maximum at ~ 536 eV (indicate by the blue arrow in figure 3.22). This peak could be confused with the O(1s), but is attributed to a copper Auger transition. Thus, if the O(1s) signal is not so intense, it is more convenient to collect the spectrum using the Al excitation source, in order to obtain a sensible evaluation of it.

A complication in the determination of the amount of cerium dosed is presented by the presence of satellite XP peaks due to the use of a not monochromated X-ray source exactly in the binding energy range where the Ce(3d) peak is expected. This situation is illustrated in figure 3.23. The black line shows that these satellite peaks are present to the lower binding energy side of the $Cu(2p_{3/2})$. In the magnification of the same spectrum (red line), all the satellite peaks expected for a not monochromated Mg source are present. In table 3.4 a comparison with literature values for displacement and area is shown.

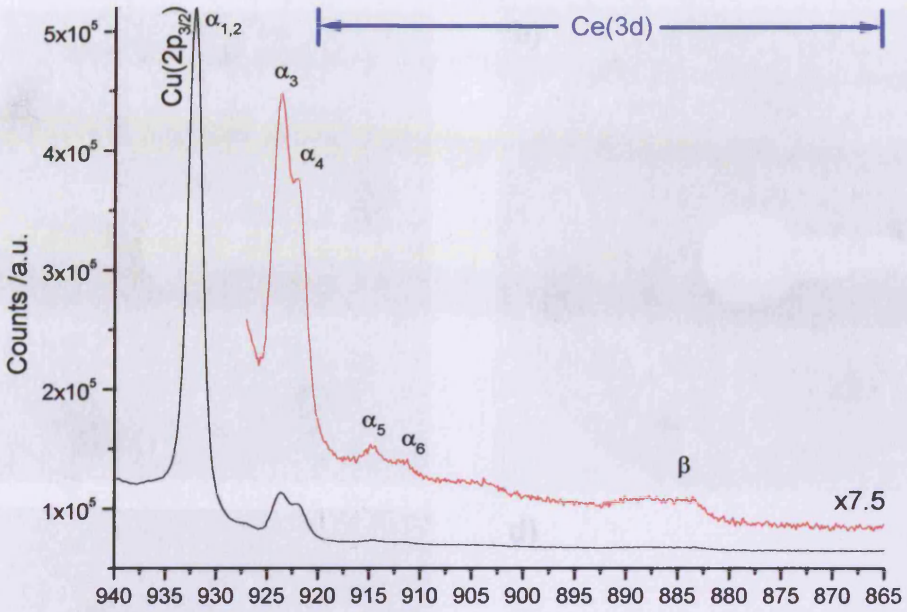

Fig. 3.23: The presence of all the satellite peaks due to the use of a not monochromatic Mg X-ray source can induce to think that some cerium is present, therefore the surface is not clean.

	$\alpha_{1,2}$	α_3	α_4	α_5	α_6	β
Displacement /eV [71]	0	8.4	10.1	17.6	20.6	48.7
Displacement /eV (fig. 3.23)	0	8.5	10	17.6	20.9	48.6
Relative height /% [71]	100	8	4.1	0.6	0.5	0.5
Relative height /% (fig. 3.23)	100	7.5	6.5	0.5	0.4	0.5

Table 3.4: Comparison between literature [71] and experimental data for the Cu(2p) main peak and satellite structure due to the use of a not monochromatic Mg X-ray source.

In figures 3.24 a, b and c, LEED patterns with hexagonal p(1×1) structures recorded at 66, 96 and 116 eV are shown. All the three LEED patterns appeared to have reasonably sharp spots, with a good contrast with the background. Moreover, three spots (indicated as 1) appeared to be narrower than the other three (indicated as 0). Varying the energy, it was possible to notice that the narrow spots became broader, and the broad narrower. This effect is due to the three-fold symmetry characteristic of the Cu(111) surface due to the presence of octahedral and tetrahedral sites (figure 3.24 d).

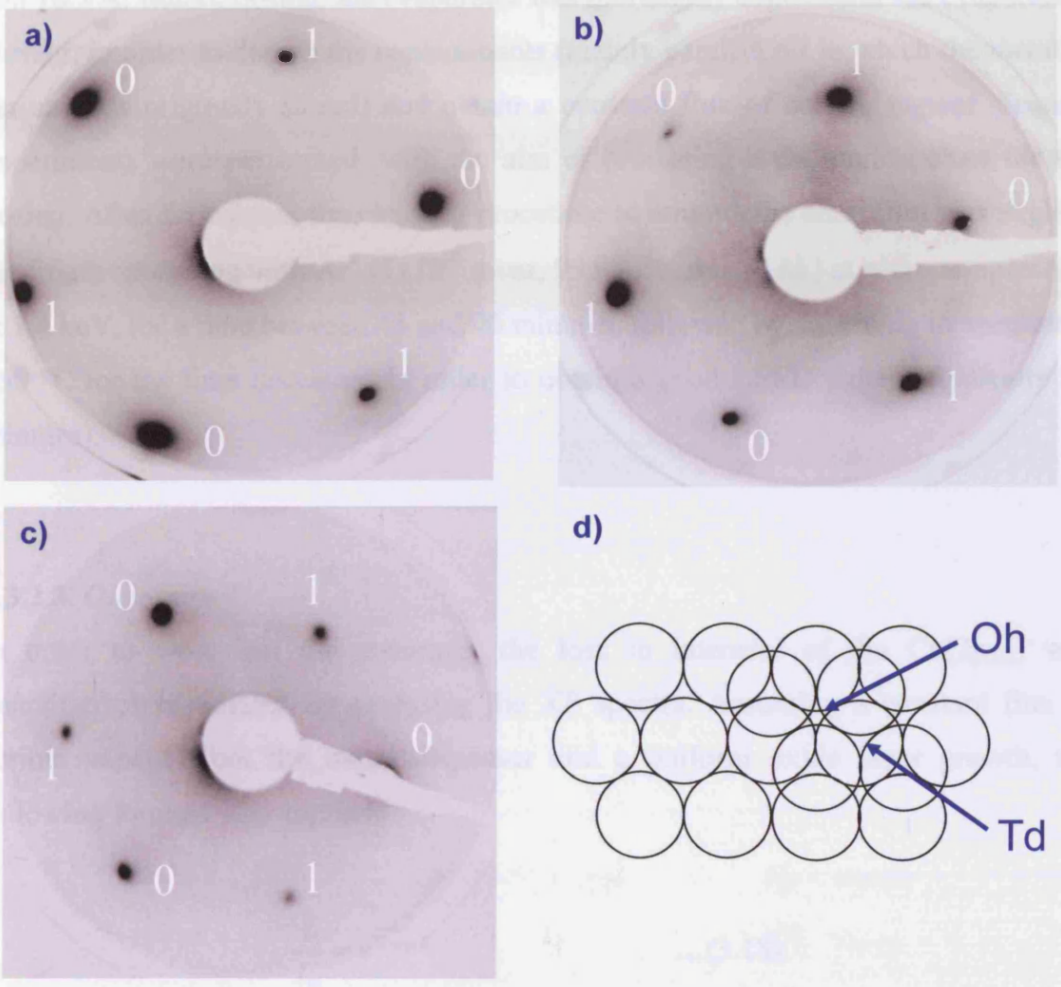

Fig. 3.24: LEED pattern of clean Cu(111) (1×1). The hexagonal pattern reflects the hexagonal arrangement of the atoms on the surface. The different intensity of the spots reflect the three-fold symmetry of the (111) surface; a) 66 eV, b) 96 eV and c) 116 eV. d) model showing octahedral (Oh) and tetrahedral (Td) sites on a fcc (111) surface.

3.3.2.2. Film preparation

Cerium was dosed by means of a cerium metal evaporator in the presence of O_2 (5×10^{-7} mbar, 99.6%, Argo Ltd.), keeping the copper single crystal at 300 °C (resistive heating, 5.8 V × 1.1 A). After deposition the sample was annealed in oxygen at 450 °C for 15 minutes and allowed to cool to room temperature in O_2 atmosphere (5×10^{-7} mbar). The cerium evaporator consisted of a lump of metallic cerium (Cerium, ingot, 99.9%, Aldrich) mounted on a resistively heated tungsten wire. Different dosing conditions were tried, resulting in optimal parameters for the current at 3.28 V

and 16.5 A. Before dosing, the evaporator was thoroughly degassed at the evaporation current, in order to desorb the contaminants (mainly paraffin oil in which the metallic cerium was originally stored) and obtain a constant flux of cerium vapour. Several experiments were performed, with the aim of producing a calibration chart for the dosing. After deposition, the cleaning procedure to remove the ceria film was slightly modified: sputtering with Ar^+ (5×10^{-6} mbar, 99.999%, Argo Ltd.) at room temperature, at 1.6 keV, for a time between 45 and 90 minutes, followed by annealing in vacuum at 650 °C for the time necessary in order to obtain a good LEED pattern (typically 30 minutes).

3.3.2.3. Coverage

In order to work out the coverage, the loss in intensity of the Cu($2p_{3/2}$) was quantitatively estimated by analysing the XP spectra. Assuming a constant flux of cerium vapour from the metal dispenser and a uniform oxide layer growth, the following formula was applied:

$$\frac{I}{I_0} = e^{\frac{-x}{\lambda \cos \vartheta}} \qquad \ldots(3.18)$$

where I is the intensity of the Cu($2p_{3/2}$) after cerium deposition, I_0 is the intensity of the Cu($2p_{3/2}$) for the clean sample, λ is the photoelectron relative inelastic mean free path (IMFP), x the thickness of the film obtained and ϑ the electron emission angle to the electron analyser normal. Even if the I/I_0 ratio is having physical meaning from 1, when $I = I_0$ and no dosing occurred, to 0.001, when the attenuation of the substrate signal is the 99.9%, there is another important limitation. In fact the equation is valid for films of a thickness less than or equal to the IMFP. The IMFP has been calculated using the TPP-2M model [65], in the way described in Appendix A. Since the Cu($2p_{3/2}$) binding energy for the samples after the formation of the CeO_2 film is around 932.9 eV, its kinetic energy, using the Mg anode radiation is 1253.6 - 932.9 = 320.7 eV. At this kinetic energy, the IMFP calculated according to TPP-2M method is around 0.8 nm. The error on the determination of the thickness is mainly related to the calculation of the IMFP. Using the method reported above, the error is unknown but

the authors reported a typical absolute accuracy of ~ 20%. On the other hand they state that "the relative accuracy, i.e. the ratio of IMFPs for the same solid at two energies is likely to be much better and could be better than 10% even for peaks at widely different energies" [65]. The values obtained for the film thickness have then to be divided by the thickness of one monolayer. Truncating the bulk cubic CeO_2, the (111) plane shows a hexagonal arrangement of the atoms, with a lattice constant of 0.383 nm. In the approximation of the stoichiometric defective free layer, one monolayer consists of two layers of oxygen atoms plus one layer of cerium atoms, giving a thickness of 0.383 nm (figure 3.25).

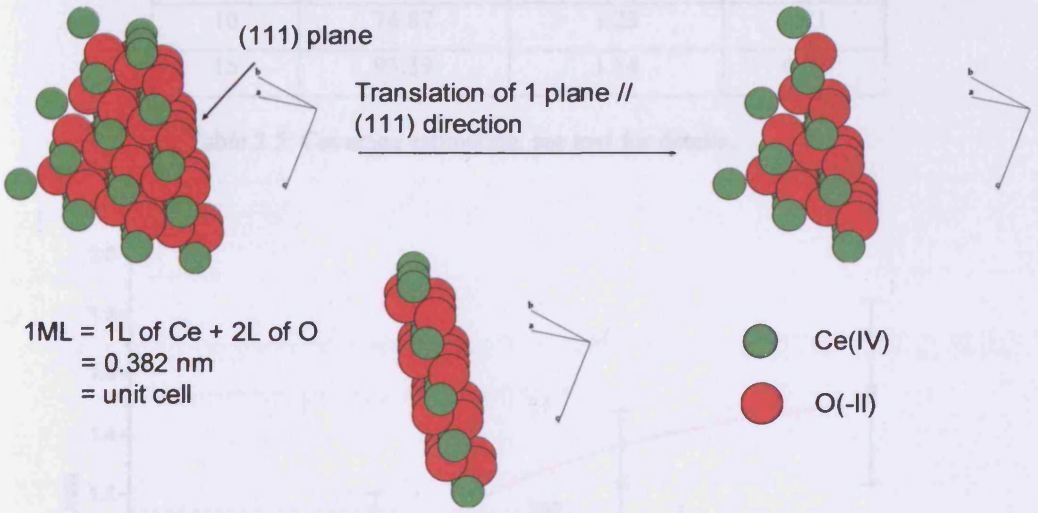

Fig. 3.25: determination of the thickness of 1 monolayer of CeO_2(111), assuming the crystal is defect free. 1L = 1 layer.

Thus, in respect of the consideration explained above, the determination of the coverage can be considered accurate up to approximately 2 ML. This limit should be reached with a time of deposition of around 3 minutes, corresponding to approximately the 50% of attenuation of the Cu($2p_{3/2}$) peak. For deposition times longer than the limiting one, the estimation of the coverage has been made considering the attenuation of the Cu($2p_{3/2}$) peak exponential with the increase of the coverage, under the hypothesis of uniform growth of the oxide layer. The results obtained are reported in table 3.5. Plotting the data in table 3.5 gives a useful calibration chart (time of dosing vs film thickness) for the deposition (figure 3.26). The experimental data can be fitted with a natural log function, which is consistent

with equation 3.19, within the error derived in the estimation of the photoelectron IMFP estimated as +/- 20% [65].

Time /min	Cu ($2p_{3/2}$) loss /Area %	thickness /nm	Coverage /ML
0	0.00	0	0
2	27.53	0.39	1.10
3	46.58	0.78	2.03
calculated	--	0.799	2.08
5	61.10	1.00	2.62
7	77.27	1.27	3.32
10	74.87	1.23	3.21
15	93.39	1.54	4.02

Table 3.5: Coverage estimation, see text for details.

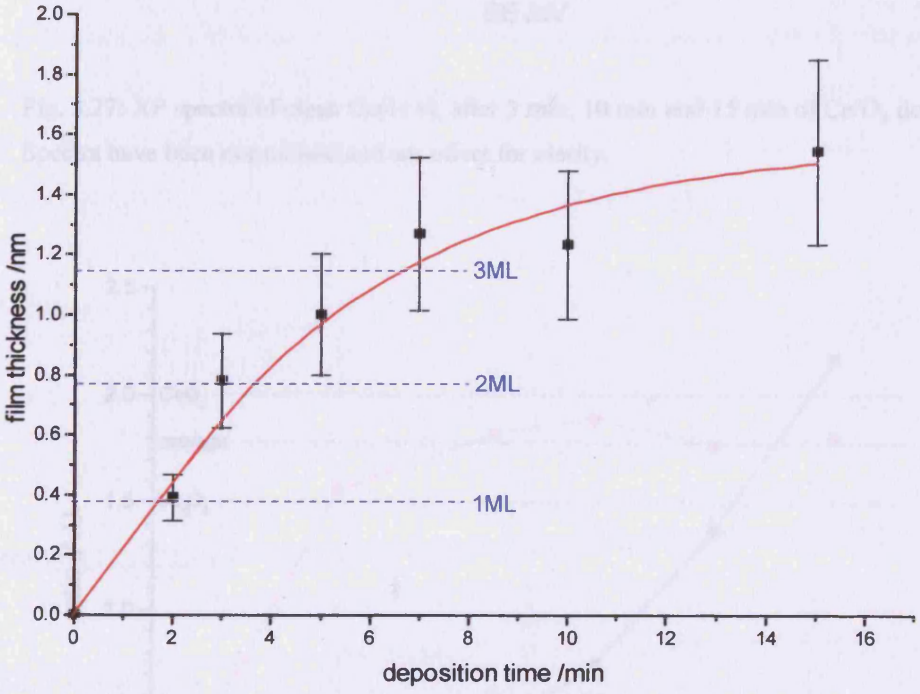

Fig. 3.26: Film thickness vs deposition time calibration chart, for depositing cerium in 5×10^{-7} mbar of O_2 keeping the Cu crystal at 300 °C.

In figure 3.27, the XP spectra for three different depositions, as well as the spectrum of the clean Cu, are reported. The spectra are offset for clarity. As expected there is a

decrease in the intensity of the peaks related to the copper substrate and the increase in intensity of the peaks related to both cerium and oxygen.

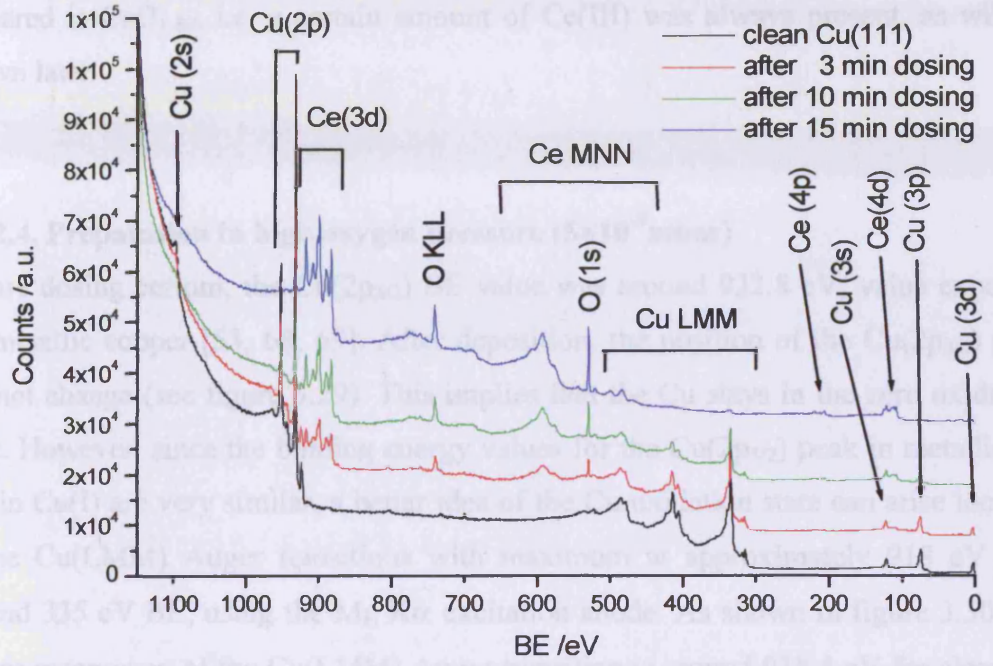

Fig. 3.27: XP spectra of clean Cu(111), after 3 min, 10 min and 15 min of Ce/O_2 dosing. Spectra have been normalised and are offset for clarity.

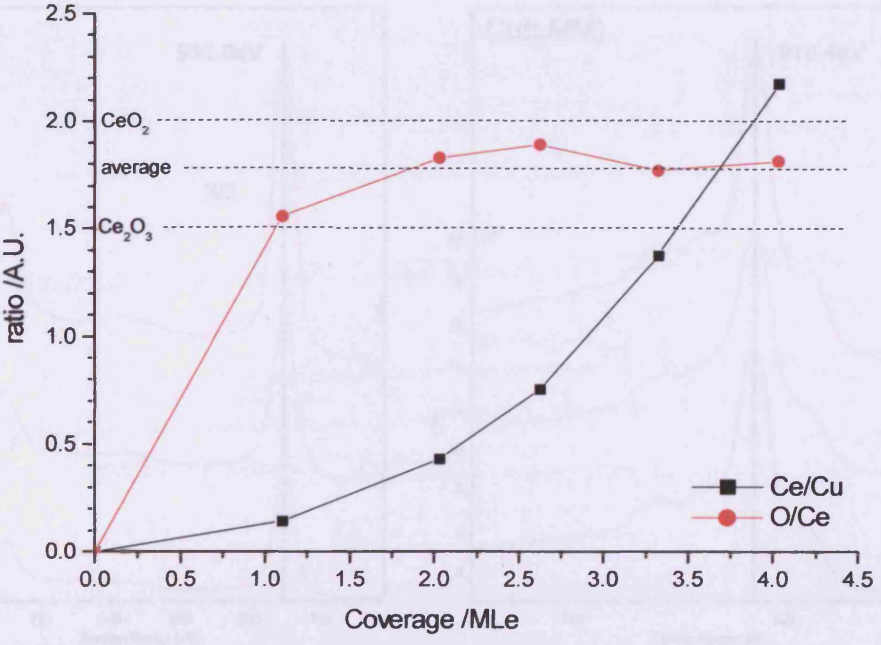

Fig. 3.89: $Ce(3d)/Cu(2p_{3/2})$ and O(1s)/Ce(3d) XP peaks vs coverage. The average stoichiometry of the oxide layer prepared is $CeO_{1.89}$.

The graph in figure 3.28 shows the Ce(3d)/Cu($2p_{3/2}$) and O(1s)/Ce(3d) XP peaks ratios vs the coverage obtained. The Ce(3d)/Cu($2p_{3/2}$) curve shows an exponential increase. For coverage greater than 2ML, the average stoichiometry of the oxide layer prepared is $CeO_{1.89}$, i.e. a certain amount of Ce(III) was always present, as will be shown later.

3.3.2.4. Preparation in high oxygen pressure (5×10^{-7}mbar)

Before dosing cerium, the Cu($2p_{3/2}$) BE value was around 932.8 eV, value expected for metallic copper [53, 68, 69]. After deposition, the position of the Cu($2p_{3/2}$) peak did not change (see figure 3.29). This implies that the Cu stays in the zero oxidation state. However, since the binding energy values for the Cu($2p_{3/2}$) peak in metallic Cu and in Cu(I) are very similar, a better idea of the Cu oxidation state can arise looking at the Cu(LMM) Auger transitions with maximum at approximately 918 eV KE, around 335 eV BE, using the Mg Kα excitation anode. As shown in figure 3.30, the bigger component of the Cu(LMM) Auger transition is around 918.4 eV for clean Cu and stays at the same values after the dosing. This is a confirmation that Cu does not oxidise, or at least the vast majority of it doesn't do it, and can be used as reference for the binding energy scale when the C(1s) peak is not present.

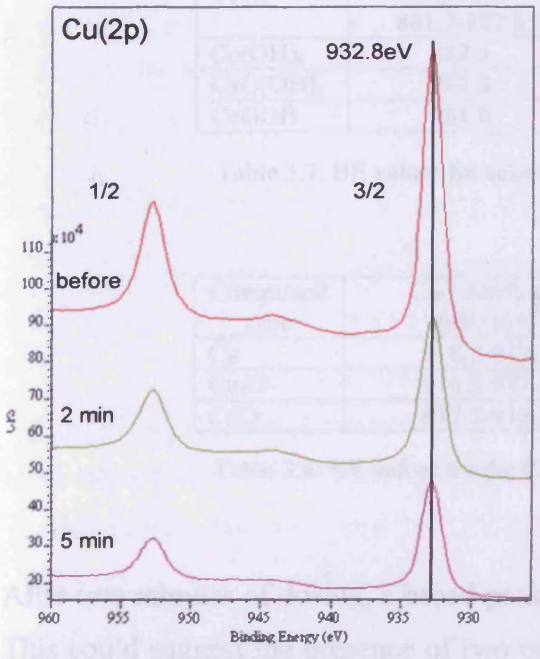

Fig. 3.29: Cu(2p) XP spectra of clean Cu(111) and after 2 and 5 min of Ce/O_2 dosing. Spectra are offset for clarity.

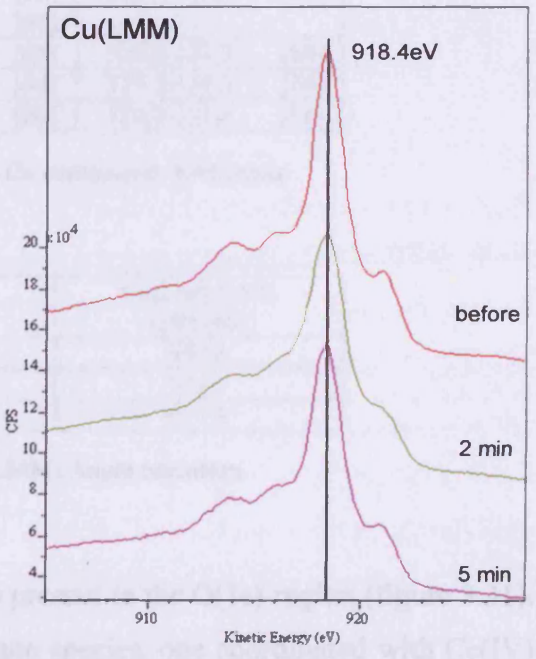

Fig. 3.30: Cu(LMM) Auger transition of clean Cu(111) and after 2 and, 5 min of Ce/O_2 dosing. Spectra are offset for clarity.

Typical values for the Cu($2p_{3/2}$) peak, the Ce($3d_{5/2}$) peak as well as for the O(1s) peak, in Cu, Ce and their different oxides and are reported in table 3.6 and 3.7. In table 3.8 typical KE values for the Cu(LMM) Auger transition are summarised.

Compound type	BE Cu($2p_{3/2}$) (eV)		BE O(1s) on CuO_x (eV)	
Cu	932.0-932.8	[66]		
	932.2-933.1	[53]		
	932.5-932.8	[67]		
Cu_2O	932.1-932.5	[66]	530.2-530.5	[66]
	932.0-932.7	[53]	530.2-531.1	[53]
	932.3-932.7	[67]		
CuO	933.4-933.9	[66]	529.4-530.5	[66]
	932.7-934.2	[53]	529.5-530.0	[53]
	933.5-934.0	[67]		
$Cu(OH)_2$	934.4-935.1	[66]	531.7	[66]
	934.4-935.1	[53]	530.9-531.2	[53]
	934.8-935.3	[67]		

Table 3.6: BE values for selected Cu compounds XPS peaks.

Compound type	BE Ce($3d_{5/2}$) (eV)		BE O(1s) on CeO_x (eV)	
Ce	883.7-884.2	[66]		
	883.2-883.9	[53]		
	883.7-884.2	[67]		
Ce_2O_3	881.45	[66]	529.1	[66]
	880.7-885.8	[53]	529.0-530.3	[53]
CeO_2	881.2-882.1	[66]	529.0-529.2	[66]
	881.8-882.7	[53]	528.7-529.6	[53]
	881.7-882.5	[67]		
$Ce(OH)_4$	882.3	[66]	529.2-531.3	[66]
$CeO(OH)_2$	882.3	[66]	529.2-531.3	[66]
CeOOH	881.0	[66]	529.0-531.3	[66]

Table 3.7: BE values for selected Cu compounds XPS peaks.

Compound type	Cu(LMM) KE (eV) [66]	Cu(LMM) KE (eV) [68]
Cu	918.2-919.2	918.4
Cu_2O	916.5-917.6	916.5
CuO	917.7-918.3	917.8

Table 3.8: KE values for the Cu(LMM) Auger transition.

After two minutes of dosing, a broad peak is present in the O(1s) region (figure 3.31). This could suggest the presence of two oxygen species, one coordinated with Ce(IV) cations (the one at around 529.6 eV) and the other at around 530.6 eV with Ce(III)

cations. These values are in good agreement with the one expected for metal oxides and also agrees with the binding energy values recorded while determining the surfaces with the maximum degree of oxidation and reduction spectra in section 3.3.2.1. a). Since the presence of oxidised Cu has not been observed, as shown by the Auger LMM transition in figure 3.30, the oxygen should belong only to the oxidised cerium.

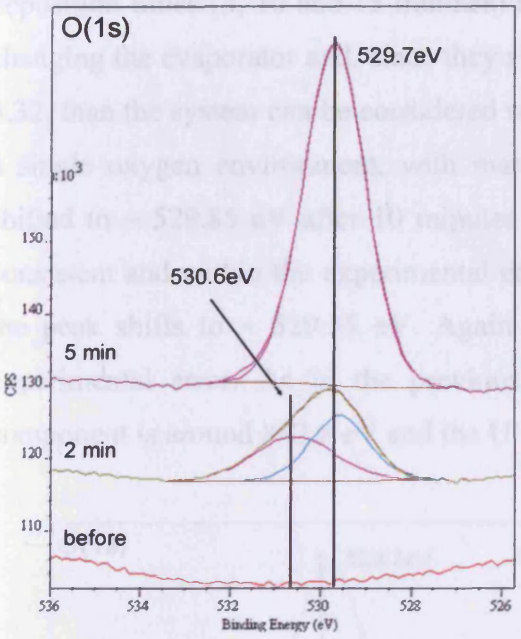

Fig. 3.31: O(1s) XP spectra collected before and after 2 and 5 min of Ce/O_2 dosing (peak fittings also shown). Spectra are offset for clarity.

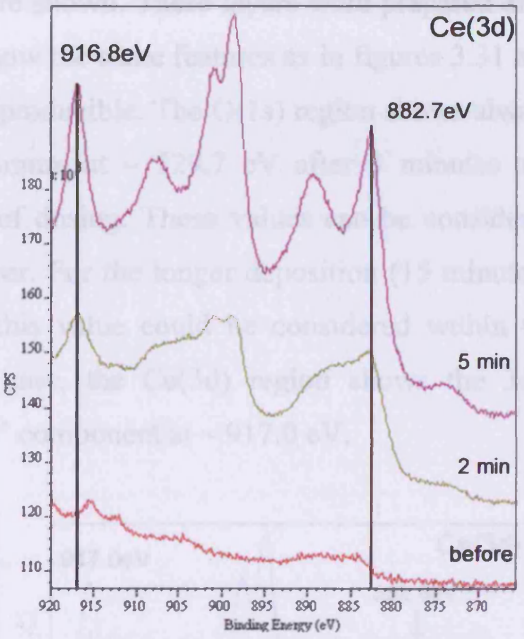

Fig. 3.32: Ce(3d) XP spectra collected before and after 2 and 5 min of Ce/O_2 dosing. Spectra are offset for clarity.

The Ce(3d) XP spectra for the same dosing experiments are reported in figure 3.32. The $3d_{5/2}$ component is around 882.7 eV and the U''' component at ~ 916.8 eV. There is a general increase in intensity for increasing times of dosing, as expected. After 2 minutes of dosing, the spectrum appears not very well resolved as after 5 minutes. This pattern is typical for a configuration in which cerium is present roughly for the same amount in both oxidation states (Ce(III) ~ 58%, Ce(IV) ~ 42%, with O/Ce integral ratio 1.56). The presence of cerium in both the oxidation states gives more credibility to the hypothesis that the two oxygen states can be correlated to the presence of the cerium ions in two different oxidation states. Nevertheless, one of the two oxygen peaks could be associated with oxygen adsorbed on copper; however, as

already observed, similar oxygen binding energy values were recorded during the experiment performed on $CeO_2(111)$ single crystal. Similar spectra were also observed for ceria nanoparticles [52, 55]. After 5 minutes of dosing, the prevalence of the Ce(IV) (>80%) is revealed by the typical 6-peak structure.

In figures 3.33 and 3.34, O(1s) and Ce(3d) regions for progressively increasing Ce/O_2 deposition times (3, 10 and 15 minutes) are shown. These layers were prepared after changing the evaporator and, since they show the same features as in figures 3.31 and 3.32, than the system can be considered reproducible. The O(1s) region shows always a single oxygen environment, with maximum at ~ 529.7 eV after 3 minutes and shifted to ~ 529.85 eV after 10 minutes of dosing. These values can be considered consistent and within the experimental error. For the longer deposition (15 minutes), the peak shifts to ~ 529.55 eV. Again this value could be considered within the experimental error. As in the previous case, the Ce(3d) region shows the $3d_{5/2}$ component is around 882.8 eV and the U''' component at ~ 917.0 eV.

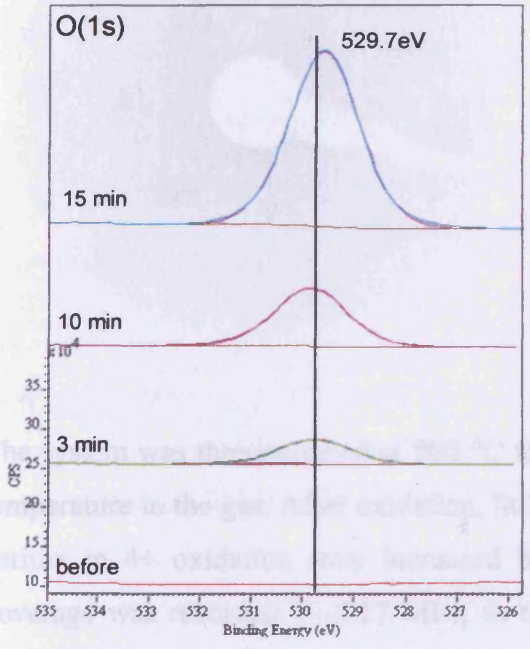

Fig. 3.33: O(1s) XP spectra collected before and after 3, 10 and 15 min of Ce/O_2 dosing (peak fittings also shown) Spectra are offset for clarity.

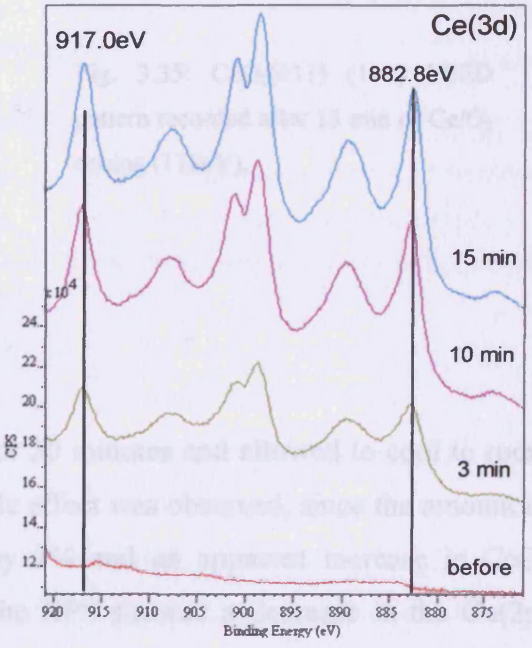

Fig. 3.34: Ce(3d) XP spectra collected before and after 3, 10 and 15 min of Ce/O_2 dosing. Spectra are offset for clarity.

After 15 minutes of Ce/O_2 dosing, a ~ 4.02 monolayers equivalent (MLe) thick film was prepared. From the XPS (see figures 3.33 and 3.34) a single oxygen environment

was present and the profile of the Ce(3d) showed that cerium was in the 4+ oxidation state mainly (~88% of the total Ce3d signal was due to Ce(IV) and O/Ce ~1.81). In figure 3.35 a LEED pattern recorded after film preparation is shown. The figure shows a hexagonal pattern, as expected for a (111) surface. This pattern is not due to Cu(111), as can be seen by comparison with the LEED pattern recorded for clean Cu(111) at approximately the same energy and showed in figure 3.24 c). Therefore the pattern corresponds to the oxidised cerium overlayer. The LEED pattern can be described as CeO_2(111) (1×1). No STM pictures were recorded, as the system was probably not conductive enough and tunnelling conditions could not be found. Attempts to scan in O_2 background pressure (5×10^{-9}mbar, then 1×10^{-8} mbar) were made, without any improvement of the stability of the system. The reason for this is because a more oxidised layer will be less conductive, therefore more difficult to image.

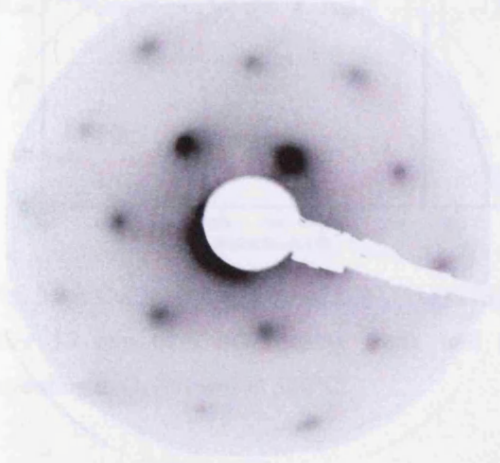

Fig. 3.35: CeO_2(111) (1×1) LEED pattern recorded after 15 min of Ce/O_2 dosing (118eV).

The system was then oxidised at 500 °C for 30 minutes and allowed to cool to room temperature in the gas. After oxidation, little effect was observed, since the amount of cerium in 4+ oxidation state increased by 3% and an apparent increase in CeO_x coverage was recorded (~ 4.17 ML), as the XPS showed a decrease in the Cu(2p) peak (figure 3.36). Moreover a shoulder appeared at lower binding energy, but only two peaks could be reasonably fitted under the curve, therefore only one copper oxidation state, the metallic, should be present. A possible mechanism of the behaviour of the CeO_x film under annealing in oxygen is shown by the scheme in figure 3.37. Under annealing the oxidised cerium overlayer reconstructed, spreading over the copper layer. As a consequence, the Copper XP signal loses intensity.

Cerium and oxygen signals appear instead to be approximately constant because the layer of oxidised cerium is probably much bigger than the escape depth of the photoelectrons. In this case a proper quantification of the film thickness is difficult and the XPS sees approximately the "same" amount of CeO_x before and after annealing. This could also explain the increase in coverage, though very small (from 4.02 to 4.17, which however could be considered within the experimental error).

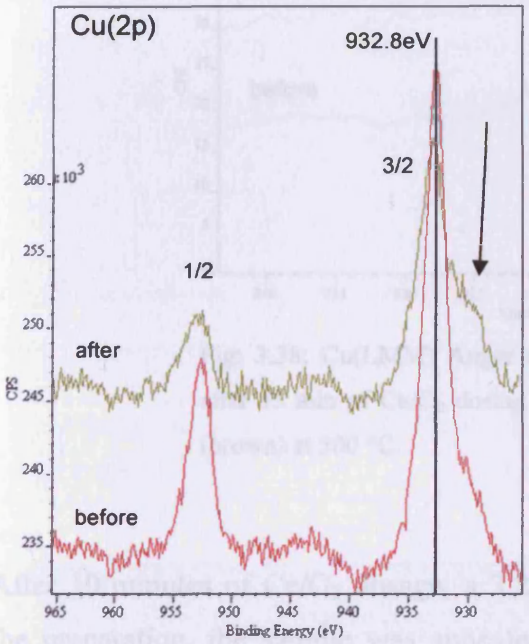

Fig. 3.36: Cu(2p) XP spectra of CeO_x(111)/Cu(111) after 15 min of Ce/O_2 dosing (red), and after annealing in O_2 (brown) at 500°C.

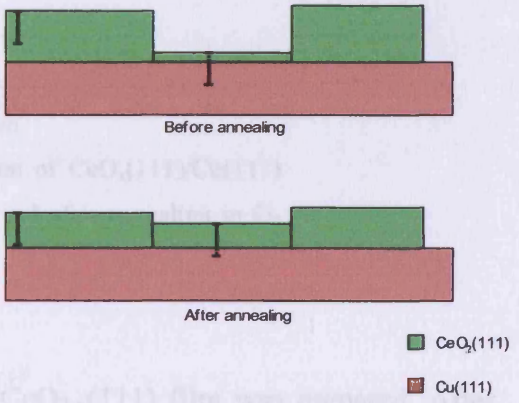

Fig. 3.37: Possible mechanism of behaviour of CeO_x film under annealing in O_2 at 500°C. The black line exemplifies the photoelectron IMFP.

Another explanation could lay on the oxidation of the surface copper suggested by the presence of the shoulder in the $Cu(2p_{3/2})$ at lower binding energy, although a similar shoulder would have been expected also for the $2p_{1/2}$ component, however, the shoulder could be in this case too small to be appreciated. From table 3.5, a binding energy of 932.8eV for $Cu(2p_{3/2})$ could be attributed to both Cu metal and Cu^+, since for Cu^{2+} the values are slightly higher. Although very attenuated, because of the large amount of CeO_x present, the maximum of the Cu(LMM) Auger transition (figure 3.38) shifted from 919.1 eV to 916.0 eV. From the comparison with the kinetic energy value in table 3.6, the species likely present was Cu^{2+}, thus copper oxidation occurred. The peak at 932.8 eV in figure 3.36 should hence be seen as Cu(II) and the shoulder at lower binding energy as Cu(0). The oxidation of the copper could also explain the

small increase in the O(1s) signal. During STM analysis, the system behaved in the same way as before oxidation, not allowing good tunnelling conditions.

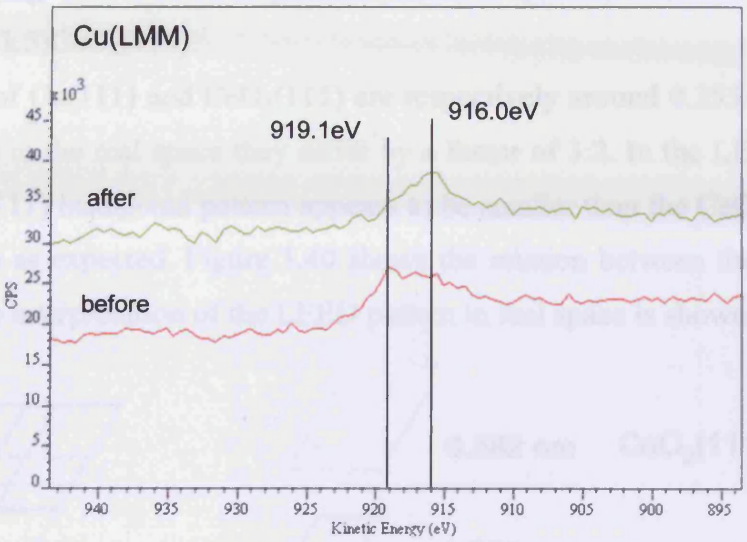

Fig: 3.38: Cu(LMM) Auger transition of CeO_x(111)/Cu(111) after 15 min of Ce/O_2 dosing (red), and after annealing in O_2 (brown) at 500 °C.

After 10 minutes of Ce/O_2 dosage, a 3.2MLe CeO_{2-x}(111) film was prepared. After the preparation, the sample was annealed to 450 °C for 15 minutes in O_2 (5×10^{-7} mbar) and then allowed to cool to room temperature in vacuum.

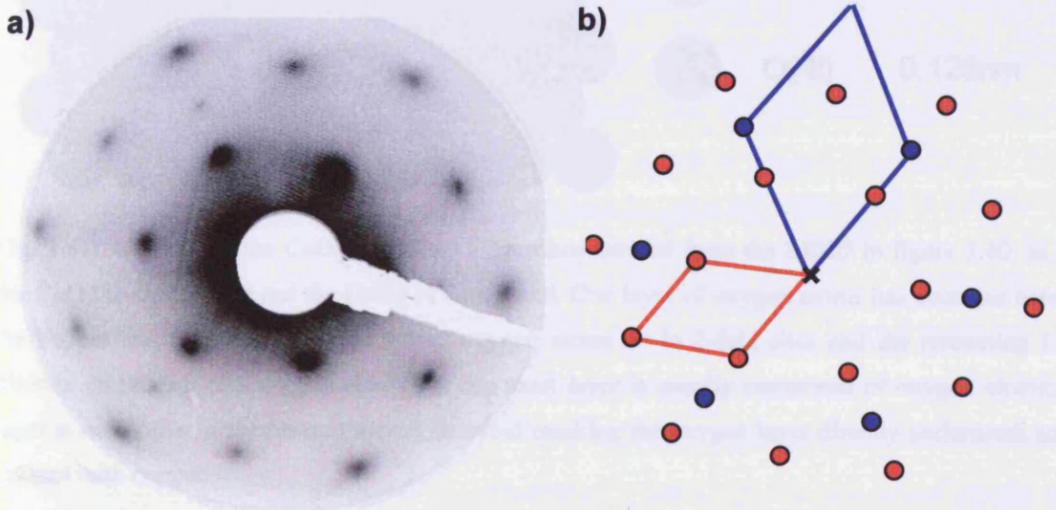

Fig. 3.39: a) LEED pattern recorded after 10 min of Ce/O_2 dosing and annealing at 450 °C in O_2 (117 eV). b) in blue the spots and the unit cell of Cu(111), in red the spots and the unit cell belonging to CeO_{2-x}, the cross is the (0,0) spot which is common to both the structures.

In the LEED pattern recorded after preparation it was possible now to observe the spots belonging to the Cu(111) (figure 3.39) and the ones belonging to the oxidized cerium, resulting in a (1.5×1.5) pattern. Thus the pattern could be described as Cu(111) (1.5×1.5)CeO_2(111).

The unit cell of Cu(111) and CeO_2(111) are respectively around 0.255 nm and 0.382 nm. Therefore in the real space they differ by a factor of 3:2. In the LEED reciprocal space the Cu(111) hexagonal pattern appears to be smaller than the CeO_2(111) one by a factor of 1.5 as expected. Figure 3.40 shows the relation between the unit cells. In figure 3.41 the interpretation of the LEED pattern in real space is shown.

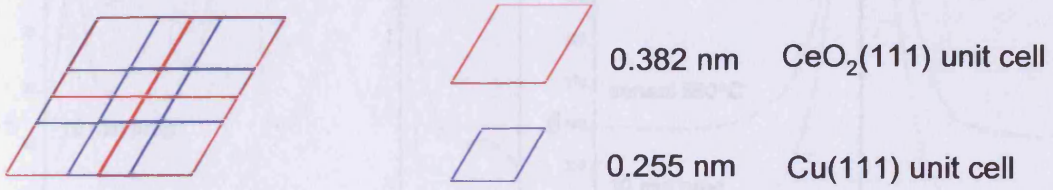

Fig. 3.40: In real space, three Cu(111) unit cell (blue) correspond to two CeO_2(111) unit cells (red) in each direction.

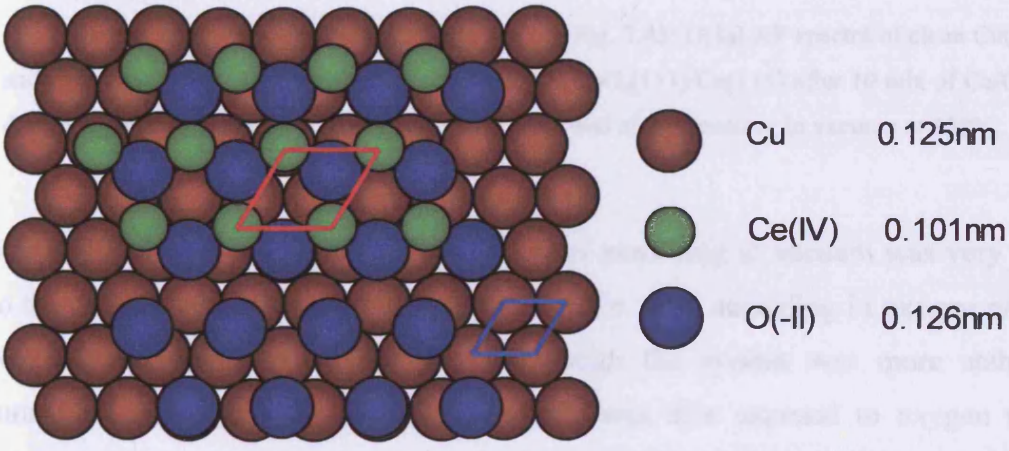

Fig. 3.41: A model of the CeO_2(111)/Cu(111) surface derived from the LEED in figure 3.40. In blue the Cu(111) unit cell, in red the CeO_2(111) unit cell. One layer of oxygen atoms has been put between the copper and the cerium layers. 2/3 of oxygen atoms sit in 2-fold sites and the remaining 1/3 is directly on the top of a copper atom. The top most layer is usually comprised of oxygen atoms; this layer is not drawn in the present model, to avoid masking the oxygen layer directly underneath and in contact with copper.

The shape of the Ce(3d) region suggested that the CeO_x over layer was well oxidized (amount of cerium in +4 oxidation state > 91%). The Ce($3d_{5/2}$) was recorded at 882.6 eV, the U''' at 917.1 eV and the O/Ce ~ 1.83. The sample was then annealed at

550 °C in vacuum for 30 minutes and allowed to cool to room temperature in vacuum. The amount of Ce(IV) cations (-4%) and the O(1s) XP peak stayed approximately constant (-1%), as well as the coverage (3.1MLe). In figure 3.42 and 3.43 the Ce(3d) and O(1s) regions are shown.

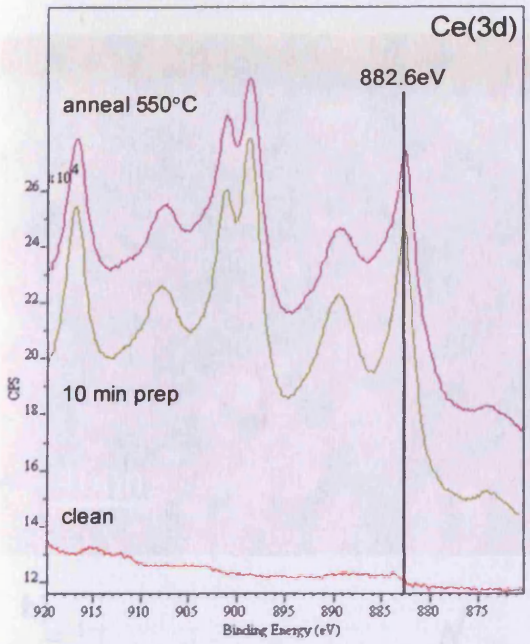

Fig. 3.42: Ce(3d) XP spectra of clean Cu(111) and CeO_x(111)/Cu(111) after 10 min of Ce/O_2 dosing and after annealing in vacuum at 500°C.

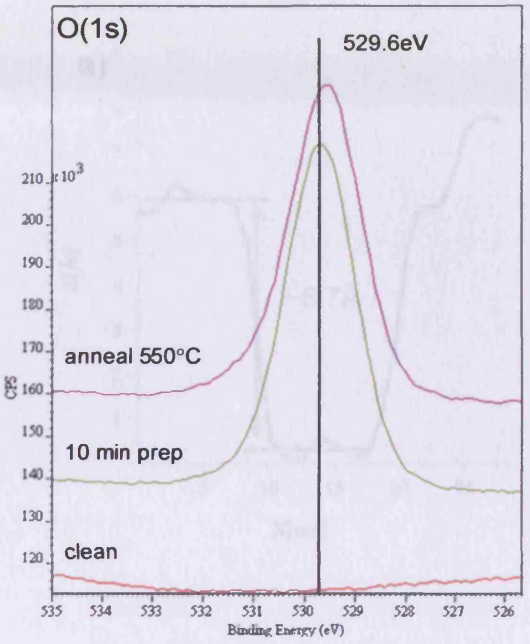

Fig. 3.43: O(1s) XP spectra of clean Cu(111) and CeO_x(111)/Cu(111) after 10 min of Ce/O_2 dosing and after annealing in vacuum at 550°C.

The LEED pattern recorded immediately after annealing in vacuum was very similar to the one recorded after the film preparation, i.e. after annealing in oxygen pressure. No STM images were obtained, even though the system was more stable and tunnelling could be established. The sample was then exposed to oxygen (5×10^{-7} mbar) at 500 °C for 30 minutes and allowed to cool to room temperature in presence of oxygen. At this stage tunnelling could be established and some large scale STM images were recorded. Figure 3.44 shows the CeO_2(111)/Cu(111) as it appeared under the STM. The features observed are difficult to interpret, nevertheless, the brighter areas represent probably the CeO_2(111) overlayer, whereas the darker ones may represent the Cu(111) substrate. To discriminate between the two areas Single Point Spectroscopy (i.e. STS) was tried. Unfortunately this did not help since when applying the voltage, some material was depositing on the surface, clear sign that some dirt was accumulated on the tip. This fact did not help during scanning either,

since an accumulation of material on the tip can dramatically change its conductivity. The aspect of the supposed $CeO_2(111)$ overlayer is likely due to sintering of the layer occurring during the annealing treatment. The line profiles show a step size of ~ 5.7 Å. The coverage estimated via XPS is ~3.2MLe. This corresponds to a height of ~1.23 nm (12.3 Å).

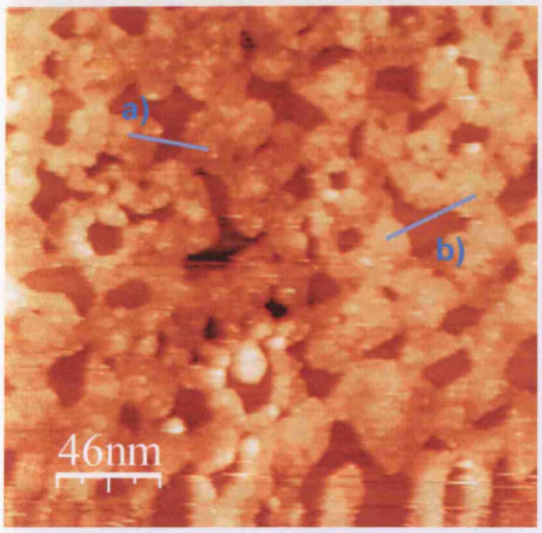

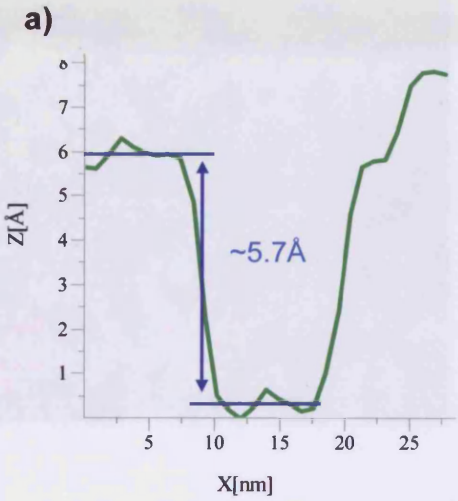

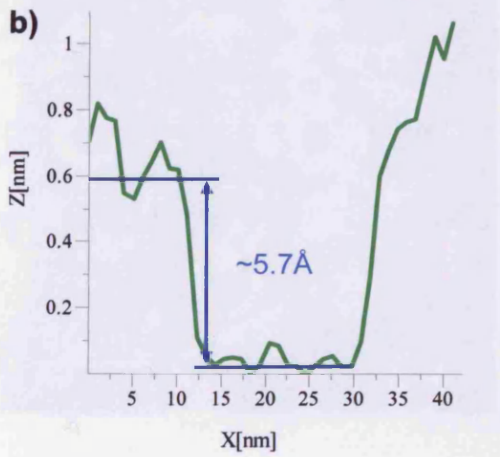

Fig. 3.44: STM image showing the topography of ~3.2MLe of $CeO_2(111)$ on Cu(111). Image size: 230×230 nm, tunnelling parameters 6 V, 2 nA. The step size in the line profiles a) and b) is around 5.7 Å.

In figure 3.45 the same STM picture as in figure 3.44 is analysed in a way to detect the $CeO_2(111)$ overlayer height and the surface area. Starting from the assumption that the lower (darker) areas should be the Cu(111) substrate, in figure 3.45 a), a threshold of 0.383 nm, corresponding to the thickness of 1 monolayer of $CeO_2(111)$ was applied. Height threshold values of 0.766 nm (2 ML) and 1.149 nm (3 ML) were applied to picture b) and c) respectively.

The darker areas are filled up when the height threshold close to 2.1 ML, therefore there is a discrepancy of approximately 1 ML between the information obtained via XPS and the one derived for the analysis of the STM picture. Nevertheless, it has to

be taken into account that STM scans a very small area, in this case ~0.053 μm^2, in respect of the 4.5 mm^2 where XPS was collected. XPS gives therefore an average information about a wider area. This could be an indication of a layer-by-layer growth mode (so called Frank Van der Merwe growth).

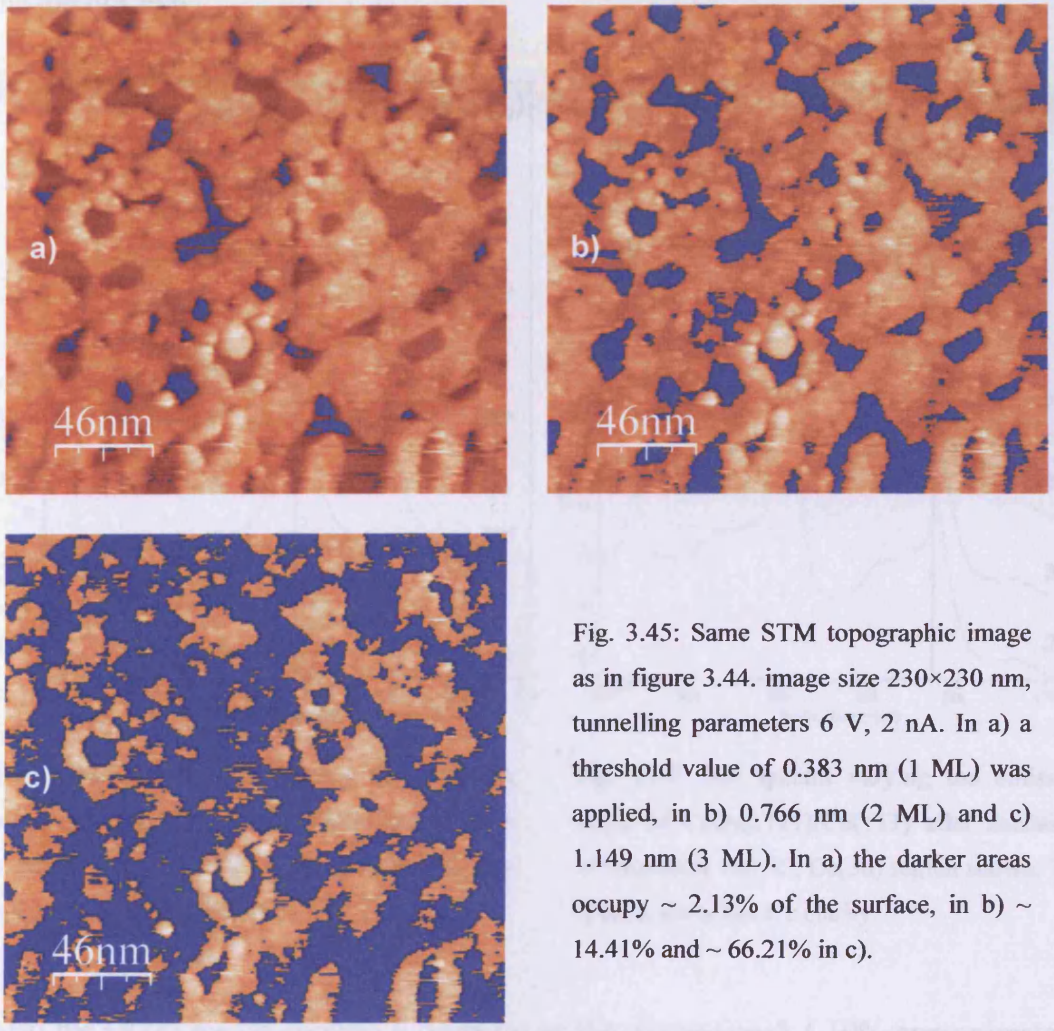

Fig. 3.45: Same STM topographic image as in figure 3.44. image size 230×230 nm, tunnelling parameters 6 V, 2 nA. In a) a threshold value of 0.383 nm (1 ML) was applied, in b) 0.766 nm (2 ML) and c) 1.149 nm (3 ML). In a) the darker areas occupy ~ 2.13% of the surface, in b) ~ 14.41% and ~ 66.21% in c).

With the aim of improving the surface sensitivity, a set of XP spectra at grazing angle were recorded. The spectra of the Cu($2p_{3/2}$) region are shown in figure 3.46, the Ce(3d) in figure 3.47 and the O(1s) in figure 3.48. The Cu(2p) region decreases in intensity with increased emission angle and no further components developed. In the Ce(3d) region, the spectrum recorded at 90° shows the typical Ce(IV) pattern, which decreases grazing the angle at which the photoelectrons are collected. The spectrum collected at 20° shows a pattern in which the 6-peaks structure is less resolved, meaning a certain amount of Ce(III) was present. Moreover, even if it is not possible to clearly distinguish the peaks characteristic of Ce(III), the deconvolution of the

spectrum recorded at 90° showed an amount of Ce(III) around 15%, value increasing to approximately 20% on the spectrum recorded at 20°. This means that there is a higher presence of Ce(III) on very top layer of the surface. In agreement with this, some authors [35, 37, 40] reported about the existence of a Ce_2O_3 passivation layer on the top of CeO_2.

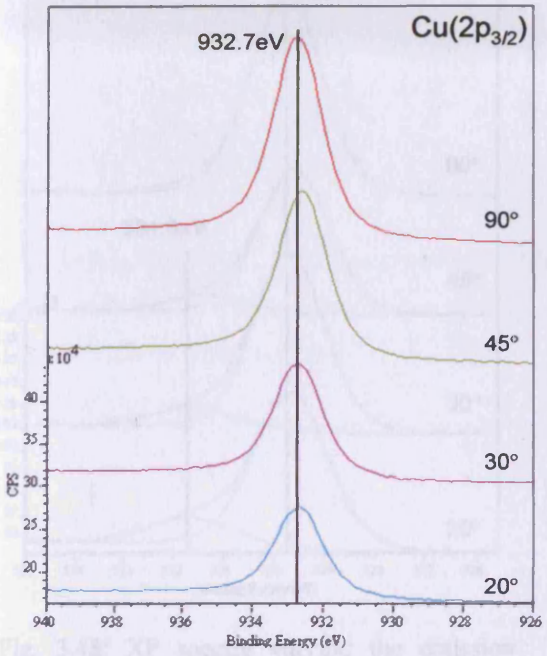

Fig. 3.46: XP spectra varying the emission angle of CeO_{2-x}(111)/Cu(111) after annealing in vacuum at 700 °C. $Cu(2p_{3/2})$ region shown. The spectra are offset for clarity.

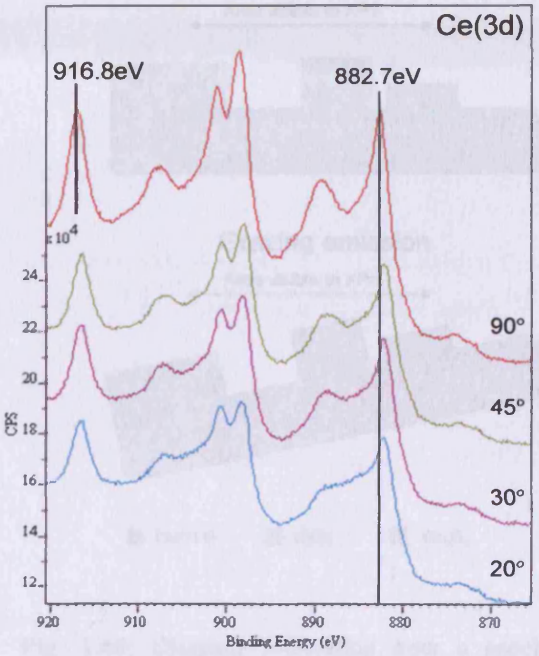

Fig. 3.47: XP spectra varying the emission angle of CeO_{2-x}(111)/Cu(111) after annealing in vacuum at 700 °C. Ce(3d) region shown. The spectra are offset for clarity.

Also the O(1s) region showed a decrease of the oxygen peak (-10% approximately). Moreover, starting at 45° it was possible to appreciate the presence of a shoulder towards higher binding energy. The peak fitting showed that two components are evident, with maxima at 529.7 and 531.6 eV. The peak at 529.7 eV is in good agreement with the one expected for metal oxides. The peak at 531.6 eV could be attributed to the presence of some CuO, but this is not confirmed by the position of the $Cu(2p_{3/2})$ being at 932.7 eV (figure 3.51). Moreover, no shoulders appeared on the $Cu(2p_{3/2})$ suggesting the presence of a second copper species. On the other hand, Hardacre *et al.* [40] observed a peak in a similar position studying the adsorption of oxygen on ceria films prepared on a Pt(111) single crystal. They attributed the peak to adsorbed O^- species. A different interpretation could attribute the higher binding

energy component to the oxygen in Ce_2O_3. In the spectrum collected at 20°, the component at 531.6 eV counts approximately for the 17% of the total oxygen peak. Thus, a correlation with the amount of Ce(III) can be made and the oxygen identified as the one belonging the to Ce_2O_3 passivation layer.

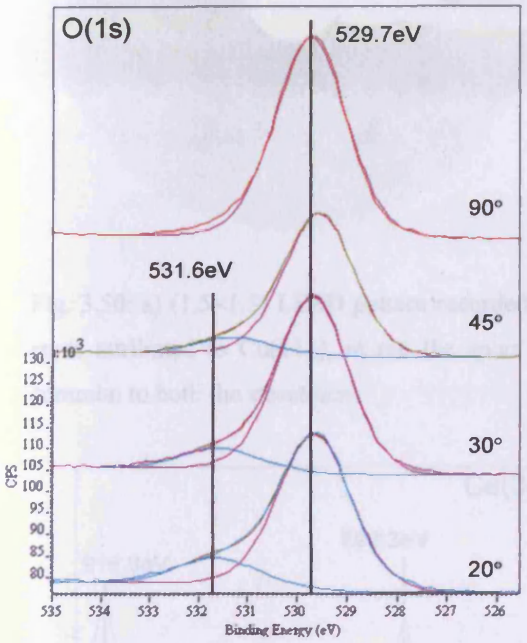

Fig. 3.48: XP spectra varying the emission angle of CeO_{2-x}(111)/Cu(111) after annealing in vacuum at 700 °C. O(1s) region and peak fittings shown. Grazing the emission angle a shoulder with maximum at ~531.6 eV appears evident. The spectra are offset for clarity.

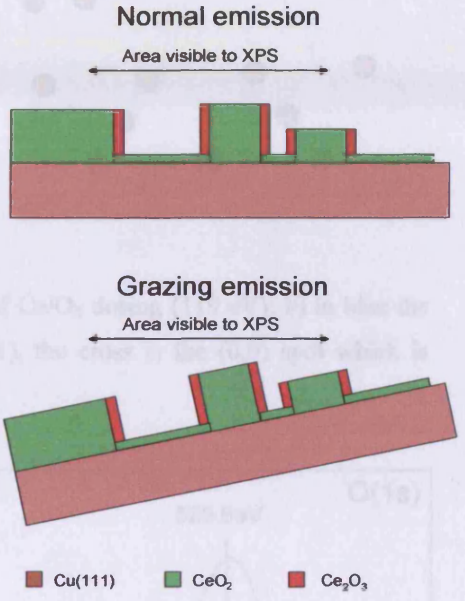

Fig. 3.49: Diagram illustrating how a species located in a particular position can produce a bigger signal at the grazing angle, than at the normal angle.

Note that the component at 531.6 eV appears to increase in the spectrum recorded at 20°. This is surprising, because a general attenuation of the peak would have been expected; however, it can be that the oxygen species generating this peak is located in an area that appears only when the angle is grazed, like the side of grain boundaries. Figure 3.49 illustrates the situation.

As a result of 3 minutes of cerium and oxygen co-dosing, a CeO_{2-x}(111) film ~2.03 MLe thick was prepared. The LEED showed that the film was ordered (figure 3.50) and the XPS that it was less oxidised that in all the previous cases, being the relative amount of Ce(IV) atoms ~82.5% of the total (figure 3.51).

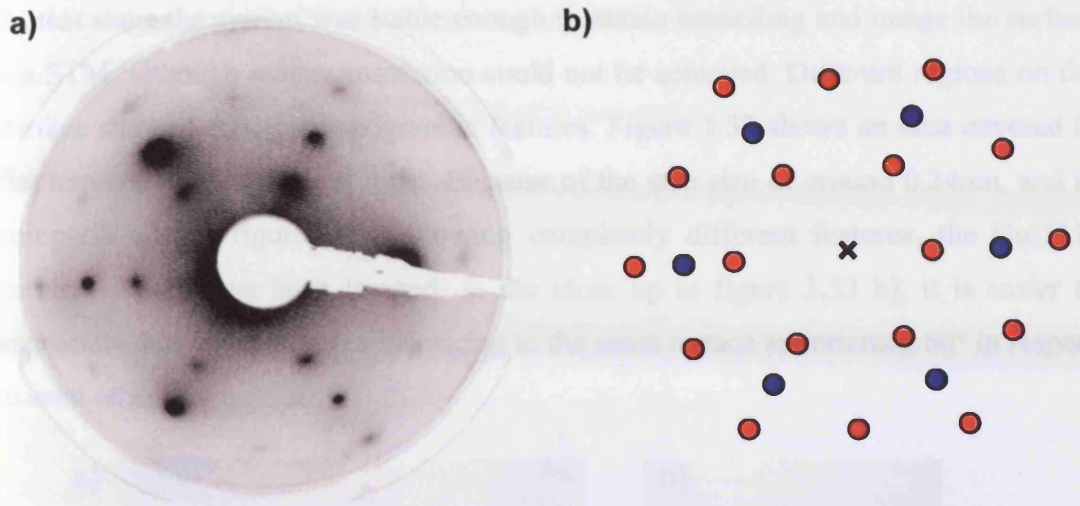

Fig. 3.50: a) (1.5×1.5) LEED pattern recorded after 3 min of Ce/O_2 dosing (119 eV); b) in blue the spots attributed to Cu(111), in red the spots of CeO_{2-x}(111), the cross is the (0,0) spot which is common to both the structures.

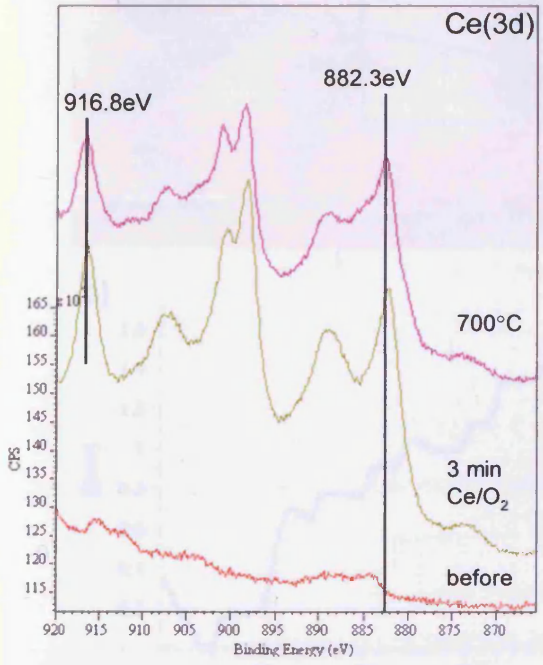

Fig. 3.51: XP spectra of the ceria layer obtained after 3 minutes of Ce/O_2 dosing, after annealing in vacuum at 700 °C. Ce(3d) region shown. The spectra are offset for clarity.

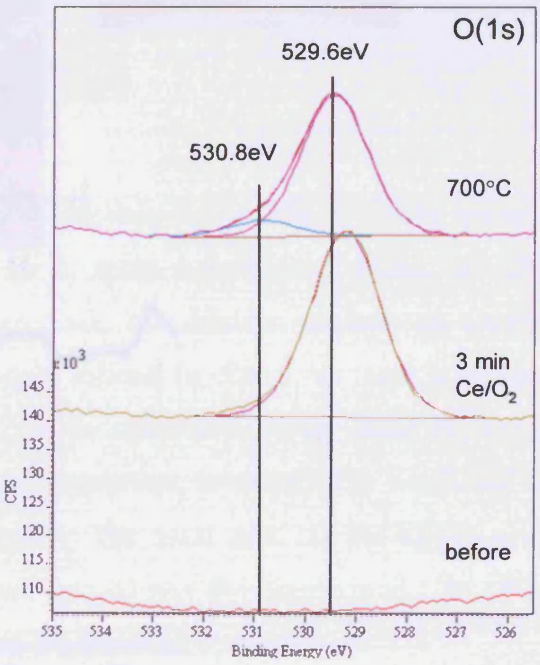

Fig. 3.52: XP spectra of the ceria layer obtained after 5 minutes of Ce/O_2 dosing, after annealing in vacuum at 700 °C. O(1s) region and peak fittings shown. The spectra are offset for clarity.

The $Ce(3d_{5/2})$ was recorded at 882.3 eV and the oxygen showed a single environment at maximum at ~529.6 eV (figure 3.52). After the annealing the LEED showed a pattern slightly sharper. The O/Ce ratio was 1.86.

At this stage the system was stable enough to obtain tunnelling and image the surface via STM, although atomic resolution could not be achieved. Different regions on the surface showed different topographic features. Figure 3.53 shows an area covered in flat terraces with islands on them. Because of the step size of around 0.24nm, and in comparison with figure 3.54, showing completely different features, the Cu(111) surface should have been imaged. In the close up in figure 3.53 b), it is easier to appreciate that the step-edges belonging to the same terrace are oriented 60° in respect to each other.

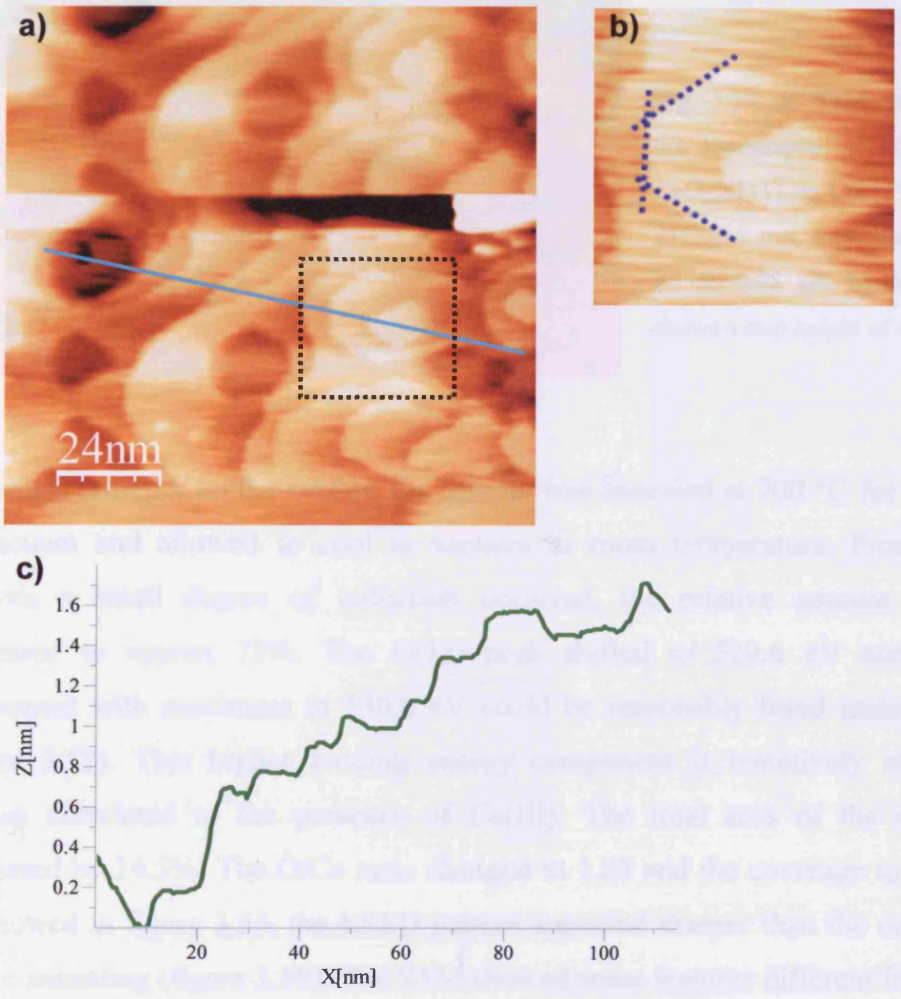

Fig. 3.53: a) STM image showing the topography of ~2.03 MLe of CeO_{2-x}(111) on Cu(111). Image size 120×120nm, tunnelling parameters -1.5 V, 0.79 nA. b) close-up on the area in the dashed line in a) and c) the step size in the line profile in a) is around 1.8 Å.

Moving onto another region, some different and apparently disordered features were observed (figure 3.54). The line profile shows a step height of ~ 3.9 Å. As this value is in good agreement with the theoretical one for a single monolayer thickness (3.83

Å), the feature where the line scan was taken can represent a step from one ceria monolayer to the following.

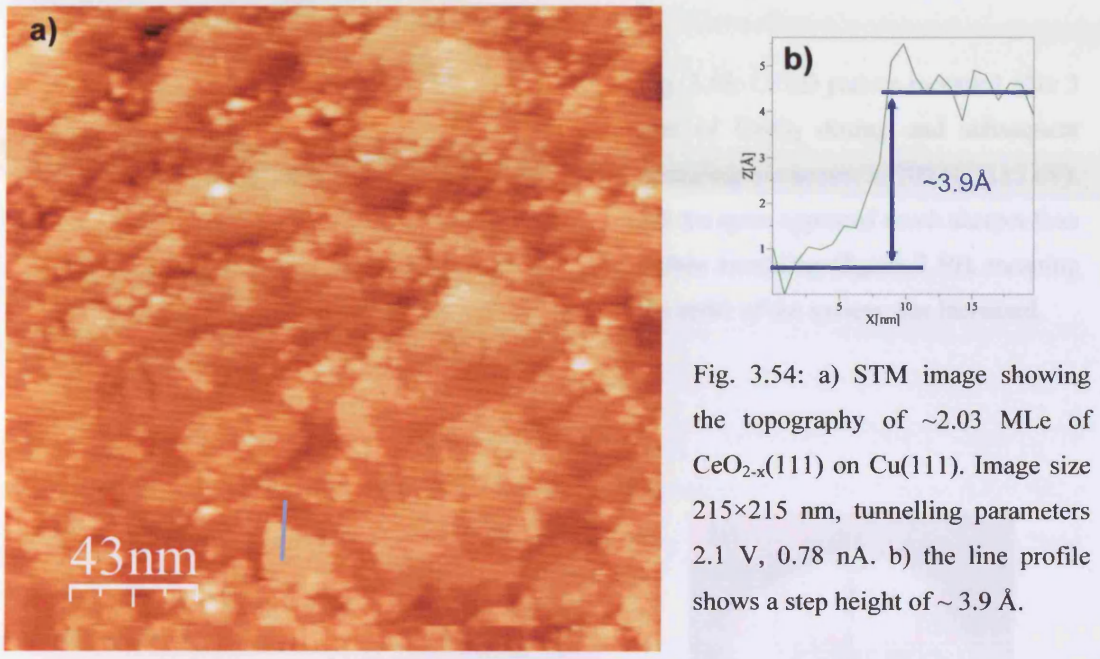

Fig. 3.54: a) STM image showing the topography of ~2.03 MLe of CeO_{2-x}(111) on Cu(111). Image size 215×215 nm, tunnelling parameters 2.1 V, 0.78 nA. b) the line profile shows a step height of ~ 3.9 Å.

To induce ordering on the surface the sample was annealed at 700 °C for 30 minutes in vacuum and allowed to cool in vacuum to room temperature. From the XPS analysis a small degree of reduction occurred, the relative amount of Ce(IV) decreased to approx 73%. The O(1s) peak shifted to 529.6 eV and a second component with maximum at 530.8 eV could be reasonably fitted under the curve (figure 3.52). This higher binding energy component is tentatively attributed to oxygen correlated to the presence of Ce(III). The total area of the O(1s) peak decreased by 24.5%. The O/Ce ratio changed to 1.83 and the coverage to 1.84 MLe. As showed in figure 3.55, the LEED pattern appeared sharper than the one recorded before annealing (figure 3.50). The STM showed some features different from the one recorded before. The bright island in figure 3.56 are attributed to the CeO_2(111) layer; the background texture has to be attributed to AC noise. The line profile showed a step height of ~1.25 nm, value corresponding to approximately 3.3 ML of CeO_2(111). Once again, the step-edges belonging to the same terrace are oriented 60° in respect to each other (figure 3.56 c).

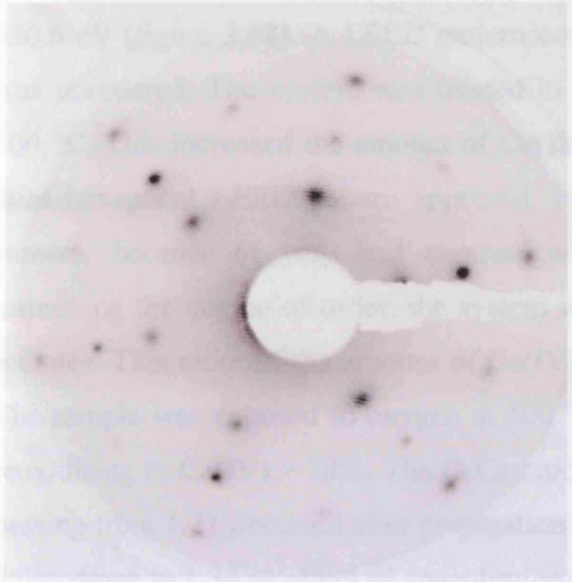

Fig. 3.58: LEED pattern recorded after 3 min of Ce/O_2 dosing and subsequent annealing in vacuum at 700 °C (115 eV). All the spots appeared much sharper than before annealing (figure 3.50), meaning the order of the system was increased.

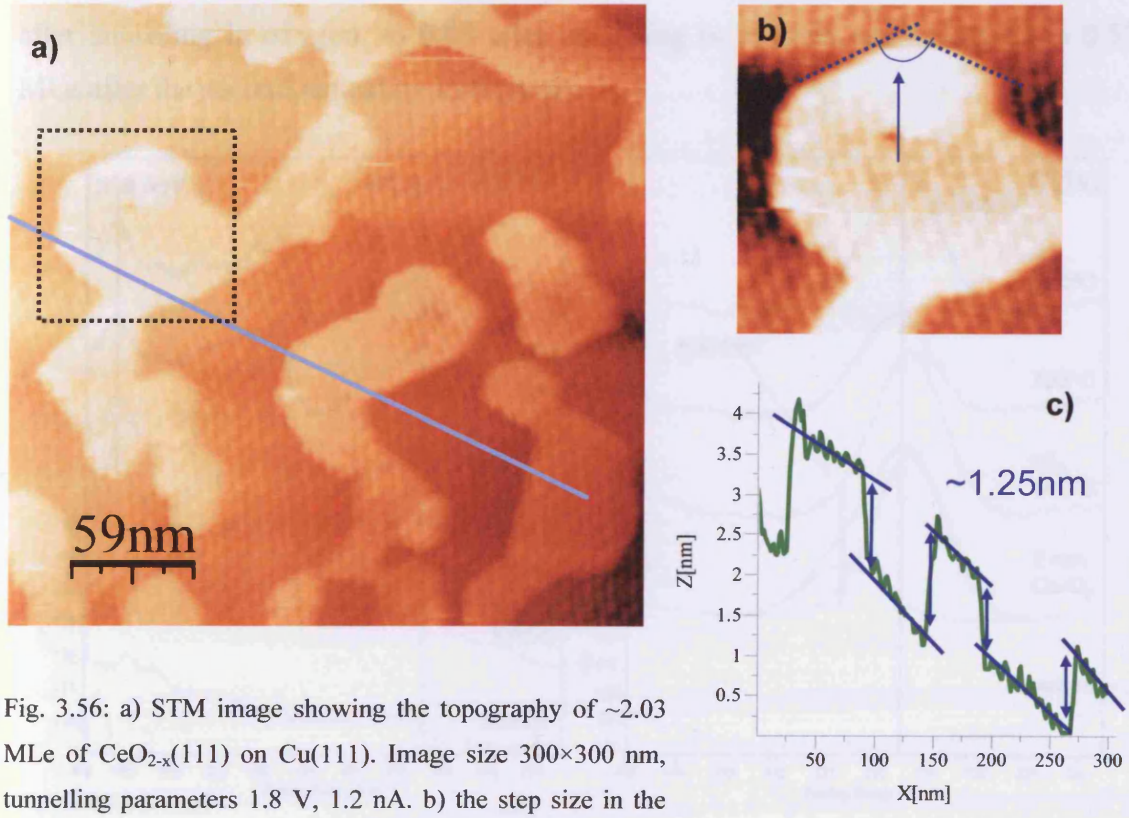

Fig. 3.56: a) STM image showing the topography of ~2.03 MLe of CeO_{2-x}(111) on Cu(111). Image size 300×300 nm, tunnelling parameters 1.8 V, 1.2 nA. b) the step size in the line profile in a) is around 1.25 nm and c) close-up on the area in the dashed line in a).

After 2 minutes of cerium dosing in oxygen atmosphere, a ceria layer 1.10 MLe thick was produced. The Ce(3d) XP spectrum showed 60% of Ce(IV) (figure 3.57) and a broad oxygen peak with maximum at 529.3 eV and a shoulder with maximum at

530.6 eV (figure 3.58). A LEED pattern could not be recorded, meaning the surface was unordered. The system was treated in oxygen (5×10^{-7} mbar) for 30 minutes at 500 °C. This increased the amount of Ce(IV) to ~87% of the total cerium cations. A faint hexagonal LEED pattern appeared, but could have not been recorded by the camera, because of very bad contrast with the background. In the attempt of improving the degree of order, the system was annealed at 700 °C in vacuum for 30 minutes. This reduced the amount of Ce(IV) to 71% and did not improve the LEED. The sample was exposed to oxygen at 500 °C a second time for 30 minutes, slightly reoxidising it, Ce(IV) > 78%. The O/Ce ratio varied accordingly the heating treatment, passing from 1.31 obtained after preparation to 1.60 after the first annealing in oxygen, going down to 1.34 as effect of annealing in vacuum at 700 °C and increasing again to 1.78 after the second oxidation treatment. The coverage varies significantly during the thermal treatments: from the original 1.10 MLe coverage, it dropped to a 0.81 MLe after annealing in oxygen, to 0.48 after annealing in vacuum and increased to 0.53 MLe after the second annealing in oxygen.

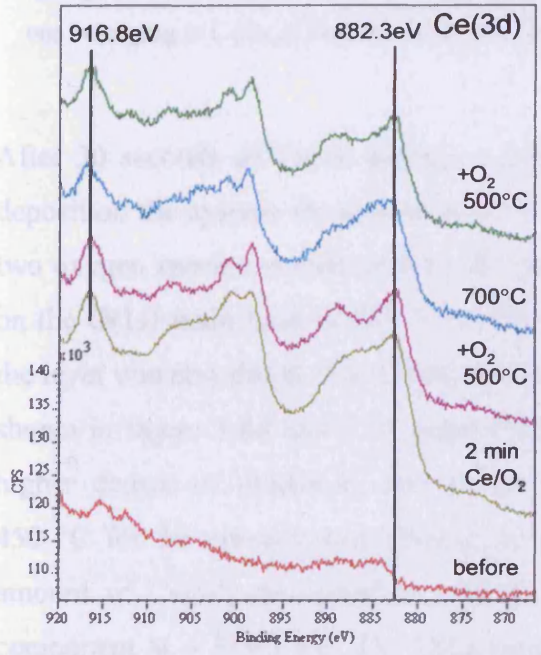

Fig 3.57: XP spectra of the ceria layer obtained after 2 minutes of Ce/O_2 dosing in and after the different oxidation and reduction steps. Ce(3d) region shown.

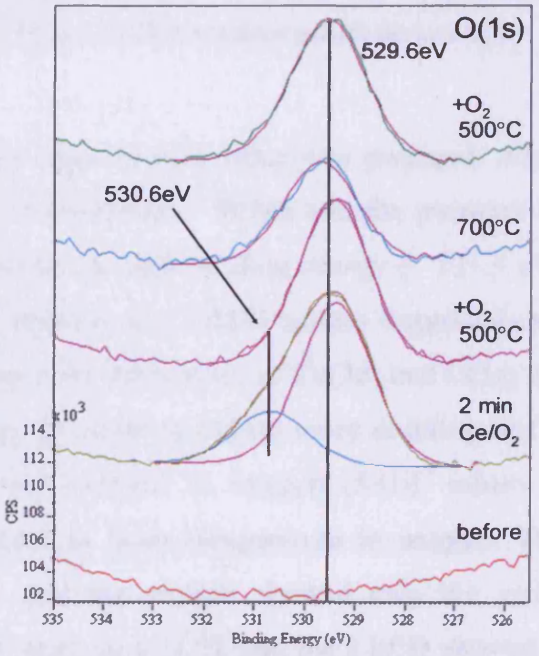

Fig 3.58: XP spectra of the ceria layer obtained after 2 minutes of Ce/O_2 dosing and after the different oxidation and reduction steps. O(1s) region and peak fittings shown.

At this stage the LEED was reasonably sharp (figure 3.59). The pattern shows the hexagonal structure of Cu(111), blue in figure 3.59 b), and of CeO_{2-x}(111), red spots

aligned with the Cu(111). The others, at the same distance from the (0,0) as the CeO_{2-x}(111), may represent other two CeO_{2-x}(111) domains rotated +/-26° in respect of the one aligned with the Cu(111) spots. Attempt to image the surface with the STM was made, but were unsuccessful.

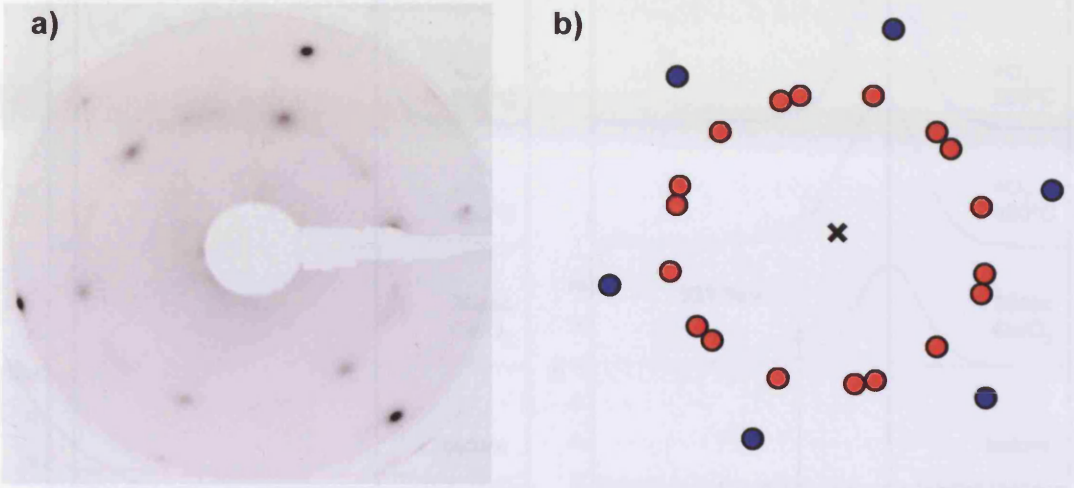

Fig 3.59: a) LEED pattern recorded after the second oxidation at 500 °C of the layer obtained by dosing Ce/O_2 for 2 minutes (56 eV); b) in blue the spots attributed to Cu(111). The red spots are the one belonging to CeO_{2-x}(111). The cross is the (0,0) spot which is common to both the structure.

After 30 seconds of Ce/O_2 dosing, a ceria layer of 0.26 MLe was prepared. After deposition the system showed an amount of Ce(III) of ~ 38.6% and the presence of two oxygen species as indicated by the shoulder at high binding energy (~ 531.3 eV) on the O(1s) main peak at 529.3 eV. The absence of a LEED pattern suggested that the layer was unordered. The O/Ce ratio was 1.76. XP spectra of Ce(3d) and O(1s) are shown in figure 3.60 and 3.61 respectively. In order to induce more ordering and a higher degree of oxidation, the system was exposed to oxygen (5×10^{-7} mbar) at 450 °C for 30 minutes and allowed to cool to room temperature in oxygen. The amount of Ce(III) decreased to ~20.5% and the oxygen showed only the usual component at ~ 529.3 eV. The O/Ce ratio went up to 1.92 and the LEED showed a pattern very similar to the one presented in figure 3.59. Full oxidation (O/Ce ~ 2.02) was achieved after exposing the system to 5×10^{-7} mbar of oxygen for 30 minutes at 500 °C and allowing to cool to room temperature in the gas. The LEED was sharper than before and it is showed in figure 3.62. As it was collected at a higher energy, 72 eV, it is now possible to appreciate the three CeO_2(111) patterns rotated +/-26°

degrees in respect to each other, represented by the red spots in the model. Figure 3.63 shows a model of the surface.

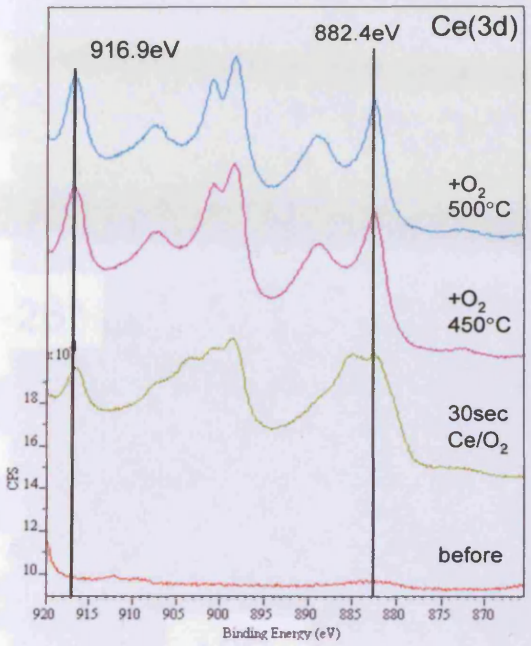

Fig. 3.60: XP spectra of the ceria layer obtained after 30 seconds of Ce/O_2 dosing in and after the different oxidation steps. Ce(3d) region shown.

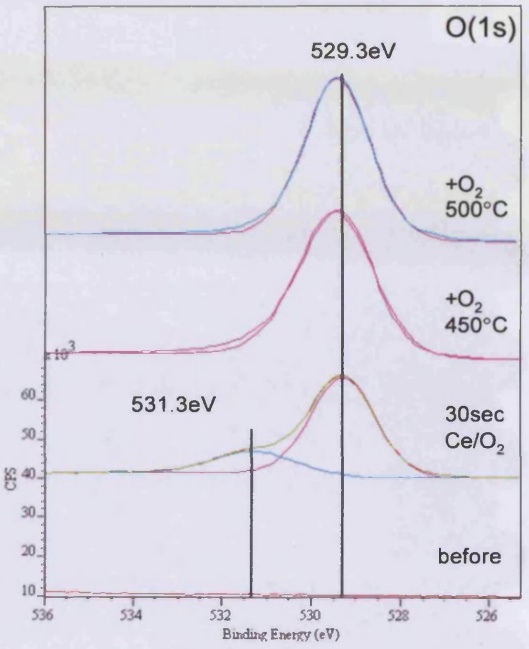

Fig. 3.61: XP spectra of the ceria layer obtained after 30 seconds of Ce/O_2 dosing and after the different oxidation steps. O(1s) region and peak fittings shown.

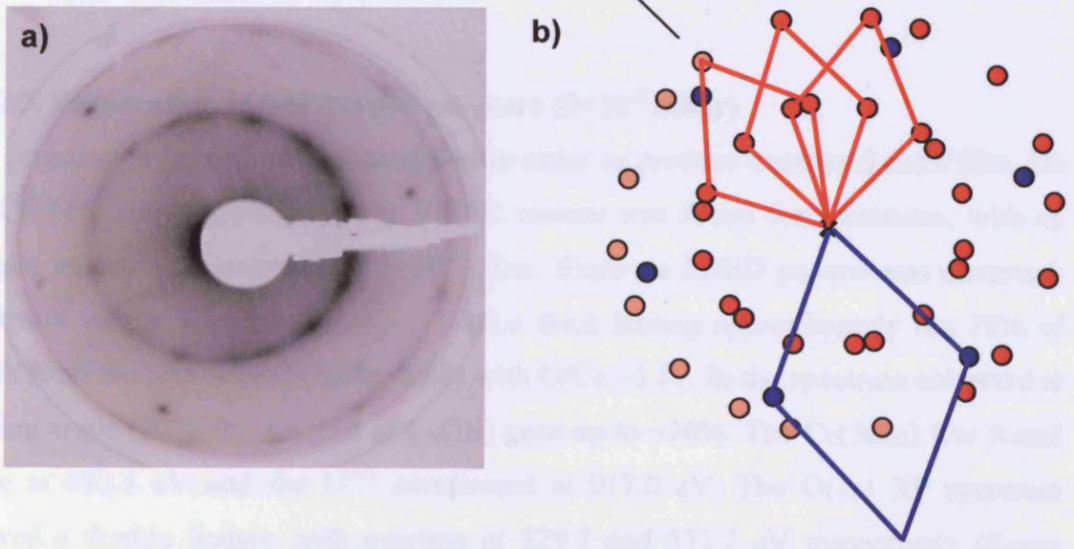

Fig 3.62: a) LEED pattern recorded after the second oxidation at 500 °C of the layer obtained by dosing Ce/O_2 for 30 seconds (72 eV); b) in blue the spots attributed to Cu(111). The red spots are the ones belonging to CeO_{2-x}(111), the three unit cell with +/-26° rotation are highlighted. The cross is the (0,0) spot which is common to both the structure.

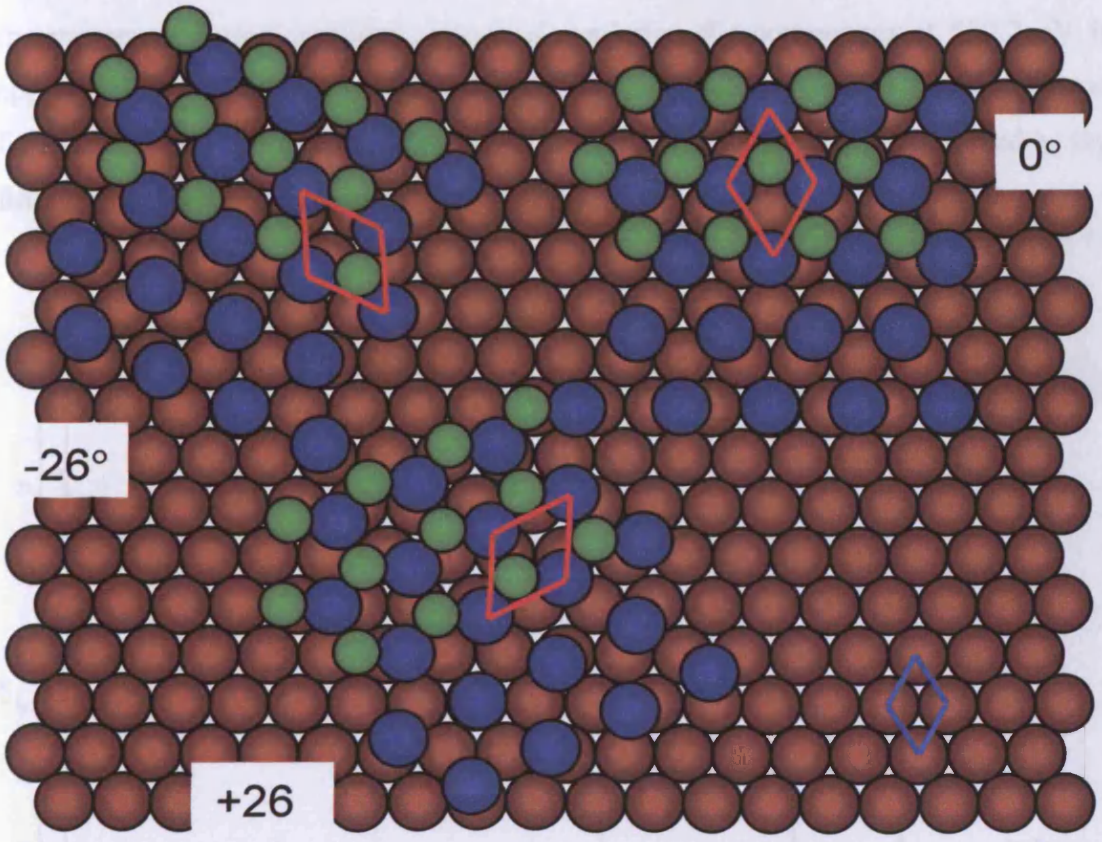

Fig. 3.63: A model of the CeO_{2-x}(111)/Cu(111) surface derived from the LEED in figure 3.62. Cu atoms are brown, O atoms are blue, Ce atoms are green. In blue the Cu(111) unit cell, in red the CeO_2(111) unit cell. The 15% of the oxygen atoms are on 3-fold sites, the 55% in 2-fold sites and the remaining 30% directly on top of a copper atom.

3.3.2.5. Preparation in low oxygen pressure (5×10^{-8} mbar)

The preparation procedure was modified in order to produce a reduced ceria film. On the Cu(111) single crystal kept at 300 °C cerium was dosed for 7 minutes, with an oxygen background pressure of 5×10^{-8} mbar. Since no LEED pattern was observed, the result was a disordered film ~1.3 MLe thick having approximately the 78% of Ce(IV) and the rest Ce(III) (figure 3.64) with O/Ce ~1.87. In the spectrum collected at grazing angle (20°), the amount of Ce(III) goes up to ~30%. The Ce($3d_{5/2}$) was found to be at 882.4 eV and the U''' component at 917.0 eV. The O(1s) XP spectrum showed a double feature with maxima at 529.7 and 532.2 eV respectively (figure 3.65). The shift towards higher binding energy for the oxygen peak belonging to reduced ceria was established during the experiments undertaken with the CeO_2(111) single crystal, but the extent of the shift was only of few tenth of eV, not 2.5 eV as in

the present case. Nevertheless, at normal emission the component at 532.2 eV is approximately 20% of the total oxygen signal and the 32% at grazing emission. These figures are in agreement with the relative amount of Ce(IV)/Ce(III) determined by the fitting procedure (78/22 at normal emission).

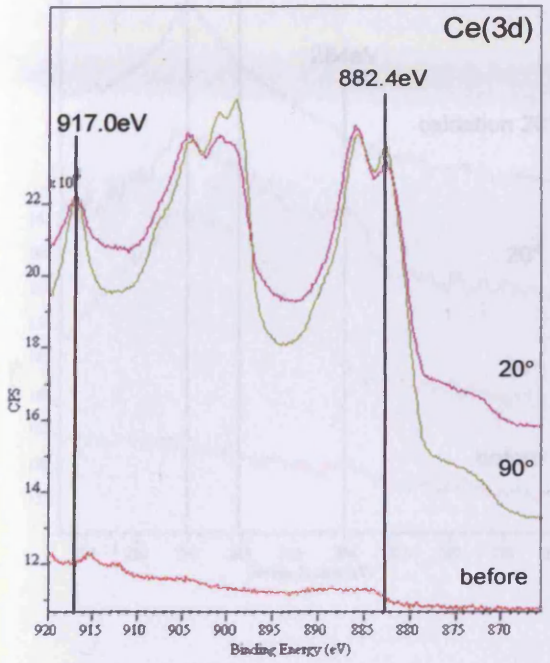

Fig 3.64: Reduced ceria layer XP spectra obtained after 7 minutes dosage. Ce(3d) region shown. The spectra are offset for clarity.

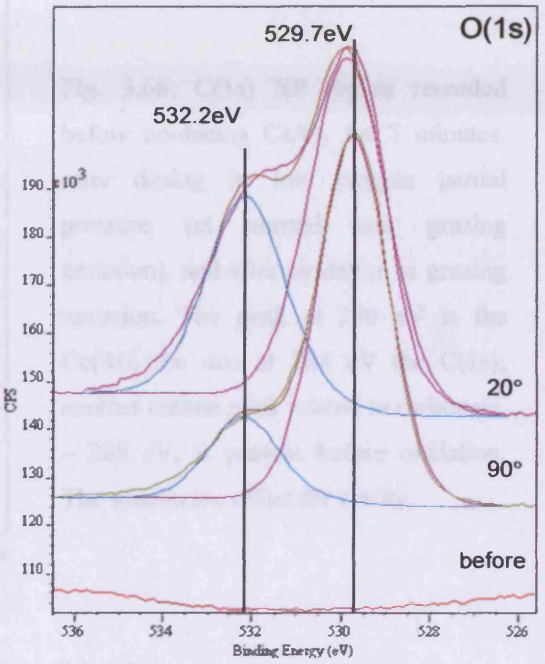

Fig. 3.65: Reduced ceria layer XP spectra obtained after 7 minutes dosage. O(1s) region and peak fittings shown. Grazing the emission angle a shoulder with maximum at ~532.2 eV appears evident. The spectra are offset for clarity.

However, since a carbon peak at ~ 288 eV was present, it is very likely that the higher binding energy oxygen peak was due to the presence of carbonates, which were located on the very top layer. Note that the binding energy of the Ce(4s) peak is ~ 290 eV [70]; this can therefore create some ambiguity in the assignment of the peak (figure 3.66). In an attempt of ordering the reduced ceria overlayer, the sample was annealed to 500 °C in vacuum and allowed to cool to room temperature. Since the LEED showed a very blurry hexagonal pattern, the annealing treatment was repeated. The LEED improved slightly, but still was not good because of very faint spots and bad contrast with the background. Since the attempt of obtaining an ordered surface was unsuccessful, the film was annealed to 500 °C in oxygen (5×10^{-7} mbar) for 30 minutes, resulting in good oxidation of the surface (Ce(IV) > 92%, O/Ce integral ratio

~1.94) and disappearance of the oxygen peak at ~ 532.2 eV. This is a confirmation that this oxygen species was likely linked with the carbon present (see figure 3.66).

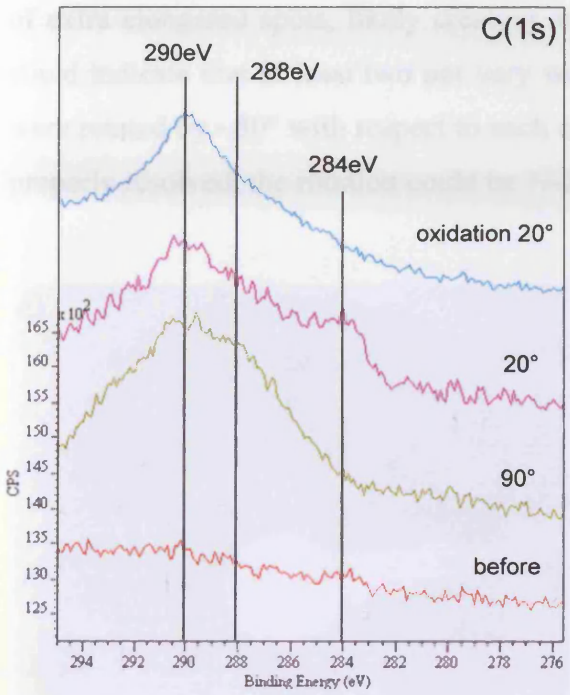

Fig. 3.66: C(1s) XP region recorded before co-dosing Ce/O_2 for 7 minutes, after dosing in low oxygen partial pressure (at normal and grazing emission), and after oxidation at grazing emission. The peak at 290 eV is the Ce(4s), the one at 284 eV the C(1s); another carbon peak related to carbonate, ~ 288 eV, is present before oxidation. The spectra are offset for clarity.

Again, the LEED pattern was very blurry. The film was then reduced again by annealing in vacuum for 30 minutes at 550 °C but the degree of reduction did not change since Ce(IV)/Ce(III) was calculated as 76/24 and O/Ce atomic ratio ~1.86. On the other hand a LEED pattern could be recorded (figure 3.67).

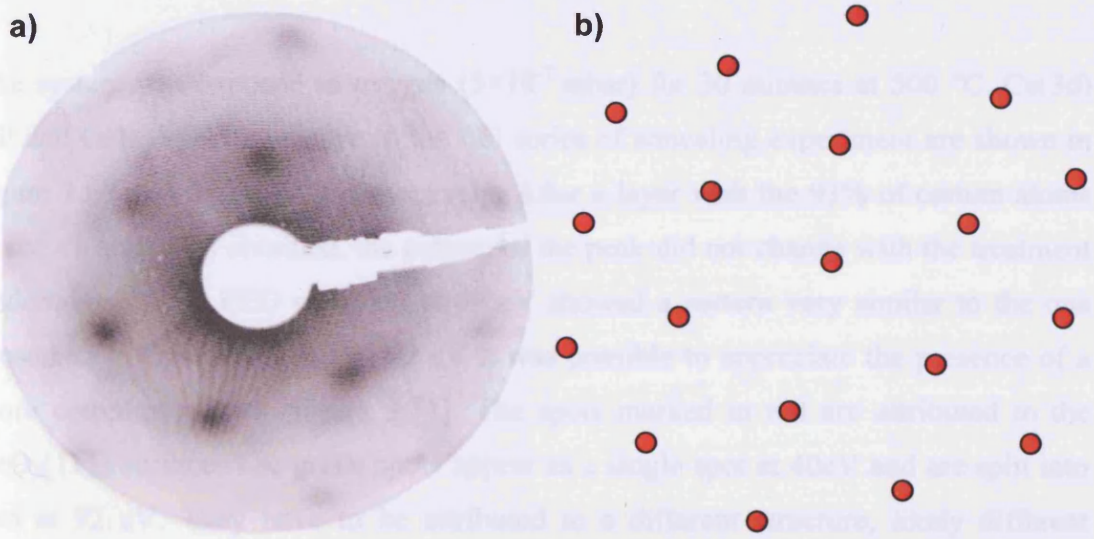

Fig 3.67: a) LEED pattern collected after treating the reduced ceria film as describe in the text (88 eV); b) only the $CeO_2(111)$ (1×1) spots appear visible.

The LEED showed a hexagonal pattern with the centre very blurry (88 eV) attributed to the reduced ceria overlayer. A pattern recorded at lower energy (40 eV) allowed resolving the blurry centre of the pattern in figure 3.67, making evident the presence of extra elongated spots, likely creating another hexagonal array (figure 3.68). This could indicate that at least two not very well ordered domains were present and they were rotated by ~30° with respect to each other. However, since the pattern is still not properly resolved, the rotation could be +/-26° as previously observed (figure 3.62).

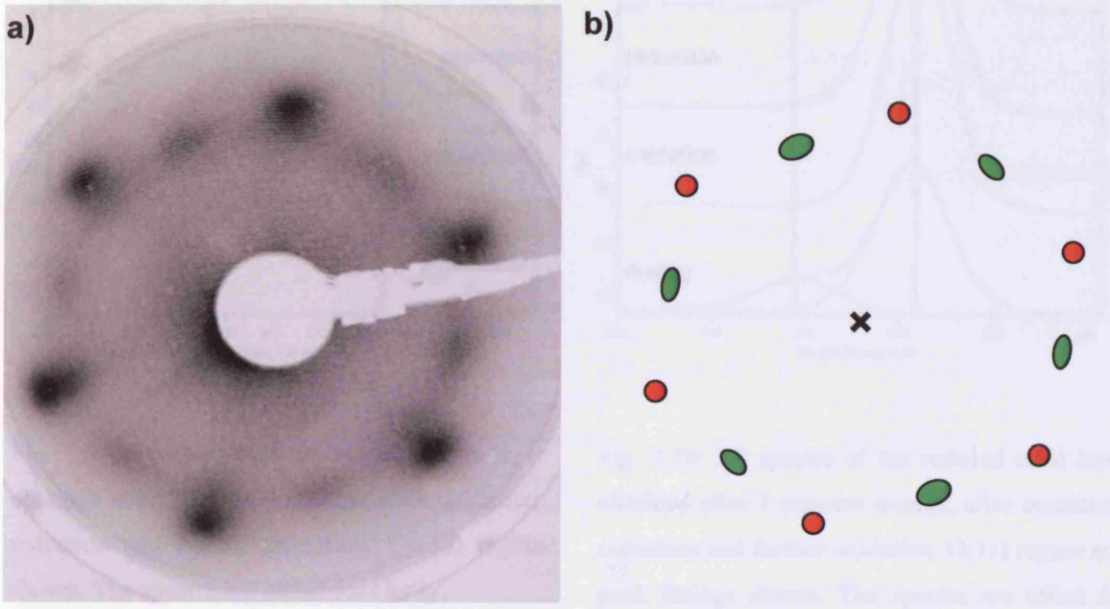

Fig 3.68: a) LEED pattern of the same surface as in figure 3.57 (40 eV), more spots are evident; b) the spots form two hexagonal arrays rotated 30° in respect to each other.

The system was exposed to oxygen (5×10^{-7} mbar) for 30 minutes at 500 °C. Ce(3d) XP and O(1s) spectra relative to the full series of annealing experiment are shown in figure 3.69 and figure 3.70 respectively. After a layer with the 93% of cerium atoms in the 4+ state was obtained, the pattern of the peak did not change with the treatment undertaken. The LEED recorded at 40 eV showed a pattern very similar to the one presented in figure 3.67 but at 92 eV it was possible to appreciate the presence of a more complex pattern (figure 3.71). The spots marked in red are attributed to the CeO_2(111) surface. The green spots appear as a single spot at 40eV and are split into two at 92 eV. They have to be attributed to a different structure, likely different domains oriented +/-17° with respect to the CeO_2(111) spots, having still hexagonal

symmetry and a smaller unit cell (~0.328 nm). Attempt to image the surface via STM were unsuccessful.

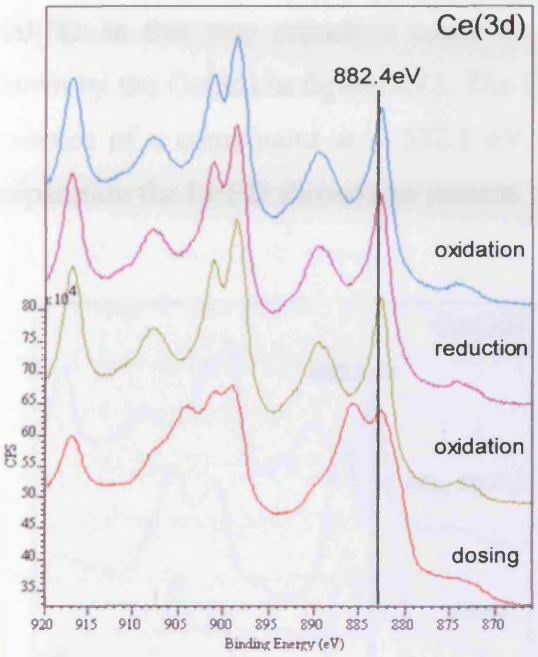

Fig. 3.69: XP spectra of the reduced ceria layer obtained after 7 minutes dosage, after oxidation, reduction and further oxidation. Ce(3d) region shown. The spectra are offset for clarity.

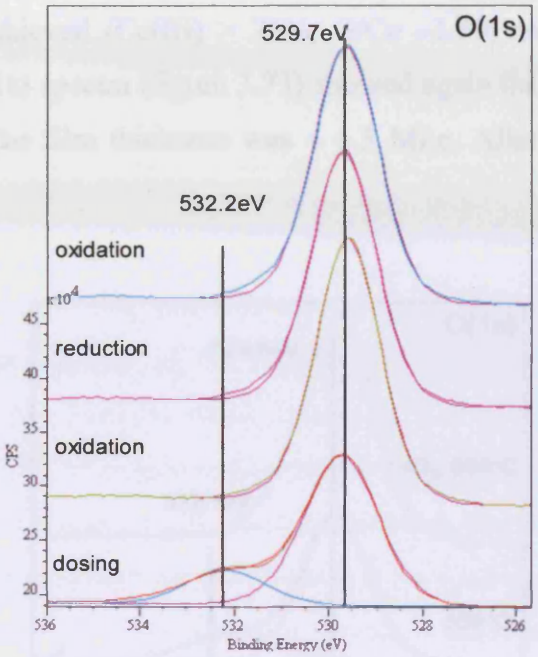

Fig. 3.70: XP spectra of the reduced ceria layer obtained after 7 minutes dosage, after oxidation, reduction and further oxidation. O(1s) region and peak fittings shown. The spectra are offset for clarity.

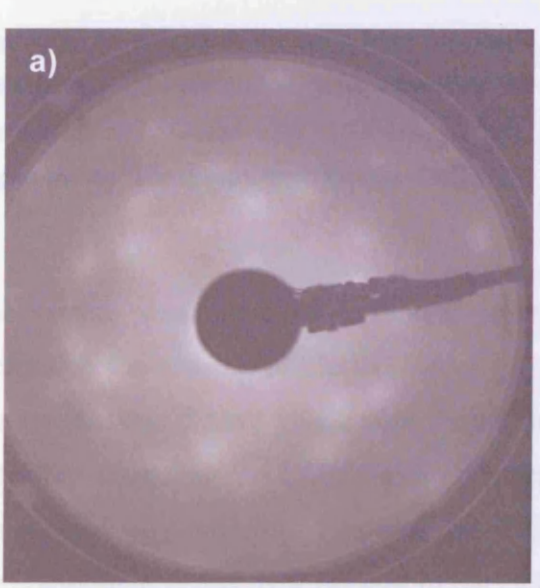

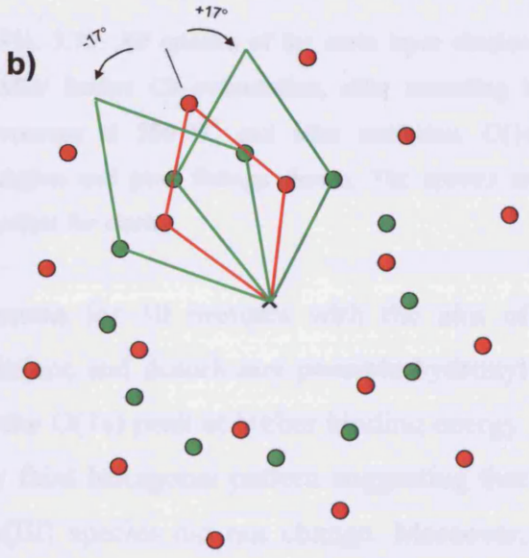

Fig. 3.71: a) LEED pattern obtained after heating treatments as described in the text (92 eV), more spots are evident; b) the $CeO_2(111)$ spots are represented in red, in green the spots belonging to another structure, different domains orientation +/-17° with respect of $CeO_2(111)$ spots.

Since only a partial reduction (Ce(IV)/Ce(III) 76/24) and O/Ce ~1.86) could be obtained by simply annealing the preparation in vacuum, additional cerium was evaporated on the surface for 1 minute, without oxygen, keeping the substrate at 300 °C. In this way reduction could be achieved (Ce(III) > 76%, O/Ce ~1.59) as shown by the Ce(3d) in figure 3.72. The O(1s) spectra (figure 3.73) showed again the presence of a component at ~ 532.1 eV. The film thickness was ~ 6.3 MLe. After preparation the LEED showed no pattern.

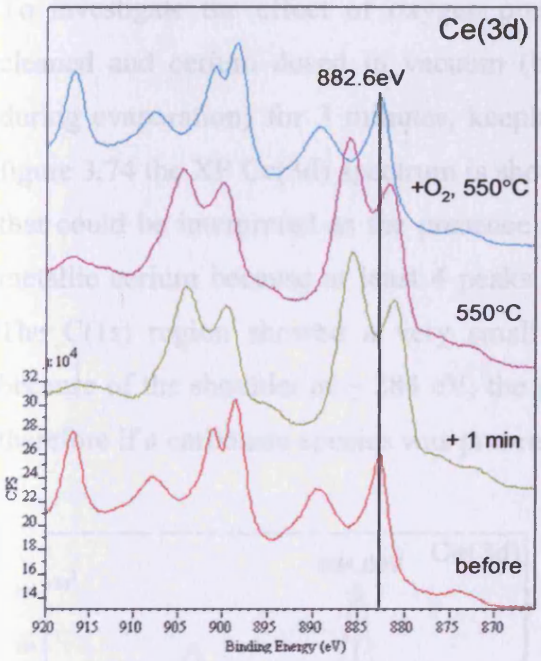

Fig. 3.72: XP spectra of the ceria layer obtained after further Ce evaporation, after annealing in vacuum at 550 °C and after oxidation. Ce(3d) region shown. The spectra are offset for clarity.

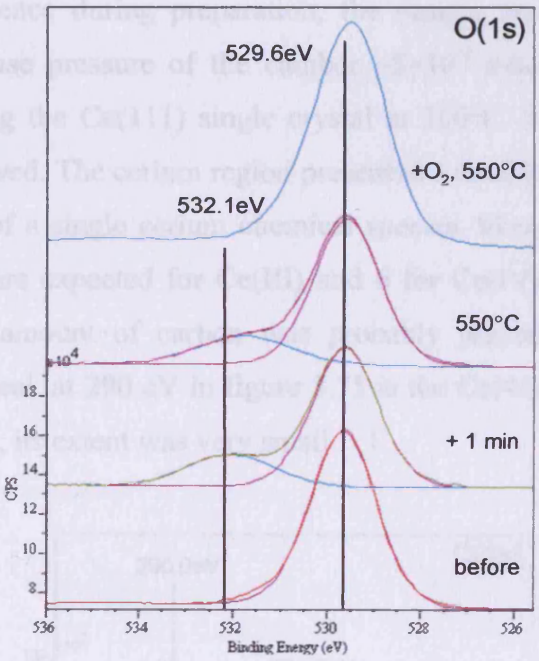

Fig. 3.73: XP spectra of the ceria layer obtained after further Ce evaporation, after annealing in vacuum at 550 °C and after oxidation. O(1s) region and peak fittings shown. The spectra are offset for clarity.

The system was annealed to 550°C in vacuum for 30 minutes with the aim of increasing the amount of Ce(III), order the surface and desorb any possible hydroxyl species that could have give a contribution to the O(1s) peak at higher binding energy. After the annealing the LEED showed a very faint hexagonal pattern suggesting that the surface was ordering. The amount of Ce(III) species did not change. Moreover, the component at 532.1eV present in the O(1s) spectrum did not disappear, but shifted slightly to lower binding energy (~531.7eV). This high binding energy component completely disappeared after annealing in oxygen ($5x10^{-7}$mbar) to 550°C for 30

minutes. As previously seen (see figure 3.66 which shows a similar experiment), this was likely related to the presence of carbonate species that could be desorbed annealing in oxygen. The maximum degree of oxidation achieved was Ce(IV) > 89% with O/Ce ~1.93. At this stage the LEED showed the same pattern as in figure 3.82. STM imaging was again unsuccessful.

3.3.2.6. Preparation in vacuum

To investigate the effect of oxygen presence during preparation, the sample was cleaned and cerium dosed in vacuum (base pressure of the camber ~5×10^{-9} mbar during evaporation) for 3 minutes, keeping the Cu(111) single crystal at 300°C. In figure 3.74 the XP Ce(3d) spectrum is showed. The cerium region presented a doublet that could be interpreted as the presence of a single cerium chemical species, likely metallic cerium because at least 4 peaks are expected for Ce(III) and 6 for Ce(IV). The C(1s) region showed a very small amount of carbon was probably present because of the shoulder at ~ 284 eV; the peak at 290 eV in figure 3.75 is the Ce(4s), therefore if a carbonate species was present, its extent was very small .

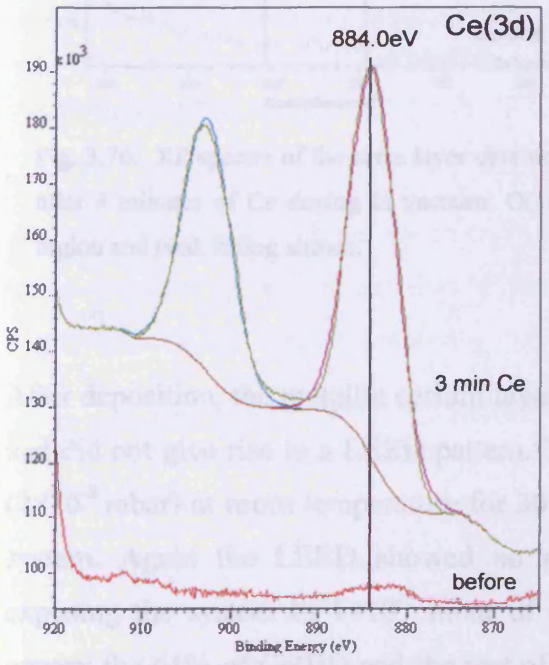

Fig. 3.74: XP spectra of the ceria layer obtained after 3 minutes of Ce dosing in vacuum. Ce(3d) region and peak fitting shown.

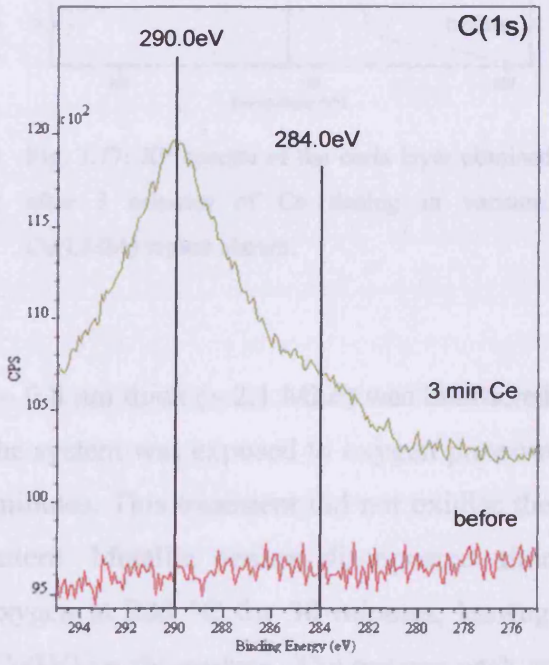

Fig. 3.75: XP spectra of the ceria layer obtained after 3 minutes of Ce dosing in vacuum. C(1s) region shown.

Also a small amount of oxygen in two different chemical species was present on the surface (figure 3.76). Since the copper did not appear oxidised as shown by the position of the Cu(LMM) Auger transition at ~ 918.7 eV in kinetic energy scale (figure 3.77), the oxygen component at 529.8 eV can be tentatively attributed to a small amount of oxidised cerium, taking also into account the large FWHM (~ 6.25 eV) of the Ce(0). The higher binding energy component is probably due to a small amount of carbonate, the carbon signal of which was not detectable.

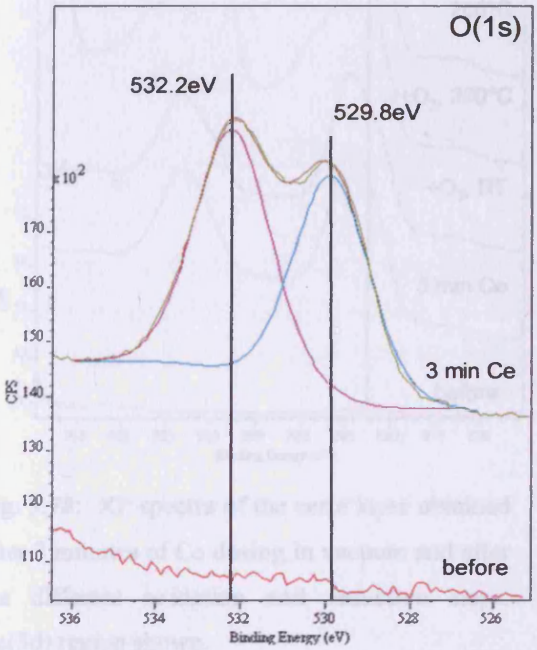

Fig. 3.76: XP spectra of the ceria layer obtained after 3 minutes of Ce dosing in vacuum. O(1s) region and peak fitting shown.

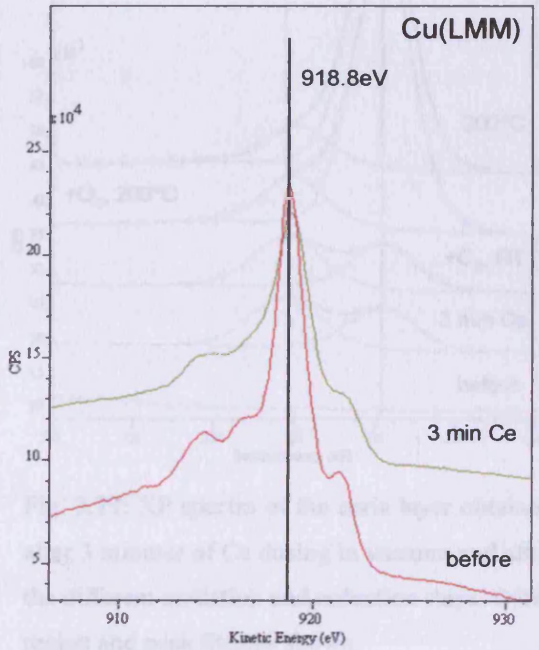

Fig. 3.77: XP spectra of the ceria layer obtained after 3 minutes of Ce dosing in vacuum. Cu(LMM) region shown.

After deposition, the metallic cerium layer ~ 0.8 nm thick (~ 2.1 MLe) was unordered and did not give rise to a LEED pattern. The system was exposed to oxygen pressure (2×10^{-8} mbar) at room temperature for 30 minutes. This treatment did not oxidise the system. Again the LEED showed no pattern. Metallic cerium disappeared after exposing the system to 1×10^{-7} mbar of oxygen at 200 °C for 30 minutes, leaving approx the 61% of Ce(III) and the rest of Ce(IV) on the surface. The oxygen peak at 529.7 eV increased approximately by 6 times, whereas the one at ~ 532.1 eV stayed approximately constant in intensity. As a result of annealing at 200 °C in vacuum, the amount of Ce(III) stayed approximately constant (63.5%), as well as the oxygen peak.

The experimental sequence described is shown in figures 3.78, Ce(3d) XP region and 3.79, O(1s) XP region. No LEED patterns were recorded, meaning that it was not possible to reorder the surface starting from a metallic layer, at least in these conditions. After these experiments the film thickness was constant.

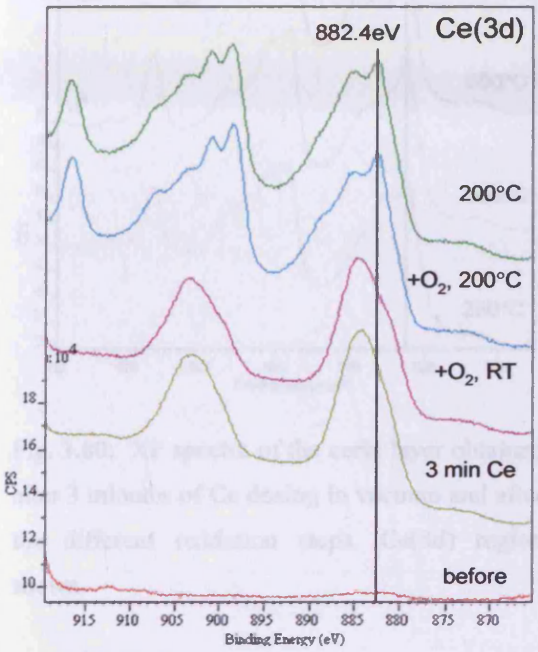

Fig. 3.78: XP spectra of the ceria layer obtained after 3 minutes of Ce dosing in vacuum and after the different oxidation and reduction steps. Ce(3d) region shown.

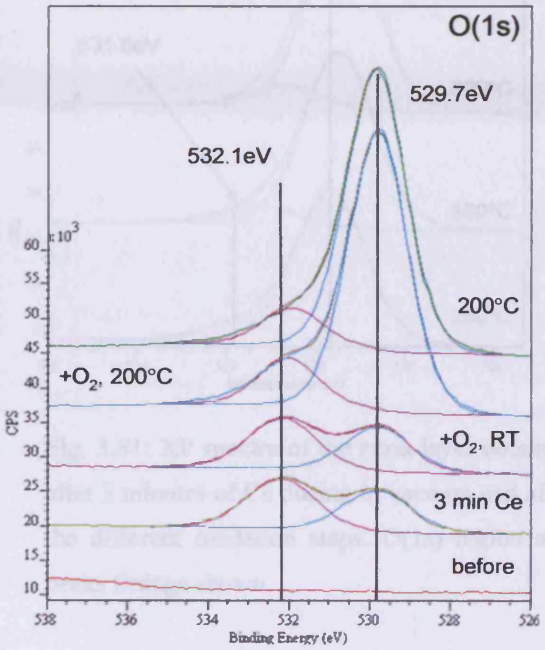

Fig. 3.79: XP spectra of the ceria layer obtained after 3 minutes of Ce dosing in vacuum and after the different oxidation and reduction steps. O(1s) region and peak fittings shown.

As the oxidation proceeded, by exposing the sample to oxygen (1×10^{-7} mabr) for 30 minutes at 250 °C, 500 °C and 600 °C the amount of Ce(III) decreased and the Ce(IV) increased. The XP spectra describing the oxidation experiments are reported in figure 3.80, Ce(3d) region, and 3.81, O(1s). The relative amount of Ce(0)/Ce(III)/Ce(IV) obtained after each single oxidation step is showed in table 3.9. As shown in table 3.9 and figure 3.81, the amount of oxygen adsorbed by the system increased accordingly to the increase of the Ce(III) first and the Ce(IV) after. After the second exposure to oxygen at 600 °C, the O/Ce ratio went up to 2.06, meaning that a stoichiometry corresponding to CeO_2 was obtained and some excess of oxygen was likely present on a fully oxidised ceria layer. Moreover, the component at higher binding energy appeared to shift to lower values with the decrease of Ce(III).

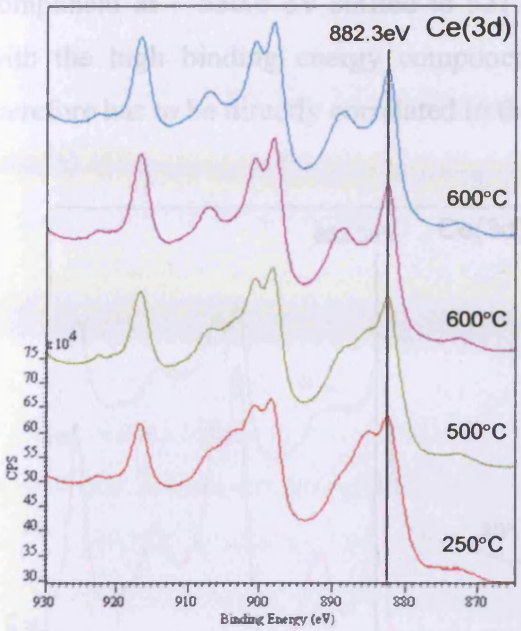

Fig. 3.80: XP spectra of the ceria layer obtained after 3 minutes of Ce dosing in vacuum and after the different oxidation steps. Ce(3d) region shown.

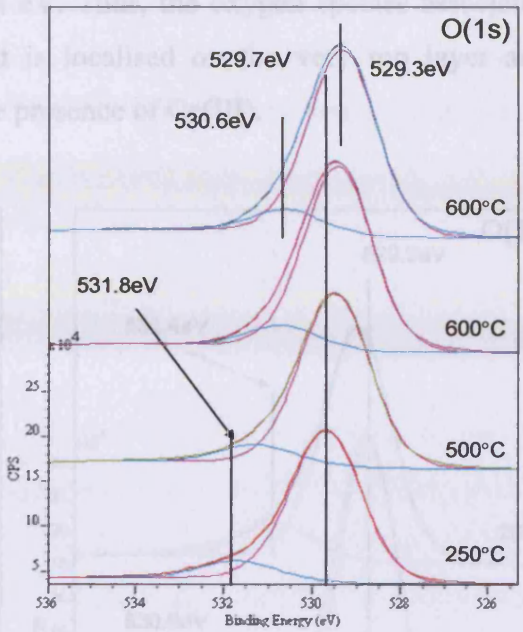

Fig. 3.81: XP spectra of the ceria layer obtained after 3 minutes of Ce dosing in vacuum and after the different oxidation steps. O(1s) region and peaks fittings shown.

Temp/°C	Ce(0)	Ce(III)	Ce(IV)	O/Ce
As prepared	~100	-	-	0.15
RT	~100	-	-	0.17
200	-	61.2	38.8	1.58
250	-	41.1	64.3	1.66
500	-	12.0	88.0	1.80
600	-	8.9	91.1	1.95
600	-	9.0	91.0	2.06

Table 3.9: Relative amount of Ce(0)/Ce(III)/Ce(IV) and O/Ce ratio obtain after each single oxidation step.

A comparison between the XP spectra collected after this last oxygen exposure at normal and grazing incidence (figure 3.82 and 3.83) showed once again that the topmost layer was richer in cations in the +3 oxidation state. From the fitting, the amount of Ce(III) in the spectrum recorded at 20° is almost the 40% of the total Ce(3d) signal. The main O(1s) peak stayed approximately constant, whereas the

component at ~ 530.6 eV shifted to 531.4 eV. Thus, the oxygen species associated with the high binding energy component is localised on the very top layer and therefore has to be directly correlated to the presence of Ce(III).

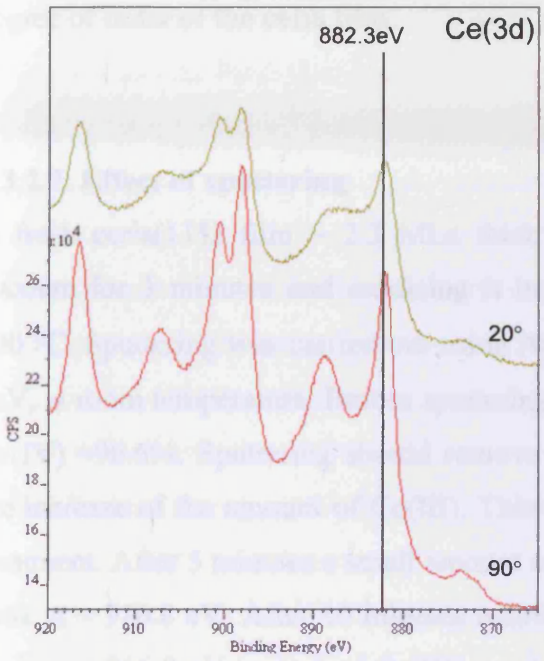

Fig. 3.82: XP spectra of the ceria layer obtained after 3 minutes of Ce dosing in vacuum and after the second oxidation at 600 °C at normal (90°) and grazing (20°) incidence. Ce(3d) region shown.

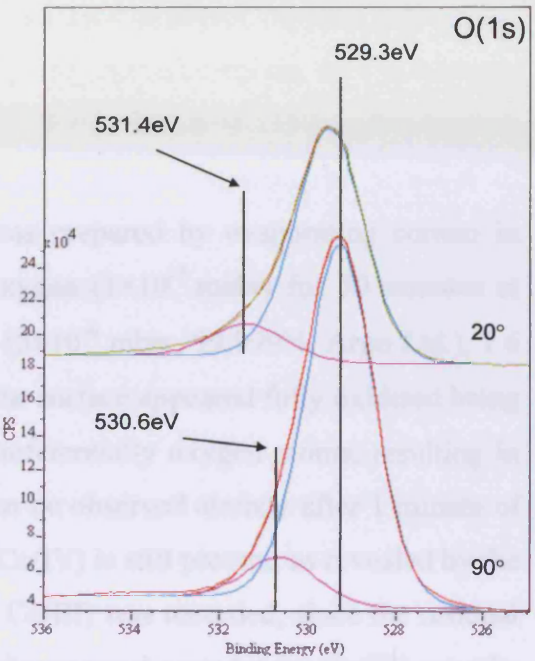

Fig. 3.83: XP spectra of the ceria layer obtained after 3 minutes of Ce dosing in vacuum and after the second oxidation at 600 °C at normal (90°) and grazing (20°) incidence. O(1s) region with peak fitting shown.

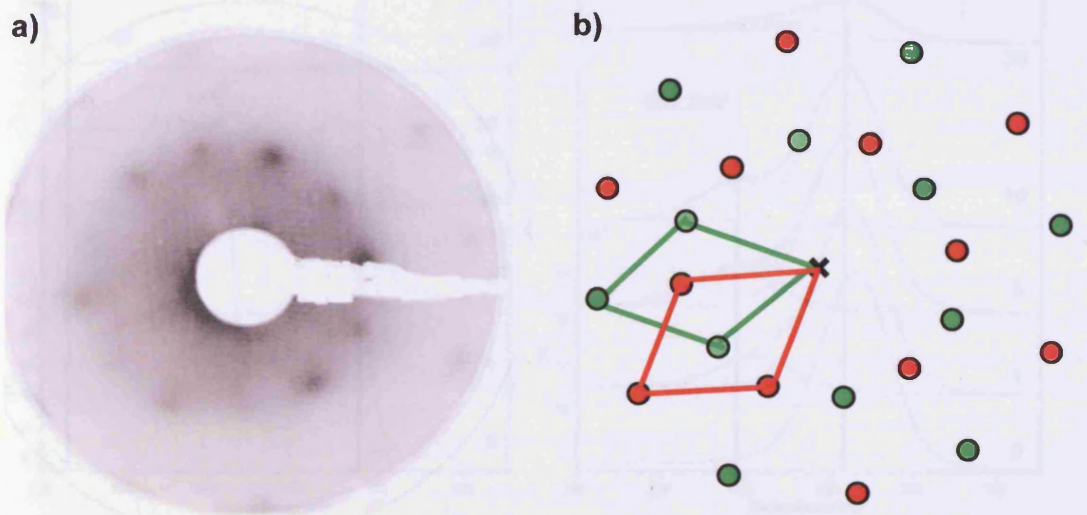

Fig. 3.84: a) LEED pattern (71 eV) recorded after the second oxidation at 600 °C of the layer obtained by dosing cerium for 3 min in vacuum; b) in red and green the spots due to the ceria overlayer in 2 different domains rotated 30° to each other, the cross is the (0,0) spot which is common to both the structure.

After the oxidation treatment at 600 °C a LEED pattern could be recorded (figure 3.84). The spots have to be attributed to the ceria (111) overlayer that appears to be organised in two different domains rotated by 30° with respect to each other. The Cu(111) spots may not be present because of the thickness (~ 2.1 MLe) and the low degree of order of the ceria film.

3.3.2.7. Effect of sputtering

A fresh ceria(111) film ~ 2.3 MLe thick was prepared by evaporating cerium in vacuum for 3 minutes and oxidising it in oxygen (1×10^{-7} mabr) for 30 minutes at 600 °C. Sputtering was carried out using Ar^+ (5×10^{-6} mbar, 99.999%, Argo Ltd.), 1.6 keV, at room temperature. Before sputtering the surface appeared fully oxidised being Ce(IV) ~90.6%. Sputtering should remove preferentially oxygen atoms, resulting in the increase of the amount of Ce(III). This can be observed already after 1 minute of treatment. After 5 minutes a small amount of Ce(IV) is still present, as revealed by the peak at ~ 916.8 eV. After 10 minutes mainly Ce(III) was recorded, since the residual peak at ~ 916.8 eV typical of Ce(IV) nearly disappeared completely. Ce(III) was the only species recorded until the complete disappearance of the cerium signals, after 40 minutes of sputtering (figure 3.85).

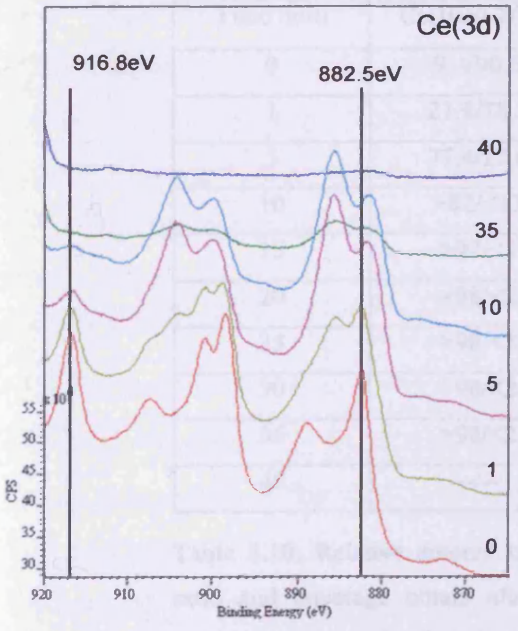

Fig. 3.85: XP spectra describing the sputtering experiment. The numbers indicate the minutes of sputtering. Ce(3d) region shown.

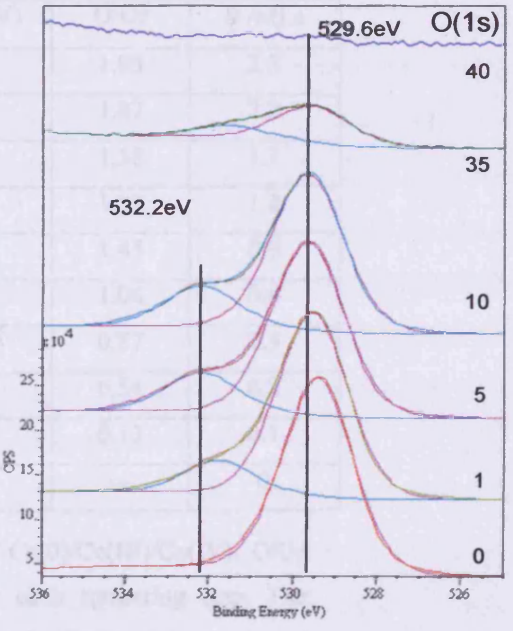

Fig. 3.86: XP spectra describing the sputtering experiment. The numbers indicate the minutes of sputtering. O(1s) region and peaks fittings shown.

The oxygen peak showed a single species on the fully oxidised sample with maximum at 529.4 eV. After sputtering the peak shifted to 529.6 eV and a second component appeared at higher binding energies (532.2 eV). The component at 529.6 eV decreased in intensity during sputtering and its position stay approximately constant (+/- 0.2 eV) (figure 3.86). The component at 532.2 eV appeared initially to increase, up to 10 minutes, when the reduction to Ce(III) was almost complete, then to decrease linearly with the time of sputtering. Once again, the presence of a this higher binding energies oxygen peak associated with the main one accompanies the presence of Ce(III) cations. Table 3.10 shows the coverage, the O/Ce ratio and the Ce(III)/Ce(IV) relative amount recorded after each sputtering treatment. It is assumed that sputtering should preferentially remove oxygen atoms. This is mainly because the very top layer of an oxide is likely represented by an oxygen layer and oxygen atoms have a cross section higher than the cerium atoms (radius of O(-II) ~ 0.126 nm, of Ce(IV) ~ 0.101 nm). Although removing this layer effectively reduces the overall ceria oxidation state after a very short sputtering time, the O/Ce ratio appeared to decrease linearly with the increasing of the time of sputtering (fig 3.87). Therefore, the removal of the very top atomic layer has a significant effect on the stoichiometry of the whole oxide. Interestingly, the only cerium species always present after reduction from Ce(IV) to Ce(III) was Ce(III), meaning a reduction to Ce(0) can not be achieved.

Time /min	Ce(III)/Ce(IV)	O/Ce	ϑ /MLe
0	9.4/90.6	1.93	2.3
1	21.8/78.2	1.87	2.2
5	77.4/22.6	1.58	1.7
10	>82/<13	1.53	1.2
15	>97/<3	1.45	0.9
20	>98/<2	1.06	0.6
25	>98/<2	0.87	0.3
30	>98/<2	0.54	0.2
35	>98/<2	0.13	0.1
40	--/--	---	0

Table 3.10: Relative amount of Ce(0)/Ce(III)/Ce(IV), O/Ce ratio and coverage obtain after each sputtering step. The coverage was calculated evaluating the $Cu(2p_{3/2})$ increase.

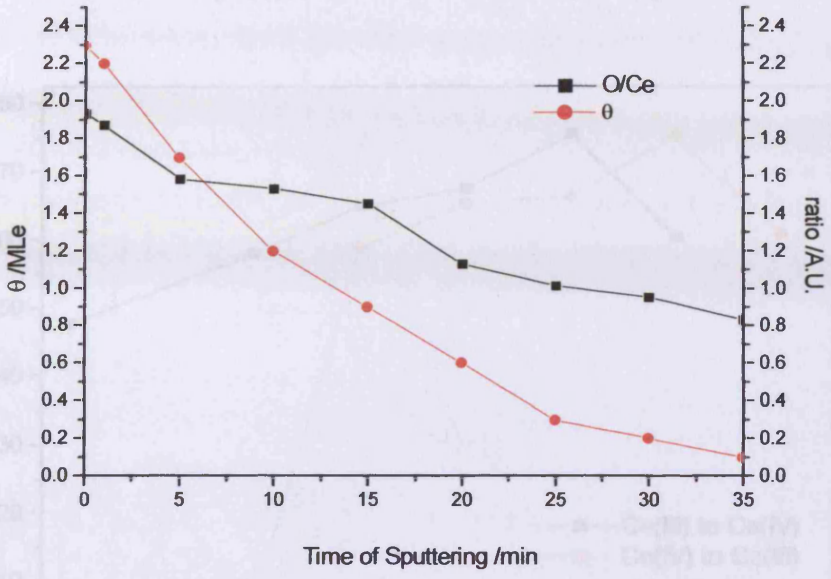

Fig. 3.87: CeO_{2-x} coverage (left vertical axis) and O/Ce ratio (right vertical scale) vs time of sputtering. The O/Ce ratio appears to decrease linearly whereas the coverage decreases with a steeper slope.

3.4. Discussion

3.4.1. Oxygen adsorption on CeO_2(111) single crystal

Oxygen adsorption on CeO_2 single crystal was studied evaluating the change in oxidation state of cerium cations by annealing in vacuum to reduce the crystal and by exposure to oxygen, to oxidise it. From the data summarised in table 3.3, and reported in the diagram in figure 3.88, there is an interval in which approximately the same amount of oxygen can be stored and then removed. This happens for temperatures higher than 300 °C. At room temperature only half of the Ce(III) ions were oxidised to Ce(IV) and the following reduction treatment (annealing at 200 °C in vacuum) did not alter significantly the chemical composition of the system. At 200 °C approximately 60% of the Ce(III) cations can be oxidised and subsequently reduced. The experiments undertaken at 300 °C and 400 °C showed that approximately the 70% can be oxidised and successively reduced. Exposure to oxygen at 500 °C oxidises the 75% of the cerium atoms that can be reversely reduced. At this

temperature the maximum conversion was obtained, in fact, oxidation at 600 °C showed a conversion of only ~60% and was followed by complete reduction.

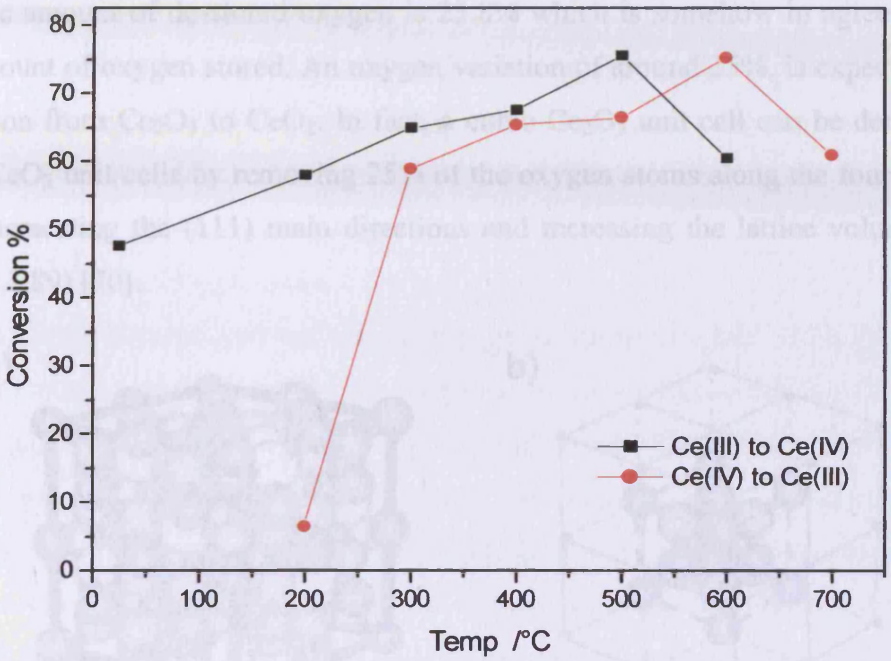

Fig. 3.88: Degree of oxidation of Ce(III) to Ce(IV) and degree of reduction of Ce(IV) to Ce(III) vs Temperature at which the experiments have been undertaken. See section 3.3.1.2 b) for details.

An explanation for this behaviour lays in an activation energy barrier that needs to be overcome for oxidation to occur at lower temperatures. The activation barrier is probably higher for reduction, as it was necessary to heat the system at least to 300 °C, for it to occur. At 500 °C oxidation extent reaches its maximum, then decreases. This could be due to competitive oxygen desorption, enhanced at these conditions.

The average amount of oxygen stored counts for the 25.5% of the total O(1s) XP peak, value which is in agreement with the one expected for the full conversion from Ce_2O_3 to CeO_2 [69]. Although oxygen adsorption does not appear to alter the profile of the O(1s) XP peak, which stays as a singlet, a binding energy shift is observed. This means that XPS reveals a single oxygen species in bulk ceria. Nevertheless, sometimes a peak at lower binding energies attributed by comparison with the literature [64] to oxygen in the lattice with a stronger ionic character may be present. Also after exposure XPS reveals only one oxygen environment, meaning the adsorbed oxygen (revealed by the increase of the total O(1s) integral) should be chemically equivalent to the one present in the oxide. On a reduced surface the oxygen peak

maximum occurs in the 530.8 - 531.2 eV energy range, whereas on an oxidised surface it is recorded at ~ 529.6 eV. A similar behaviour was observed by Mullins and co-workers [50], however, they recorded only a moderate shift (~ 0.4 eV). The average amount of de-stored oxygen is 23.8% which is somehow in agreement with the amount of oxygen stored. An oxygen variation of around 25%, is expected for the transition from Ce_2O_3 to CeO_2. In fact, a cubic Ce_2O_3 unit cell can be derived from eight CeO_2 unit cells by removing 25% of the oxygen atoms along the four diagonals non-intersecting the (111) main directions and increasing the lattice volume by 3% (figure 3.89) [70].

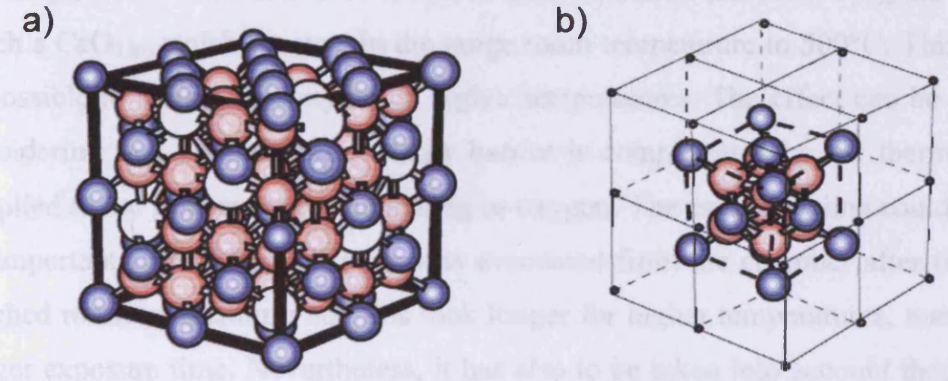

Fig. 3.89: Lattice unit cells for Ce_2O_3 (*C*-type) (a) and CeO_2 (b). A cubic unit cell of *C*-type Ce_2O_3 can be obtained from eight CeO_2 unit cells by increasing their volume by 3% and removing 25% of the oxygen atoms along four diagonals non-intersecting the (111) main directions. Blue, red, and white spheres indicate the cerium, oxygen atoms, and vacancies, respectively. From ref [70].

Up to now the reduction was considered in conjunction with removal, de-storage of oxygen from an oxidised system. However, there is another way for reduction to occur, without oxygen de-storage. Oxygen removal at relatively low temperatures is in fact in contrast with what was reported by Putna and co-workers [71, 72]. They observed from TPD studies that there is no substantial desorption of oxygen from a CeO_2(111) single crystal below ~ 1030 °C, although between 530 and 1000 °C an oxygen desorption could be recorded on ceria thin films initially exposed to oxygen. However, a TPD experiment is normally undertaken in a very short time, so in a completely different experimental condition. On the other hand, the high oxygen exchange could be justified because of the high mobility of the oxygen ions, which appears to be enhanced at temperatures higher than 270 °C [73]. Unfortunately, in the

present case, TPD experiments could not be performed because the system was not equipped with this facility. Studying a CeO_x/Pd(111) system Alexandrou and co-workers [35] made very similar observation: annealing thick films at high temperatures cause the disappearance of both cerium and oxygen peaks from their XP spectra. This was interpreted as decomposition of the oxide with both cerium and oxygen diffusing into the bulk palladium at a different rate. Oxygen was reported to diffuse subsurface firstly, hence reduction of the ceria layer, and subsequently into the bulk palladium. The loss of oxygen will then destabilise the oxide and trigger cerium incorporation into the palladium.

Looking at the stoichiometry of the oxide after oxidation (see table 3.3), the oxide can reach a $CeO_{1.86}$ stoichiometry, in the range room temperature to 500°C. This means it is possible to store more oxygen at higher temperatures. The effect can be explained considering that the activation energy barrier is compensated by the thermal energy supplied to the system during annealing in oxygen. The exposure time could also play an important role; in fact, oxygen was evacuated from the chamber after the sample reached room temperature and this took longer for higher temperatures, resulting in a longer exposure time. Nevertheless, it has also to be taken into account that diffusion rate is in general limited at lower temperatures. Therefore, diffusion and activation energy barrier can play a synergistic role.

Since complete oxidation could not be achieved, this means that a substantial amount of Ce(III) was always present. It is accepted that a Ce_2O_3 layer is present on the topmost layers of a CeO_2 film. Therefore, if the top layer is comprised of Ce(III) mainly, oxygen penetration through the surface, followed by migration into the bulk, thus without changing the oxidation state of the topmost layer has to be acknowledge, in order change the overall oxidation state as revealed by XPS. This conclusion does not surprise, since experimentally cerium cations are reported to be essentially immobile with respect to diffusion into the bulk for temperatures up to ~ 630 °C. On the contrary, oxygen appears to diffuse into the bulk at around 270 °C [73]. The re-oxidation process can be represented as follows [71]:

$$O_{2\,gas} \rightarrow O^-_{2\,ads} \rightarrow O^{2-}_{2\ ads} \rightarrow 2O^-_{ads} \rightarrow 2O^{2-}_{2\ lattice} \qquad \ldots(3.20)$$

As the temperature increases, the superoxide ion, produced by oxygen adsorption on an electron rich vacancy, converts into peroxide. These vacancies may be produced by mild annealing at temperature lower than 200 °C. The peroxide decomposes in two oxide ions which will penetrate the surface and migrate into the bulk becoming lattice oxygen. The total effect can be considered as re-oxidation of the bulk. Note that all the oxygen species mentioned in equation 3.20, the gas molecule and the lattice oxide ion excepted, are probably transient species and therefore they have a very short lifetime. Although is very unlikely to be able to record their presence with XPS at room temperature, they have been observed via Raman spectroscopy [74] and low temperature EPR investigation [75].

A final comment about reduction of ceria surfaces has to take into account the effects of the X-rays in the surface during collection of XPS spectra. It has been shown by Paparazzo and co-workers [59] that a prolonged X-ray exposure (300 minutes) can induce reduction on high purity commercial CeO_2 pellets. In the present case this effect was not considered, since the total time necessary to collect a full set of scans was around 45 minutes.

3.4.2. Preparation of CeO_{2-x}/Cu(111) films

One of the reasons to prepare insulating layers on conductive materials is to improve the conductivity of the insulator, mainly for STM purposes, and being able to minimise charging effects (for XPS). Choosing the appropriate substrate allows to epitaxially grow the insulating film on an oriented metallic substrate. Ceria layers were prepared in the past on several substrates Pd(111) [35], Rh(111) [36 – 38, 76], Ru(0001) and Ni(111) [39], and Pt(111) [40 – 44, 77], using essentially two different preparation procedures:

- evaporation of cerium in vacuum keeping the substrate at room temperature followed by low [35, 40] or high temperature oxidation [41, 42];
- evaporation of cerium in oxygen background pressure keeping the substrate at relatively high temperatures (600 – 700 K) [36, 39, 44].

In the present case, ceria layers were prepared on a Cu(111) single crystal, because of the favourable ratio, 1.5, between the unit cells of CeO_2(111), 0.382 nm, and Cu(111), 0.255 nm. Only one work related to the study of ceria overlayers on copper single crystal was found in the literature. Siokou and Nix [78] prepared well-defined ceria

surfaces in order to study methanol adsorption. They prepared their films by cerium evaporation at room temperature, followed by oxidation at room temperature obtaining unordered films. In order to obtained a LEED pattern they annealed up to 700 K.

A different preparation recipe was used in the present work, since cerium was mainly evaporated in high oxygen background pressure (5×10^{-7} mbar), keeping the copper crystal at 300 °C. In this way ordered films could be prepared, since a LEED pattern could be observed. The orientation of the ceria overlayer can not be determined by analysing the LEED pattern only. In fact, $CeO_2(111)$ and $Ce_2O_3(0001)$ have both hexagonal structure and a very close lattice constant, 0.382 nm for CeO_2 and 0.388 nm for Ce_2O_3. Xiao and co-workers [79], studying the transition of stoichiometric $CeO_2(111)$ prepared on Re(0001) to stoichiometric $Ce_2O_3(0001)$, suggested a 30° rotation of one LEED pattern with respect to the other. This criterion alone, however, does not appear to be adequate, since different rotational domains and non stoichiometricity were observed during the experiments. A discriminating factor is nevertheless the O/Ce atomic ratio. During the experimental work, a O/Ce of 1.5, typical of the sesquioxide was rarely obtained; however, even if the stoichiometry was normally closer to the one expected for the oxide, also a O/Ce of 2 was not very often seen, therefore, the films were indicated as $CeO_{2-x}(111)/Cu(111)$. The formation of Ce/Cu alloys was not observed [80], likely because the cerium vapours were reacting readily with oxygen, before landing on the copper substrate, thus limiting the time in which the two metals could have intermixed.

It has also been found that the CeO_x overlayer oxidation state strongly depends upon oxygen partial pressure during preparation. As summarised in table 3.11, the main oxidation state for the cerium cations was 0 dosing cerium in vacuum. Dosing in oxygen pressure resulted in a larger amount of cerium 3+ dosing in low pressure (5×10^{-8} mbar) than at high oxygen pressures (5×10^{-7} mbar).

P_{O2} /mbar	Ce(0)	Ce(III)	Ce(IV)
5×10^{-7}	--	<15	>85
5×10^{-8}	--	~25	~75
vacuum	>99	<1	--

Table 3.11: Different cerium oxidation states observed during preparation with different oxygen background pressures.

3.4.3. Oxygen adsorption on CeO_{2-x}(111) films on Cu(111)

In general the effect of annealing in vacuum is a decrease in the O(1s) XP signal and a decrease of the O/Ce ratio is observed, whereas, when annealing is performed in oxygen atmosphere, oxygen normally adsorbs and the O/Ce ratio increases.

Dependent upon the film thickness two different situations can present: below 2.6 MLe the films tend to exchange a large amount of oxygen, often more than the theoretical decrease of 25% expected to convert CeO_2 to Ce_2O_3 [70]. Over 3.21 MLe the films appear more difficult to oxidise/reduce, since the oxygen variation recorded is only few percent.

In general the larger oxygen variation happens when a Cu(111)-(1.5×1.5)CeO_{2-x}(111) is present, and even more when the structure is Cu(111)-(1.5×1.5)CeO_{2-x}(111)R+/-26°. When this LEED pattern is present, the CeO_x overlayer grows in different crystallites, on the Cu(111) crystal. Some of the CeO_x areas are oriented along the <111> main directions, some other are rotated +/-26° in respect of them (see model in figure 3.63). When the film grows along the main <111> directions, 2/3 (66%) of the oxygen layer between cerium and copper sits on 2-fold sites and the remaining 1/3 (33%) is directly on top of the copper atoms (see model in figure 3.41). At low coverage, when the 26° rotation is observed, the 15% of the oxygen atoms are on 3-fold sites, the 55% in 2-fold sites and the remaining 30% directly on top of a copper atom. In terms of energy minimisation, the stability of the sites goes as 3-fold > 2-fold > a-top. Since their ratio is approximately the same in both cases, the a-top atoms count for the same extent. Because of the increase in 3-fold sites, the rotated lattice should be more stable than the aligned one. At high coverage only the aligned lattice is observed, therefore it appears to be the more stable structure. The high oxygen mobility recorded at low coverage could depend upon the intrinsically lower stability of the rotated lattice. This could also explain why a full oxidised stoichiometry ($CeO_{2.02}$) could be observed only after preparing the 0.26MLe film, initially unordered, but showing the (1.5×1.5)R+/-26° pattern after annealing in oxygen. Full oxidation could also be achieved as a result of the preparation in vacuum, but in this case the LEED showed a superimposition of a CeO_2(111) (1×1) and (1×1)R30° patterns (figure 3.84). Moreover, with the +/-26° rotated structure, more grain boundaries should be present between the crystal phases; these could represent more reactive, low coordination sites at which oxygen can be easier exchanged with the surrounding.

3.4.4. Nature of the O(1s) high binding energy peak

In the present work, several binding energies were recorded for the oxide oxygen in ceria. From the single crystal work, ceria was found to be characterised by an O(1s) XP peak around 531.2 - 530.8 eV for the oxide rich in Ce(III) and at lower binding energies, 529.8 - 529.4 eV for a Ce(IV) rich system. Although the previous values were in good agreement also for the thin films prepared on Cu(111), from time to time, a higher binding energy component at around 532.2 eV was observed.

The presence of the component at higher binding energies in the oxygen peak for reduced ceria has already been taken in account from different authors. Some attributed it to the presence of carbonate species formed by the oxygen removed by the Ar^+ ions and some carbon already present on the surface [81]. The presence of carbonates has only partially been confirmed in the present set of experiments. Since cerium has one of is XP transition, the 4s, at 290 eV, there are some difficulties in recording a carbonate signal. Other authors, analysing reduced ceria prepared by wet methods, related the peak to the presence of OH groups that disappeared after calcination [82]. They also proposed the hypothesis that these groups could be formed by reaction with the residual water gas present inside the system. The possibility of lack of structural homogeneity at the grain boundaries of CeO_2 particles has been invoked by other research groups [48]. In the present work, the oxygen high binding energy peak was not only observed during sputtering, but also preparing the ceria thin films in particular when dosing cerium at low oxygen pressure (5×10^{-8} mbar) and in vacuum. When cerium was dosed at a higher oxygen pressure (5×10^{-7} mabr), this component appeared present as a tail to the high binding energy side of the O(1s) peak only at grazing emission. Taking all these considerations into account, it appears that this component is likely an intrinsic characteristic of defective Ce_2O_3 and may represented an oxygen atom with a negative charge < -2. In this case electron delocalisation has to be considered over a cluster of atoms. Kang *et al.* [83] proposed that this particular oxygen species is due to the existence of a superstructure for fluorite-type oxides, as CeO_2, on the basis of neutron and electron diffraction data and identify a "coordination defect". As sputtering preferentially removes oxygen atoms, in principle this can create a defect rich and unordered CeO_{2-x} film. This defect is described as a tetrahedron of cerium cations that encloses a vacant oxygen site with six neighbour oxygen atoms with an overall double positive charge, $[Ce_4O_6]^{2+}$ units. If we consider the cerium cations in the +3 oxidation state, this means the overall charge

on each of the oxygen atoms is ~-1.67, although distribute in the whole cluster. Nevertheless, for the defect to give a net contribution at higher binding energies (therefore with a "very low" negative charge, -1 or less [84]), a localised state is more likely to be present and it may be represented by the vacant site. In this case, considering all the oxygen atoms of the cluster to be doubly negatively charged, the vacant site would have neutral charge. Therefore the negative charge on the oxygen has to vary between 0 and -2 depending upon the case. Although this seems unlikely, Kang *et al.* say that appropriate combinations of this defective unit can explain the structures of the whole range of cerium oxides form CeO_2 to Ce_2O_3. Holgado *et al.* [46] studied the characteristics of this second component, calling it "lateral", O_{lat}. They attributed the O_{lat} peak to the presence of oxides ions at the exposed surface in their CeO_2 original film, become defective, hence CeO_{2-x}, due to the action of Ar^+ sputtering. The bombardment removes preferentially oxygen atoms, creating a large amount of oxygen vacancies. This was evident during the experiment performed in this work, since it was observed that the high binding energy component appeared when cerium 3+ was formed by sputtering a ceria layer rich in cerium 4+ and increased linearly with the decrease of the amount of cerium 4+ (figures 3.85 and 3.86).

The attribution of this so-called O_{lat} peak to oxygen defects, when generated by sputtering, creating an increased degree of disorder on the surface, is also supported by the LEED analysis. Even if numerous attempts to collect a pattern have been made, none had been obtained, although in this case reordering of the surface would have been necessary.

In summary, the high binding energy O(1s) component is considered as an intrinsic feature correlated with the Ce(III) cation and, from grazing emission XPS, it appeared that it is localised on the very top layers of the ceria films, at the solid-vacuum interface.

3.4.5. LEED patterns and coverage

Differently organised CeO_x layers giving rise to different LEED patterns were observed during the preparation of the layers in high oxygen pressure (5×10^{-7} mbar). After preparation, depending upon the coverage, the CeO_x layers were unordered, for

coverage up to 1.1 MLe, then a Cu(111)-(1.5×1.5)CeO_{2-x}(111) was observed for coverage up to 4 MLe. Over 4MLe only the pattern for CeO_{2-x}(111) could be observed. For low coverages, the attempt to order the ceria overlayer resulted in a faint hexagonal halo or a mixture of Cu(111)-(1.5×1.5)CeO_{2-x}(111) and Cu(111)-(1.5×1.5)CeO_{2-x}(111)R+/-26°. For higher coverage, although the coverage determined by XPS was in general decreasing with the annealing, the patterns tend to stay the same as after preparation. A change in pattern, from Cu(111)-(1.5×1.5)CeO_{2-x}(111) to CeO_{2-x}(111) (1×1) was observed for the ~ 2.6 MLe thick layer when annealing it in oxygen. The LEED patterns observed are summarised in figure 3.90.

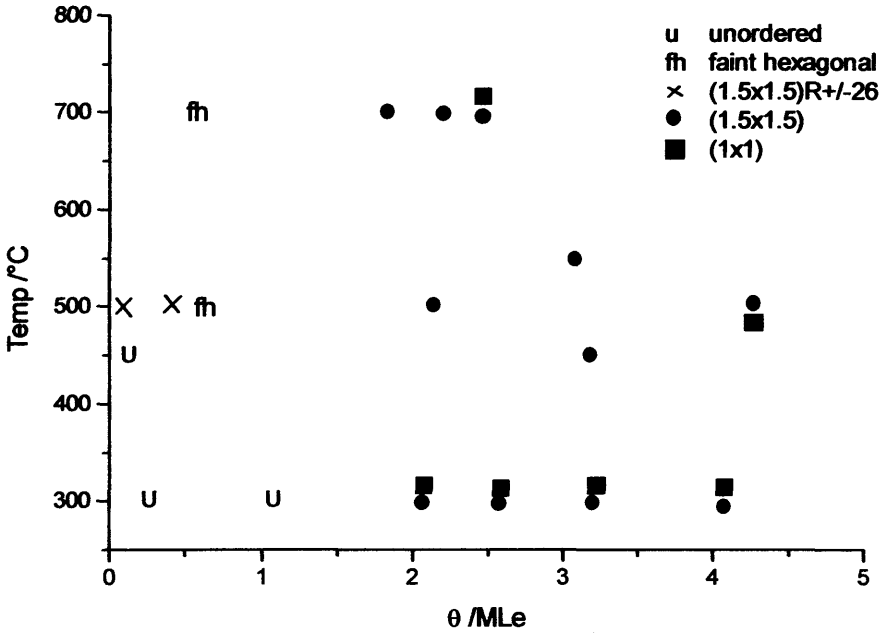

Fig. 3.90: LEED patterns collected obtained for the preparation in high oxygen pressure (5×10^{-7} mabr) at different temperatures.

The most commonly pattern observed by LEED, the Cu(111)-(1.5×1.5)CeO_{2-x}(111) pattern, shows an epitaxial relationship between the Cu(111) crystal and the CeO_{2-x}(111) overlayer. In fact the ceria spots appeared aligned with the Cu(111) spots and the ratio between their lattices vectors stays in the ratio expected (see figure 3.41 for example). Since at low coverage the CeO_x domains rotated by +/-26° in respect of the main <111> direction appear to form, other patterns may also present. In this case (see figure 3.74) the spots related to the aligned (1.5×1.5) are sharper and better defined

than the one belonging to the (1.5×1.5)R+/-26°, meaning that the domains with a rotated structure are probably less extended and less ordered than the aligned ones.
No LEED patterns were observed after cerium dosing for both the preparation at low oxygen pressure (5×10^{-8}mbar) and in vacuum. Faint hexagonal patterns appeared after oxidation of these layers, suggesting the presence of a (1×1) pattern likely due to ceria and the Cu(111) spots could not be observed. For the preparation in vacuum a pattern described as CeO_{2-x}(111) (1×1) + (1×1)R30° was likely present (see figure 3.84).

3.5. Conclusions

An introduction to the Oxygen Storage Capacity (OSC) of ceria was given, considering firstly the structures of unreduced and reduced, unrelaxed and relaxed ceria low index surfaces (111), (110) and (100). All theoretical studies agree in the order of surface energy as follows: (111) > (110) > (100), while the extent of surface relaxation is in the opposite order. The main defect present on ceria is oxygen vacancy which is believed to be correlated to the oxygen partial pressure surrounding the oxide. Oxygen mobility is responsible for the OSC and for the presence of intrinsic defects, which play an important role in heterogeneous catalysis. Ceria (111) single crystal and thin ceria films on transition metal have successfully been resolved at atomic level from different groups.
The CeO_2(111) single crystal has revealed to be of very hard to work with, mainly because of the difficulty in obtaining a smooth and clean surface. Although conductivity could not be induced to the crystal to the extent of been able to use successfully the STM technique, it was possible to study its reaction with oxygen. By exposure of the crystal to oxidation / reaction condition, a certain extent of oxidation / reduction of the surface was achieved.
CeO_{2-x}(111)/Cu(111) ordered films were successfully prepared and the epitaxial relationship between the two verified. Oxygen exposure experiments showed that the films behave in two different ways, depending upon their thicknesses: below 2.62 MLe the films tend to exchange a large amount of oxygen, often more than the theoretical 25% expected to covert CeO_2 to Ce_2O_3. Over 3.21MLe the films appeared

more difficult to oxidise/reduce, since the oxygen variation recorded was only a few percent.

It has also been found that the CeO_x overlayer oxidation state depends upon oxygen partial pressure during preparation. The main oxidation state for the cerium cations was 0, for dosing cerium in vacuum, 3+, for dosing in low oxygen pressure and 4+ at high oxygen pressures

The layers prepared are normally unordered at low coverage (less than 1 MLe) and the LEED showed ordered patterns at higher coverages. Although the surface sinters upon annealing, the LEED does not seem to change, meaning a strong epitaxial relationship with the substrate is present.

3.6. References

1. S.N. Jacobsen, U. Helmersson, R. Erlandsson, B. Skårman, L.R. Wallenberg, *Surf. Sci.*, 429, 1999, 22
2. M. Mogensen, N.M. Sammes, G.A. Tompsett, *Solid State Ionics*, 129, 2000, 63
3. Y. Namai, K. Fuki, Y. Iwasawa, *J. Phys. Chem. B*, 107, 2003, 11666
4. E. Mamonton, T. Egami, R. Brezny, M. Koranne, S. Tyagi, *J. Phys. Chem. B*, 104, 2000, 11110
5. T.X.T. Sayle, S.C. Parker, C.R.A. Catlow, *Surf. Sci.*, 316, 1994, 329
6. P.W. Tasker, *J. Phys. C: Solid State Phys.*, 12 , 1979, 4977
7. J.C. Conesa, *Surf. Sci.*, 339, 1995, 337
8. M. Baudin, M. Wójcik, K. Hermansson, *Surf. Sci.*, 468, 2000, 51
9. N. V. Skorodumova, M. Baudin, K. Hermansson, *Phys. Rev. B*, 69, 2004, 075401
10. Z. Yang, T.K. Woo, M. Baudin, K. Hermansson, *J. Chem. Phys.*, 120, 2004, 7741
11. A. Gotte, M. Baudin, K. Hermansson, *Surf. Sci.*, 552, 2004, 273
12. Y. Jiang, J.B. Adams, M. van Schilfgaarde, *J. Chem. Phys.*, 123, 2005, 064701
13. M. Nolan, S. Grigoleit, D.C. Sayle, S.C. Parker, G.W. Watson, *Surf. Sci.*, 576, 2005, 217
14. S.H. Overbury and D.R. Mullins, in A. Trovarelli, *Catalysis by Ceria and Related Materials*. Imperial College Press ed. Catalytic Science, ed. G.J. Hutchings. 2001, 311

15. J. Kašpar, P. Fornasiero, M. Graziani, *Catal. Today*, 50, 1999, 285
16. M. Ozawa, C.-K. Loong, *Catal. Today*, 50, 1999, 329
17. M. Boaro, M. Vicario, C. de Leitenburg, G. Dolcetti, A. Trovarelli, *Catal. Today*, 77, 2003, 407
18. A. Trovarelli, M. Boaro, E. Rocchini, C. de Leitenburg, G. Dolcetti, *J. Alloys and Compounds*, 323-324, 2001, 584
19. M. Bowker, *The Basis and Applications of Heterogeneous Catalysis*, Oxford University Press, 1998.
20. N.N. Bulgakov, V.A. Sadykov, V.V. Lunin, E. Kemnitz, *React. Kinet. Catal. Lett.*, 76, 2002, L103
21. D. Xu, Q. Wang, Y. Tang, Z. Lu, Z. Liu, S. Liu, G. Zhang, W. Su, *J. Phys.: Condens. Matter*, 14, 2002, 11265
22. W.J. Stark, M Maciejewski, L. Mädler, S.E. Pratsinis, A. Baiker, *J. Catal.*, 220, 2003, 35
23. P. Knauth, H.L. Tuller, *Solid State Ionics*, 136-137, 2000, 1215
24. H. Nörenberg, G.A.D. Briggs, *Phys. Rev. Lett.*, 79 (21), 1997, 4222
25. H. Nörenberg, G.A.D. Briggs, *Surf. Sci.*, 402-404, 1998, 734
26. H. Nörenberg, G.A.D. Briggs, *Surf. Sci.*, 424, 1999, L352
27. H. Nörenberg, G.A.D. Briggs, *Surf. Sci.*, 433-435,1998, 127
28. H. Nörenberg, J.H. Hardimg, *Surf. Sci.*, 477, 2001, 17
29. K. Fukui, Y. Namai, Y. Iwasawa, *App. Surf. Sci.*, 188, 2002, 252
30. Y. Namai, K. Fuki, Y. Iwasawa, *J. Phys. Chem. B*, 107, 2003, 11666
31. Y. Namai, K. Fuki, Y. Iwasawa, *Cat. Today*, 85, 2003, 79
32. K. Fukui, S. Takakusagi, R. Tero, M. Aizawa, Y. Namai, Y. Iwasawa, *PCCP*, 5, 2003, 5349
33. Y. Namai, K. Fuki, Y. Iwasawa, *Nanothechnology*, 15, 2004, 549
34. F. Esch, S. Fabris, L. Zhou, T. Montini, C. Africh, P. Fornasiero, G. Comelli, R. Rosei, *Science*, 309, 2005, 752
35. M. Alexandrou, R. M. Nix, *Surf. Sci.*, 321, 1994, 47
36. S. Eck, C. Castellarin-Cudia, S. Surnev, K.C. Prince, M.G. Ramsey, F.P. Netzer, *Surf. Sci.*, 536, 2003, 166
37. S. Eck, C. Castellarin-Cudia, S.Surnev, M.G. Ramsey, F.P. Netzer, *Surf Sci.*, 520, 2002, 173
38. D.N. Belton, S.J. Schmieg, *J. Vac. Sci. & Techn. A*, 11, 1993, 2330

39. D.R. Mullins, P.V. Radulovic, S.H. Overbury, *Surf. Sci.*, 429, 1999, 186
40. C. Hardacre, G.M. Roe, R.M. Lambert, Surf. Sci., 326 ,1995) 1
41. U. Berner and K.-D. Schierbaum, *Phys. Rev. B*, 65, 2002, 235404
42. U. Berner, K. Schierbaum, *Thin Solid Films*, 400, 2001, 46
43. U. Berner, K. Schierbaum, G. Jones, P. Wincott, S. Haq, G. Thornton, *Surf. Sci.*, 467, 2000, 201
44. K.-D. Schierbaum, *Surf. Sci.*, 399, 1998, 29
45. J. Zarraga-Colina, R.M. Nix, H. Weiss, *Surf. Sci. Lett.*, 563, 2004, L251
46. J.P. Holgado, G. Munuera, J.P. Espinos, A.R. Gonzalez-Elipe, *App. Surf. Sci.*, 158, 2000, 164
47. P. Burroughs, A. Hamnett, A.F. Orchard, G. Thornton, *J. Chem. Soc Dalton Trans.*, 17, 1976, 1686
48. M.V. Rama Rao, T. Shripathi, *J. Electr. Spec. Rel. Phen.*, 87, 1997, 121
49. A. Laachir, V. Perrichon, A. Badri, J. Lamotte, E. Catherine, J.C. Lavalley, J. Al Fallah, L. Hilaire, F. le Normand, E Quemere, G.N. Sauvion O. Touret, *J. Chem. Soc, Fraday Trans.*, 87 (10), 1991, 1601
50. D.R. Mullins, S.H. Overbury, D.R. Huntley, *Surf. Sci.*, 409, 1998, 307
51. J.P. Holgado, R. Alvarez, G. Munuera, *App. Surf. Sci.*, 161, 2000, 301
52. F. Zhang, P. Wang, J. Koberstein, S. Khalid, S-W. Chan, *Surf. Sci.*, 563, 2004, 74
53. X-ray Photoelectron Spectroscopy Database 20, Version 3.0, National Institute of Standards and Technology, Gaithersburg, MD
54. R.M. Nix, private communication
55. S. Tsunekawa, T. Fukuda, A. Kasuya, *Surf. Sci.*, 457, 2000, L437
56. R. Vercaemst, D. Poelman, R.L. Van Meirhaeghe, L. Fiermans, W.H. Leflère, F. Cardon, *J. Lumin.*, 63, 1995, 19
57. Yu.A. Teterin, A.Yu. Teterin, A.M. Lebedev, I.O. Utkin, *J. Elec. Spect. Rel. Phen.*, 88-91, 1998, 275
58. G. Praline B.E. Koel, R.L. Hance, H.I. Lee, J.M. White, *J. Elec. Spect. Rel. Phen.*, 21, 1980, 17
59. E. Paparazzo, G.M. Ingo, N. Zacchetti, *J. Vac. Sci. Technol. A* , 9 (3), 1991, 1416
60. **CasaXPS software demo version downloadable at** http://www.casaxps.com
61. **WSxM free software downloadable at** http://www.nanotec.es
62. Veeco Nanoscope Software, version 6R3, Veeco 2006

63. H Weiss, private communication
64. Z. Ma, Y.N. Qin, X.Z. Qi, F, He, *Chinese Chem. Lett.*, 10 (12), 1999, 1049
65. S. Tanuma, C. J. Powell, D. R. Penn, *Surf. Interf. Anal.*, 21, 1994, 165
66. www.lasurface.com, web-based XPS database.
67. J.F. Moulder, W.F. Stickle, P.E. Sobol, K.D. Bomben in: J. Chastain ,Ed.), *Handbook of X-ray Photoelectron Spectroscopy*, Physical Electronics, Eden Prairie, MN, 1992.
68. S. Poulston, P.M. Parlett, P.Stone, M. Bowker, *Surf. Interf. Anal.*, 24, 1996, 811
69. L. Saraf, V. Shutthanandan, Y. Zhang, S. Thevuthasan, C.M. Wang, A. El-Azab, D.R. Baer, *J. App. Cat.*, 96 (10), 2004, 5756
70. N.V. Skorodumova, S.I. Simak, B.I. Lundqvist, I.A. Abrikosov, B. Johansson, *Phys. Rev. Lett.*, 89 (16),2002, 166601-1
71. E.S. Putna, J.M. Vohs, R.J. Gorte, *J. Phys. Chem.*, 100, 1996, 17862
72. E.S. Putna, J.M. Vohs, R.J. Gorte, *Cat. Lett.*, 45, 1997, 143
73. C.L. Perkins, M.A. Henderson, C.H.F. Peden, G.S. Herman, *J. Vac. Sci. Thecnol. A*, 19 (4), 2001, 1942
74. V.V. Pushkarev, V.I.Kovalchuk, J.L. d'Itri, *J. Phys. Chem. B*, 108, 2004, 5341
75. J. Soria, A. Martinez-Arias, J.C. Conesa, *J. Chem. Soc. Faraday Trans.*, 91(11), 1995, 1669
76. E.L. Wilson, PhD Thesis, University College London, 2006
77. E.L. Wilson, W.A. Brown, G. Thornton, *Surf. Sci.*, 600, 2006, 2555
78. A. Siokou, R.M. Nix, *J. Phys. Chem. B*, 103, 1999, 6984
79. W. Xiao, Q. Guo, E.G. Wang, *Chem. Phys. Lett.*, 368, 2003, 527
80. N.A. Braaten, K.J. Grepstad, S. Raaen, *Phys. Rev. B*, 40, 1989, 7969
81. E. Paparazzo, *Surf. Sci. Lett.*, 234, 1990, L253
82. E. Abi-aad, R. Bechara, J. Grimblot, A. Aboukais, *Chem. Mater.*, 5, 1993, 793
83. Z.C. Kang, L. Eyring, *J. Alloys Compd.*, 206, 1997, 249
84. J.-C. Dupin, D. Gonbeau, P. Vinatier, A. Levasseur, *PCCP*, 2, 2000, 1319

Chapter 4

Surface Studies of oxidised barium layers for NO_x storage

This chapter presents experiments undertaken to improve the knowledge about the preparation of storage medium layers for NO_x Storage and Reduction (NSR) catalysis. The first part gives an overview of the topic, including proposals for the mechanism of NSR, the effect of the storage medium used (BaO_x) and the previous work undertaken within the group. In the second part, results related to the structural and reactivity study of BaO_x layers on a Pt(111) single crystal will be presented. Finally, results of gas mixtures (NO/O_2, $NO + O_2$) dosing experiments performed in collaboration with Queen Mary University of London on BaO/Cu(111) will be presented.

4.1. Introduction

Since the establishment of very severe emission control standards in the 1970s, catalytic converters have been developed for automobile emission control. Today the catalysts are fully established as the emission control device for gasoline engine vehicles. When a vehicle equipped with a catalyst is started at a low temperature, a large amount of hydrocarbons (HC) is emitted because the catalyst is not active at low temperature. Thus quick warm-up of the catalyst is necessary to reduce the HC emission. This can be realized by reducing the catalytic converter volume and positioning it close to the engine. On the other hand NO_x is emitted even after the catalyst is activated. An additional catalyst is necessary to supplement the TWC performance [1]. Further, the demand to improve the fuel efficiency of vehicles and the need to decrease their associated CO_2 emissions has led to the introduction of lean-burn engine technology, where the engine is operated in the presence of excess oxygen. This type of engine operation can reduce the fuel consumption and provide

more efficient combustion in comparison with stoichiometric operating conditions. The increased combustion efficiency reduces the amounts of CO_2, CO and hydrocarbons emitted during driving, and hence more fuel is directly converted into useful energy. Unfortunately, the presence of excess oxygen under lean-burn conditions renders the catalytic reduction of NO_x difficult. A variety of strategies are currently being investigated to rectify the problem. One solution involves the use of a NO_x storage-reduction (NSR) catalyst in combination with mixed-lean engine operation, as developed and introduced in the Japan market by Toyota during the early 1990's [2 - 4].

A NO_x Storage and Reduction (NSR) catalytic system consists of a noble metal component and a storage additive on a high surface area support [5, 6]. In the Toyota formulation the noble metal component used is a Pt/Rh mix, where Platinum is used for its NO_x oxidation abilities and Rhodium for its reduction capabilities, although the system was reported to work also without the presence of rhodium. As an example, figure 4.1 shows a model of the NSR catalyst based on Pt and Ba only [6].

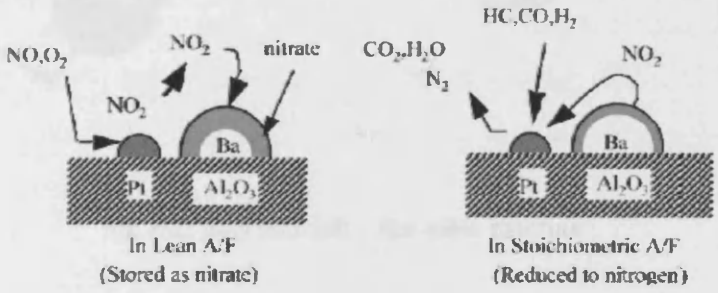

Fig. 4.1: Description of the NSR mechanism on a model comprising Pt and Ba (oxide) on alumina support. From [6].

The storage component is represented by an alkali or alkaline metal oxide (BaO) and the support is a high surface area γ-alumina. During the NSR reaction in lean air/fuel conditions, the normal engine operating conditions, NO is supposed to be oxidised to NO_2 catalysed by the presence of Pt nanoparticles. NO_2 should then be stored onto the BaO_x particles as $Ba(NO_3)_2$. Every few minutes, stoichiometric air/fuel conditions are created via the injection of fuel into the combustion mix. This provides a reducing environment where unburned hydrocarbons, carbon monoxide and hydrogen are present. In these conditions the stored NO_x is reduced over the noble metal acting as a

reductant (Rh) and released as N_2. The oxygen species generated, combine with CO and unburned hydrocarbons to give CO_2 and H_2O.

4.2. Barium oxides and NO_x Storage and Reduction

The two barium oxides of interest in this chapter are barium oxide (BaO) and barium peroxide (BaO_2).

BaO has a cubic sodium chloride–like bulk structure with a lattice parameter a of 0.552 nm [7]. In figure 4.2 the BaO crystal structure is shown.

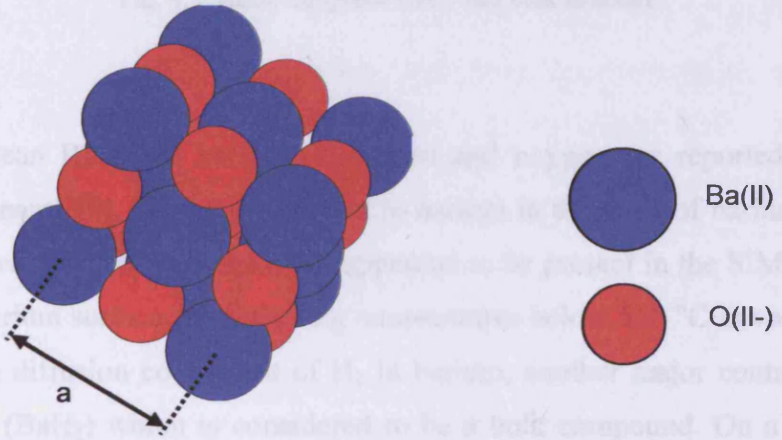

Fig. 4.2: BaO rock salt – like cubic structure.

Barium oxide is a white hygroscopic compound which transforms into barium hydroxide on contact with water. Barium oxide is mainly used as a coating for hot cathodes, because of its low work function (~ 1.5 eV [8]), as an additive in optical quality glass, and in cathode ray tubes.

Barium peroxide is a grey-white crystalline solid with a tetragonal unit cell, with lattice parameters a = 0.538 nm and c = 0.684 nm [7]. It decomposes at 450 °C to give barium oxide and oxygen. It is commonly used as an oxidizing agent in various pyrotechnic mixtures and organic synthesis, to bleach animal substances, vegetable fibres and straw and in combination with aluminium it is used in the welding industry. The BaO_2 crystal structure is shown in figure 4.3.

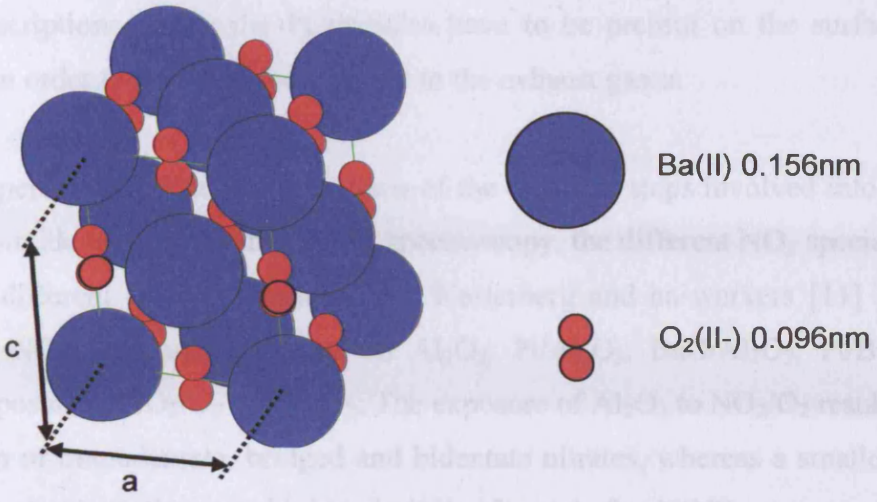

Fig. 4.3: BaO_2 tetragonal CaC_2-like bulk structure.

On a clean Ba metal surface, hydrogen and oxygen are reported to be the major contaminants [9]. Oxygen is bonded to barium in the form of barium oxide, peroxide and hydroxide. These compounds appeared to be present in the SIMS spectrum of the clean barium surface for annealing temperatures below 550 °C in vacuum. Because of the high diffusion coefficient of H_2 in barium, another major contaminant is barium hydride (BaH_2) which is considered to be a bulk compound. On a BaO surface, the peroxo species has been calculated to show a variable binding energy, dependent upon the site where the species forms: +2.5 eV are expected for a peroxide in a corner site, +2.7 eV for a peroxide localised on a step edge and +2.9 eV for a peroxide on a terrace [10].

Although few publications regarding UHV studies of NSR systems are present in the literature, several works on powder samples are addressed to the reaction mechanism optimisation and explanation in catalytic reactors. Different models have been proposed in the attempt to explain the NSR mechanism on Pt/BaO and on Pt/BaO/alumina substrates, with different storage medium and noble metal loadings taking into consideration a crucial point: whether or not the noble metal and the storage medium have to be in "intimate contact" between each other for the NSR catalyst to work [2, 5, 6]. The contact between the components seems to be the most logical configuration, but speculations are still on going. The common point of all

these descriptions is that the Pt particles have to be present on the surface of the catalyst in order to be able to be exposed to the exhaust gases.

Some papers give a detailed description of the different steps involved into the NSR mechanism identifying, mainly via IR spectroscopy, the different NO_x species present into the different catalyst formulations. Westerberg and co-workers [11] identified different NO_x compounds formed on Al_2O_3, Pt/Al_2O_3, BaO/Al_2O_3, $Pt/BaO/Al_2O_3$ under exposure to NO_2/O_2 or NO/O_2. The exposure of Al_2O_3 to NO_2/O_2 resulted in the formation of monodentate, bridged and bidentate nitrates, whereas a smaller amount of nitrates, but both linear and bridged nitrites formed after NO/O_2 exposure. When Pt is present, NO is oxidised to NO_2 at temperature above 150 °C and forms nitrates. On BaO/Al_2O_3, nitrites and hyponitrites were observed after exposure to NO/O_2 below 200 °C. After exposure to NO_2/O_2, nitrates are formed on BaO, as well as bidentate and bridged nitrate are formed on alumina at the barium oxide-alumina interface. At above 350 °C surface nitrates on BaO are the most abundant species and, although the NO_x groups are reported to move from the alumina to the BaO, bulk $Ba(NO_3)_2$ was not observed. Su and co-workers [18] reported that the conversion of the surface barium nitrite to bulk barium nitrate occurs during the storage phase only in the presence of Pt, and this step is accelerated by the presence of gas phase oxygen and at elevated temperatures. Similar nitrite and nitrate species were also observed on alumina, but their concentration and stability are reported to be lower that those of the corresponding barium species. Both barium nitrite and nitrate could only be fully reduced when Pt was present in the system, as the reduction did not occur on the BaO/Al_2O_3 sample.

The NO_x storage on BaO(100) was simulated via DFT calculation by Broquist and co-workers [13 - 15]. The mechanism proposed included initial chemisorption of a pair of NO_2 at both Ba^{2+} and O^{2-} surface sites to form surface nitrites and nitrates, respectively, then a surface redox reaction to form nitrate-nitrite pairs is postulated to occur. The final step is a heterogeneous oxidation of the remaining nitrite to form an all-nitrate final product.

Olsson and co-workers [16] investigate the influence of platinum oxide presence on the dissociation of NO_2 over Pt/Al_2O_3 and $Pt/BaO/Al_2O_3$ systems. They noticed that

the NO_2 dissociation rate over a Pt/Al_2O_3 system decreased at 350 °C because of PtO formation. Moreover, on the same system they reported a decrease in reactivity with increase in temperature (from room temperature, to 300 °C) during NO oxidation experiments. The decrease in activity in this second case was correlated with the increase in dispersion of Pt particles that could be readily oxidised when exposed to NO_2 or O_2; in fact the less the dispersion the lower the amount of platinum oxide, the higher the activity. $Pt/BaO/Al_2O_3$ was found to be even less active than Pt/Al_2O_3 for both NO oxidation and NO_2 dissociation because much more platinum oxide could form. Another poisoning agent is reported to be SO_x [12, 17]

The role played by barium carbonate species, likely to be present because of the high levels of CO and CO_2 in the exhaust gases, was also considered by Burch [18], who proposed that NO is oxidised on the platinum to form NO_2, which then migrates to the $BaCO_3$ to form $Ba(NO_3)_2$, giving off CO_2 as a product. A difference between this mechanism and the others mentioned is that it includes rhodium to reduce the NO_x during the rich phase. Also Sedlmair and co-workers [19] reported that NO was found to be active in displacing barium carbonate to form $Ba(NO_x)_y$ species. A NSR mechanism for a model catalyst in which also carbonate species are taken into account (figure 4.4) was proposed by Gill and co-workers [20].

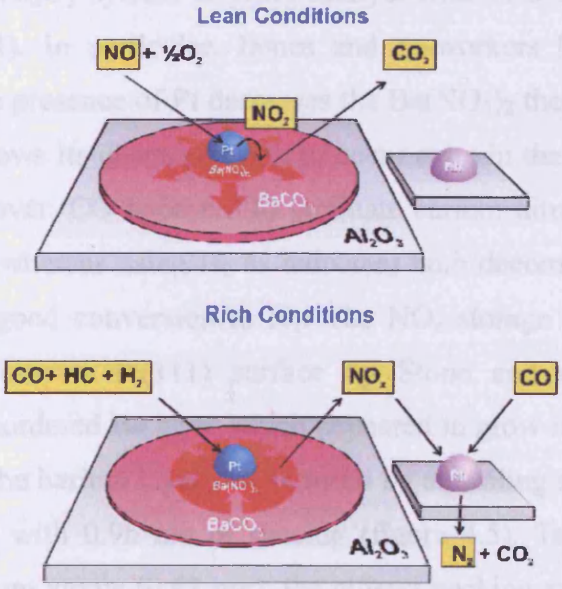

Fig. 4.4: Schematic showing the reactions occurring on a NSR model catalyst involving carbonate species, during fuel lean and rich condition [20].

Few models studies in UHV environment are reported in literature. Schmitz and Braid [21] prepared 15-20 Å thick BaO films, in UHV conditions, over a thin aluminium sheet with a native aluminium oxide surface on it. They exposed the films to high pressures (typically 40 mTorr, ~5×10^6 L) of NO or NO_2 at room temperature, concluding that NO adsorbs mainly as nitrite and NO_2 as nitrate which appear to form via a nitrite intermediate. After preliminary work on BaO/Al_2O_3 powder samples [22], Wang and co-workers prepared $Ba(NO_3)_2$ particles supported on a-Al_2O_3(0001) and studied their decomposition upon annealing via in situ TEM [23]. The $Ba(NO_3)_2$ particles appeared to have triangular and polygonal morphologies, with flat top surface, the reason for this being the different growth rate between the direction parallel and perpendicular to the hcp substrate surface, for a cubic structure. The decomposition of these barium nitrate particles produced barium oxide particles that retained an overall morphology similar to the one shown by their parental single-crystals barium nitrate particles. However, the oxide particles appeared to have shrunk and their surfaces became rougher, this indicating that the BaO particles are not single crystals, but an ensemble of clusters.

In collaboration with Toyota during the few past years, work has been done by our group, evaluating the characteristics of these systems, mainly the catalytic behaviour of the $Pt/Ba(NO_3)_2/Al_2O_3$ system as NSR catalyst with TPD methods and a Pulsed-Flow Reactor (PFR). In particular, James and co-workers [2] observed via TPD experiments that the presence of Pt decreases the $Ba(NO_3)_2$ thermal stability, by more than 200 K, and allows its decomposition to occur even in the absence of a reducing environment. Moreover, CO appeared to facilitate barium nitrate decomposition, but not NO_x reduction, whereas using H_2 as reductant both decomposition and reduction take place, with a good conversion to N_2. The NO_x storage process has also been studied via STM over a Pt(111) surface by Stone and co-workers [24] after preparation of an unordered Ba layer which appeared to grow in a Stranski-Krastanov mode. Ordering of the barium layer was induced by annealing at 500 K, resulting in a hexagonal structure with 0.96 nm of spacing (figure 4.5). Taking into account the atomic radii of barium atoms (0.43 nm), the closest packing surface adlayer allowed would be (111) oriented with a (2×2) structure. In this case, this should correspond to a coverage of 0.15 - 0.20 ML, where a 1 ML coverage is defined as 1 adatom (Ba) per 1 substrate atom (Pt).

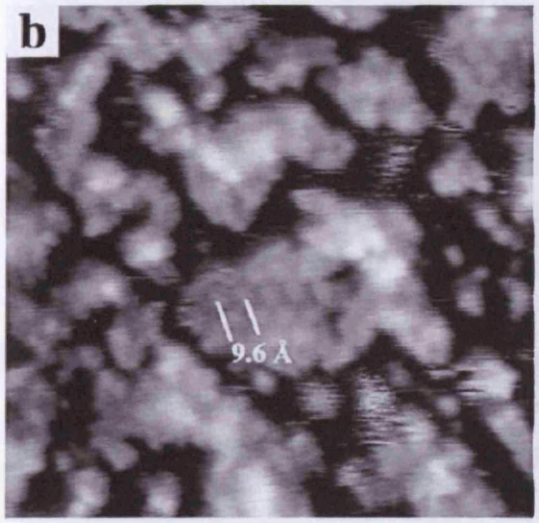

Fig. 4.5: STM image after annealing the as deposited Ba overlayer to 500 K for 15 min. Moiré pattern on the Ba islands is observed and displays a separation of 0.96 nm. Tunnelling parameters: 20×20 nm, 100 pA, 1000 mV. From [24].

The BaO was produced by exposure to oxygen at 573 K and imaged *in situ* and it appeared as an apparent change in height of the Ba particles. This phenomenon was attributed to the lower work-function of the oxide compared to the metal.
At around 300 °C, a metastable oxygen species on the surface was observed and attributed to the formation of BaO_2. Other than the oxidation of the barium layer, also the NO_x storage process was imaged in situ: during NO and O_2 co-dosing at 573 K onto the BaO/Pt(111) surface resulted in reaction. The particles attributed to BaO appeared to stay fairly constant in height but their area increased by about a factor of two, value in agreement to the one expected for the conversion from oxide to nitrate.

A BaO(111)-(2×2) reconstruction was recently presented and supported by theoretical calculations by Bowker and co-workers [25]. This particular reconstruction of the (111) plane, leads to a BaO surface layer that is terminated by three-sided pyramids composed of a barium (oxygen) ion at the apex bonded to three oxygen (barium) atoms at the base of the pyramid, which in turn are bonded to the four nearest barium (oxygen) ions in the manner predicted for rocksalt-structure materials (figure 4.6 shows the Ba-terminated 2×2 surface reconstruction). The sides of these pyramids are BaO(100) surfaces, which are low energy surfaces. (4×4) surface reconstructions have also been predicted to form, as larger pyramids, and have even lower surface energy; however these are much less common than the (2×2) reconstructions mentioned above mainly for the increased amount of BaO needed for them to form.

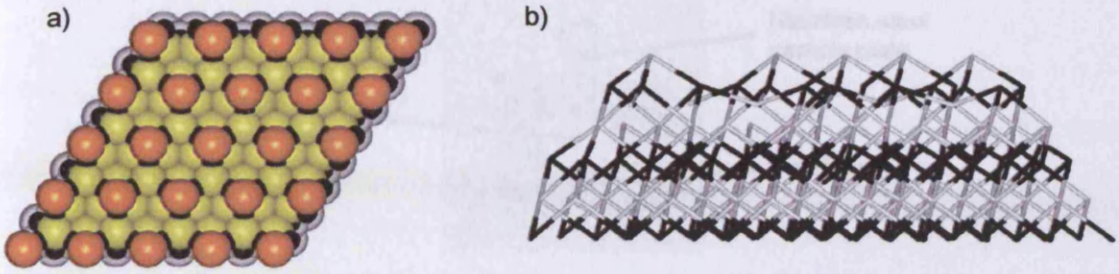

Fig. 4.6: Computer modelling of the BaO(111)-(2x2) surface reconstruction; (a) top view, (b) side view of the (2×2) reconstructed surface, showing the pyramidal structures. In (a) O = black, topmost Ba = orange, 2nd layer Ba = yellow, lower layers Ba = white; in (b) O = black, Ba = grey. [25]

4.3. Experimental setup

All the experiments described in sections 4.3.1 were performed on the Omicron Multiprobe ® Surface Science System described in Chapter 2. The UHV chamber had a typical base pressure of ~3×10^{-10} mbar, which increased to ~1×10^{-9} mbar during XPS and LEED analysis. The base pressure during STM was ~9×10^{-11} mbar. The XP spectra were collected using both a Mg Kα x-ray source (1253.6 eV) and an Al Kα x-ray source (1486.6 eV) depending upon the case. A pass energy of 100 eV was used to collect the survey spectra, whilst a pass energy of 50 eV was used while collecting the multiplex spectra. Binding energies were calibrated with respect to the C(1s) (BE = 284.5 eV), feature corresponding to the presence of adventitious carbon. When carbon was not present the calibration was done according to the $Pt(4f_{7/2})$ at 71.2 eV and $Pt(4p_{3/2})$ at 520 eV for the clean Pt(111) crystal. The electron emission angle generally employed was 0°, measured from the sample normal. The standard deviation in the binding energies values is 0.1 eV. All the data were recorded at room temperature. All STM measurements were acquired using a W tip obtained by electrochemical etch of a W wire (99.995% purity, 0.39 mm Ø).

The support used was a brand new Pt single crystal, 5N purity, Metal Crystals and Oxides Ltd, 10×5×1 mm, cut and polished in the (111) plane. The crystal was mounted according to figure 4.7.

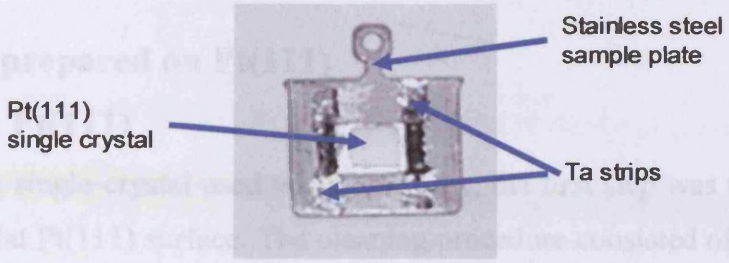

Fig. 4.7: Sample mounting.

The experiments described in section 4.4.2. (collaboration with Queen Mary, University of London) were performed in an UHV chamber having a base pressure of 1×10^{-10} mbar, equipped with a VG CLAM-2 XP spectrometer and Mg Kα single-anode X-ray source, Omicron LEED optics and a quadrupole mass spectrometer for TPD measurements. Infrared (IR) spectra were collected by translation of the sample into an independently-pumped IR cell attached to the main analytical chamber and using a Mattson RS2 FTIR spectrometer equipped with a narrowband MCT detector (see section 2.8.1). Binding energies were calibrated using the Cu($2p_{3/2}$) and Cu(3p) peaks (with assigned binding energies of 932.6 eV and 75.1 eV, respectively [26]) of the clean Cu(111) crystal. Pass energies of 20 eV for the Cu($2p_{3/2}$) region, 50 eV for the Ba($3d_{5/2}$), O(1s), and N(1s) regions, 100 eV for the C(1s) region and survey were used. The electron emission angle generally employed was 50°, measured from the sample normal. The standard deviation in the binding energies values is 0.1 eV.

IR spectra were generally recorded at a resolution of 4 cm^{-1}, using a grazing angle of approximately 87° to the surface normal and 512 scans. TPD measurements were acquired in a multiple ion monitoring mode and with the ion source aperture located within a few millimetres of the crystal surface, so as to maximize the direct line-of-sight desorption signal.

XPS data analysis and interpretation were done using CasaXPS [27] software, STM images using WSxM package [28].

4.4. Results

4.4.1 Layers prepared on Pt(111)

4.4.1.1 Clean Pt(111)

As the platinum single crystal used was brand new, the first step was the preparation of a clean and flat Pt(111) surface. The cleaning procedure consisted of several cycles of sputtering with Ar^+ (5×10^{-6} mbar, 99.999%, Argo Ltd.) using different ionisation energies (500 eV and 1000 eV, 14 $\mu A/cm^2$) for different times (from 10 minutes to 1 hour) and annealing (during the sputtering, in vacuum, in O_2, 99.6%, Argo Ltd.) at different temperatures, from room temperature up to 1100K. The major contaminant to be removed was residual material left after the polishing procedure from the manufacturer, consisting mainly in carbon and oxygen compounds. The crystal cleanliness was checked step by step by means of XPS and LEED. Figure 4.8 shows an XP survey spectrum of clean platinum.

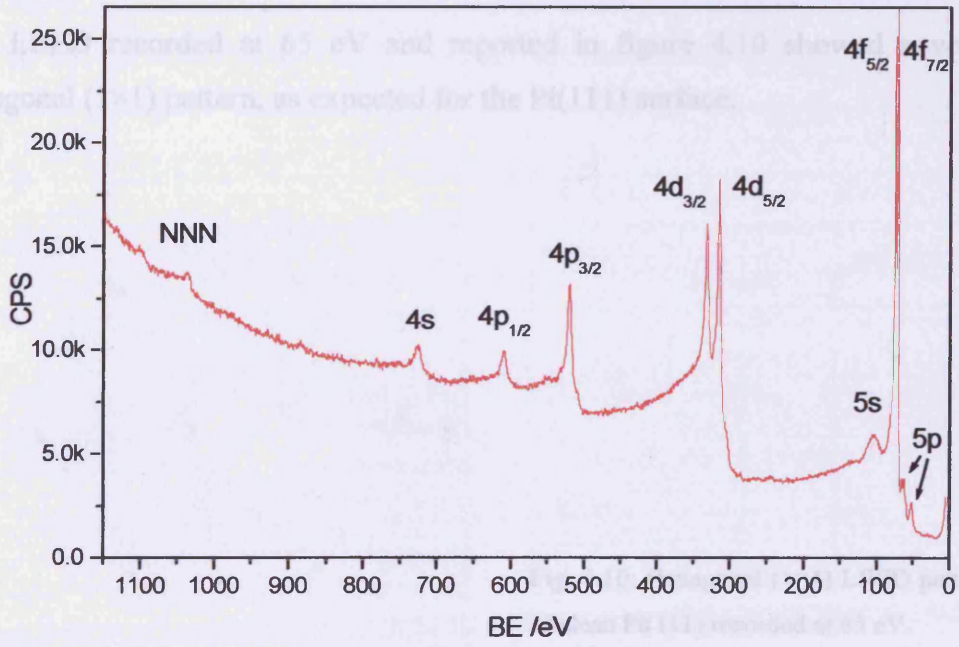

Fig. 4.8: XP survey spectrum of clean Pt. Platinum peaks are labelled.

After cleaning, STM showed the presence of flat terraces between 10 and 100 nm wide (figure 4.9 a). From the line profile (see figure 4.9 b), an average step height of ~0.226 nm was observed, a value in good agreement with the one expected of 2.275±0.002 Å and derived from XRD experiments [29]. Atomic resolution on the clean platinum was not achieved during cleaning.

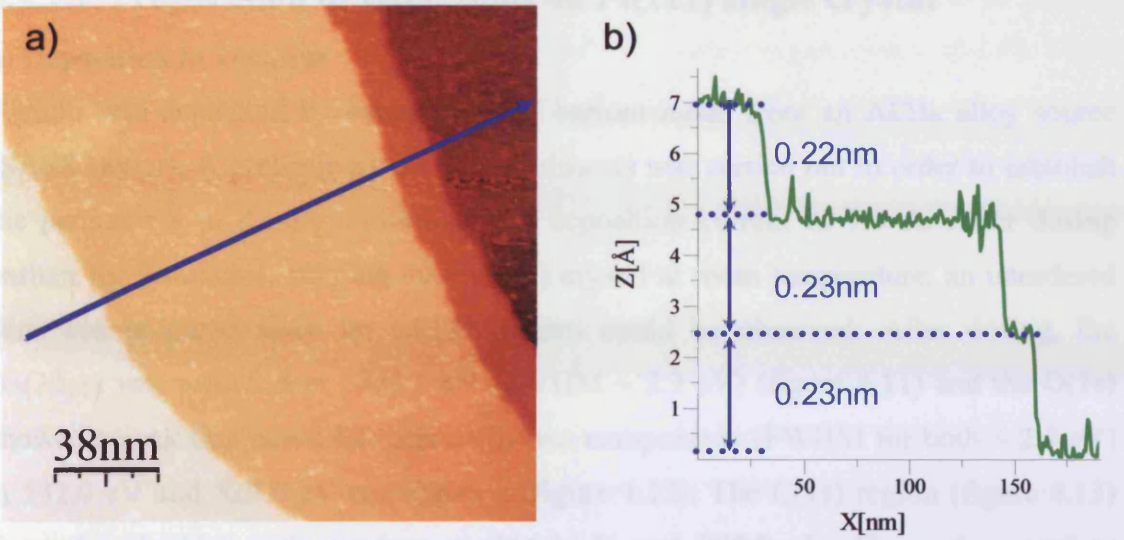

Fig. 4.9: a) STM image showing the topography of clean Pt(111). Image size 190×190 nm. Tunnelling parameters: -0.5 V, 1.25 nA. b) line profile as in a) showing an average step height of 0.23 nm.

The LEED recorded at 65 eV and reported in figure 4.10 showed a very sharp hexagonal (1×1) pattern, as expected for the Pt(111) surface.

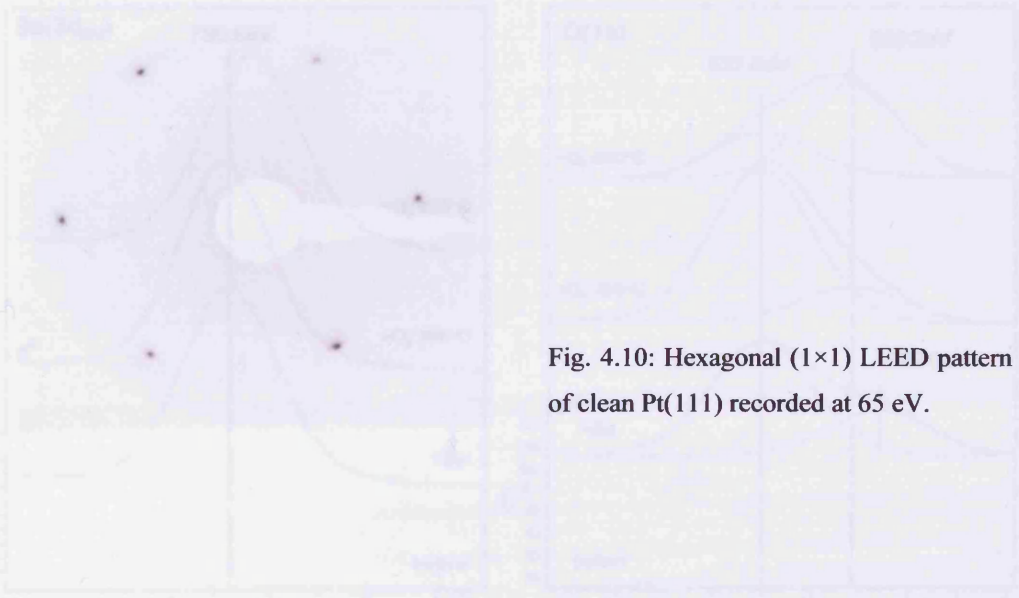

Fig. 4.10: Hexagonal (1×1) LEED pattern of clean Pt(111) recorded at 65 eV.

4.4.1.2. Preparation of BaO_x films on Pt(111) single crystal

a) Deposition in vacuum

Barium was deposited by evaporation of barium metal from an Al/Ba alloy source (SAES Getter). A preliminary set of experiments was carried out in order to establish the parameters of dosing, resulting in a deposition current of 7.9 A. After dosing barium for 2 minutes, keeping the Pt(111) crystal at room temperature, an unordered film was prepared since no LEED pattern could be observed. After dosing, the $Ba(3d_{5/2})$ was recorded at ~780.8 eV (FWHM ~ 2.3 eV) (figure 4.11) and the O(1s) showed a peak that could be fitted with two components (FWHM for both ~ 2.4 eV) at 532.0 eV and 529.6 eV respectively (figure 4.12). The C(1s) region (figure 4.13) showed a doublet with maxima at 284.5 eV and 288.8 eV. The carbon surface concentration was calculated as 4.4% atomic concentration. The majority of the carbon species is represented by carbonaceous contamination (peak at 284.5 eV) which counted for approximately 65% of the total C(1s) signal. The carbonate species represented therefore ~1.5% of atomic concentration. Taking into consideration the binding energy values reported in table 4.1 for barium and selected compounds, the effect of dosing in vacuum was the preparation of an oxidised barium layer, comprised of BaO_2 mainly.

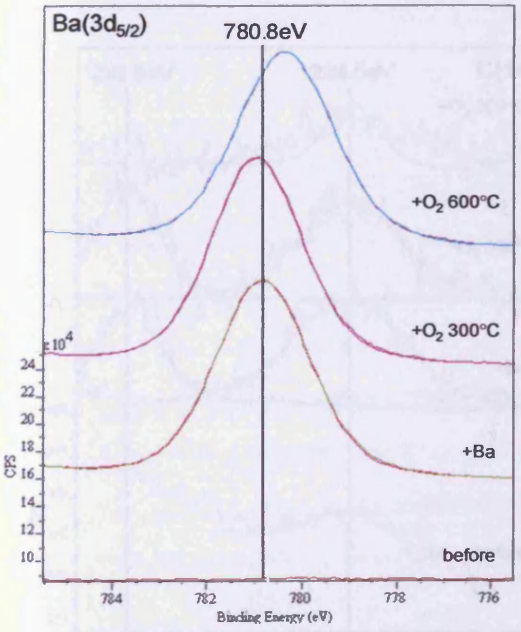

Fig. 4.11: $Ba(3d_{5/2})$ XP region, before, after barium dosing, after annealing in O_2 at 300 °C and 600 °C. Spectra are offset for clarity.

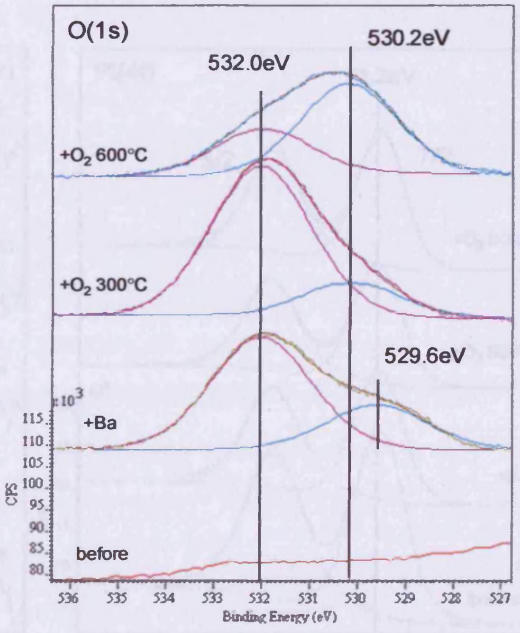

Fig. 4.12: O(1s) XP region and peaks fittings, before, after barium dosing, after annealing in O_2 at 300 °C and 600 °C. Spectra are offset for clarity.

A small amount of $BaCO_3$ was present, because of the O(1s) component at 532 eV which could correspond to both peroxide and carbonate oxygen atoms, and the C(1s) at 288.8 eV. Nevertheless BaO was also present, because of the oxygen component at 529.6 eV. The ratio BaO_2/BaO was ~3/2. The formation of carbonate probably occurred because the vapours of barium atoms coming from the metal dispenser could react with the residual gases in the chamber, which mainly comprised of CO and CO_2, or during the transfer of the sample from the preparation chamber to the analysis chamber. This operation takes approximately 5 minutes and during the transfer, the base pressure in the chamber could reach 1×10^{-8} mbar. Another species that could form as a result of interaction between the system deposited and the residual gases in the chamber, water, would be $Ba(OH)_2$, however, this species is excluded because an O(1s) at around 531.2 eV would been expected for it to be present. From the attenuation of the Pt(4f) XP signal (figure 4.14) the film thickness was estimated as ~1.93 nm, using a value of 2.41 nm (calculated according to the TPP–2M model [30], a description of the TPP-2M model is presented in Appendix A) for the IMFP of the electrons emerging from a mixed layer formed of 66% BaO_2 and 33% BaO, at a kinetic energy of 1181.4 eV (binding energy of MgKα X-ray source, 1253.6 eV, minus binding energy of Pt(4f) electrons 71.2 eV).

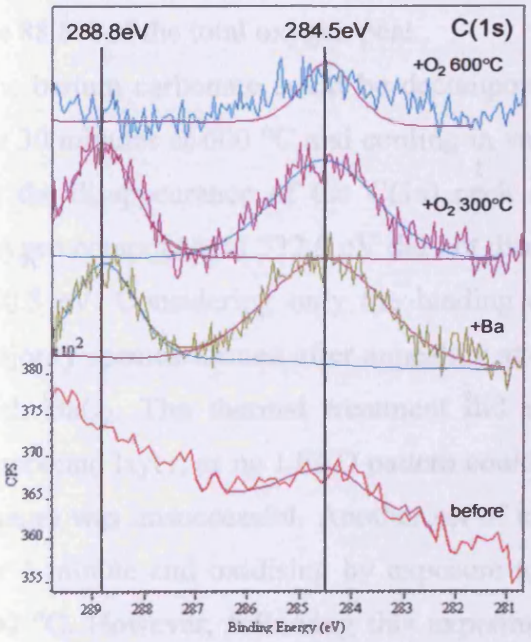

Fig. 4.13: C(1s) XP region, before, after barium dosing, after annealing in O_2 at 300 °C and 600 °C. Peaks fitting are also shown. Spectra are offset for clarity.

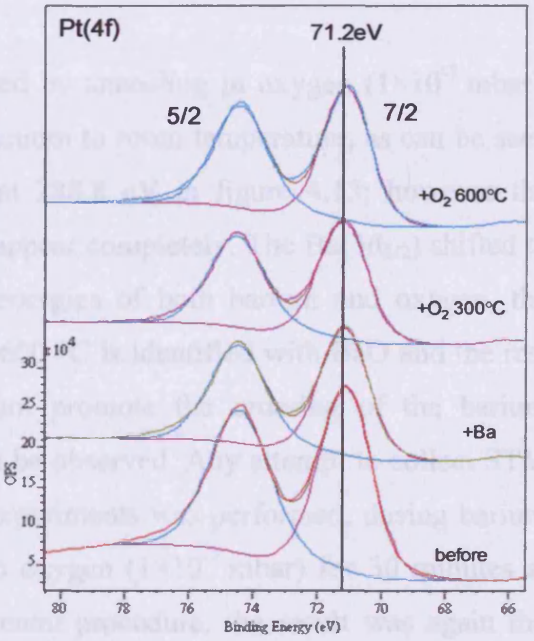

Fig. 4.14: Pt(4f) XP region, before, after barium dosing, after annealing in O_2 at 300 °C and 600 °C. Peaks fitting are also shown. Spectra are offset for clarity.

Compound	Ba($3d_{5/2}$)		O(1s)		N(1s)		C(1s)	
Ba	779.3-780.5 779.3-780.6 780.1-780.6	[31] [32] [33]						
$Ba(OH)_2$	779.5	[31]	531.2	[32]				
BaO_2	780.3-781.2	[34]	532.0-532.7	[34]				
BaO	779.1-779.9 779.2-779.8	[32] [33]	528.3-530.2	[32]				
$Ba(NO_2)_2$[i]					403.2-403.6 403.3-405.0 403.8-404.7	[31] [32] [33]		
$Ba(NO_3)_2$	780.5 780.3-780.7 780.5-781	[31] [32] [33]	532.9-533.0	[32]	407.1-407.3 407.3-408.2 407.1-408.2	[31] [32] [33]		
$BaCO_3$	779.7 779.8-779.9 779.7-780.2	[31] [32] [33]	531.1-532.2	[32]			289.4-290.8 289.0-291.5	[32] [33]
$BaHCO_3$[ii]							285.5-286.1	[35]

Note
i) No reference for $Ba(NO_2)_2$ were found, data are related to N(1s).
ii) No reference for $BaHCO_3$ where found, data are related to C(1s).

Table 4.1: Barium and barium selected compounds binding energy values.

After dosing, the system was exposed to oxygen (1×10^{-7}mbar) for 30 minutes at 300 °C and cooled in oxygen to room temperature. The system appeared to adsorb some oxygen, as the component at 532.0 eV of the oxygen peak increased by ~17%; moreover, the component at 529.6 eV was shifted at 530.2 eV, thus signifying a chemical change occurred. The peroxide like oxygen represented now approximately the 88.8% of the total oxygen peak.

The barium carbonate could be decomposed by annealing in oxygen (1×10^{-7} mbar), for 30 minutes at 600 °C and cooling in vacuum to room temperature, as can be seen by the disappearance of the C(1s) peak at 288.8 eV in figure 4.13; however the oxygen component at 532.0 eV did not disappear completely. The Ba($3d_{5/2}$) shifted to 780.3 eV. Considering only the binding energies of both barium and oxygen, the majority species formed after annealing at 600 °C is identified with BaO and the rest with BaO_2. The thermal treatment did not promote the ordering of the barium compound layer, as no LEED pattern could be observed. Any attempt to collect STM images was unsuccessful. Another set of experiments was performed, dosing barium for 1 minute and oxidising by exposure to oxygen (1×10^{-7} mbar) for 30 minutes at 300 °C. However, following this experimental procedure, the result was again the preparation of an unordered 1.48nm thick film of BaO_2/BaO in ratio 3/2, with a small $BaCO_3$ contamination.

The previous sets of experiments were undertaken in collaboration with Dr. A.J. McDowall.

b) Deposition in oxygen pressure, sample at 200 °C.

In order to avoid the formation of barium carbonate, the preparation procedure was modified. Barium was dosed for a time variable between 15 and 90 seconds in oxygen background pressure (typically 1×10^{-7} mbar), keeping the Pt(111) single crystal at 200 °C. After barium dosing, the system was allowed to cool to room temperature in vacuum. In order to promote the maximum degree of order the films were annealed in vacuum at 300 °C for 30 minutes. The modifications were introduced for different reasons: by co-dosing barium and oxygen, the vapours of barium coming from the metal dispenser, should react preferentially with the oxygen, which has higher partial pressure than CO (less than 2×10^{-9} mbar) and CO_2 (less than 1×10^{-9} mbar), producing a BaO_x compound, before landing on the platinum crystal; at 200 °C the coverage of CO on the platinum is negligible, since CO should desorb at above 150 °C, therefore less contamination of the platinum surface is expected [36]. Moreover, the deposition current was set to 6.9 A, 1 A lower than before to generate a slower desorption rate and try to improve ordering allowing more time for the barium compounds to reconstruct after landing on the surface.

After barium and oxygen co-deposition the Ba($3d_{5/2}$) XP peak was at ~ 780.0 eV and was characterised by a FWHM of ~ 2.9 eV (figure 4.15). The O(1s) XP region, showed a peak with an asymmetry at higher binding energy. The spectrum could be fitted with two peaks having maxima at 531.9 eV (~14% of the total integral) and 529.5 eV (~86% of the total integral), with FWHM ~ 2.4 eV, as shown in figure 4.16. The carbon region (figure 4.17) shows that after barium and oxygen co-dosing, carbon is not present. Figure 4.18 shows the Pt(4f) XP region according to which the binding energy scale calibration was made. Therefore, in this work, the oxygen peak in the range 529.5 eV is assigned to BaO, whereas the one at 531.9 eV is assigned to BaO_2, after verification of the absence C(1s) signals suggesting the absence of carbonates.

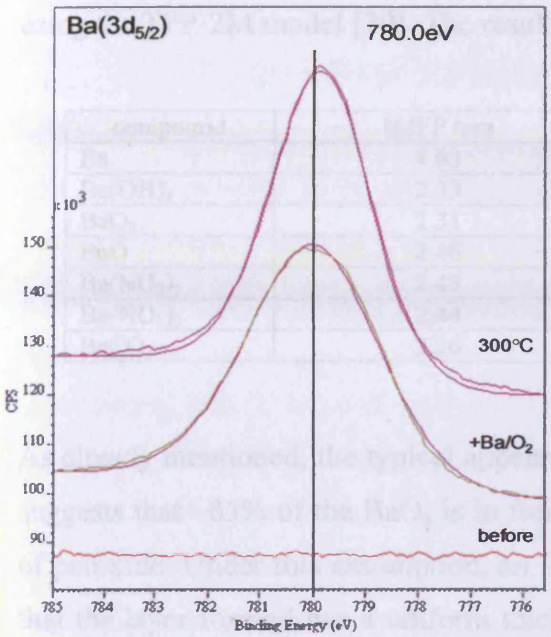

Fig. 4.15: $Ba(3d_{5/2})$ XP region, before, after 1 minute of Ba/O_2 co-dosing, after annealing at 300 °C. Peaks fitting are also shown. Spectra are offset for clarity.

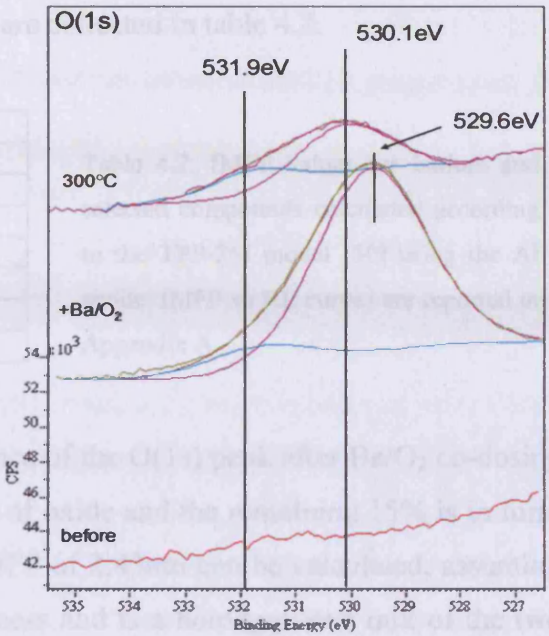

Fig. 4.16: O(1s) XP region, before, after 1 minute of Ba/O_2 co-dosing, after annealing at 300 °C. Peaks fitting are also shown. Spectra are offset for clarity.

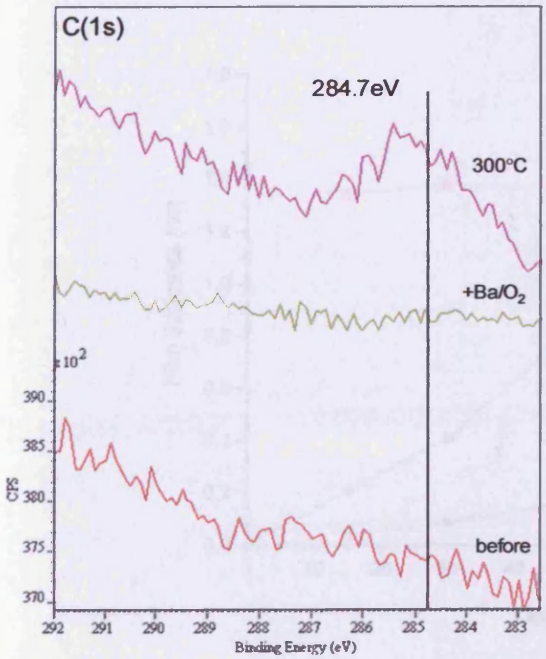

Fig. 4.17: C(1s) XP region, before, after 1 minute of Ba/O_2 co-dosing, after annealing at 300 °C. Peaks fitting are also shown. Spectra are offset for clarity.

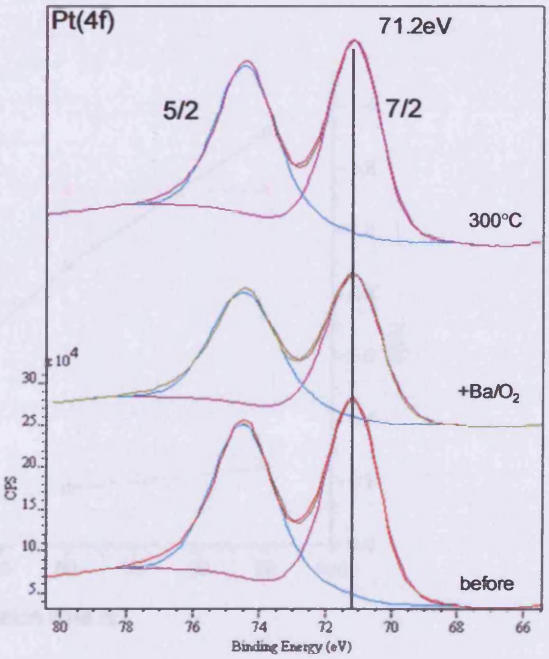

Fig. 4.18: Pt(4f) XP region, before, after 1 minute of Ba/O_2 co-dosing, after annealing at 300 °C. Peaks fitting are also shown. Spectra are offset for clarity.

Different IMFP values for barium and different barium compounds were calculated using the TPP-2M model [30]. The results are collected in table 4.2.

compound	IMFP /nm
Ba	4.63
$Ba(OH)_2$	2.33
BaO_2	2.31
BaO	2.46
$Ba(NO_2)_2$	2.43
$Ba(NO_3)_2$	2.44
$BaCO_3$	2.26

Table 4.2: IMFP values for barium and selected compounds calculated according to the TPP-2M model [30] using the Al anode. IMFP vs KE curves are reported in Appendix A.

As already mentioned, the typical appearance of the O(1s) peak after Ba/O_2 co-dosing suggests that ~85% of the BaO_x is in form of oxide and the remaining 15% is in form of peroxide. Under this assumption, an IMFP of 2.43nm can be calculated, assuming that the layer formed has a uniform thickness and is a homogeneous mix of the two species. This value was used to calculate the film thickness of the layers prepared from the attenuation of the Pt(4f) signal. In figure 4.19 a diagram of film thickness vs deposition time and O/Ba atomic ratio and Ba/Pt atomic ratio vs deposition time are shown. The O/Ba atomic ratio appears to be constant, this means that with this preparation recipe there is a good reproducibility of the oxidation state of the adlayer.

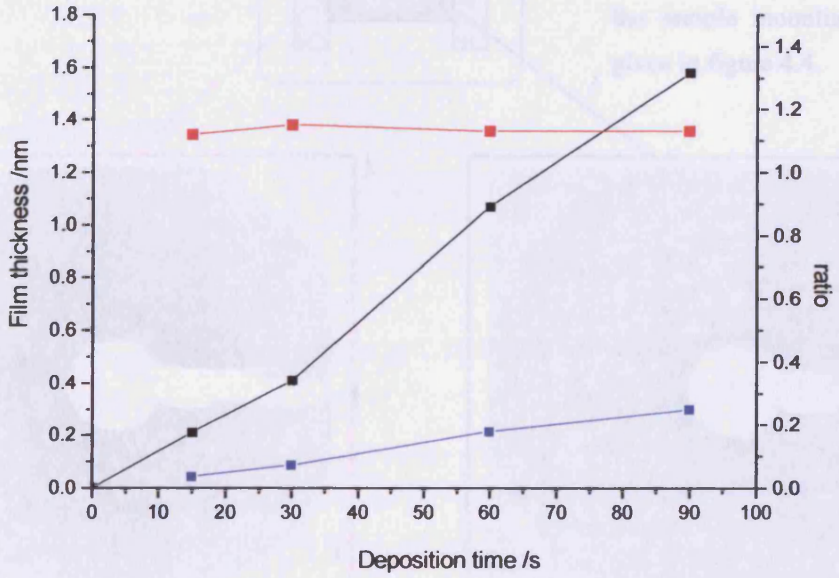

Fig. 4.19: Film thickness vs deposition time (black line), O/Ba atomic ratio (red line) and Ba/Pt atomic ratio (blue line) vs deposition time diagram for the Ba/O co-deposition.

For the estimation of the coverage in monolayers, it will be necessary to know the thickness of 1 monolayer of oxidised barium film, but this can be derived only after a single chemical species can be identified and an ordered LEED pattern can be observed.

The LEED patterns after deposition generally showed only the hexagonal (1×1) structure typical of Pt(111), although very faint (see figure 4.8 for comparison), thus indicating the BaO_x adlayer is unordered, for film thicknesses less than 1.1nm; for thicker films the Pt(111) spots could not be seen anymore. The LEED recorded after annealing at 300 °C have the same appearance than the one observed just after Ba/O_2 co-dosing. The patterns roughly correspond to the areas indicated in figure 4.20.

Even if the difference doesn't appear so clear on the images recorded, the patterns were also sharper on the sides of the crystal. This could be due to the presence of unordered BaO_x concentrated in the middle of the crystal but also to the presence of the Ta strips. Where the crystal is in contact with the strips there is a better thermal transfer resulting in better efficiency of the annealing process.

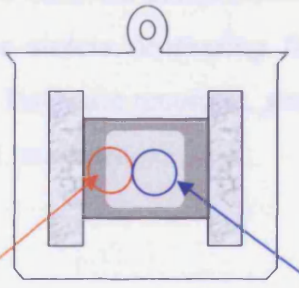

Fig. 4.20: Positions where the LEED patterns have been recorded. The description of the sample mounting itself is given in figure 4.4.

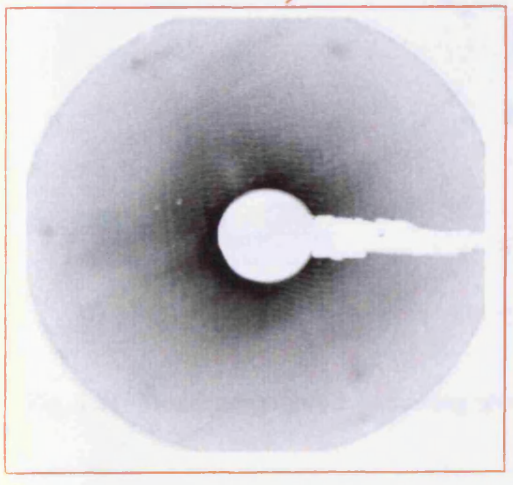

LEED pattern (60 eV) recorded on the side of the crystal after annealing at 300 °C a 1.1 nm BaO/BaO_2 film.

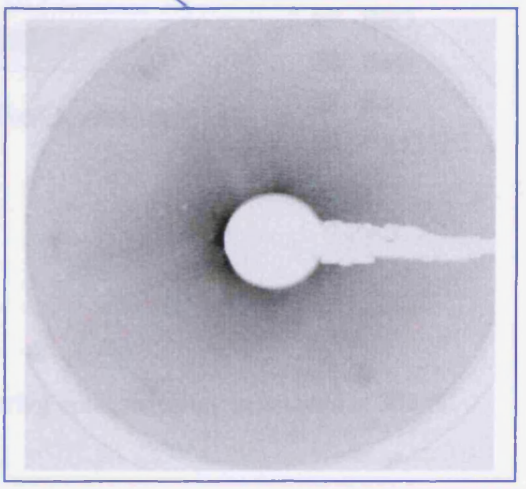

LEED pattern (65 eV) recorded on the centre of the crystal after annealing at 300 °C a 1.1 nm BaO/BaO_2 film.

After annealing in vacuum for 30 minutes at 300 °C, however, the LEED pattern did not improve. The peak Ba($3d_{5/2}$) appeared to shift to lower binding energy (779.8 eV) and to narrow (FWHM ~ 2.3 eV); in the O(1s) region, although the component at 531.9 eV stayed constant in position and area, the one formerly at 529.6 eV moved to 530.1 eV and decreased by ~70%. This could be interpreted as sintering of the oxidised barium layer, since desorption at this temperatures seems unlikely. As a comparison, Ba^{2+} and BaO^{+} desorption were not observed below ~ 830 °C for approximately 6 layers of oxidised barium on polycrystalline W [37]. However, a lower decomposition onset temperature of around 500 °C was observed for BaO_2 powders during DSC studies [38]. The sintering process in described in figure 4.21. After deposition in oxygen, since the oxygen exposure is not high (1 minute of oxygen exposure at 1×10^{-7} mbar is around 6Langmuirs), only the very top of an unordered barium layer is oxidised. The oxidised layer comprises a mixture of BaO and BaO_2 in approximately 5.6/1 ratio. The FWHM of the Ba($3d_{5/2}$) is large likely because more than one barium chemical environment is see by XPS, however, the deconvolution of the peak into different components does not seem reasonable. Upon annealing, the oxidised layer sinters decreasing the area visible to the XPS and relatively less BaO and more BaO_2 are recorded, since the ratio goes to 1.6/1. On the same time the platinum signal increases.

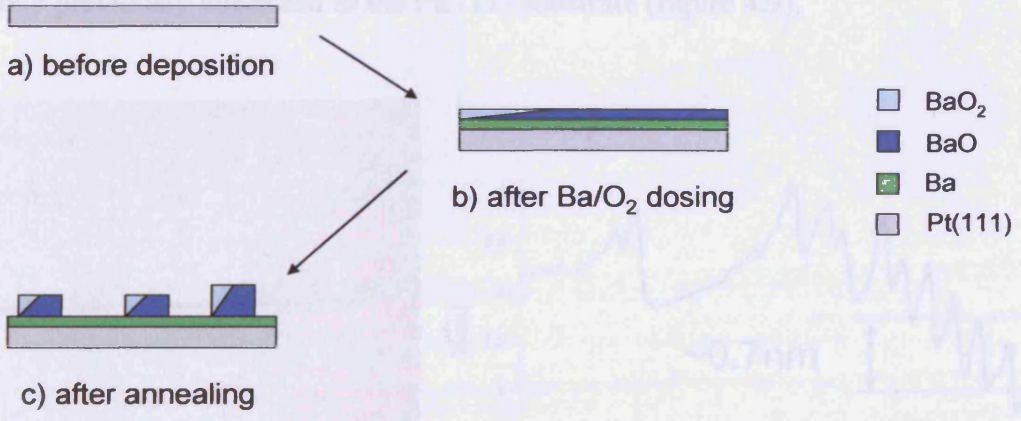

Fig. 4.21: Model describing the sintering process occurring upon annealing in vacuum at 300 °C.

The binding energy values for the oxygen peak are, generally, higher than the one reported in table 4.1. A mixture of BaO and BaO_2 was likely formed, as suggested by

the oxygen peak at 529.5 eV for the oxide and at 531.9 eV for the peroxide. An oxygen peak at 532 eV was formerly attributed to the presence of barium carbonate, however this time carbonate can be ruled out because a carbon peak at the typical binding energy for carbonate groups (289.0 - 291.5 eV) was not observed. A progressive shift of the O(1s) peak from 529.5 eV, corresponding to the "as prepared" BaO, towards higher binding energy values (~ 532.8 eV) was already observed by Ozensoy and co-workers [39, 40]. BaO_x of less than 2ML, was prepared co-dosing barium and oxygen, on oxygen terminated θ-Al_2O_3/NiAl(100) and exposed to oxygen at different temperatures. The O(1s) binding energy shift was attributed to the conversion of the disordered oxide, which grows forming 2D and 3D structures rather than in a layer by layer way, to peroxo-like structures after saturation of the surface with 6000 L of O_2 at 300 K. Upon this observation, was derived an apparent isosbestic point at ~ 531.2 eV, where a singular feature should appear when the amount of oxo-oxygen (O^{2-}) and peroxo-oxygen (O_2^{2-}) should be equal. Although a carbonate free layer was prepared, after annealing some carbon contamination (284.7 eV) appeared.

For a 1.07 nm thick BaO_x layer, which did not show a LEED pattern, some STM images were recorded. They show the presence of different features in different area of the crystal. In general the topography of the terraces (figure 4.22) is different from the one previously attributed to the Pt(111) substrate (figure 4.9).

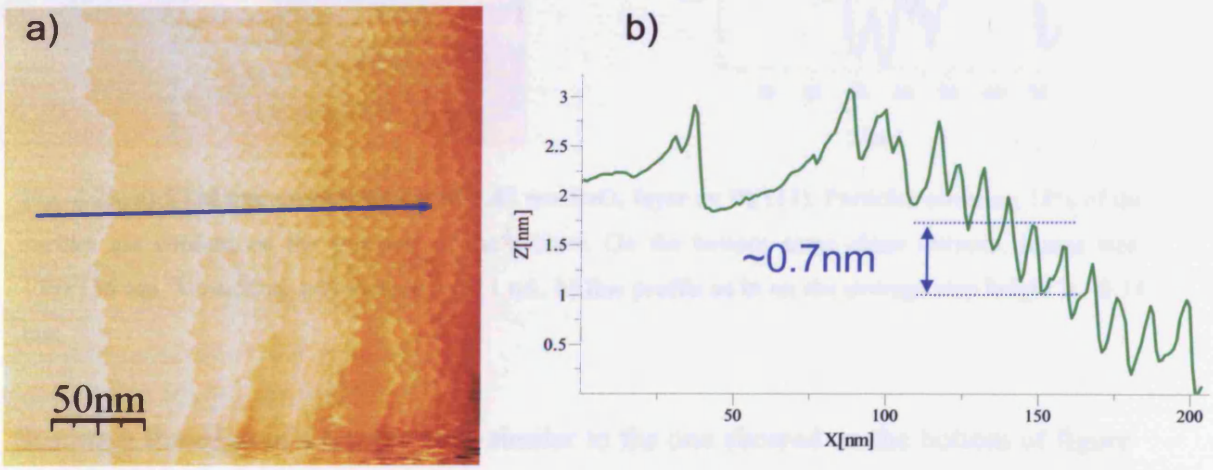

Fig. 4.22: a) STM topographic image of 1.07 nm BaO_x layer on Pt(111). Terraces between 4 and 50 nm wide with teeth-saw like step edges are present. Image size: 250×250 nm. Tunnelling parameters: 0.5 V, 1 nA. b) line profile as in a); the average step height is ~ 0.697 nm.

The terraces are now between 4 and 50 nm wide and the step edges assumed a teeth-saw like configuration. Their average height is around 0.697 nm, value in good agreement with the "c" size for the BaO_2 unit cell (0.677 nm) [7]. Thus an area where BaO_2 was present should have been imaged. In this case a surface coverage of ~1.58 ML should have been obtained.

Another area of the same surface is shown in figure 4.23. A few particles, average 10 nm tall and 4 nm wide, appeared scattered on the surface (covering approx 18% of the area imaged). These particles may well represent BaO_x species, since similar particles were already observed during experiments performed by our group using an STM into a different UHV chamber [41]. On the bottom of figure 4.23, a flat area with a step size of ~ 0.34 nm is present. This value is in agreement with the one expected for the BaO step size, but also for the "a" size of BaO_2 unit cell. In agreement with the O(1s) XP region showing a broad peak resolved as a doublet, this somehow can suggest the presence of both BaO and BaO_2 on the surface.

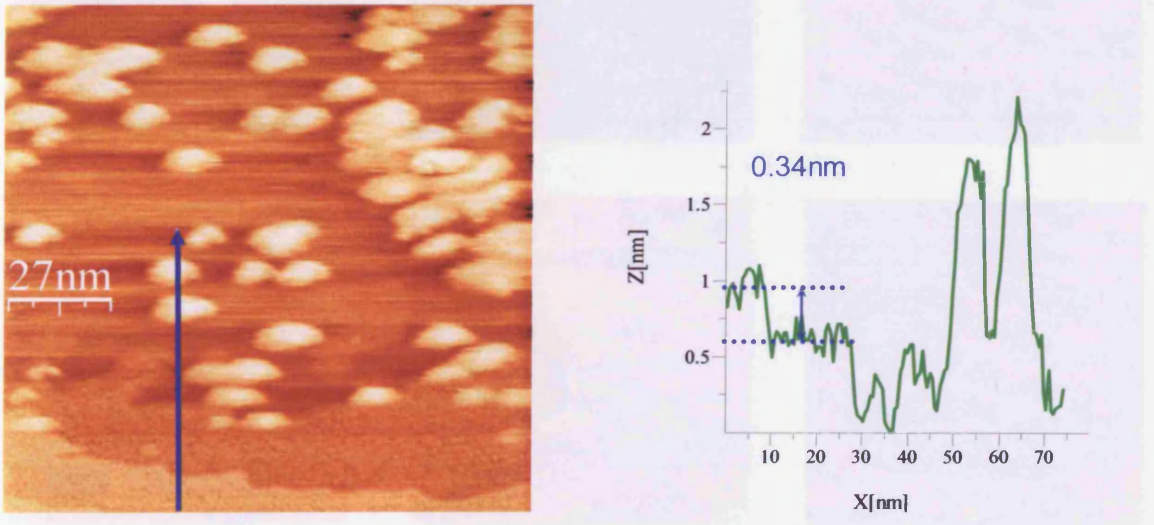

Fig. 4.23: a) STM topographic image of 1.07 nm BaO_x layer on Pt(111). Particles covering 18% of the surface are evident on the top part of the picture. On the bottom some clean terraces. Image size: 136×136 nm. Tunnelling parameters: 1 V, 1 nA. b) line profile as in a); the average step height is ~0.34 nm.

Scanning the edge of a terrace very similar to the one showed on the bottom of figure 4.23, but with a step height of ~ 1.15 nm, elongated triangular features were recorded. These features appeared to change under the influence of the STM tip as shown on the sequence reported in figure 4.24. In particular, some small elongated particles tended

to detach from the finger like structures, became rounded and eventually disappeared, as highlighted by the blue square in frames 1 – 3 and the blue oval in frames 6 - 9. This could be somehow correlated to a not fully oxidised barium layer, which occurred after the annealing at 300 °C.

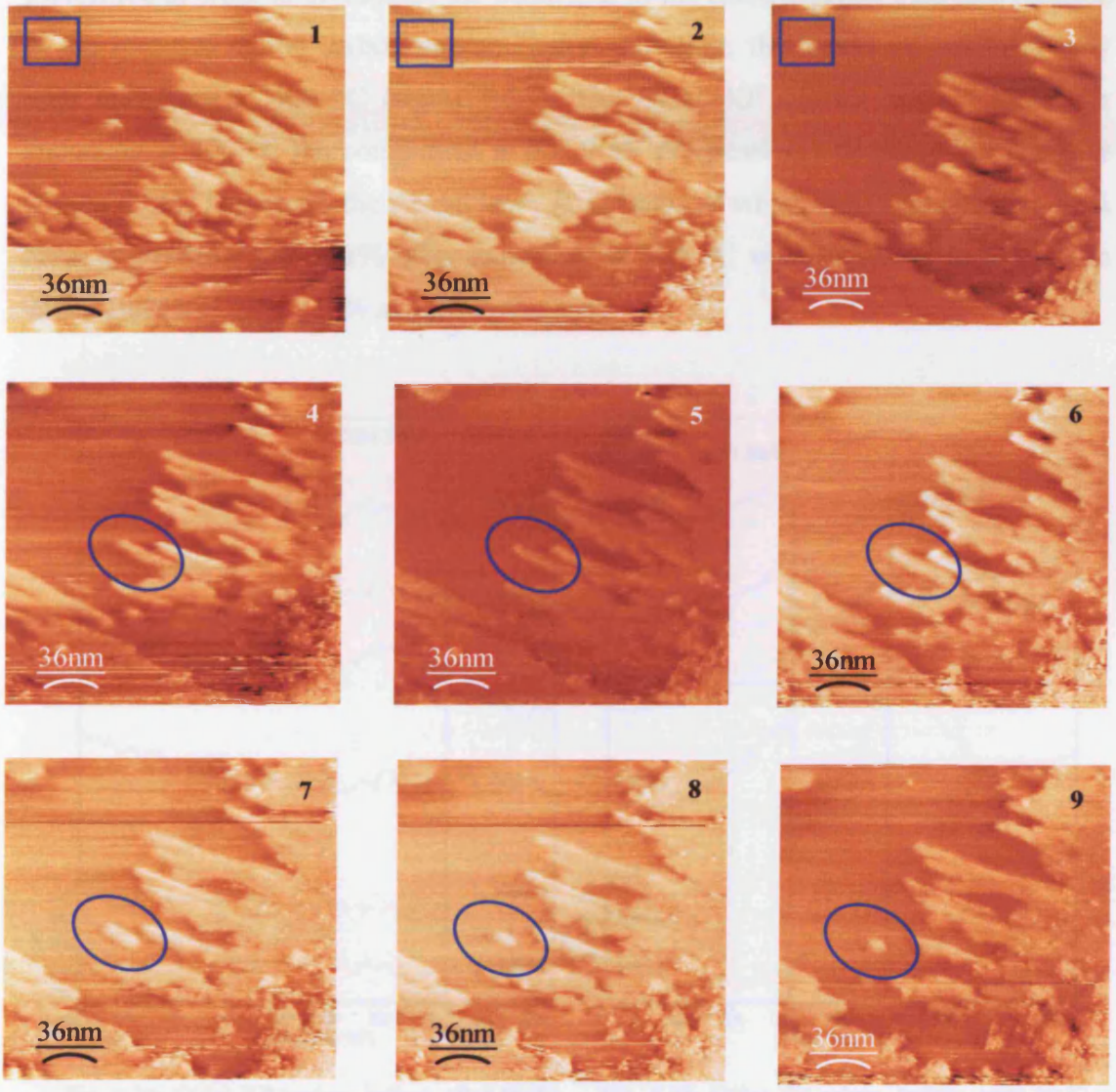

Fig. 4.24: The sequence of topographic STM images of 1.07 nm BaO_x layer on Pt(111) shows that the features present on the same area appear to change while scanning. Frames 1 – 3: an elongated particle in the blue square became rounded and disappears; in the blue oval, the particle detaches from the finger like structure, became rounded and disappears, frames 6 - 9. Images size: 180×180 nm. Tunnelling parameters: 0.5 V, 1 nA.

A similar behaviour was also observed during the experiments performed by our group on KO_x/Pt(111) system [42] and was attributed to the extremely high mobility

of the oxidised potassium on the surface of the Pt(111). Therefore this could also be a common behaviour of not fully oxidised alkaline metal oxides deposited on the platinum surface. Atomic resolution was not achieved during these measurements.

Several annealing treatments at higher temperatures, in vacuum for 30 minutes, were performed in order to investigate the behaviour of the BaO_x adlayer. This also resulted in the removal of the carbon contamination, however, this could be achieved only after annealing at 400 °C (figure 4.25). The O(1s) XP spectra showed that after annealing at 400 °C the component at 531.9 eV progressively decreased in intensity (figure 4.26). Therefore, the mixed layer BaO/BaO_2 of which BaO represented ~85% after preparation and ~61% after annealing at 300 °C was converted to a layer in which BaO was now ~72% and BaO_2 the rest.

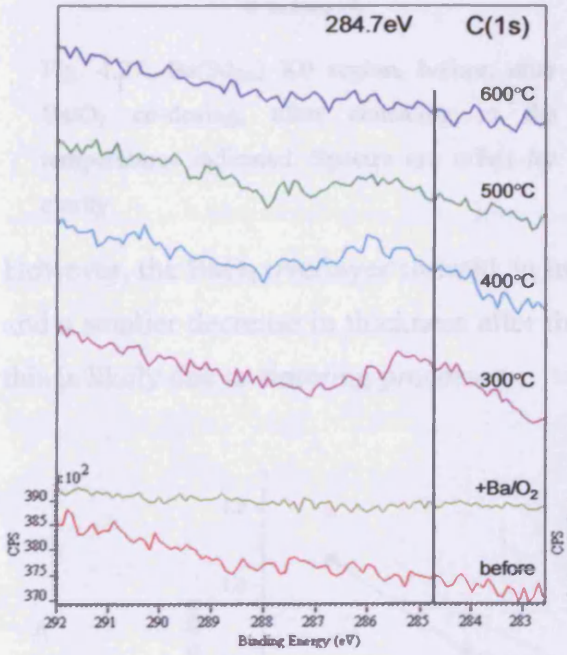

Fig. 4.25: C(1s) XP region, before, after Ba/O_2 co-dosing, after annealing at the temperatures indicated. Spectra are offset for clarity.

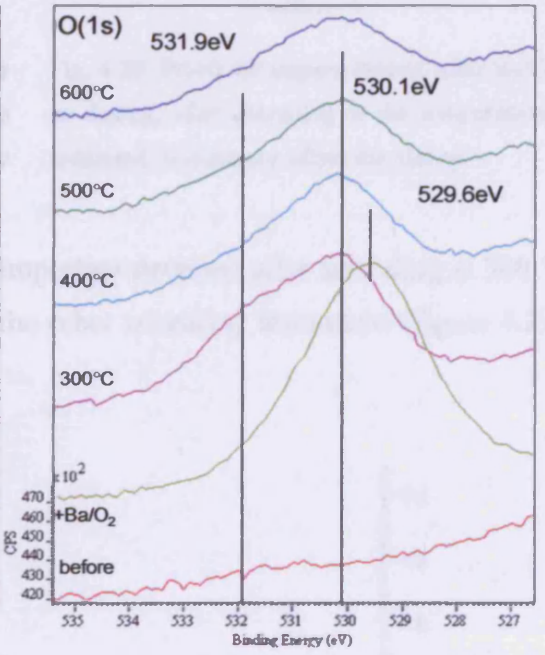

Fig. 4.26: O(1s) XP region, before, after Ba/O_2 co-dosing, after annealing at the temperatures indicated. Spectra are offset for clarity.

This typical composition observed after annealing at 400 °C stayed unchanged after annealing at 500 °C and 600 °C. The $Ba(3d_{5/2})$ peaks shifts to 779.8 eV after annealing at 300 °C and then to 780.3 eV after annealing at 600 °C (figure 4.27). The Pt(4f) regions did not appear to change in shape during the different annealing steps (figure 4.28).

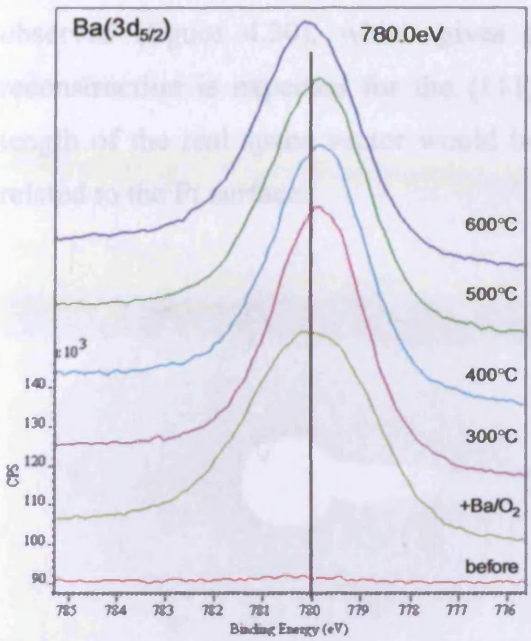

Fig. 4.27: $Ba(3d_{5/2})$ XP region, before, after Ba/O_2 co-dosing, after annealing at the temperatures indicated. Spectra are offset for clarity.

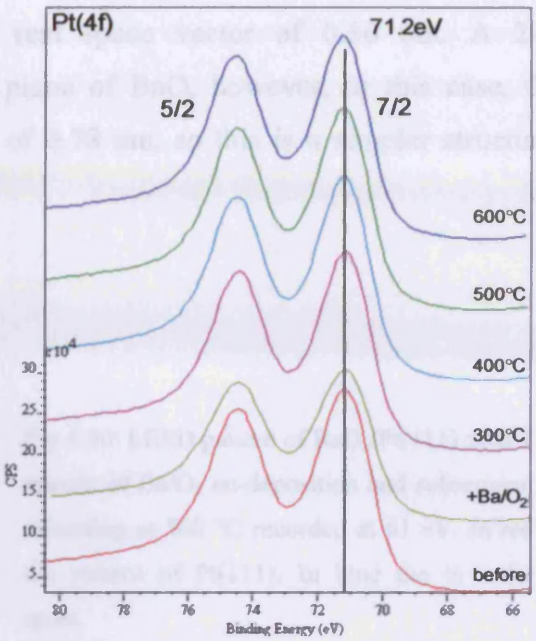

Fig. 4.28: Pt(4f) XP region, before, after Ba/O_2 co-dosing, after annealing at the temperatures indicated. Spectra are offset for clarity.

However, the BaO_x overlayer showed an important decrease after annealing at 300 °C and a smaller decrease in thickness after the other annealing testaments (figure 4.29); this is likely due to sintering processes.

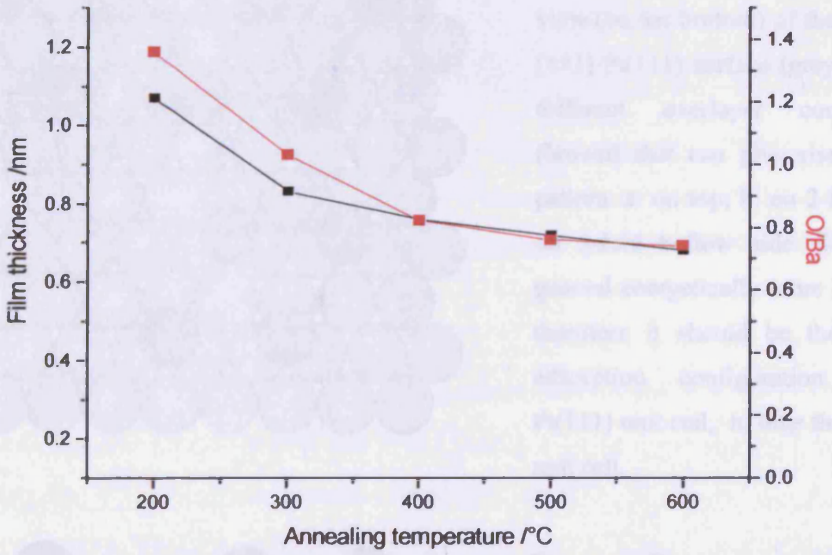

Fig. 4.29: Graph showing the change in film thickness vs annealing temperature (black curve) and the correspondent O/Ba atomic ratio (red curve).

After annealing at 500 °C a very sharp LEED showing a Pt(111) 2×2 pattern was observed (figure 4.30), which gives a real space vector of 0.56 nm. A 2×2 reconstruction is expected for the (111) plane of BaO, however, in this case, the length of the real space vector would be of 0.78 nm, so this is a simpler structure, related to the Pt surface.

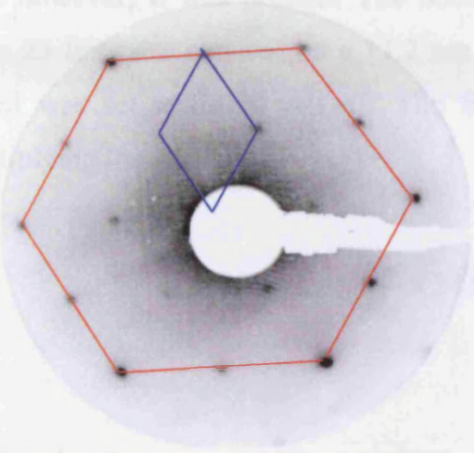

Fig 4.30: LEED pattern of BaO_x/Pt(111) after 1 minute of Ba/O_2 co-deposition and subsequent annealing at 500 °C recorded at 61 eV. In red the pattern of Pt(111). In blue the ½ order spots.

The LEED shows a Pt(111) 2×2 reconstruction is also a known pattern for 0.25 ML of oxygen adsorbed threefold hollow sites on Pt(111) [43]. In figure 4.31 c) a model of the surface corresponding to the 2×2 LEED pattern is shown.

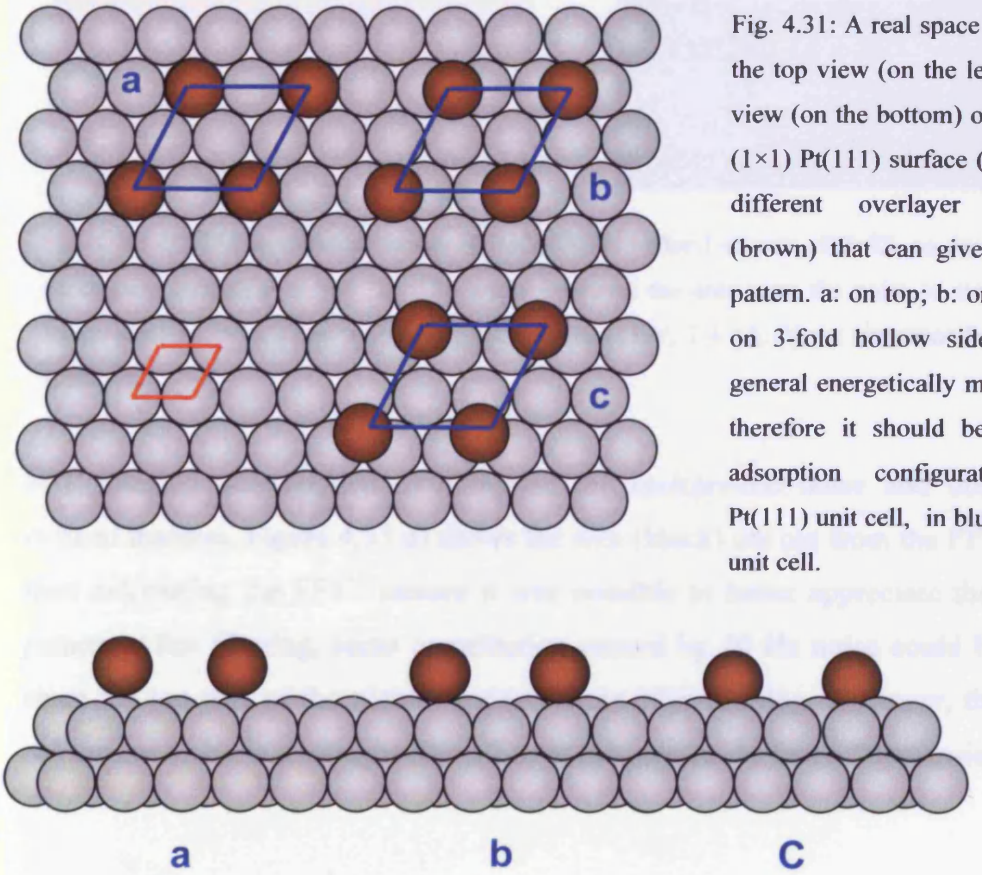

Fig. 4.31: A real space model showing the top view (on the left) and the side view (on the bottom) of the hexagonal (1×1) Pt(111) surface (grey) and three different overlayer configurations (brown) that can give rise to a 2×2 pattern. a: on top; b: on 2-fold site; c: on 3-fold hollow side. 3-fold is in general energetically more favourable, therefore it should be the preferred adsorption configuration. In red Pt(111) unit cell, in blue the overlayer unit cell.

STM analysis revealed that some ordered areas were present. Figure 4.32 a) shows a distorted hexagonal arrangement of atoms, and b) is the associated Fast Fourier Transform. Some interference shown as diagonal lines due to background 50 Hz noise, indicated by the arrow, was present on the image. This kind of noise is normally due to interference with the mains and is efficiently suppressed with digital filters. In this case however, it was present. The noise frequency was calculated in the following way: 23 lines are counted on a 11.2 nm length, this means 2.05 lines nm^{-1}. The scan speed was set to 24.96 nm s^{-1}. The frequency of the lines can be calculated by multiplying the two:

$$2.05\frac{line}{nm}\times 24.96\frac{nm}{s}=51.16\frac{line}{s}$$

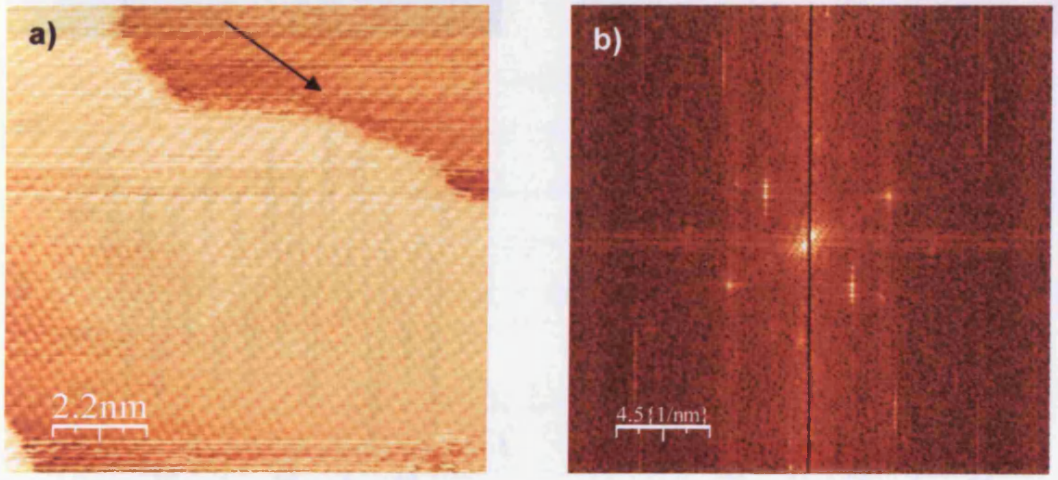

Fig. 4.32: a) STM topographic image of BaO_x/Pt(111) after 1 minute of Ba/O_2 co-deposition and subsequent annealing at 500 °C; The arrow indicates the area were the noise is more evident. Image size: 11.2×11.2 nm. Tunnelling parameters: 0.3 V, 2.4 nA. b) the correspondent 2D-FFT spectrum.

FFT filtering was applied to minimise the background noise and observe better defined features. Figure 4.33 a) shows the area (black) cut out from the FFT spectrum, then calculating the FFT^{-1} picture it was possible to better appreciate the hexagonal pattern. After filtering, some contribution caused by 50 Hz noise could be removed, since the top part of the picture appears clear after filtering. However, the atoms do not appear to be in a straight line all over the picture. In fact a "depression" that can

distort the lattice is present on the left side (red circle in figure 4.31 b). The line profiles taken along the three directions as in figure 4.31 b), showed a spacing of ~0.26±0.2 nm between the atoms, so it appears that the Pt(111) surface should have been atomically resolved.

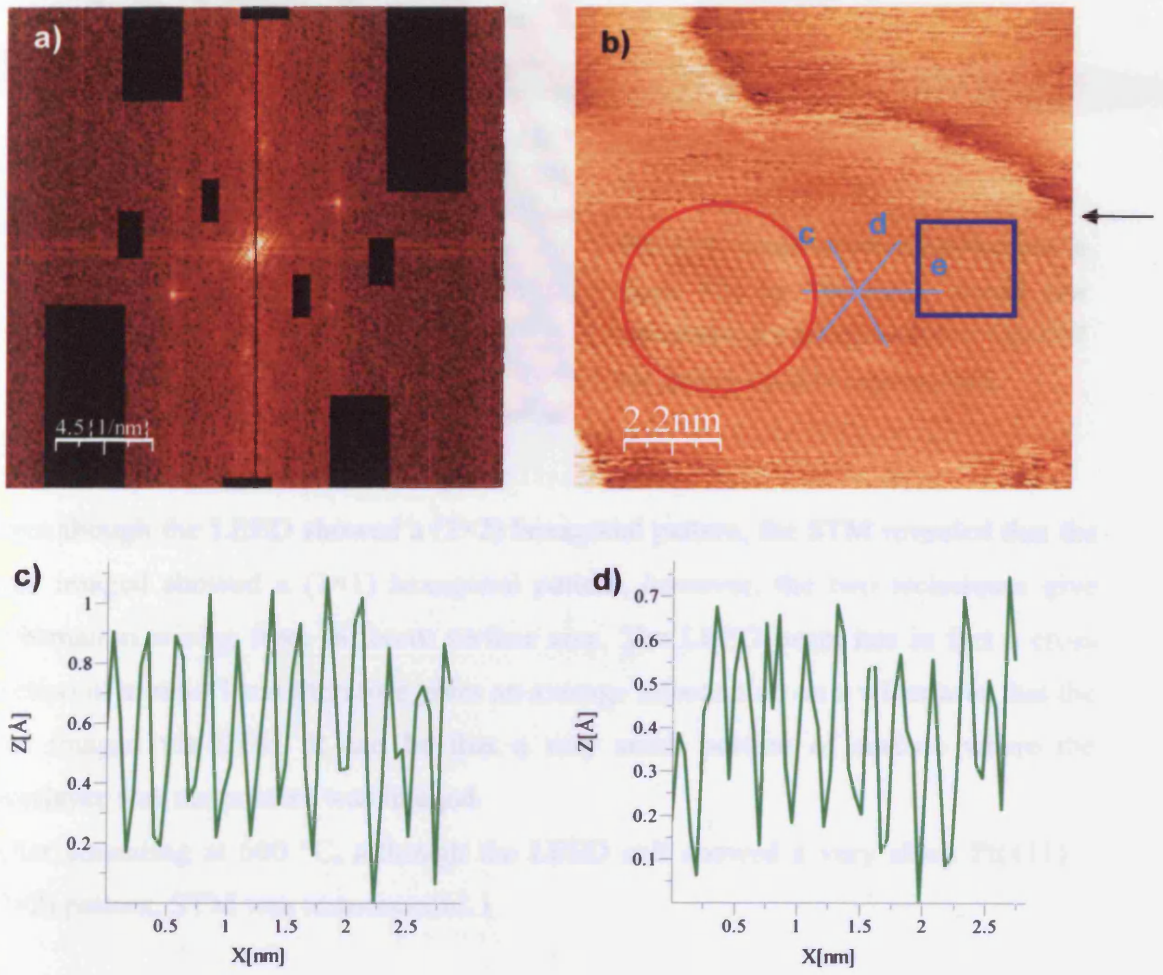

Fig. 4.33: a) the 2D-FFT spectrum after the filtering process was applied; b) the correspondent FFT^{-1} image, allows to better distinguish the features on the surface, the black arrow indicates a tip change, the red circle a depression and the blue square the area magnified in fig 4.34; c), d) and e) line profiles as in b).

Figure 4.34 shows a magnification of the blue area in figure 4.31 b). The image was equalized to enhance the contrast and a hexagonal lattice with 0.27 nm spacing was superimposed to it.

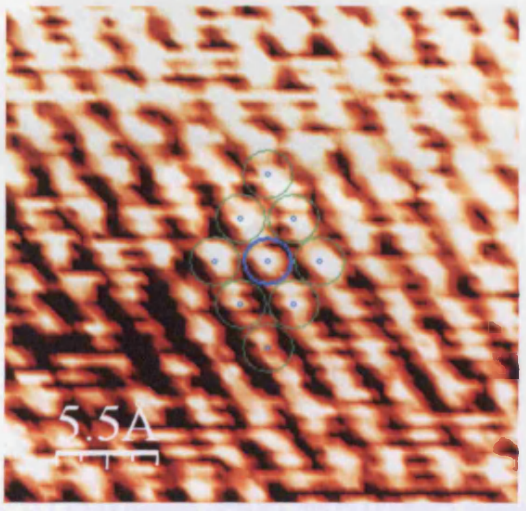

Fig. 4.34: magnification of the blue area in figure 4.33 b). The image contrast was enhanced and a hexagonal lattice with 0.27 nm spacing could be superimposed.

Even though the LEED showed a (2×2) hexagonal pattern, the STM revealed that the area imaged showed a (1×1) hexagonal pattern, however, the two techniques give information arising from different surface area. The LEED beam has in fact a cross section of around 1mm therefore gives an average information on a wider area that the one imaged via STM. It can be that a very small portion of surface where the overlayer was not present was imaged.
After annealing at 600 °C, although the LEED still showed a very sharp Pt(111) – (2×2) pattern, STM was unsuccessful.

For the thicker BaO_x film prepared (1.58 nm after preparation), after annealing at 400 °C (0.94 nm new thickness) a hexagonal LEED pattern showing a reconstruction that can be described as the superimposition of the Pt(111) (1×1) pattern, plus three (8x2) domains rotated 30° was observed. Although the poor background contrast does not allow appreciating all the diffractions maxima in the pattern, the pattern in figure 4.35 a) was reconstructed by symmetrical relationship in figure 4.35 b) showing the 1/8 of order spots in blue. A (8×2) reconstruction should correspond to a real space unit cell of 2.22 × 0.54 nm, meaning that at least three different domains with three different orientations of a very long range ordered structure was present on the crystal.

A real space model of this surface is proposed in figure 4.36. Unfortunately, attempts to image it via STM were unsuccessful.

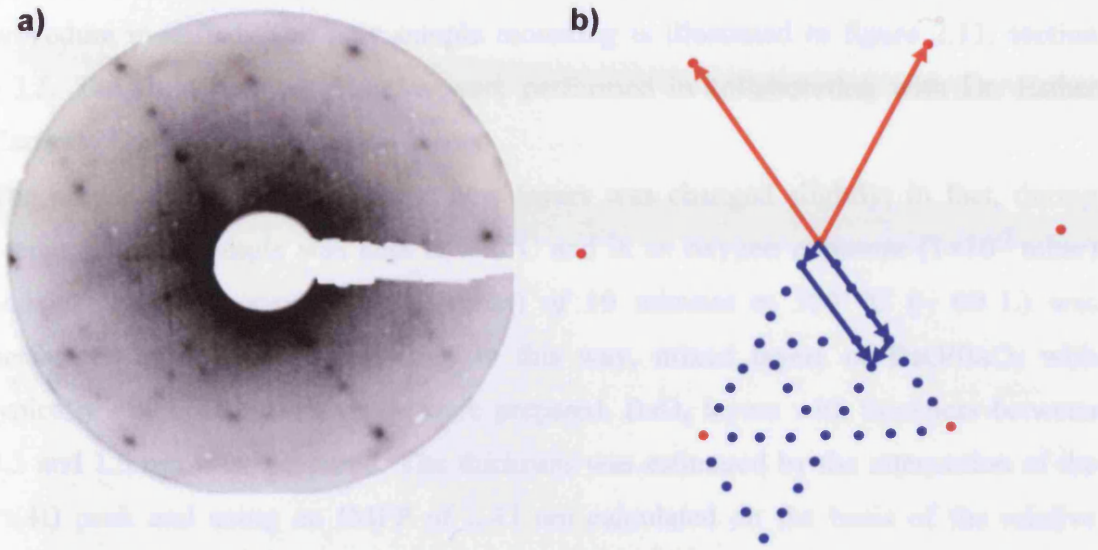

Fig. 4.35: a) LEED pattern of BaO_x/Pt(111) after 1 minute and 30 seconds of Ba/O_2 co-deposition and subsequent annealing at 400 °C recorded at 50 eV. b) attribution of the diffraction spots of a): in red the Pt(111) lattice vectors and spots, in blue the unit cell and spots originated by the overlayer.

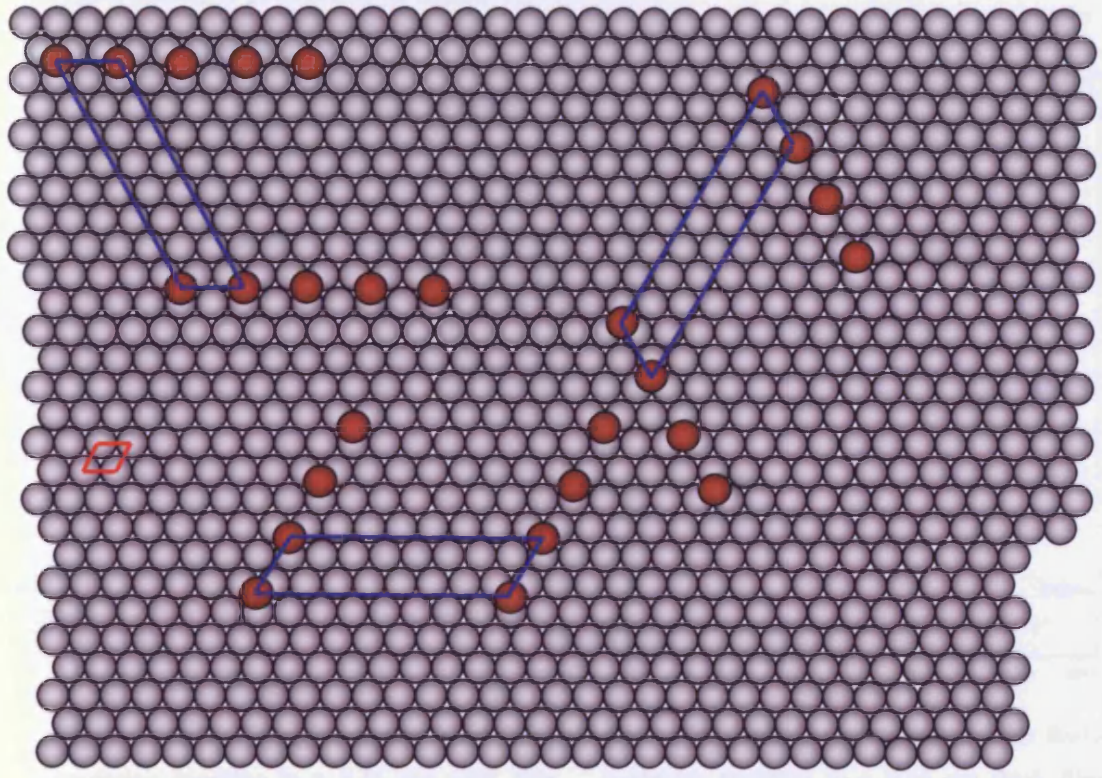

Fig. 4.36: A real space model showing the hexagonal (1×1) Pt(111) surface (grey) and three domains of a 8×2 overlayer (brown). In red the Pt(111) unit cell, in blue the unit cells of the overlayer.

c) Deposition in oxygen pressure, sample at 300°C

In the attempt to improve the resolution of the STM pictures, the Pt(111) single crystal was mounted on a variable temperature sample holder and the preparation procedure modified. The new sample mounting is illustrated in figure 2.11, section 2.3.5. The following experiments were performed in collaboration with Dr. Esther Carrasco Burgos.

The preparation method for these new layers was changed slightly; in fact, during preparation the sample was kept at 300°C and in an oxygen exposure (1×10^{-7} mbar) and an oxygen exposure (1×10^{-7} mbar) of 10 minutes at 500 °C (~ 60 L) was performed after the Ba/O_2 dosing. In this way, mixed layers of BaO/BaO_2 with typically ~80% of barium oxide were prepared. BaO_x layers with thickness between 0.3 and 1.5 nm were prepared. The thickness was estimated by the attenuation of the Pt(4f) peak and using an IMFP of 2.43 nm calculated on the basis of the relative amount of oxide and peroxide as described earlier (see Appendix A). The behaviour of these layers is described, using as an example a 0.45 nm thick film. The O(1s) XP region, showing the two oxygen components (FWHM ~1.95 eV) related to the two oxygen states, is presented in figure 4.37.

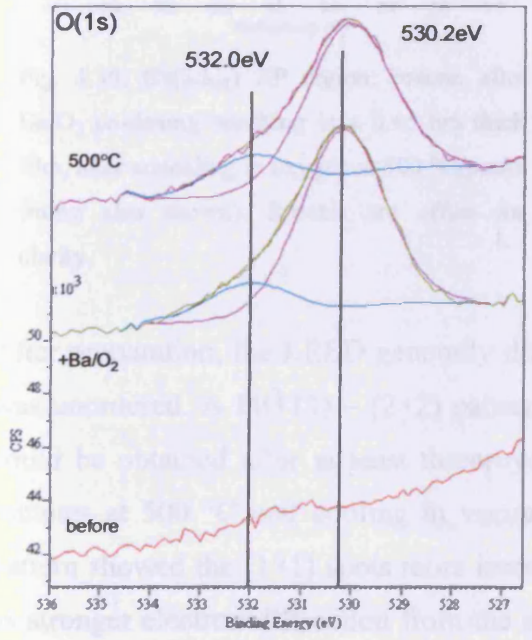

Fig. 4.37: O(1s) XP region, before, after Ba/O_2 co-dosing resulting in a 0.45 nm thick film, after annealing in oxygen at 500 °C (peaks fitting also shown). Spectra are offset for clarity.

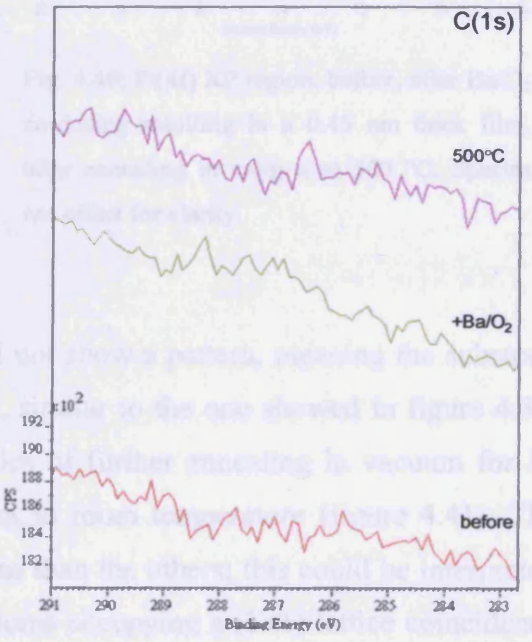

Fig. 4.38: C(1s) XP region, before, after Ba/O_2 co-dosing resulting in a 0.45 nm thick film, after annealing in oxygen at 500 °C (peaks fitting also shown). Spectra are offset for clarity.

The barium overlayers prepared using this new preparation were more oxidised than the ones prepared with the preparation described in b). Moreover, the relative amount BaO/BaO_2 stayed approximately constant after annealing in oxygen. The C(1s) in figure 4.38, demonstrated that carbon was not present. The $Ba(3d_{5/2})$ peak (figure 4.39) was recorded at 780 eV and moved to 780.2 eV after annealing in oxygen at 500 °C. The Pt(4f) region upon which the calibration was made is shown in figure 3.40.

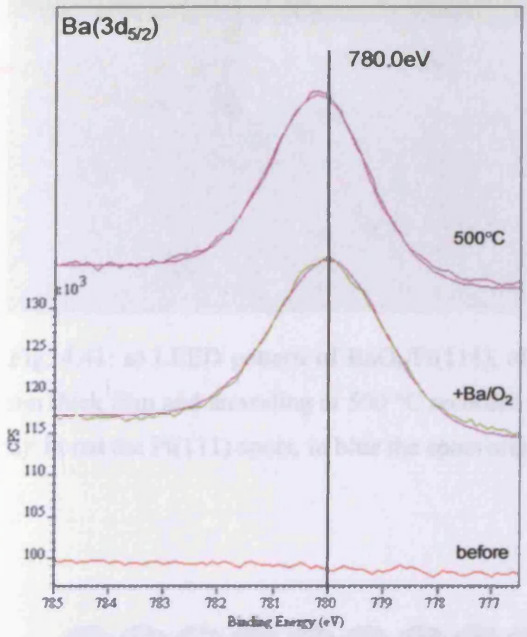

Fig. 4.39: $Ba(3d_{5/2})$ XP region, before, after Ba/O_2 co-dosing resulting in a 0.45 nm thick film, after annealing in oxygen at 500 °C(peaks fitting also shown). Spectra are offset for clarity.

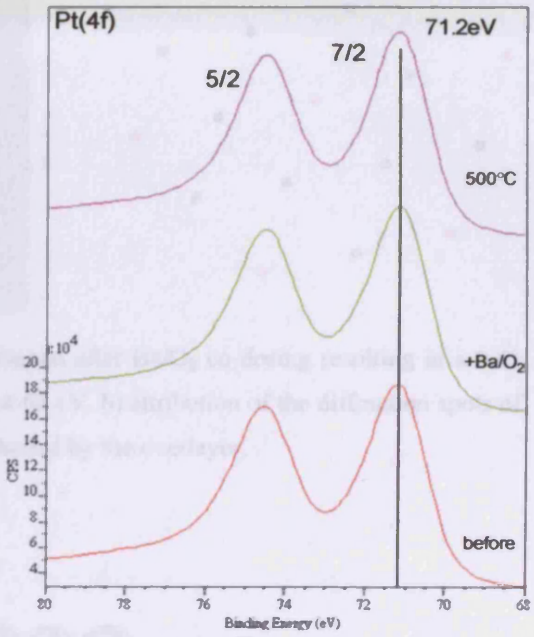

Fig. 4.40: Pt(4f) XP region, before, after Ba/O_2 co-dosing resulting in a 0.45 nm thick film, after annealing in oxygen at 500 °C. Spectra are offset for clarity.

After preparation, the LEED generally did not show a pattern, meaning the substrate was unordered. A Pt(111) – (2×2) pattern, similar to the one showed in figure 4.30, could be obtained after at least three cycles of further annealing in vacuum for 10 minutes at 500 °C and cooling in vacuum to room temperature (figure 4.41). The pattern showed the (1×1) spots more intense than the others; this could be interpreted as stronger electron diffraction from the atoms occupying a (1×1) lattice coincidence point on the surface. A model to describe this situation is shown in figure 4.42. The lattice coincidence point could be represented by a barium (2×2) overlayer, on top of an oxygen (2×2) overlayer. The barium atoms will then be directly "on top" of some

of the platinum atoms. Therefore some BaO/BaO_2 units should be present on the surface.

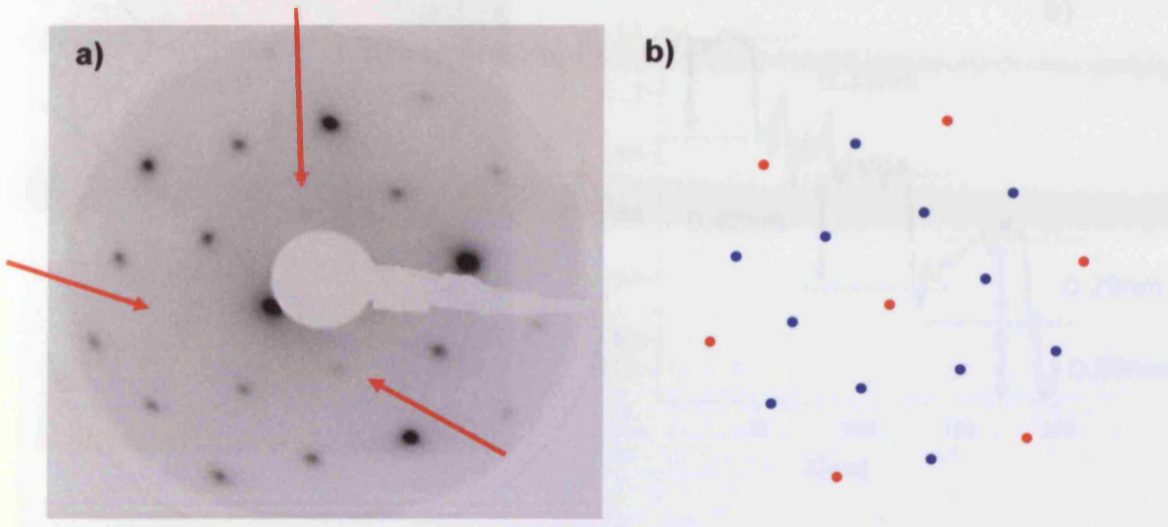

Fig. 4.41: a) LEED pattern of $BaO_x/Pt(111)$, obtained after Ba/O_2 co-dosing resulting in a 0.45 nm thick film and annealing at 500 °C recorded at 62 eV. b) attribution of the diffraction spots of a): in red the Pt(111) spots, in blue the spots originated by the overlayer.

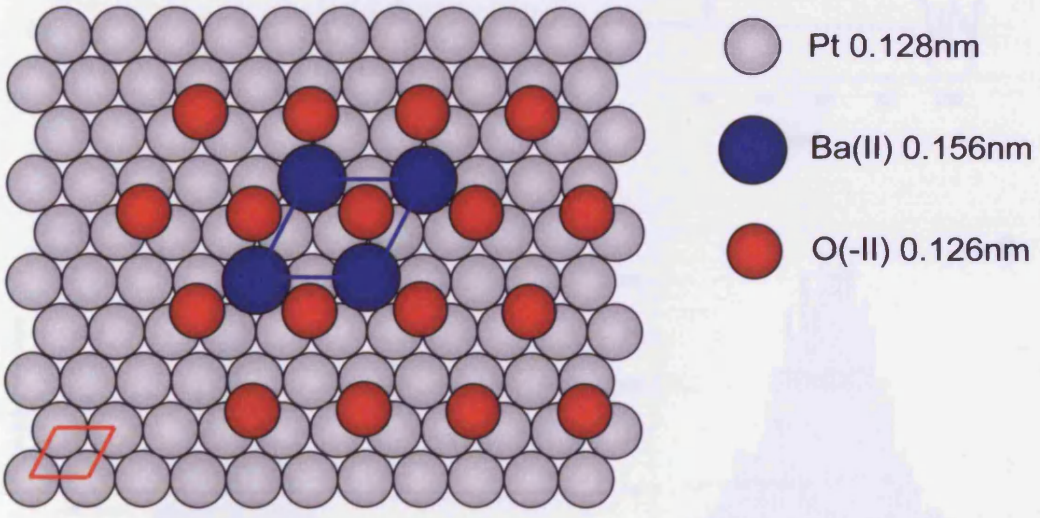

Fig. 4.42: Model to interpret the LEED pattern in figure 4.41. In LEED, the (2×2) arrangement has spots in the (½,½) and (1×1) position with respect to the (1×1) substrate. However, in the (1×1) position also the substrate spots are visible. This gives higher intensity of the spots in the (1×1) positions. In red the Pt(111) unit cell, in blue the BaO unit cell.

STM showed some terraces covered with an unordered and rough adlayer, (figure 4.43, area type 1), with patches that appeared even rougher (area type 2).

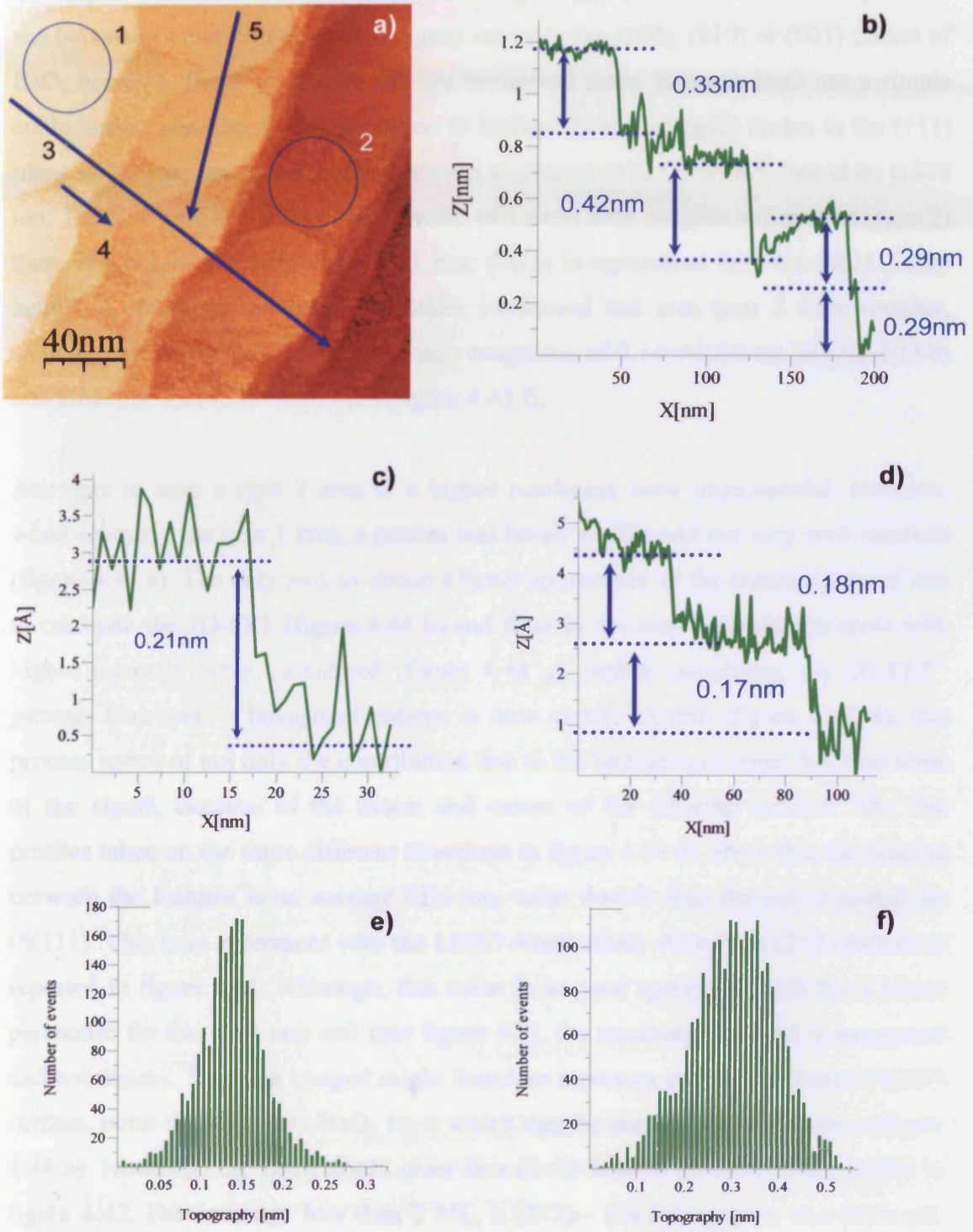

Fig. 4.43: a) STM topographic image of BaO_x/Pt(111) obtained after Ba/O_2 co-dosing resulting in a 0.45 nm thick film and annealing at 500 °C. Image size: 200×200 nm. Tunnelling parameters: 0.21 V, 0.09 nA. b) line profile 3 as in a); c) line profile 4 as in a); d) line profile 5 as in a); e) roughness analysis of area 1 in a) and f) roughness analysis of area 2 in a).

The line profile b shows that the step heights between the area type 1 and type 2 vary between 0.29 and 0.42 nm, values higher than the one for Pt(111). A step size of 0.42 nm may be considered in agreement with the spacing expected for the distance of 0.39 nm between two barium (or two oxygen) atoms in the (100), (010) or (001) planes of BaO, however, these are square and not hexagonal faces. Because BaO has a simple cubic lattice, also the distance between to barium (or two oxygen) atoms in the (111) plane is 0.39 nm and the distance between to planes <111> oriented should be 0.478 nm. The line profile c shows that between two areas with rougher appearance (type 2) there is a height difference of ~ 0.21 nm; this is in agreement with the Pt(111) step height. A roughness analysis evaluation, confirmed that area type 2 were rougher, showing that area type 1 have an average roughness of 0.14+/-0.04 nm (figure 4.43 e) and area type 2 of 0.30+/-0.09 nm (figure 4.43 f).

Attempts to scan a type 2 area to a higher resolution were unsuccessful; however, when scanning the type 1 area, a pattern was barely visible and not very well resolved (figure 4.44 a). The only way to obtain a better appearance of the features present was to calculate the 2D-FFT (figure 4.44 b) and filter in the way that only the spots with higher intensity were considered (figure 4.44 c), before calculating the $2D\text{-}FFT^{-1}$ picture. However, a hexagonal pattern is now clearly visible (figure 4.44 d), this process removed not only the contribution due to the background noise, but also some of the signal, because of the extent and nature of the filtering process. The line profiles taken on the three different directions in figure 4.44 d), show that the spacing between the features is on average 0.54 nm, value double than the one expected for Pt(111). This is in agreement with the LEED observations showing a (2×2) pattern as reported in figure 4.41. Although, this value is in good agreement with the a lattice parameter for the BaO unit cell (see figure 4.2), the structure observed is hexagonal and not square. The area imaged might therefore represent only a O-covered Pt(111) surface, more than the BaO/BaO_2 layer which may be the unordered feature in figure 4.44 a). However, the BaO_x could grow in a (2×2) fashion as show in the model in figure 4.42. For coverage less than 2 ML, a (2×2) - Cu(111) pattern was observed, also when preparing the BaO(100)/Cu(111) system (see section 4.4.2.1.).

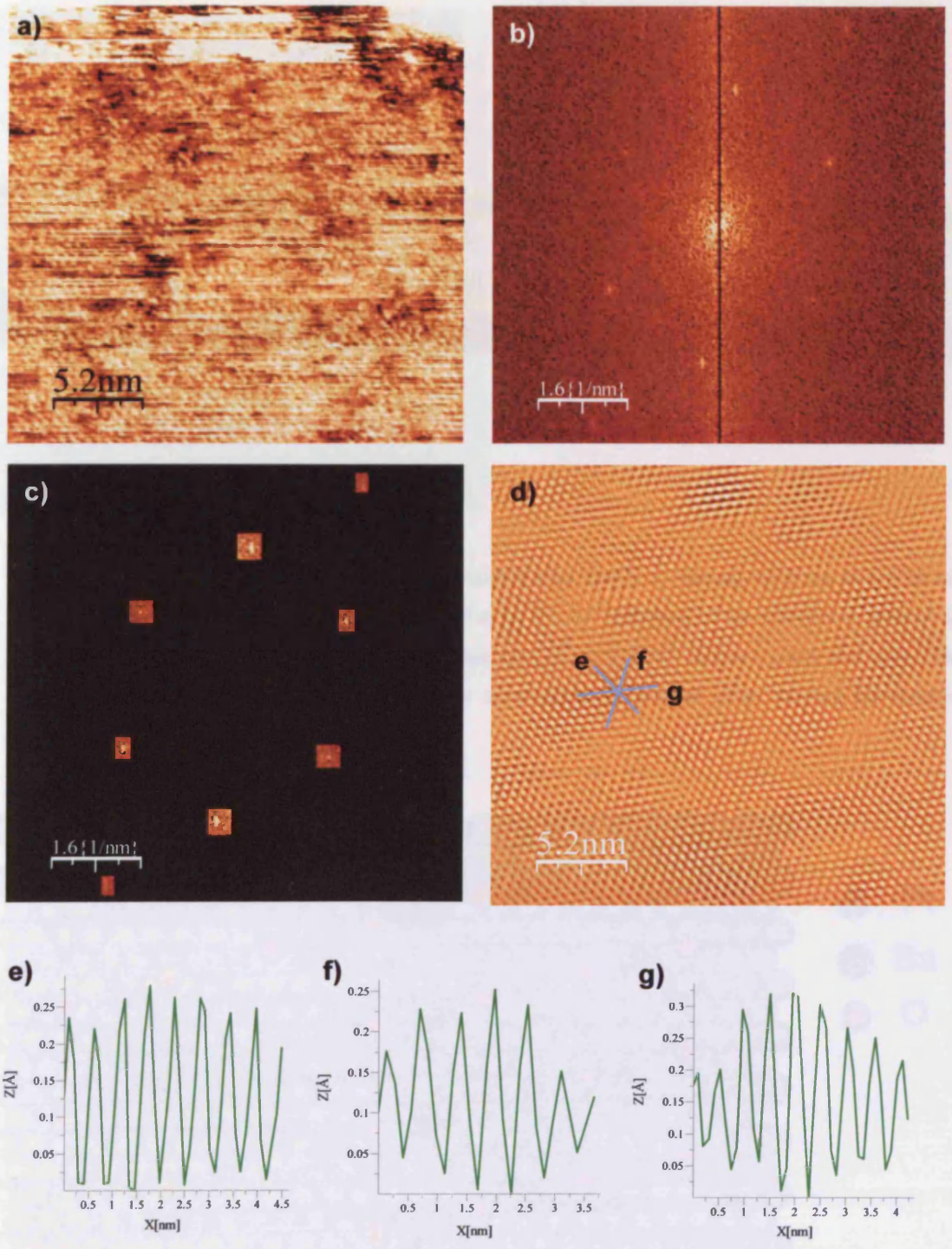

Fig. 4.44: a) STM topographic image of the area type 2 in figure 4.43. Image size: 26×26 nm. Tunnelling parameters: 0.09 V, 0.05 nA. b) 2D-FFT spectrum of a); c) the area used for filtering; d) the $2D\text{-}FFT^{-1}$ image; e), f) and g), line profiles as in d).

Upon flash annealing to 700 °C the previous preparation, the system showed a $(2\sqrt{3}\times2\sqrt{3})$-R30° LEED. A model to interpret this LEED pattern is shown in figure 4.46.

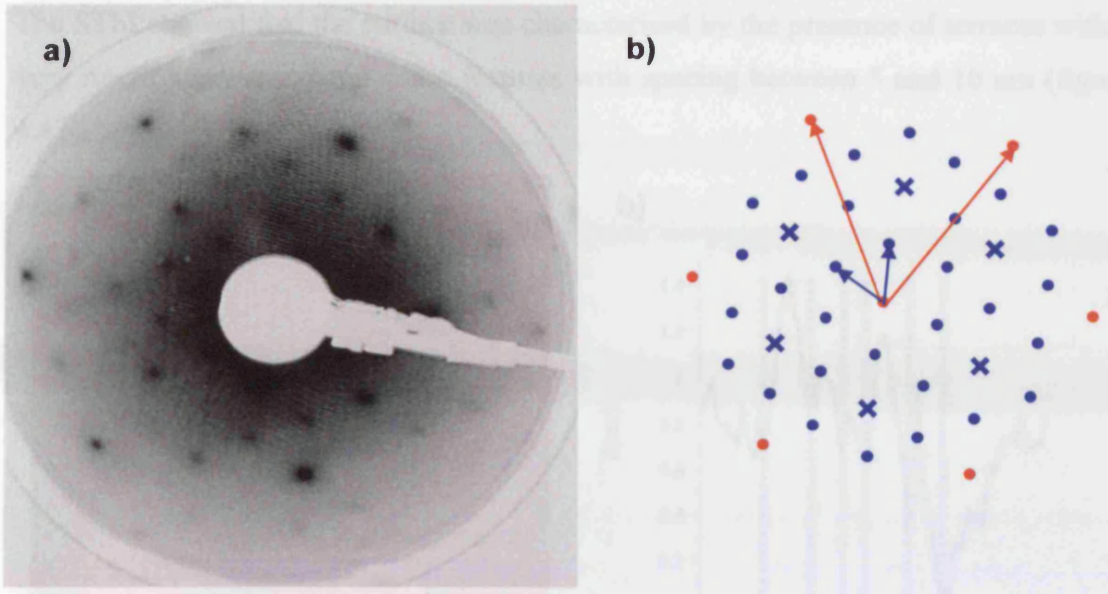

Fig 4.45: a) LEED pattern of BaO_x/Pt(111), obtained after Ba/O_2 co-dosing resulting in a 0.45 nm thick film and flash annealing at 700 °C recorded at 68 eV. b) attribution of the diffraction spots of a): in red the Pt(111) lattice vectors and spots, in blue the $(2\sqrt{3}\times2\sqrt{3})R30°$ lattice vectors and spots. The crosses indicate very faint diffraction spots that appeared to be present when varying the electron energy.

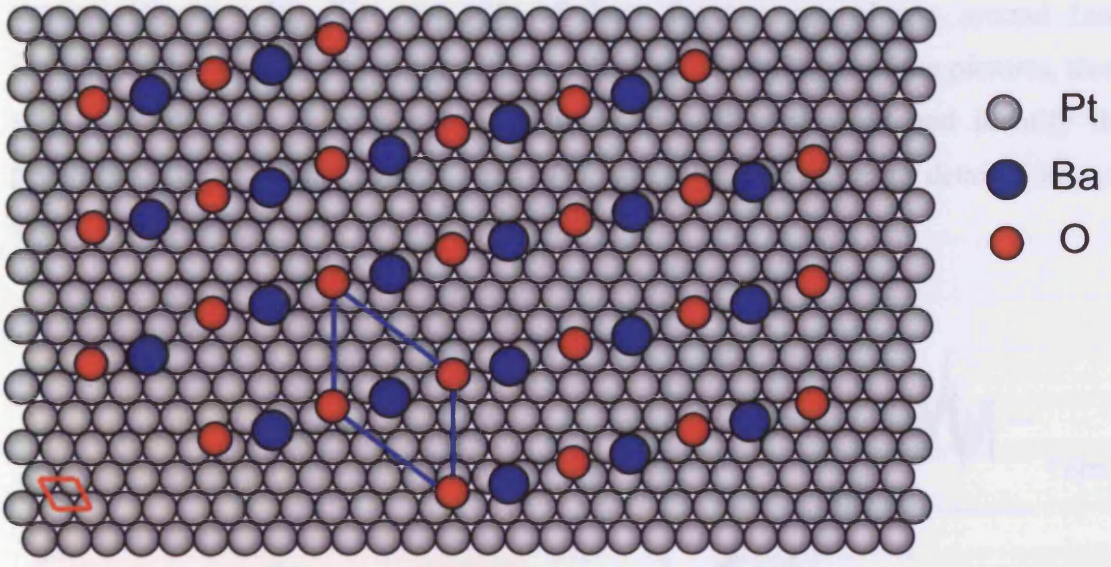

Fig. 4.46: Model to interpret the LEED pattern in figure 4.45. In red the Pt(111) unit cell, in blue the BaO unit cell.

Being the Pt(111) unit cell ~ 0.27 nm, the unit cell of the $(2\sqrt{3}\times2\sqrt{3})$-R30° overlayer is ~ 0.93 nm. This value is in good agreement with the one relative to the moiré pattern observed via STM by Stone and co-workers [24].

The STM showed that the surface was characterised by the presence of terraces with a very rough appearance and some features with spacing between 5 and 10 nm (figure 4.47).

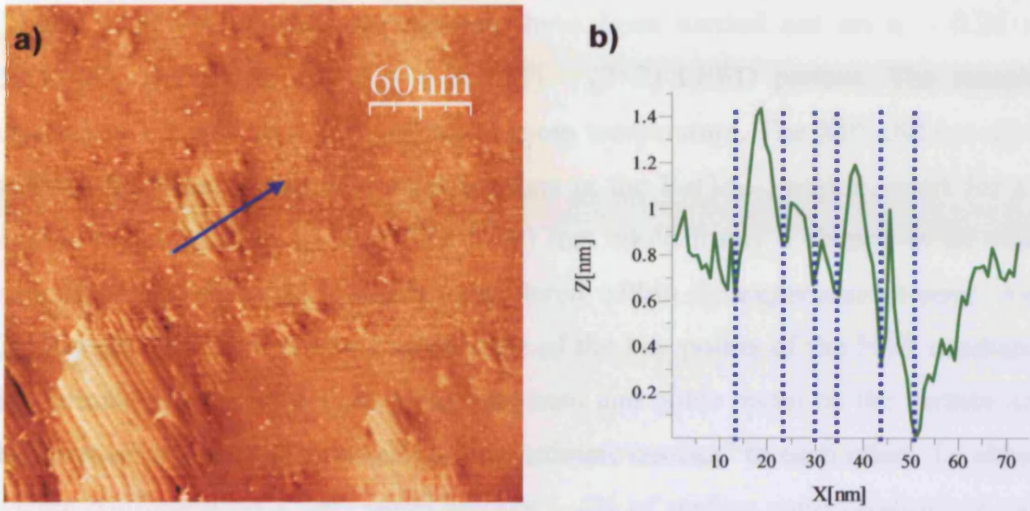

Fig 4.47: a) STM topographic image of the same preparation as in figure 4.44, after flash annealing at 700 °C. Image size: 298×298 nm. Tunnelling parameters: 2 V, 1.98 nA. b) line profile as in a).

Another area showed the presence of features that can be described as "holes" on the terraces (figure 4.48). The step size of these features was always around 1nm. Unfortunately, because of the big scale and the lack of resolution of the pictures, there was again no way to discriminate between the different areas and identify the presence of the oxidised barium Any other attempt to obtain more detailed images was not successful.

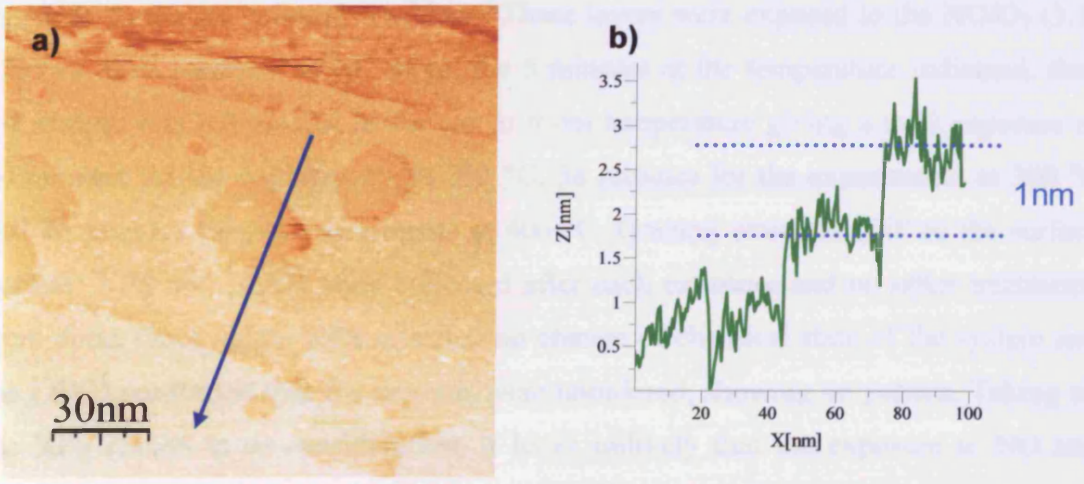

Fig. 4.48: a) STM topographic image of the same preparation as in figure 4.44, after flash annealing at 700 °C. Image size: 150×150 nm. Tunnelling parameters: 2 V, 1.98 nA. b) line profile as in a).

4.4.1.3. NO and NO/O_2 exposures

On very thin layers (~ 0.2 nm) of oxidised barium, some NO and NO/O_2 dosing experiments have been performed in order to investigate the NO_x storage process.

Firstly, some NO dosing experiments have been carried out on a ~ 0.24 nm of BaO/BaO_2 thick film showing a Pt(111) – (2×2) LEED pattern. The sample was exposed to 1 L and then 10 L of NO at room temperature. The XPS did not show any peak in the N(1s) region nor modifications in the $Ba(3d_{5/2})$ region, apart for a small shift to lower binding energy (779.7 eV) that could imply a change in its oxidation state, however, this shift could be considered within the experimental error. Also the O(1s) peak appeared to be constant. One of the key points of the NSR mechanism is the simultaneous presence of storage medium and noble metal on the surface and, for the reaction to occur, they should be in "intimate contact" to each other. To obtain this system configuration a very small amount (~4% of surface concentration) of oxidised barium was left on the surface after sputtering and flash annealing to 500 °C a 4.3 nm thick preparation. Barium was visible only when collecting the XP spectra at grazing emission (20° from the surface normal) and the LEED did not show any pattern. This sample was exposed to 5×10^{-8} mbar of NO/O_2 (2:1) at 200 °C for 5 minutes (15 Langmuirs) and then allowed to cool to room temperature in the gas mixture obtaining a total exposure time of 30 minutes. XP spectra did not show changes in chemical state nor amount of the species present. In particular no N(1s) peak was observed. Different sets of NO/O_2 (3:1) dosing experiments were carried out on a ~ 0.12 nm thick BaO/BaO_2 unordered films with the aim of varying the temperature at which the exposure to the gas mixture was done. These layers were exposed to the NO/O_2 (3:1) mixture, total pressure 5×10^{-8} mbar, for 5 minutes at the temperature indicated, then the sample was left to cool in the gas to room temperature giving a total exposure of 30 minutes for the experiments at 200 °C, 38 minutes for the experiments at 300 °C and 46 minutes for the experiments at 400 °C. Grazing emission (20° to the surface normal) XPS and LEED were collected after each exposure and no other treatments were done. Once again, XPS revealed no change of chemical state of the system and the LEED confirmed that the systems were unordered, showing no pattern. Taking all the XPS results in to consideration, it looks unlikely that the exposure to NO and NO/O_2 had any effect, at least at the conditions in which the experiments were performed.

4.4.2. Layers prepared on Cu(111)

4.4.2.1. BaO film preparation

The Cu(111) single crystal was cleaned by means of Ar^+ sputtering at 1 keV and annealing 650 °C for 10 minutes. To prepare the BaO film, Ba was evaporated at room temperature using a current of 6.9 A, for 3 minutes, for 4 times. At the end of the depositions, evaluating the attenuation of the $Cu(2p_{3/2})$ peak, a barium layer of ~ 6.9 ML was deposited. Figure 4.49 shows the sequence of $Cu(2d_{3/2})$ XP spectra for the full BaO preparation). The XPS showed the $Ba(3d_{5/2})$ peak at ~ 780.7 eV, value in agreement with the one expected for metallic barium (see table 4.1). Figure 4.50 shows the sequence of $Ba(3d_{5/2})$ XP spectra for the full BaO preparation.

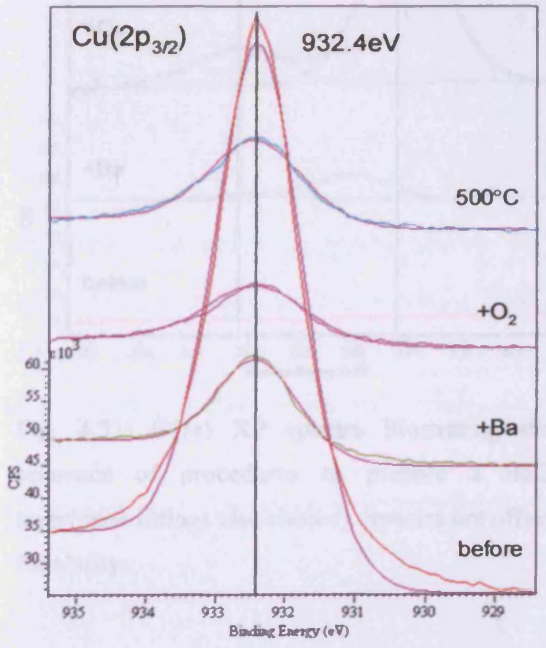

Fig. 4.49: $Cu(2p_{3/2})$ XP spectra illustrating the sequence of procedures to prepare a BaO layer (peak fittings also shown). Spectra are offset for clarity.

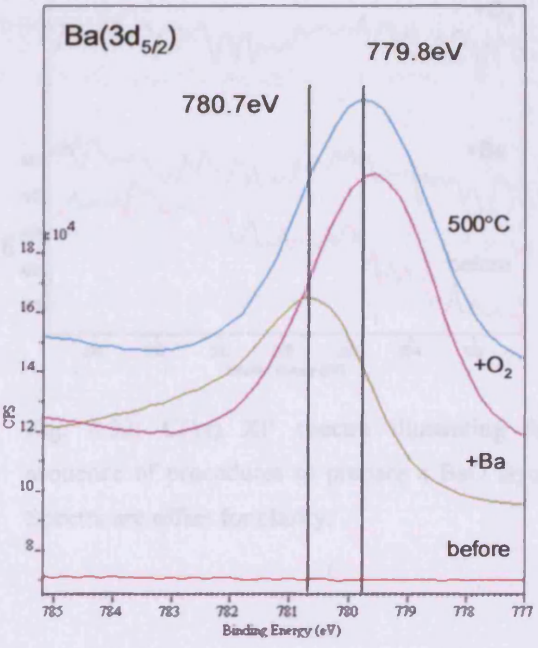

Fig. 4.50: $Ba(3d_{5/2})$ XP spectra illustrating the sequence of procedures to prepare a BaO layer. Spectra are offset for clarity.

The presence of an oxygen peak at ~ 530.0 eV was also recorded; figure 4.51 shows the sequence of O(1s) XP spectra for the full BaO preparation. The barium film was then oxidised by exposure to O_2 (5×10^{-8} mbar, 400 seconds) at room temperature and subsequently at 100 °C (5×10^{-8} mbar, 200 seconds). The XPS showed the presence of a single environment for the barium, with maximum at ~ 779.8 eV, and a double feature for the oxygen with maxima respectively at 529.2 eV and 532.2 eV. The

positions of the barium peak and the oxygen peak at lower binding energy are likely to be due to the presence of BaO. The second oxygen peak could correspond to the presence of carbonates or barium peroxide. The presence of carbonates could be ruled out because no signals were recorded in the C(1s) region (figure 4.52), therefore a certain amount of BaO_2 (~20%) was probably present.

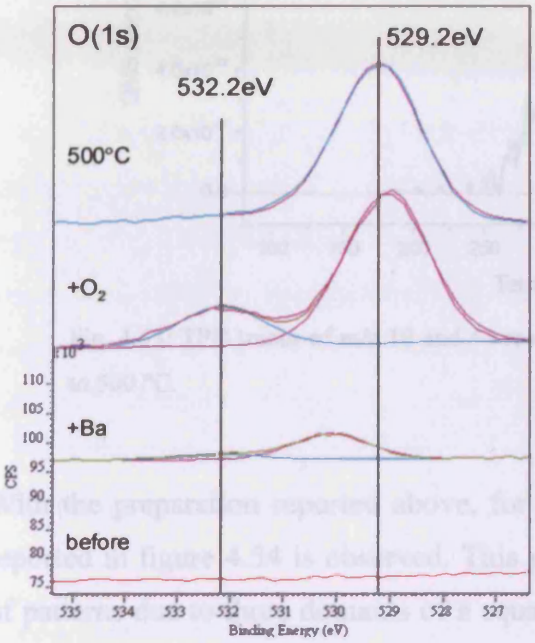

Fig. 4.51: O(1s) XP spectra illustrating the sequence of procedures to prepare a BaO layer(peak fittings also shown). Spectra are offset for clarity.

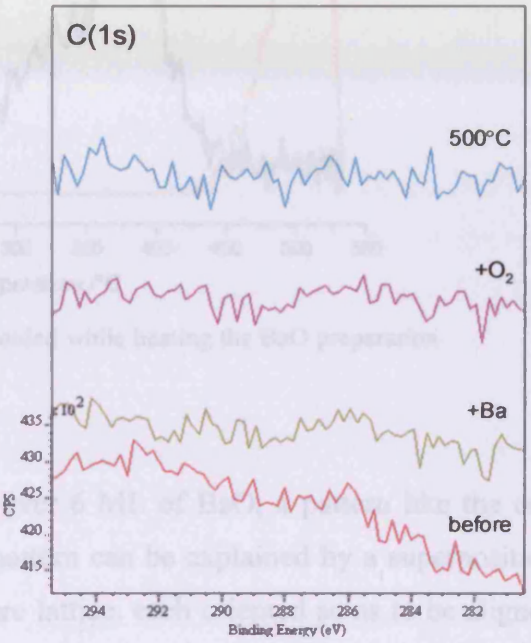

Fig. 4.52: C(1s) XP spectra illustrating the sequence of procedures to prepare a BaO layer. Spectra are offset for clarity.

During a Temperature Programmed Desorption (TPD) experiment (figure 4.53), desorption of water (m/z 18 on the mass spec) and CO_2 (m/z 44) were recognized. The onset of water desorption was just above 255 °C, with a maximum around 385°C. Desorption of CO_2 started at ~ 435 °C and with the maximum of desorption at ~ 500 °C. The order of magnitude or these desorption peaks is however very small and can be considered negligible. This can help to rule out the presence of barium carbonate and barium hydroxide and confirms the attribution of the O(1s) XP peak at 532.2 eV to barium peroxide.

The XPS recorded after the TPD shows the disappearance of the component at higher binding energies on the O(1s) peak. This is in line with the presence of BaO_2, since barium peroxide decomposition should occur slightly below 500 °C.

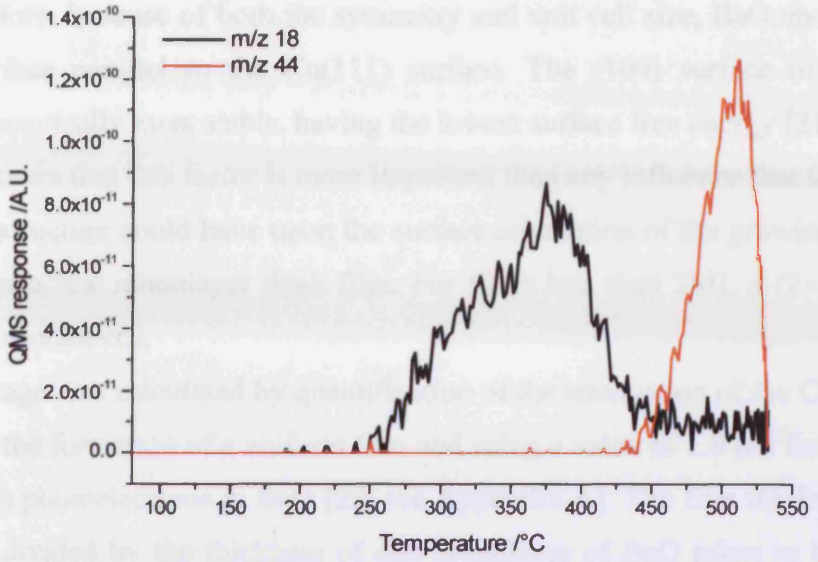

Fig. 4.53: TPD traces of m/z 18 and 44 recorded while heating the BaO preparation to 500 °C.

With the preparation reported above, for over 6 ML of BaO, a pattern like the one reported in figure 4.54 is observed. This pattern can be explained by a superposition of patterns due to three domains of a square lattice, each oriented so as to be aligned with one of the three principle directions of the Cu(111) substrate.

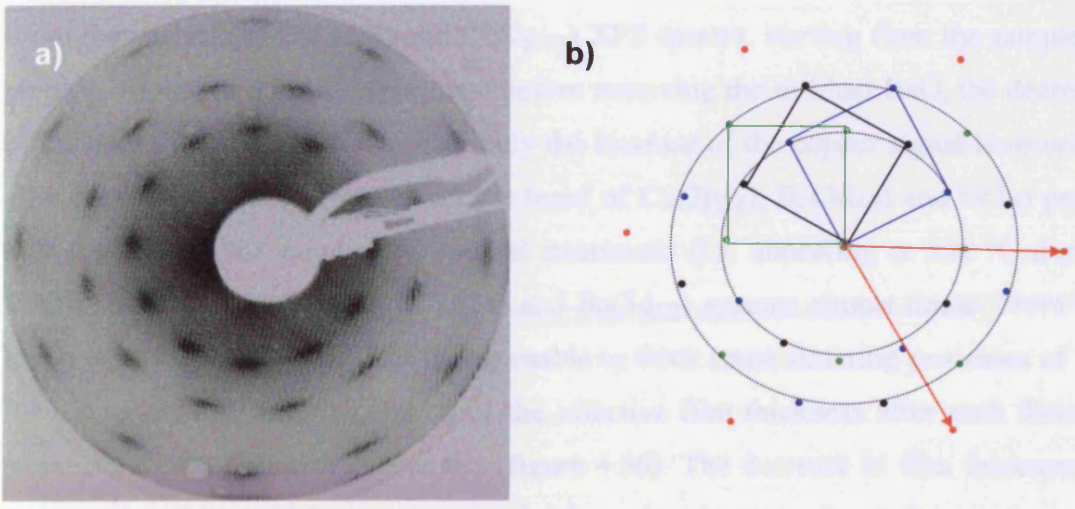

Fig. 4.54: a) LEED pattern observed after preparation of a ~ 7 ML BaO, recorded at 67 eV. Courtesy A. Tsami, R.M. Nix; b) the three different orientation of the BaO(100) domains are highlighted in different colours; in red the expected position for the Cu(111) diffraction spots (over 5 ML of BaO the Cu(111) spots are not visible anymore).

The size of the square surface unit cell derived from the LEED pattern is around 0.382 nm, therefore, because of both the symmetry and unit cell size, BaO should have the (100) surface parallel to the Cu(111) surface. The (100) surface of BaO is the thermodynamically most stable, having the lowest surface free energy [21], and in this case it appears that this factor is more important than any influence that the hexagonal substrate structure could have upon the surface orientation of the growing oxide film, at least for a few monolayer thick film. For films less than 2ML a (2×2) - Cu(111) pattern was observed.

The coverage was calculated by quantification of the attenuation of the $Cu(2p_{3/2})$ peak, assuming the formation of a uniform film and using a value of 1.0 nm for the IMFP of the Cu(2p) photoelectrons in BaO [29, see Appendix A]. The film thickness obtained was then divided by the thickness of one monolayer of BaO taken to be 0.276 nm, corresponding to the interlayer spacing (distance between one Ba and one O atom) in the <100> direction in the bulk crystal [7].

After TPD, the coverage of the film obtained, supposed to be BaO, was estimated as 3.8 monolayers.

4.4.2.2. BaO films thermal stability

From the analysis of $Ba(3d_{5/2})$ and $Cu(2p_{3/2})$ XPS spectra, starting from the sample as prepared, going to the last experiment before removing the residual BaO, the decrease of the barium signal and correspondingly the increase of the copper signal is recorded after each TPD step. In figure 4.55 the trend of $Cu(2p_{3/2})$, $Ba(3d_{5/2})$ and O(1s) peaks as a function of the number of thermal treatments (i.e. annealing at 530 °C during TPD) is shown. The decrease of O(1s) and $Ba(3d_{5/2})$ appears almost linear. From the graph reported in figure 4.75, it is reasonable to think some sintering processes of the BaO layer occurs. The calculation of the effective film thickness after each thermal treatment shows a dramatic decrease (figure 4.56). The decrease in film thickness is due to sintering, which can in turn lead to the decrease in surface active site concentration, thus a decrease in reactivity. This can be considered ageing of the BaO layer.

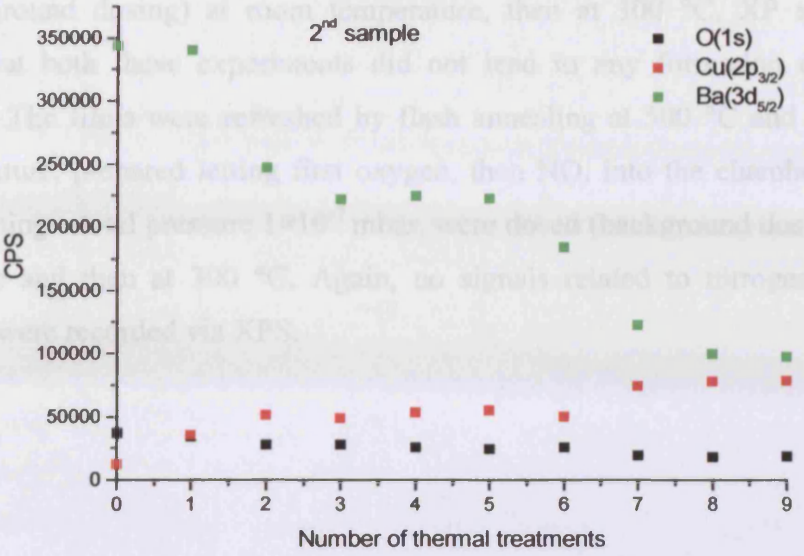

Fig. 4.55: O(1s), $Cu(2p_{3/2})$ and $Ba(3d_{5/2})$ as a function of the thermal treatments (typically annealing up to 530 °C, in vacuum, during TPD experiments) performed on the sample.

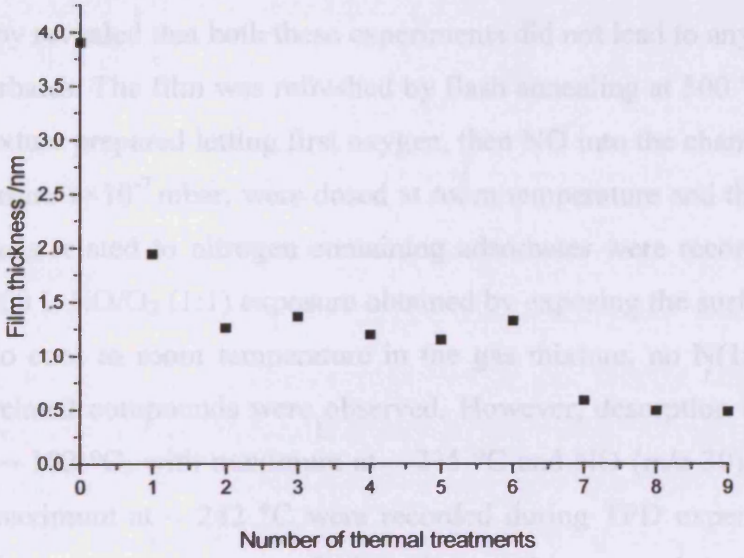

Fig. 4.56: Film thickness as a function of the thermal treatments (typically annealing up to 530 °C, in vacuum, during TPD experiments) performed on the sample.

4.4.2.3. Exposure of sub-monolayer films to NO and NO/O_2.

Sub-monolayer BaO films ($0.3 < \vartheta$), showing no LEED pattern, were prepared according to the preparation exposed above. The films were firstly exposed to 12 L of

NO (background dosing) at room temperature, then at 300 °C. XP spectroscopy revealed that both these experiments did not lead to any formation of N-related adsorbates. The films were refreshed by flash annealing at 500 °C and a 12 L of a NO/O_2 mixture, prepared letting first oxygen, then NO, into the chamber in a (1:1) ratio, obtaining a total pressure 1×10^{-7} mbar, were dosed (background dosing) at room temperature and then at 300 °C. Again, no signals related to nitrogen containing adsorbates were recorded via XPS.

4.4.2.4. Exposure of thick films to NO and NO/O_2.

a) Background dosing

Thick BaO films (~ 4 ML) were prepared according to the preparation exposed above. The films were initially exposed to 12 L of NO at room temperature, then at 300 °C. XP spectroscopy revealed that both these experiments did not lead to any formation of N-related adsorbates. The film was refreshed by flash annealing at 500 °C and a 12 L of a NO/O_2 mixture prepared letting first oxygen, then NO into the chamber in a (1:1) ratio, total pressure 1×10^{-7} mbar, were dosed at room temperature and then at 300 °C. Again, no signals related to nitrogen containing adsorbates were recorded via XPS. Also after a 1000 L NO/O_2 (1:1) exposure obtained by exposing the surface at 300 °C and allowing to cool to room temperature in the gas mixture, no N(1s) XP signals suggesting N-related compounds were observed. However, desorption of water (m/z 18) starting at ~ 102 °C, with maximum at ~ 235 °C and NO (m/z 30), starting at ~ 195 °C with maximum at ~ 242 °C were recorded during TPD experiment (figure 4.57). The TPD trace suggests a sort of adsorption on N-compounds onto the surface, but these compounds were not revealed by XPS. M/z 30 is directly correlated to NO. Making the m/z 30 signal as 100% [44], the fragmentation pattern of NO_2 shows a 38% of contribution due to m/z 46. Evolution of NO_2 should show these two traces with the same trend, but a desorption peak for m/z 46 was not observed, although m/z 46 monitored. This could be due to fast dissociation of NO_2 into part of the vacuum chamber, for example the copper gaskets, before reaching the mass spectrometer.

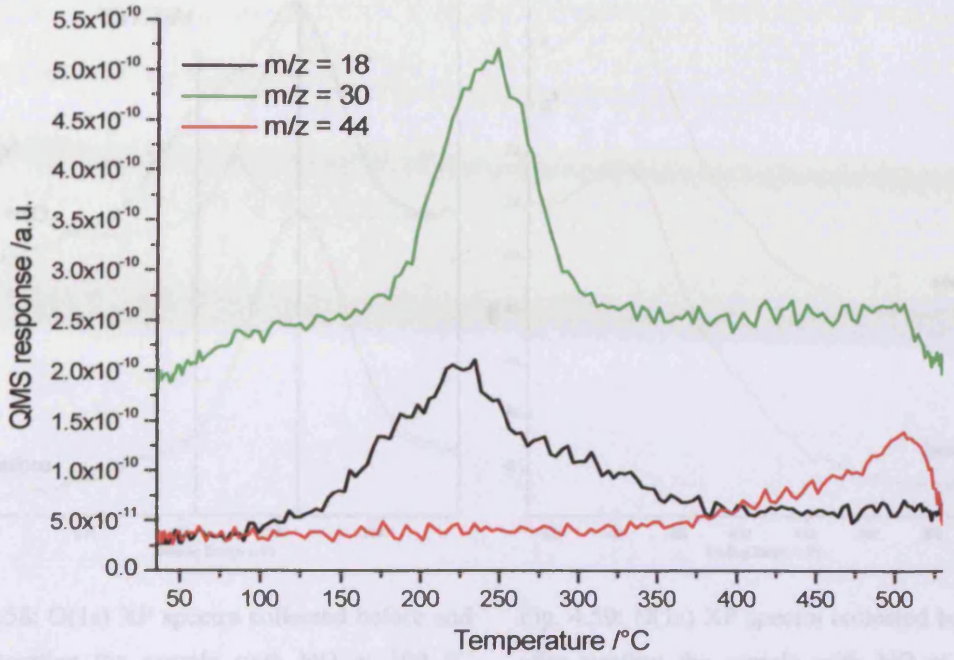

Fig. 4.57: TPD traces of m/z 18, 30 and 44 from a 6 ML BaO exposed to 1000L of NO/O_2 (background dosing) at 300 °C.

b) Directional dosing

The previous experiments were repeated using a directional doser. The characteristic of this way of dosing is the production of a flux of gas directly onto the sample, resulting in a higher gas pressure localised only on the crystal. The sample, a ~ 4 ML BaO film, was heated to 300 °C, NO (1×10^{-7} mbar) introduced into the chamber via the directional doser, and the sample allowed to cool to room temperature in the gas; this resulted in a total dosing time of 25 minutes. XPS showed a broadening of the oxygen peak towards higher binding energy in the O(1s) region (figure 4.58), which could be fitted with a second peak with maximum at ~ 531.5 eV. A different oxygen species was therefore produced, however no features appeared in the N(1s) region (figure 4.59). The $Ba(3d_{5/2})$ peak stayed unchanged in shape and constant in area at 779.8 eV.

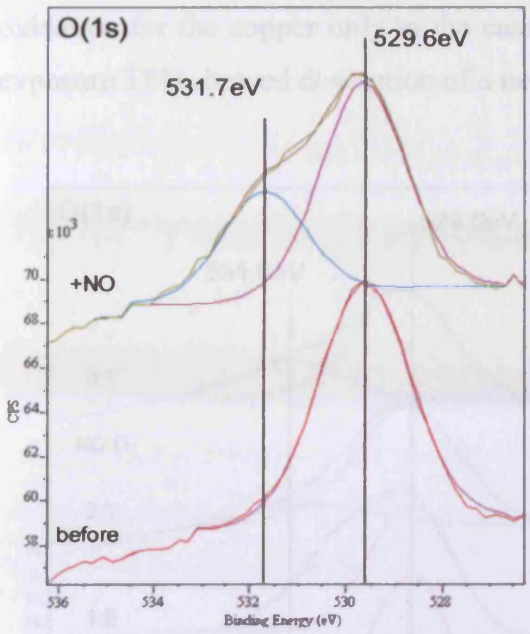

Fig. 4.58: O(1s) XP spectra collected before and after treating the sample with NO at 300 °C (peak fittings also shown). Spectra are offset for clarity.

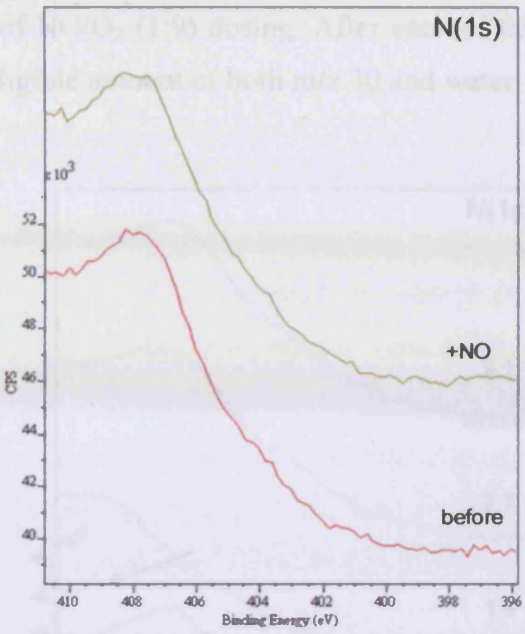

Fig. 4.59: N(1s) XP spectra collected before and after treating the sample with NO at 300 °C. Spectra are offset for clarity.

After an initial annealing to 550 °C, the sample was exposed to the so called "extreme mixtures" NO/O_2 (1:9), (2:1) and (9:1). The system was heated up to 300 °C, O_2 introduced back filling the chamber, then NO via directional doser, obtaining the desired gas mixture of a total pressure of 1×10^{-7} mbar. While the system was allowed to cool to room temperature, XPS measurements were recorded. The total exposure to the gases was of about 25 minutes. In general, the $Ba(3d_{5/2})$ peak stays constant at 779.8 eV. After the exposure to these mixtures, the O(1s) peak appeared broader (figure 4.60). In particular, the oxide peak stays constantly at ~ 529.4 eV. After NO/O_2 (1:9) dosing, a second component at ~ 530.5 eV can be fitted under the curve. After NO/O_2 (2:1) exposure, the second component can be fitted at ~ 530.3 eV and at ~ 531.1 eV after (9:1) dosing. The second component shifts more towards higher binding energies, with the increase of the relative amount of NO in the mixture. Its area decreases with the increase of NO, thus the oxidation effect is limited by the partial pressure of oxygen in the mixture. Moreover, the total integral under the curve stays constant after the exposures and after each TPD performed after each exposure. The N(1s) (figure 4.61) did not show any adsorption of N-related compounds, however, a change in shape of the Cu(LMM) Auger peak suggests a certain degree of

oxidation for the copper only in the case of NO/O_2 (1:9) dosing. After each of these exposure TPD showed desorption of a negligible amount of both m/z 30 and water.

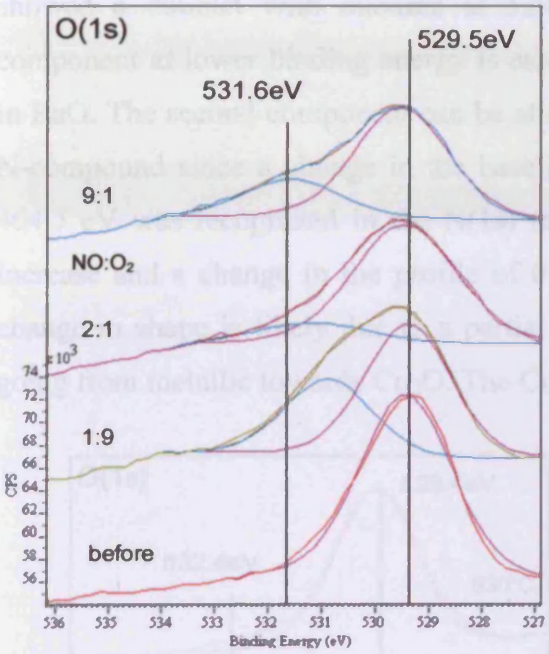

Fig. 4.60: O(1s) XP spectra collected before and after treating the sample with NO/O_2, in different ratios, at 300 °C (peak fitting also shown). Spectra are offset for clarity.

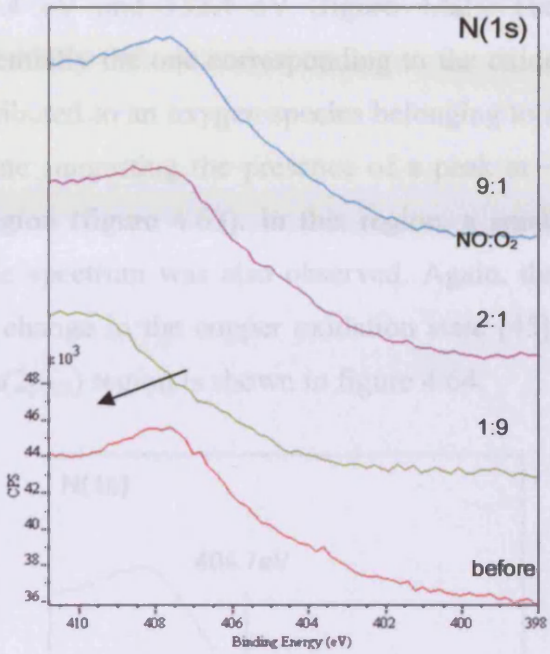

Fig. 4.61: O(1s) XP spectra collected before and after treating the sample with NO/O_2, in different ratios, at 300 °C. The arrow highlights the change in shape. Spectra are offset for clarity.

4.4.2.5. Exposure of thick films to "NO_x mixture".

The samples, usually ~ 6 ML thick BaO films, were flashed to 530 °C and prepared for the exposure to a premixed NO/O_2. The mixture was prepared in a glass flask, leaving O_2 to expand in it first, and then NO in 2:1 ratio at room temperature. The formation a brown gas, indicative of the presence of NO_2, which normally exists in equilibrium with its dimer N_2O_4, was seen inside the flask. The mixture was left to equilibrate overnight; in this way, the relative amount of the four gases, $N_2O_4/NO_2/NO/O_2$ should be dictated by the achievement of the equilibrium. For

practicalities this mixture will be called "NO_x mixture" in the rest of this section. The mixture was dosed by means of the directional doser.

The sample was firstly dosed with 1L of "NO_x mixture" at 300 °C. The O(1s) region showed a doublet with maxima at 529.4 eV and 532.4 eV (figure 4.62). The component at lower binding energy is essentially the one corresponding to the oxide in BaO. The second component can be attributed to an oxygen species belonging to a N-compound since a change in the baseline suggesting the presence of a peak at ~ 404.7 eV was recognized in the N(1s) region (figure 4.63). In this region, a small increase and a change in the profile of the spectrum was also observed. Again, the change in shape is likely due to a partial change in the copper oxidation state [45], going from metallic towards Cu_2O. The $Cu(2p_{3/2})$ region is shown in figure 4.64.

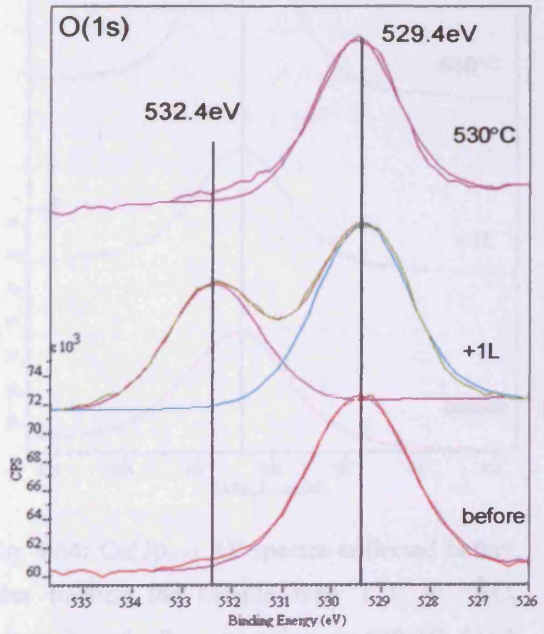

Fig. 4.62: O(1s) XP spectra collected before, after treating the sample with 1 L of "NO_x mixture" and after annealing at 530 °C (peak fitting also shown). Spectra are offset for clarity.

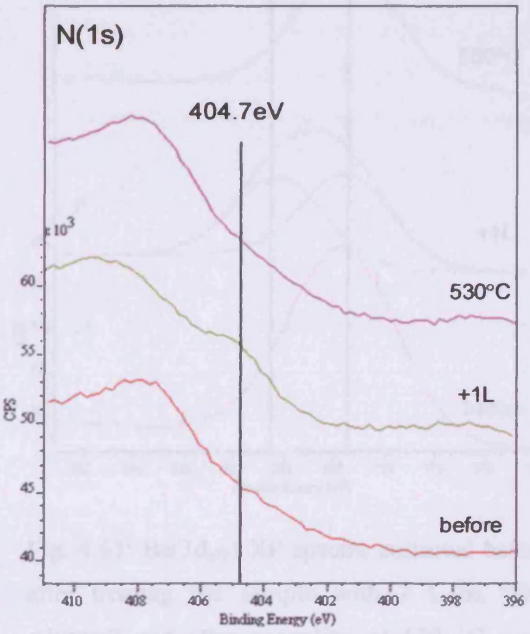

Fig. 4.63: N(1s) XP spectra collected before, after treating the sample with 1 L of "NO_x mixture" and after annealing at 530 °C. Spectra are offset for clarity.

To oxidise the (111) plane of copper at room temperature it is normally necessary to use a big oxygen exposure (> 100 L) [45, 46]. NO_2 is known to be a strong oxidising agent. NO_2 decomposition in vacuum leads to the production of atomic oxygen which is more oxidising than O_2 itself, therefore oxidation of the copper could occur. The $Ba(3d_{5/2})$ (figure 4.65) appeared broader after the gas exposure, and could be fitted

with two peaks with maxima at 779.7 eV and 781.3 eV respectively, meaning a change in its chemical state occurred. Taking into account the position of the nitrogen peak, 404.7 eV, the position of the second oxygen component, 532.4 eV and the broadening of the barium peak, barium nitrite should have been produced on the surface (see table 4.1). Subsequently the system was refreshed by annealing up to 530 °C. A substantial decrease of the $Ba(3d_{5/2})$ and a correspondent increase of the $Cu(2p_{3/2})$ were observed. This is likely due to sintering of the BaO overlayer as it will be shown later.

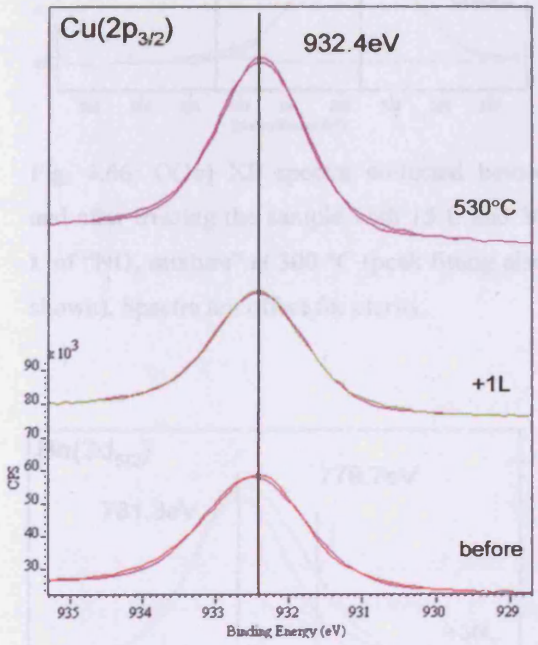

Fig. 4.64: $Cu(2p_{3/2})$ XP spectra collected before, after treating the sample with 1 L of "NO_x mixture" and after annealing at 530 °C (peak fitting also shown). Spectra are offset for clarity.

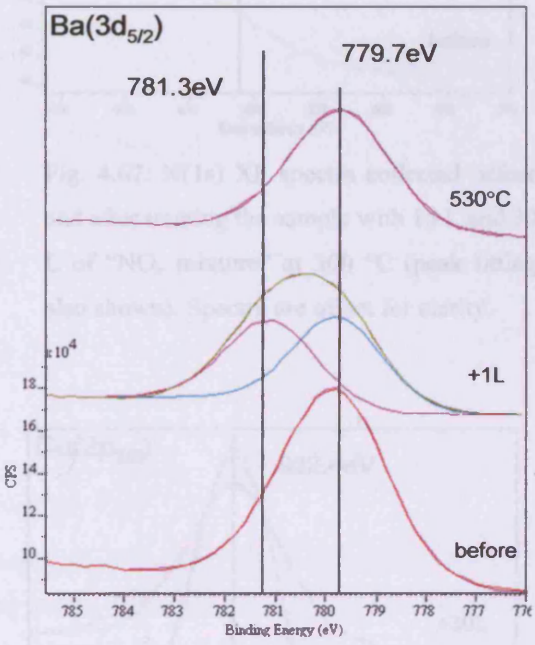

Fig. 4.65: $Ba(3d_{5/2})$ XP spectra collected before, after treating the sample with 1 L of "NO_x mixture" and after annealing at 530 °C (peak fitting also shown). Spectra are offset for clarity.

The remaining BaO film, ~ 5.6 ML thick, was dosed with progressively increasing amount of "NO_x mixture", up to 30 L. Figures 4.66, 4.67, 4.68 and 4.69 show the O(1s), N(1s), $Ba(3d_{5/2})$ and $Cu(2p_{3/2})$ regions respectively, for the 15 L and 30 L exposures. As the exposure increased, an increase of the oxygen peak at ~ 532.5 eV and the nitrogen peak at ~ 404.5 eV were observed; moreover, a change in shape of the Cu(LMM) transition was again seen. At the same time, the $Ba(3d_{5/2})$ appeared broader and could be fitted with two peaks with maxima at 779.7 eV and 781.3 eV respectively.

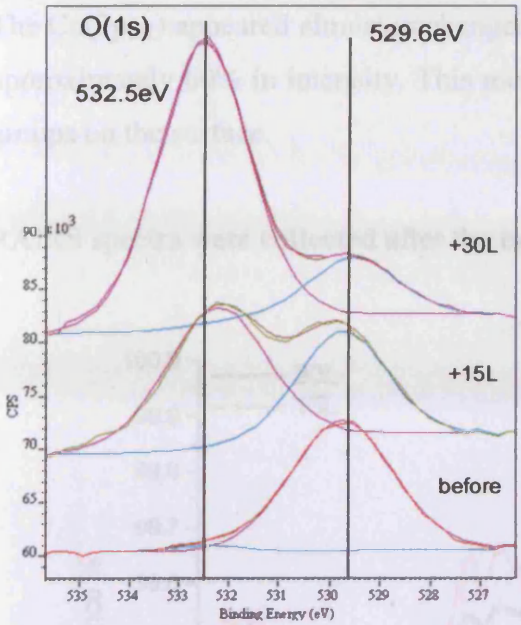

Fig. 4.66: O(1s) XP spectra collected before and after treating the sample with 15 L and 30 L of "NO_x mixture" at 300 °C (peak fitting also shown). Spectra are offset for clarity.

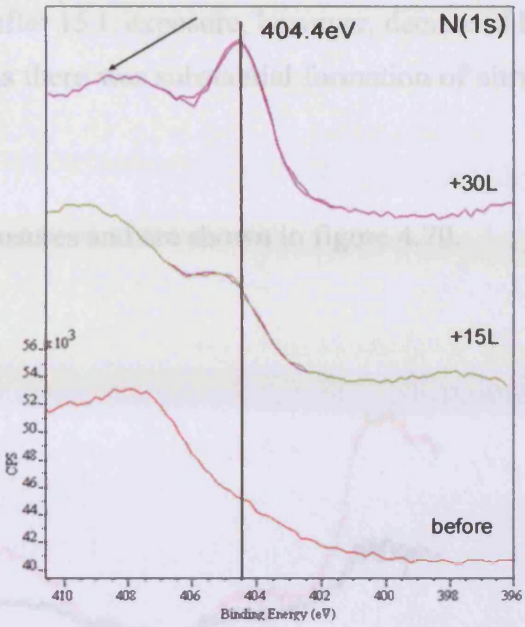

Fig. 4.67: N(1s) XP spectra collected before and after treating the sample with 15 L and 30 L of "NO_x mixture" at 300 °C (peak fitting also shown). Spectra are offset for clarity.

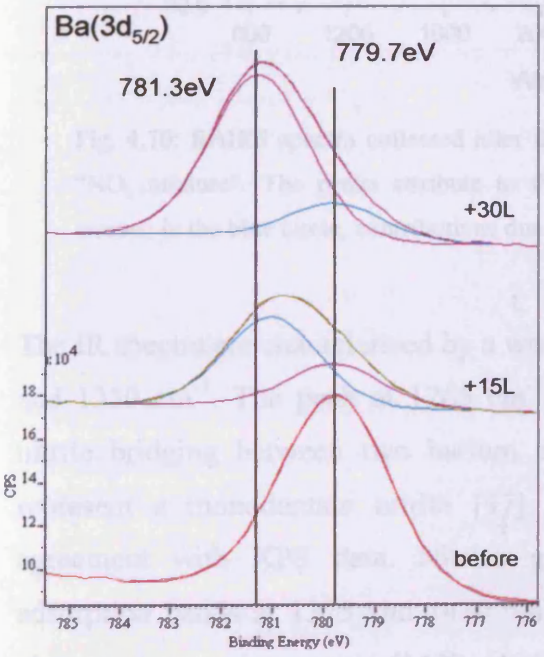

Fig. 4.68: $Ba(3d_{5/2})$ XP spectra collected before and after treating the sample with 15 L and 30 L of "NO_x mixture" at 300°C (peak fitting also shown). Spectra are offset for clarity.

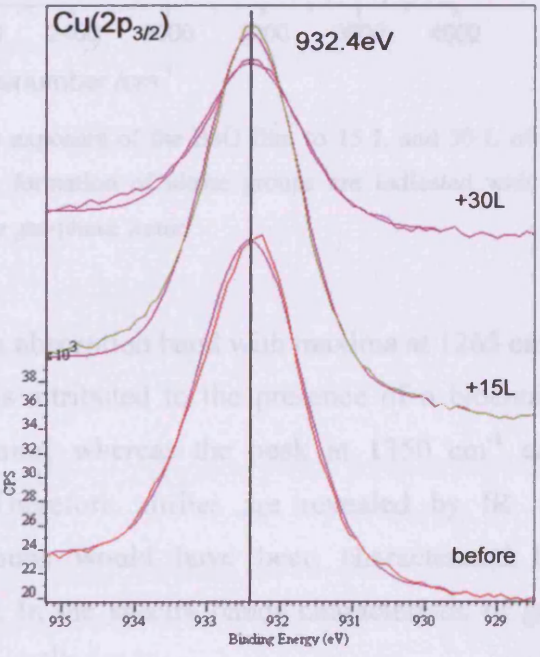

Fig. 4.69: $Cu(2p_{3/2})$ XP spectra collected before and after treating the sample with 15 L and 30 L of "NO_x mixture" at 300 °C (peak fitting also shown). Spectra are offset for clarity.

The $Cu(2p_{3/2})$ appeared almost unchanged after 15 L exposure, however, decreased by approximately 60% in intensity. This means there was substantial formation of nitrite groups on the surface.

RAIRS spectra were collected after the exposures and are shown in figure 4.70.

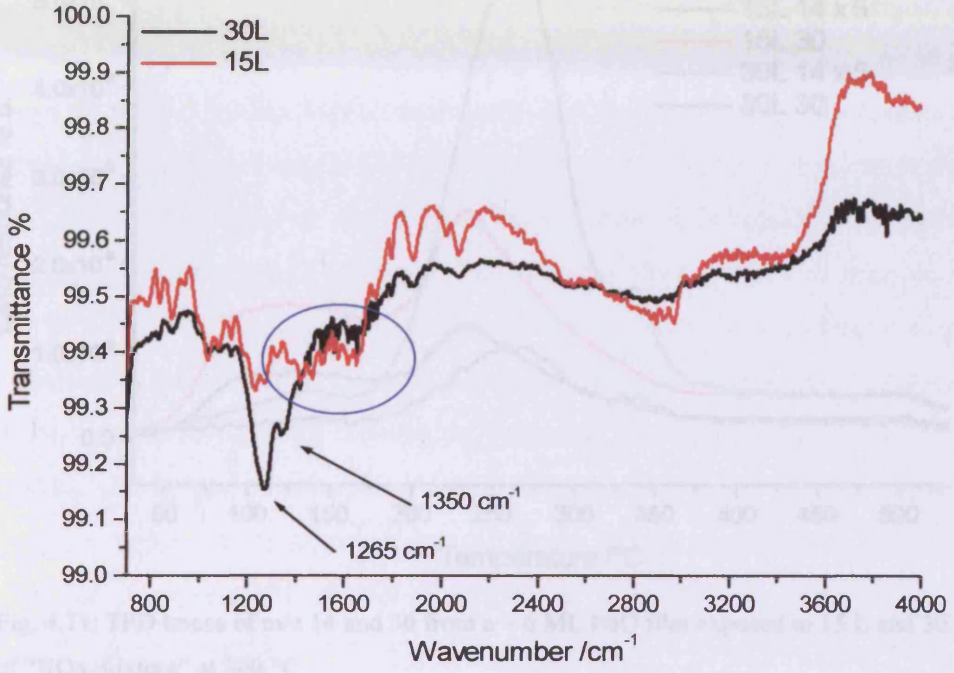

Fig. 4.70: RAIRS spectra collected after the exposure of the BaO film to 15 L and 30 L of "NO_x mixture". The peaks attribute to the formation of nitrite groups are indicated with arrows; in the blue circle, contributions due to gas-phase water.

The IR spectra are characterised by a weak absorption band with maxima at 1265 cm^{-1} and 1350 cm^{-1}. The peak at 1265 cm^{-1} is attributed to the presence of a bidentate nitrite bridging between two barium atoms, whereas the peak at 1350 cm^{-1} can represent a monodentate nitrite [47]. Therefore nitrites are revealed by IR, in agreement with XPS data. Nitrate groups would have been characterized by adsorption bands at 1375 and 1430 cm^{-1}. In the spectra bands characteristic of gas phase-water are also present (1450 – 1750 cm^{-1}).

TPD was performed after each exposure. In figure 4.71, m/z 30, indicative of the presence of NO, and 14, indicative of the presence of N_2, are shown. Both the traces present the same trend for both the exposures of 15 L and 30 L, meaning the nitrite

groups desorb from the surface as N_2 and NO mainly. Desorption of oxygen would have been expected, but both m/z 16 and 32 did not show any response, though monitored.

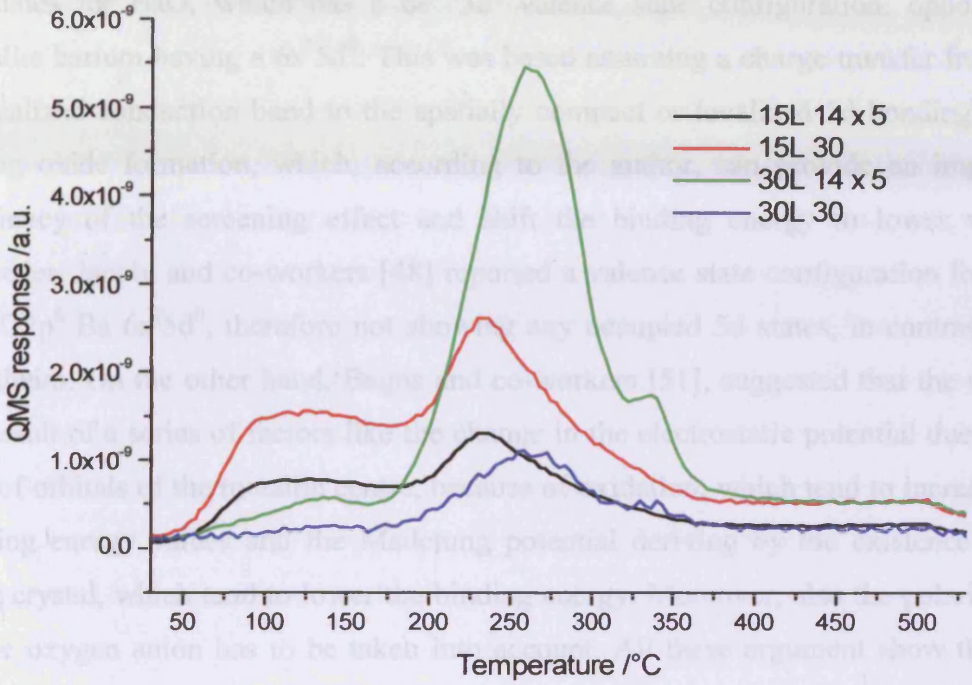

Fig. 4.71: TPD traces of m/z 14 and 30 from a ~ 6 ML BaO film exposed to 15 L and 30 L of "NOx mixture" at 300 °C.

4.5. Discussion

4.5.1. Ba(II) lower binding energy shift.

The negative binding energy shift shown by barium after oxidation is the opposite of what is normally expected for oxidation of metals. Jacobi and co-workers [48] explained the positive binding energy shift as a result of a screening charge withdrawal (leading to a decreased screening for the core levels) and changes in the final state screening. The change in the final state configuration screening is accomplished by the rearrangement of the electrons in the conduction band for metals, while for metal oxides, it is achieved by polarizing neighbouring ions. Thus, a highly polarizable O^{2-} ion in the BaO structure causes an increased final state screening and

therefore a negative binding energy shift. However, Hill and co-workers [49] reported that the negative shift is due to changes in the position of the Fermi level in the energy gap of the oxides and is sensitive to the degree of disorder and defects present on the system. Wertheim [50] suggested that the shift can be attributed to an increase in the 5d states for BaO, which has a $6s^{2-x}5d^x$ valence state configuration, opposed to metallic barium having a $6s^25d^0$. This was based assuming a charge transfer from the delocalized conduction band to the spatially compact or localized 5d bonding states during oxide formation, which, according to the author, can provide an improved efficiency of the screening effect and shift the binding energy to lower values. However, Jacobi and co-workers [48] reported a valence state configuration for BaO like $O2p^6$ Ba $6s^25d^0$, therefore not showing any occupied 5d states, in contrast with Wertheim. On the other hand, Bagus and co-workers [51], suggested that the shift is the result of a series of factors like the change in the electrostatic potential due to the loss of orbitals of the metallic centre, because of oxidation, which tend to increase the binding energy values and the Madelung potential deriving by the existence of an ionic crystal, which tend to lower the binding energy. Moreover, also the polarization of the oxygen anion has to be taken into account. All these argument show that the debate on the interpretation of this phenomenon is still open. A negative binding energy shift was observed also for other group I and II elements, like potassium [42].
Other than the negative shift of the Ba(3d) levels, in this work it was found a little difference for the binding energy values for BaO_x/Pt(111) and BaO/Cu(111). In fact, the binding energy for BaO_x on Pt(111) was estimated in ~780.1eV, whereas a value of ~779.8eV was recorded for BaO on Cu(111). This values can be considered within the experimental error, being the two systems analysed using two completely different spectrometer. Therefore no substrate electronic effect was observed.

4.5.2. Binding energy values of BaO_x

Different binding energy values for the O(1s) in barium oxide were recorded: on BaO/Pt(111) the O(1s) binding energy was 530.2 eV, whereas 529.2 eV on BaO/Cu(111). A peak at 529.6 eV was recorded also during the preparation of the BaO_x/Pt(111) system, but it appeared to shift to 530.2 eV after annealing at 300 °C. However, in the case of Pt(111), a configuration were only the oxide was present could not be prepared; in fact the presence of a second oxygen peak at ~ 532.2 eV was

always observed. Moreover, the peroxide did not appear to be a metastable species as previously reported [24], being present even after annealing at 700 °C, although the origin of the peroxide signal could be due to further contamination of BaO layer during the time in which the sample was moved from the annealing position to the XPS position. This is somehow unclear; however, the attribution of the two oxygen peaks to oxide and peroxide appeared justified, as the peroxide is expected to show a binding energy value 2 – 3 eV higher than the oxide [10]. The formation of barium peroxide on Pt(111) could be due to the different preparation procedure followed to produce the BaO film. It was verified in fact, that preparing the films in different way could lead to the persistent presence of unwanted species. In fact, preparing the BaO_x film in not optimal conditions give rise to the presence of carbonate species which are removed only after annealing at 400 °C in the case of BaO_x/Pt(111). After preparing the oxidised barium layer on both the substrate, a mixture of BaO and BaO_2 is initially present. The amount of barium peroxide can be decreased by annealing at temperature higher than 500 °C. In the case of BaO/Cu(111), BaO_2 could be completely decomposed by thermal treatments.

4.5.3. Gas exposure.

All the attempt to obtain NO_x storage via background dosing on BaO_x/Pt(111) were unsuccessful. Analogously, when background dosing was performed on BaO/Cu(111), production of N-related species was not observed. This is likely because these experiments were performed backfilling the chambers with the gases NO, and NO/O_2. On BaO/Cu(111), when using the directional doser, real features related to N-compounds could be observed. This means that a high "NO_x mixture" pressure, more than exposure, is necessary in order to produce the storage. The mixture was prepared allowing two volumes of NO and one volume of oxygen to expand into a glass flask; the composition of the mixture $N_2O_4/NO_2/NO/O_2$. The species likely present, when storage occurs, are barium nitrites. Theoretical calculations [13 - 15] showed that the formation of surface nitrites is the first step for the NO_x storage, and it has been experimentally proved that when the extent of exposures is increased, nitrate indeed form [23]. The presence of nitrates was not observed during this work, however, they

appeared to form when exposing to NO_2 pure BaO at room temperature. NO_2 reacts with barium oxide to form the nitrite then, slow formation of nitrate is observed [52].

4.5.4. Structure of BaO_x layers.

The BaO_x films prepared on Pt(111) appeared to be unordered after preparation. Ordering of the overlayer could be achieved by annealing in vacuum at different temperatures for different coverage. The reconstructions observed are a (2×2), (2√3×2√3)-R30° and (8×2), although all related to the Pt(111) substrate and not the BaO(111) surface as theoretically calculated [25]. However, the (2√3×2√3)-R30° reconstruction on Pt(111), has a lattice vector of 0.93 nm, value in good agreement with the one observed for the moiré pattern by Stone and co-workers [24] and attributed to a barium layer on Pt(111) which was starting to order.

Unfortunately, the lack of resolution observed during STM analysis did not help the interpretation of this behaviour. Only in very rare cases could atomic features be recorded. In one case the Pt(111) surface was atomically resolved as shown in figure 4.32 – 4.34. When the LEED showed a Pt(111) – (2×2) pattern (see figure 4.41), in agreement with it, the STM showed a structure on the surface that could be recognised as an hexagonal (2×2) with respect to the Pt(111) substrate, although after an important 2D-FFT filtering (see figure 4.44). This reconstruction is typical of 0.25 ML of oxygen adsorbed on the platinum surface. Parkinson and co-workers [53] reported that atomic oxygen appears to adsorb easily at room temperature as a result of low exposures (~ 5 L) giving rise to a relatively sharp (2×2) pattern. A high background intensity normally prevails on the (1×1) spots when saturation is reached (~ 50 L). A (2×2) pattern appears when desorption of the excess of oxygen, and subsequent rearrangement, occurs due to annealing to 500 °C step by step. Taking these considerations into account, the pattern observed may be due to the adsorption of molecular oxygen that dissociate on the Pt(111) surface free of BaO_x. However, this can not explain the (2√3×2√3)-R30° and (8×2) reconstructions. Another possibility to explain a (2×2) reconstruction is represented by a (2×2) oxygen overlayer on the platinum, with a barium (2×2) overlayer on top of the oxygen layer (see model in figure 4.42).

Some STM images suggest that the BaO_x overlayer was imaged. The sequence reported in figure 4.24 shows that the features change in shape during scanning. This kind of behaviour was observed during the work undertaken while studying the preparation of oxidised potassium layers on Pt(111) [42]. In that case it was also observed that the features were changing in shape while the scanning angle was changed. The dependence of the shape of the features upon the scanning direction has been already reported for a variety of pure metals, for example for Ir(111) [54] and assumed valid also for Pt(111) [55]. In these cases some criteria as different stability of the step edges has been invoked to explain the phenomenon, although the mechanism is not completely understood even if a number of theoretical works have been published. One of the explanations could lie on the level of contaminants, manly CO, in the UHV chamber. In fact the change in shape of the features appeared mediated by the preferential adsorption of CO to low coordinated Pt atoms, as in step edges, enhancing the diffusion of the Pt atoms present at the very step edge. Atoms less bounded likely interact with the tip and appeared to move away from the step edge. However, in the present case it is more likely that the overlayer is dragged around by the tip. Certainly if just single or small clusters of adsorbed molecules were moved around, they should have been visible to a atomically resolved scale. In a previous work, Michely co-workers [56] also reported that the shape of Pt particles deposited on Pt(111) strongly depends upon the thermal treatments that the system undergoes. In very recent works the observation of linear features, so called "fingers", on the Au(111) surface has been reported by Guo and co-workers [57, 58]. Scanning at room temperature, the fingers appeared to be induced by the STM tip and to grow along the <111> main directions. Moreover, they became triangular if scanned over along another direction and the triangular islands are all oriented in the same way, giving the experimental evidence that there is a large difference in surface energy between the different steps present on the surface. The energy stability criteria invoked for pure metals can not find application in this case.

In the case of an oxidised potassium film, the phenomenon could certainly be favoured by the relatively high gap voltage used during scanning (-1.2 V), having the effect of bringing the tip very close to the surface.

For low coverages (less than 2ML), also in the case of BaO/Cu(111) a hexagonal (2×2) reconstruction was observed, however, at higher coverages, up to ~ 6 ML, BaO appeared to grow with the (100) face parallel to the (111) face of the substrate. Since

the (100) face is the most stable one, because having the surface lowest free energy [22, 25, 59]; in the present case it appears that this factor is more important than any influence that the hexagonal substrate structure could have upon the surface orientation of the growing oxide film, at least for a few monolayer thick film.

4.6. Conclusions

A recipe to prepare a carbonate free BaO_x layer on Pt(111) was found. It consisted in evaporating barium kept in oxygen atmosphere (1×10^{-7} mbar) keeping the platinum substrate at 300 °C, followed by an oxygen exposure (1×10^{-7} mbar) of 10 minutes at 500 °C (~ 60 L) after the Ba/O_2 dosing. In this way, mixed layers of BaO/BaO_2 with typically ~80% of barium oxide were prepared. Immediately after preparation XPS analysis shows the $Ba(3d_{5/2})$ is at 779.8 eV and the O(1s) peak at around 531.0 eV. Under annealing the $Ba(3d_{5/2})$ peak stays usually constant in intensity and position, whereas the O(1s) peak broadens. Two components can be reasonably fitted under its spectrum. The component at higher binding energies (532.2 eV) can be attributed to the presence of peroxide species and the component at lower binding energies (530.2 eV) to the presence of oxide species.

The LEED pattern shows initially only the Pt(111) spots, meaning that the BaO_x overlayer is unordered. A Pt(111) – (2×2) pattern appears only after annealing up to 500 °C. The system does not undergo sintering up to 700 °C. STM showed the overlayer is extremely mobile, thus difficult to be imaged, but some pictures showing hexagonal domains have been recorded, possibly representing the Pt(111) substrate. Although not very well resolved, a hexagonal structure with spacing double than the one of Pt(111) was observed. This could either represent oxygen adsorbed on the platinum surface, or the BaO_x overlayer itself.

The exposure of the BaO_x/Pt(111) system shows no reactivity towards NO only or to a NO/O_2 mixture.

On the Cu(111) substrate, a BaO layer could be prepared. This layer is characterized by an O(1s) peak at 529.6 eV and a $Ba(3d_{5/2})$ peak at 780.1 eV. The LEED showed that when in thick film form, the overlayer shows square (100) oriented domains. Exposure to NO and NO/O_2 background dosing does not show the presence of N-

related compounds. When the dosing is done via directional doser, form a mixed reservoir of NO and O_2, nitrite groups form on the surface. This is probably due to a high gas pressure localised on the sample and to the formation of NO_2 in the dosing gas.

4.7. References

1. S. Matsumoto, *Cat. Surv. From Japan* 1, 1997, 111
2. D. James, E. Fourré, M. Ishii, M. Bowker, *App. Cat. B.* 45, 2003, 147
3. N. Miyoshini, S. Matsumoto, K. Katoh, T. Tanaka, J. Harada, N. Takahashi, K. Yokota, M. Sugiura, K. Kasahara, *SAE Technical Paper 950809*, 1995
4. S. Matsumoto, *CatTech* ,4 - 2, 2000, 102
5. N. Takahashi, H. Shinjoh, T. Iijima, T, Suzuki, K. Yamazaki, K. Yokota, H. Suzuki, N. Miyoshi, S. Matsumoto, T. Tanizawa, T. Tanaka, S. Tateishi, K. Kasahara, *Cat Today*, 27, 1996, 63
6. M. Takeuchi, S. Matsumoto, *Topics in Cat*, 28, 2004, 151
7. S. Zhou, R. Arroyave, C.A. Randall, Z. Liu, *J. Am. Chem. Soc.*, 88, 2005, 1943
8. G.A. Haas, A. Shih, *Appl. Surf. Sci.*, 8, 1981, 102
9. O.M.N.D. Teodoro, A.M.C. Moutinho, *Vacuum,* 64, 2002, 431
10. C. Di Valentin, R. Ferullo, R. Binda, G. Pacchioni, *Surf. Sci.*, 600, 2006, 1147
11. B. Westerberg, E. Fridell, *J. Mol. Cat. A: Chemical*, 165, 2001, 249
12. Y. Su, M.D. Amiridis, *Cat. Today*, 96, 2004, 31
13. P. Broqvist, I. Panas, E. Fridell, H. Persson, *J. Phys. Chem. B*, 106, 2002, 137
14. P. Broqvist, H. Grönbeck, E. Fridell, I. Panas, *Cat. Today.*, 96, 2004, 71
15. H. Grönbeck, P. Broqvist, I. Panas, *Surf. Sci.*, 600, 2006, 403
16. L. Olsson, E. Fridell, *J. Cat.*, 210, 2002, 340
17. Y. Sakamoto, K. Okumura, Y. Kizaki, S. Matsunaga, N. Takahashi, H. Shinjoh, *J. Cat.*, 238, 2006, 361
18. R. Burch, *Catalysis Reviews-Science and Engineering*, 2004, 46, 271
19. C. Sedlmair, K. Seshan, A. Jentys, J.A. Lercher, *J Cat.*, 214, 2003, 308
20. L.J. Gill, G. Blakeman, M.V. Twigg, A.P. Walker, *Topics Cat.*, 28, 2004, 157

21. P.J. Schmitz, R.J. Baird, *J. Phys. Chem.* B, 106, 2002, 4172
22. J. Szanyi, J.H. Kwak, J. Hanson, C. Wang, T. Szailer, C.H.F. Peden, *J. Phys. Chem. B*, 2005, 109, 7339
23. C.M. Wang, J.H. Kwak, D.H. Kim, J. Szanyi, R. Sharma, S. Thevuthasan, C.H.F. Peden, *J. Phys. Chem. B*, 2006, 110, 11878
24. P. Stone, M. Ishii, M. Bowker, *Surf. Sci.*, 537, 2003, 179.
25. M. Bowker, P. Stone, R. Smith, E. Fourre, M. Ishii, N.H. de Leeuw, *Surf. Sci.*, 600, 2006, 1973
26. D. Briggs, M.P. Seah, *Practical Surface Analysis*, 2nd Edition, Auger and X-ray Photoelectron Spectroscopy, vol. 1, Wiley, 1995.
27. **Casa XPS software: free demo version downloadable at** www.casaxps.com
28. **WSxM software: free software downloadable at** www.nanotec.es
29. A. Nefedovy, A. Abromeit, C. Morawe, A. Stierle, *J. Phys.: Condens. Matter* 10, 1998, 717
30. See Appendix A; IMFP calculated using the TPP-2M model in: S. Tanuma, C.J. Powell, D.R. Penn, *Surf. Interf. Anal.*, 21, 1994, 165
31. www.lasurface.com, **web-based XPS database.**
32. X-ray Photoelectron Spectroscopy Database 20, Version 3.0, National Institute of Standards and Technology, Gaithersburg, MD, srdata.nist.gov/xps/
33. J.F. Moulder, W.F. Stickle, P.E. Sobol, K.D. Bomben in: J. Chastain (Ed.), *Handbook of X-ray Photoelectron Spectroscopy*, Physical Electronics, Eden Prairie, MN, 1992
34. P. Morrall, M. Cristofolini, M. Bowker, unpublished data
35. K. Tanaka, K. Miyahara, and I. Toyoshima, *J. Phys. Chem.*, 88, 1984, 3504
36. D. Archardt, PhD thesis, Cardiff University, 2007
37. A. Shih, J.E. Yater, C.Hor, *App. Surf. Sci.*, 242, 2005, 35
38. M.J. Tribelhorn, M.E. Brown, *Thermochimica Acta*, 255, 1995, 143
39. E. Ozensoy, C.H.F. Peden, J. Szanyi, *J. Phys. Chem. B*, 110, 2006, 17009
40. E. Ozensoy, C.H.F. Peden, J. Szanyi, *J. Phys. Chem. B*, 110, 2006, 17001
41. P. Stone, R. Smith, M. Ishii, M Bowker, unpublished data
42. A.J. McDowall, F. Grillo, M. Bowker, unpublished data
43. N. Materer, U. Starke, A. Barbieri, R. Döll, K. Heinz, M.A. Van Hove, G.A. Somorjai, *Surf. Sci.*, 325, 1995, 207
44. NIST Chemistry WebBook, webbook.nist.gov/chemistry

45. S. Poulston, P.M. Parlett, P. Stone, M. Bowker, *Surf. Interface Anal.*, 24, 1996, 811
46. T. Matsumoto, R.A. Bennett, P. Stone, T. Yamada, K. Domen, M. Bowker, *Surf. Sci.*, 471, 2001, 225
47. Ch. Sedlmair, K. Seshan, A. Jentys, J.A. Lercher, *J. Cat*, 214, 2003, 308
48. K. Jacobi, C. Astaldi, B. Frick, P. Geng, *Phys. Rev. B*, 36, 1987, 3079
49. D.M. Hill, H.M. III Meyer, J.H. Weaver, *Surf. Sci.*, 225, 1990, 63
50. G.K. Wertheim, *J. Electron Spectroscop. Relat. Phenom.*, 34, 1980, 309
51. P.S. Bagus, G. Pacchioni, C. Sousa, T. Minerva, F Parmigianini, *Chem. Phys. Lett.*, 196, 1992, 641
52. A. Tsami, F. Grillo, M. Bowker, R.M. Nix, *Surf. Sci.*, 600, 2006, 3403
53. C.R. Parkinson, M. Walker, C.F. McConville, *Surf. Sci.*, 545, 2003, 19
54. T.Y. Fu, Y.R. Tzeng, T.T. Song, *Phys. Rev. B*, 54, 1996, 5932
55. M. Kalff, G. Cosma, T. Michely, *Phys. Rev. Lett.*, 81, 1998, 1255
56. T. Michely, M. Hohage, M. Bott, G. Cosma, *Phys. Rev. Lett.*, 70, 1993, 3943
57. Q. Guo, F. Yin, R.E. Palmer, *Small*, 1, 2005, 76
58. F. Yin, R.E. Palmer, Q. Guo, *Surf. Sci.*, 600, 2006, 1504
59. P. Broqvist, H. Grönbeck, I. Panas, *Surf. Sci.* 554, 2004, 262

Chapter 5

High Pressure Study of NSR Model Catalysts

This chapter describes the preparation of the BaO*/Pt/α-Al_2O_3(0001) and Pt/BaO*/α-Al_2O_3(0001) model systems (where * indicates a mixture of BaO, $Ba(OH)_2$ and $BaCO_3$). These systems were prepared in a similar way to that the real NSR catalyst is prepared, i.e. via wet chemistry methods, without therefore any cleaning process typical of Surface Science. The systems were chemically characterized using a Kratos Axis Ultra XP Spectrometer and, because of their insulating characteristics, structurally characterized via Atomic Force Microscopy (AFM). After characterization, the systems were tested for NSR reactivity, though limited to the storage step, in an AFM environmental cell, which allows high temperature – high pressure scanning conditions, and by means of XP Spectroscopy. This was the first attempt in our group to prepare model catalysts on single crystals surfaces by wet chemistry methods.

5.1. Introduction

The NSR catalyst review was given in section 4.2, here the importance of studying a model catalyst will be briefly considered. A model system is a convenient choice to evaluate the different parameters that control its catalytic properties [1]. The NSR catalyst is extensively studied as in the commonly used powder form. Because of this, obtaining structural information such as the geometry of the different atoms in the interface between the system and the environment and investigating the reactivity at atomic level is particularly difficult [2]. Although single crystal metals have been proved in the past to be good models for correlating structure and reactivity of catalytic systems, they can not represent to the same extent the metallic nano-clusters that are considered the active component in a catalyst. Moreover, most catalysts are oxide supported; in this respect metal single crystals show another limitation because the oxide support is not present. From here the decision to prepare a model of the NSR catalytic system using α-Al_2O_3(0001) as a support and following the wet

chemistry preparation and analyse it using surface science techniques such as XPS and AFM.

5.1.1. Alumina structure

α-Al_2O_3 has a hexagonally close packed (hcp) crystal structure, with a = 0.47 nm and c = 1.29 nm [3]. For this particular investigation, α-Al_2O_3(0001) single crystals were used and considered to be clean when purchased, with no further cleaning procedures being done before their use. The structure of the bulk α-alumina crystal is shown in figure 5.1.

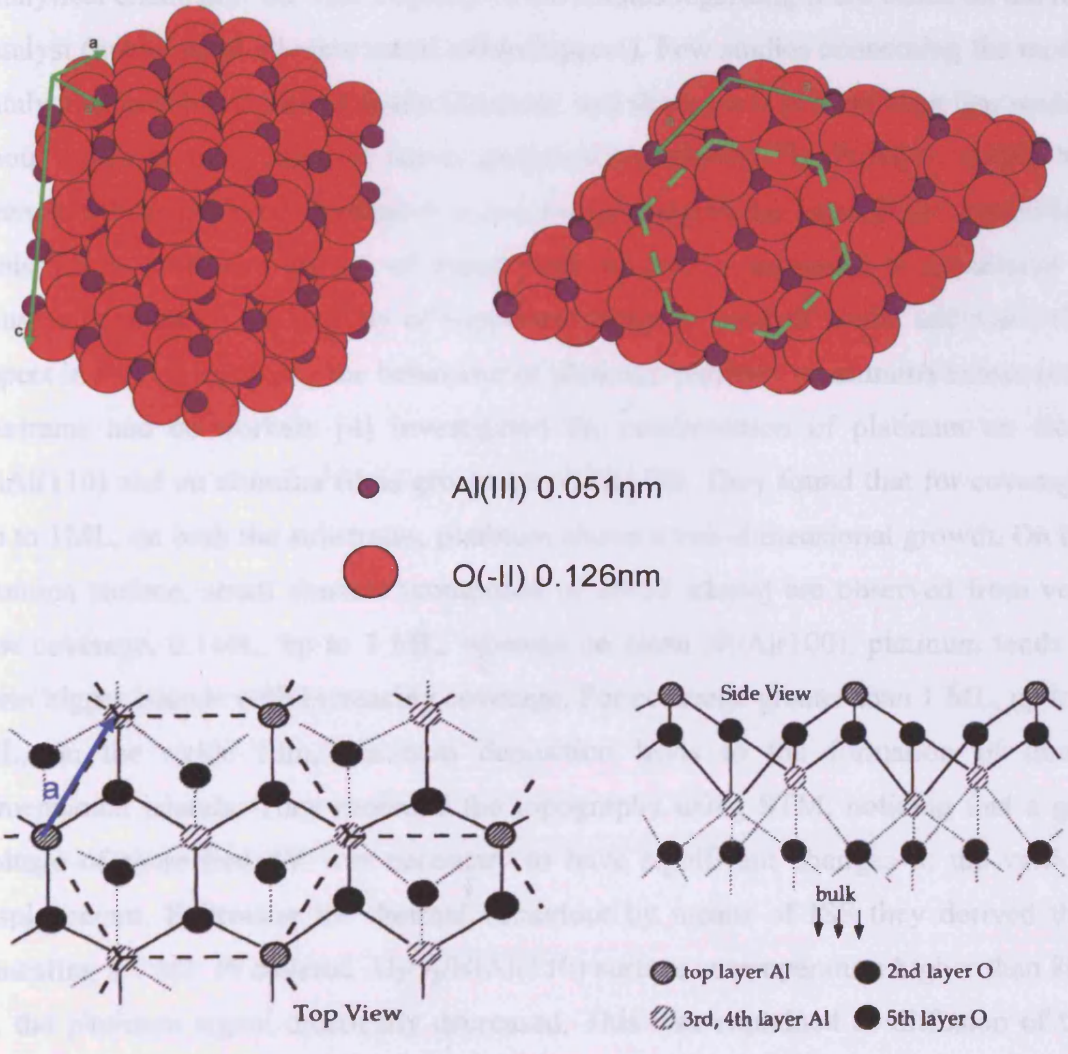

Fig. 5.1: a) schematic illustration of the bulk α-Al_2O_3 crystal structure; b) the (0001) surface and c) (black and white) a model proposed in [3].

In bulk α-Al_2O_3, each aluminium atom is bonded to six nearest-neighbour oxygen atoms in a distorted octahedral arrangement, with an Al-O distance of 0.186 nm, and each oxygen atom is bonded to four aluminium atoms in a distorted tetrahedral arrangement, with an Al-O distance of 0.196 nm. The (0001) plane showed in figure 5.1 b), is aluminium terminated and shows a hexagonal arrangement of the atoms (green dashed hexagon), with the distance of 0.47 nm between two atoms.

5.1.2. Literature survey

Although the NSR (NO_x Storage and Reduction) system is one of the hot topics in catalytical chemistry, the vast majority of the studies regarding it are based on the real catalyst (noble metal/alkaline metal oxide/support). Few studies concerning the model catalyst approach are present in the literature, and there are at present even less studies about model systems using *ex vacuo* analytical techniques. The Pt/Al_2O_3 system has been largely considered, because it is a common base of the catalyst for automobile emission control. The growth of metal particles due to annealing is considered to cause a decrease in the activity of supported catalysts. Several works addressed this aspect in studies regarding the behaviour of platinum particles on alumina substrates.

Bertrams and co-workers [4] investigated the condensation of platinum on clean NiAl(110) and on alumina films grown on NiAl(110). They found that for coverages up to 1ML, on both the substrates, platinum shows a two-dimensional growth. On the alumina surface, small clusters (composed of 20-50 atoms) are observed from very low coverage, 0.1ML, up to 1 ML, whereas on clean Ni/Al(100), platinum tends to form bigger islands with increasing coverage. For coverage greater than 1 ML, up to 6 ML, on the oxide film, platinum deposition leads to the formation of three-dimensional islands. They recorded the topography using STM, noticing that a gap voltage of more that 4V was necessary to have significant changes in the vertical displacement. Following the thermal behaviour by means of ISS they derived that annealing a 1 ML Pt covered Al_2O_3/NiAl(110) surface at temperature higher than 800 K, the platinum signal drastically decreased. This was explained as diffusion of the platinum into or through the oxide.

Recently Sartale and co-workers [5] studied the growth of platinum nanoclusters on θ-Al_2O_3/NiAl(100) thin films as a function of coverage and deposition temperature

mainly by means of low temperature STM. They prepared their samples by depositing various amounts of platinum, from 0.06 to 1.32 MLs, onto the Al_2O_3/NiAl(100) substrate at different temperatures, between 300 and 600 K, in UHV conditions. The oxide layer was grown onto the NiAl(100) substrate by exposure of 1000 L O_2 at 1000 K and subsequent annealing at 1000–1100 K for 1 hour. In this way they obtained different areas with amorphous and crystalline Al_2O_3. The crystalline Al_2O_3 area consists of stripes containing a protrusion structure that propagates along one of the two main crystallographic directions ([100] and [010]) of the NiAl alloy surface. The STM images show that platinum nanoclusters grow only on the crystalline portion of the Al_2O_3 surface layer prepared. These platinum clusters appeared to be randomly distributed and only a few formed aligned patterns. The clusters were typically 0.4nm in height and 2.25 nm in diameter and their mean size did not vary with the deposition temperature, nor with the coverage. Investigating the thermal stability, they observed that the cluster density decreased monotonically with post-deposition annealing temperature up to 1000 K at expense of smaller clusters but they did not observed coalescence.

Sella and co-workers [6] studied the behaviour of platinum particles in platinum-alumina cermet films via TEM and AFM. They noticed that while the alumina framework stayed unchanged, the diameter of the platinum nanoparticles increased as a function of annealing temperature, film thickness and metal concentration. In particular the annealing effect was to produce a monodisperse size distribution leading to homogenization of their diameters. Moreover the platinum particulate tends to aggregate and to grow in columns when the film thickness increased.

Okumura and co-workers studied the growth of platinum particles on γ- (111) and α-Al_2O_3(0001) by AFM [7, 8]. They initially prepared a 5 nm thick platinum film by RF sputtering of platinum targets. By heat treatment at 800 °C for 3 hours in 7.5%O_2 in N_2 atmosphere, this film was transformed into discrete platinum particles, whose average size was ~ 200 nm and average height ~ 20 nm. On α-Al_2O_3(0001) these particles, exhibit polygonal shape, in particular hexagonal (figure 5.2 a), generally having (111) preferred orientation, according to XRD measurements. On the contrary, on γ-Al_2O_3(111) the particles were well dispersed, roughly hemispherical of pseudo hexagonal, with an average size of 50nm in width and ~18 in height (figure 5.2 b).

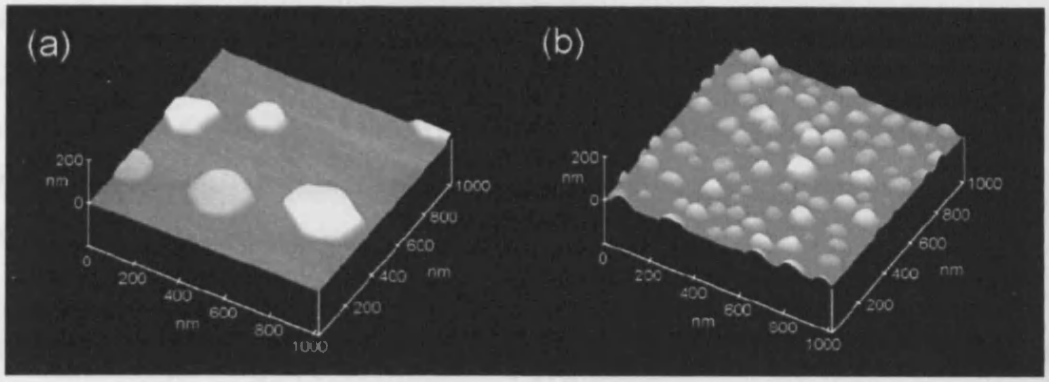

Fig. 5.2: AFM images showing the topography of Pt particles on a) α-Al_2O_3 and b) γ-Al_2O_3 derived by heating for 3 hours to 800 °C a 5 nm Pt film in 7.5% O_2 in N_2 atmosphere [7].

The study of barium compounds on α-Al_2O_3(0001) was addressed to the morphological evolution of barium nitrate species to barium oxide. Szanyi and co-workers in two publications [9, 10] followed this evolution using several techniques, TEM in particular. They found that preparing BaO/Al_2O_3 by incipient wetness using barium nitrate aqueous solutions as barium precursor, large barium nitrate crystallites are formed on the alumina support after drying at low temperatures (200 °C), but a large fraction of the support remains barium free (Al:Ba atomic ratio from ~99:1 to ~80:20). The $Ba(NO_3)_2$ particle size is in the 50-70 nm range but they observed crystals up to 300×150 nm large. Barium nitrate showed triangular and polygonal morphologies (figure 5.3 a) with crystallographic orientation relationships that they described as α-Al_2O_3(0001)//$Ba(NO_3)_2$(111) and α-Al_2O_3(1-210)//$Ba(NO_3)_2$(110).

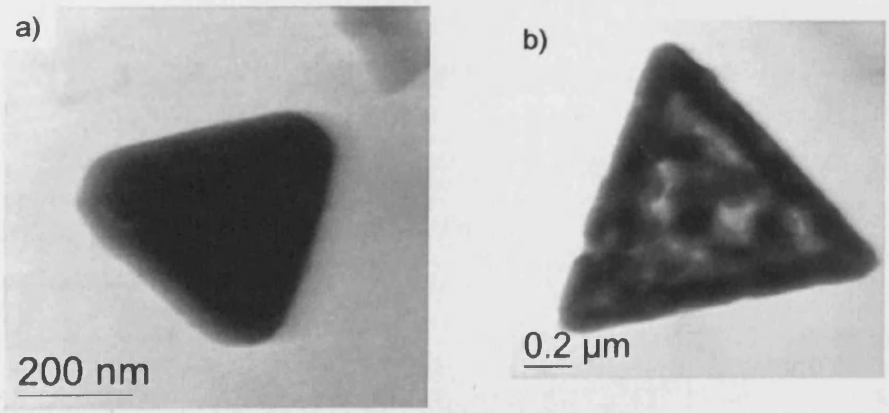

Fig. 5.3: a) As prepared truncated triangular shape $Ba(NO_3)_2$ particle on α-Al_2O_3 and b) BaO particle showing the parental morphology shape. Both images from [10].

Annealing up to ~ 800 °C has the effect of decomposing the nitrate to form BaO. The decomposition of these crystallites was monitored with in situ TEM. The resulting BaO particle showed a morphology similar to its parental single crystal barium nitrate particle, but had shrunk by ~31%. These new BaO particles are not single crystals but a collection of small barium oxide clusters (figure 5.3 b). Moreover, a phase like $BaAl_2O_4$ was probably also present.

The particular truncated triangular geometrical shape presented by the barium nitrate particles can be explained in terms of Wulff shape construction for a cubic structure in which the rates of growth along the <001> and <111> directions are equal [11]. This results in the growth of a crystal having platelet morphology, with the surfaces defined by eight <111> type planes (figure 5.4 b).

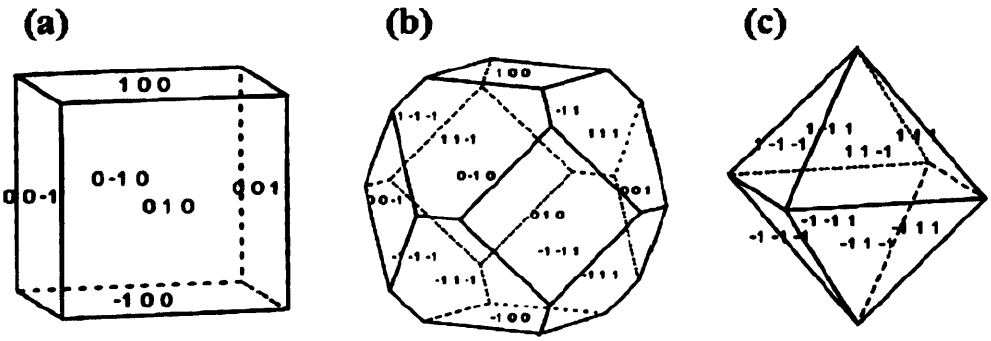

Fig. 5.4: Dependence of particle morphologies on the ratio, *R*, of the growth rate along the <100> direction to that of the <111> direction for a cubic structure. (a) *R*) 0.58 leads to six {100} planes defining a cube; (b) *R*) 1.0 leads to six {100} square planes and eight {111} truncated triangular planes. This structure is defining a truncated octahedron; (c) *R*) 1.73 leads to eight {111} planes defining an octahedron. From [11].

5.2. Experimental setup

AFM measurements were performed using the Veeco NanoscopeIII Multimode SPM described in section 2.8.4.1, and the in situ studies using the AFM environmental cell accessory described in section 2.8.4.2. Images were obtained in air and under inert or reactive atmosphere. The AFM probes used were silicon nitride cantilevers (Si_3N_4) for contact mode having a quadrangular pyramidal tip with a cone angle of 70° and a radius of 10nm, and phosphorus doped silicon having anisotropic shape, 3.5-4.5 μm long, with a force constant between 20 and 80 N/m and resonance frequency in the 251 – 287 kHz range for tapping mode. In some cases, these tips can lead to images dominated by tip artefacts on a nanometre scale [12, 13]. No correction for the tip shape was applied to the AFM images in the following data. All the XPS measurements were performed using the Kratos Axis Ultra DLD XP Spectrometer described in section 2.8.3. The XP spectra were collected using a monochromatic Al X-ray source, charge neutralization gun active, 160 eV Pass Energy for the survey spectra and 40 eV Pass Energy for individual regions. Binding energies were calibrated with respect to the C(1s) (BE = 284.5 eV), feature corresponding to the presence of adventitious carbon. The base pressure in the preparation chamber, where the samples were loaded and parked while waiting to be analysed, was ~ 3×10^{-10} Torr, the base pressure in the analysis chamber ~1×10^{-10} Torr, which increased to ~7×10^{-10} Torr during XPS analysis. XPS data analysis and interpretation was done using CasaXPS [14] software, AFM images using WSxM package [15]. Part of the AFM data presented have been collected while supervising Alexander Bishop's MChem project and part in collaboration with Chanut Bamroongwongdee, PhD student. XPS data were collected in collaboration with Dr. A.F. Carley and Dr. D.J. Morgan.

5.3. Results

5.3.1. Systems Preparation

5.3.1.1. Untreated α-Al_2O_3(0001) single crystal

An untreated α-Al_2O_3(0001) single crystal was imaged with AFM in both tapping (TM-AFM) and contact mode (CM-AFM). Both the scanning modes showed that the surface appeared quite flat. The picture reported in figure 5.5, collected in tapping mode, shows a flat surface, with small contamination, represented by particles of

different rounded shape average 3-13 nm high, 40-50 nm in diameter and covering approximately the 0.1% of the surface. Moreover, linear features are present. These lines could represent scratches on the surface resulting from the crystal polishing process. The contamination is likely due to the fact that the crystal was used without undertaking any cleaning process on it.

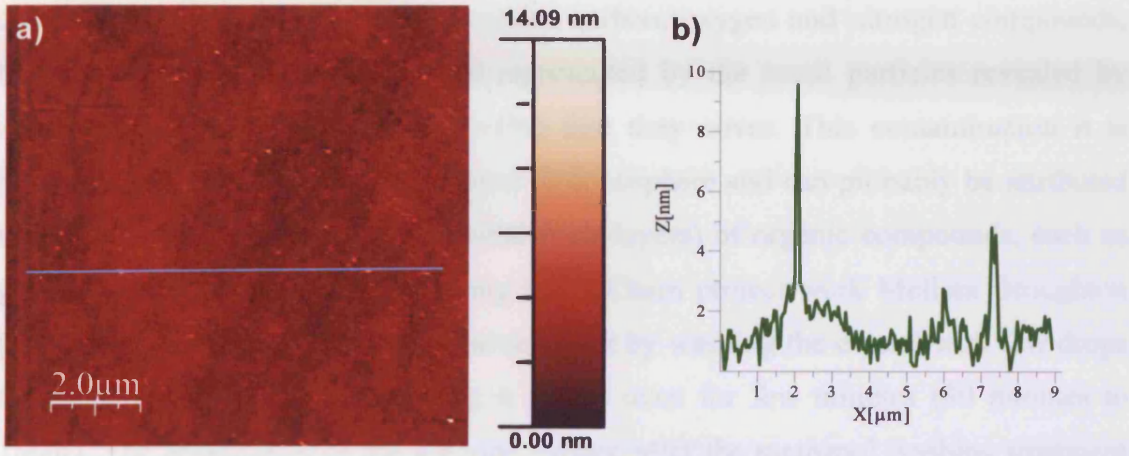

Fig. 5.5: TM-AFM image of untreated α–Al_2O_3(0001). a) Topography; lines and small particles are visible across the surface; image size 10×10 µm. b) Blue line profile as in a).

Although, very wide area appeared clean, with only few unidentified particles on top, some other were completely covered by a layer of matter, likely contamination, that appeared to be mobile under the effect scanning in contact mode (figure 5.6).

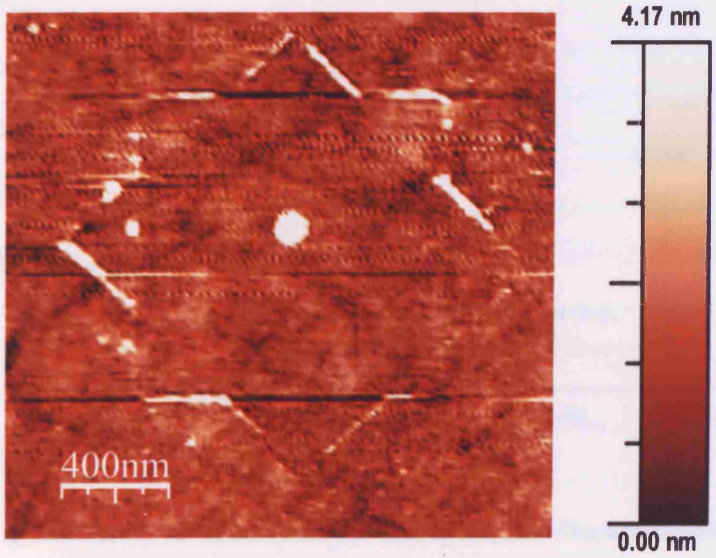

Fig. 5.6: CM-AFM image showing the topography of untreated α–Al_2O_3(0001). For contrast reasons the image has been equalised. Image size 2×2µm.

The "star shape" feature was noticed after scanning a 1.0×1.0 μm area, rotating the scanning angle by 45° and increasing the scanning size to 2.0×2.0 μm. It was attributed to lose material that was moved by the tip on the sides of the area being scanned.

The XPS analysis (figure 5.7) showed that the contamination was essentially comprised by the presence of amorphous carbon, oxygen and nitrogen compounds; however, this contaminants are not represented by the small particles revealed by AFM because of the small area (~1%) that they cover. This contamination it is normally observed on samples exposed to atmosphere and can probably be attributed to the presence of a high level (several monolayers) of organic compounds, such as grease, on the surface; in fact, during her MChem project work Melissa Broughton [16] discovered that this layer can be removed by washing the crystal with few drops methanol for few times and drying it in the oven for few minutes (30 minutes to 1hour). The appearance of the alumina surface after the methanol washing treatment is similar to the one showed in figure 5.5.

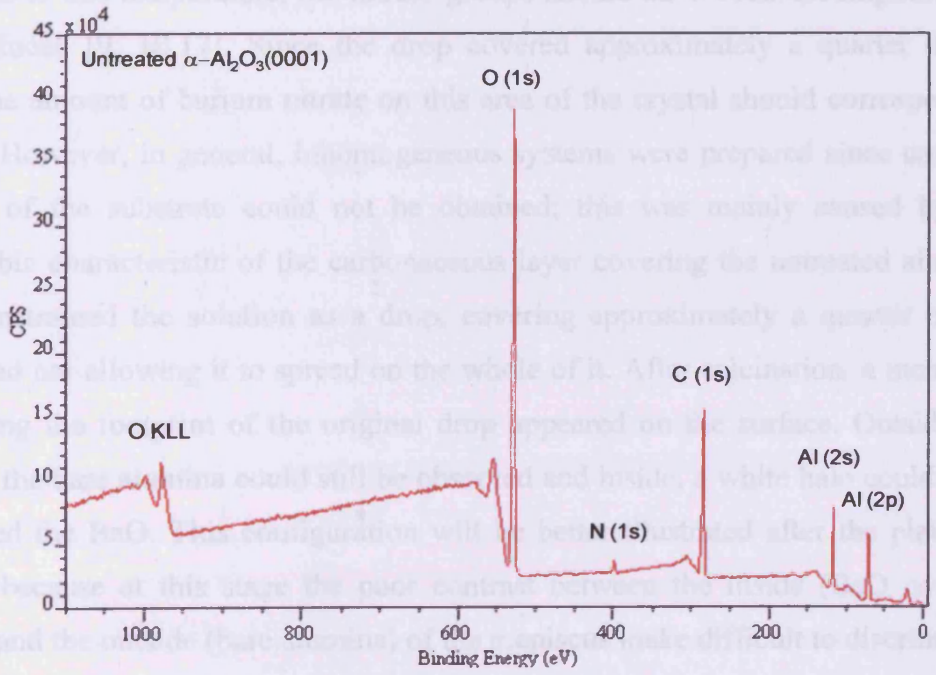

Fig 5.7: Survey XP spectrum of untreated alumina. The contaminations revealed by XPS are mainly comprised of carbon, oxygen and, in minor part nitrogen, compounds.

5.3.1.2. Pt/BaO*/α-Al_2O_3(0001)

A $Ba(NO_3)_2$ solution was prepared dissolving 0.254 g of barium nitrate in 250 ml of deionised water. 25 ml were transferred on a volumetric flask and diluted to 250 ml with deionised water, obtaining a 100 mg/l solution (~1.6×10^{-5} mol/l). This concentration was determined taking into account that BaO unit cell is 0.552 nm, therefore it will cover a surface of ~0.305 nm^2 (see figure 4.2). When decomposed, to 1 molecule of $Ba(NO_3)_2$ will correspond 1 molecule of BaO and in order to cover a 1 cm^2 surface (1×10^{14} nm^2), the alumina crystal, with a single monolayer of barium oxide, 3.3×10^{14} BaO units would be necessary. Considering the BaO units in terms of barium atoms, since a barium precursor was used, and dividing by Avogadro's number, this gives 5.4×10^{-10} moles of barium precursor needed. The solution was added onto the crystal by dropping the precursor solution on it by means of a Pasteur pipette, whose drop volume was evaluated in ~ 0.033 ml. 5.4×10^{-10} moles in 0.033 ml gives a concentration of ~1.6×10^{-5} mol/l.

After preparing the solution, one drop of the $Ba(NO_3)_2$ solution was put on an untreated α-Al_2O_3(0001) single crystal, then the crystal put in a crucible, covered, dried in furnace for 2 hours at 120 °C and calcined for 3 hours at 600 °C. By heating the system to this temperature, the nitrate groups should have been decomposed and BaO produced [9, 10,17]. Since the drop covered approximately a quarter of the crystal, the amount of barium nitrate on this area of the crystal should correspond to ~4 MLe. However, in general, inhomogeneous systems were prepared since uniform coverage of the substrate could not be obtained; this was mainly caused by the hydrophobic characteristic of the carbonaceous layer covering the untreated alumina which constrained the solution as a drop, covering approximately a quarter of the surface and not allowing it to spread on the whole of it. After calcination, a meniscus highlighting the footprint of the original drop appeared on the surface. Outside the meniscus the bare alumina could still be observed and inside, a white halo could have represented the BaO. This configuration will be better illustrated after the platinum addition, because at this stage the poor contrast between the inside (BaO covered alumina) and the outside (bare alumina) of the meniscus make difficult to discriminate between the two areas on an optical picture.

From the XP spectroscopy, figure 5.8 illustrates the preparation of the Ba-containing layer, the $Ba(3d_{5/2})$ was recorded at 779.8 eV, value in agreement with the one expected for cationic barium. The XP integral ratio $Ba(3d_{5/2})$/Al(2p) was 0.21. The

$Ba(3d_{5/2})$/O(1s) was 0.03, considering the whole O(1s) peak. For BaO an O(1s) peak at around 528.8 eV would be expected, at around 531-532 eV for barium hydroxide and carbonate. In table 5.1 binding energies for barium and relevant compounds are reported.

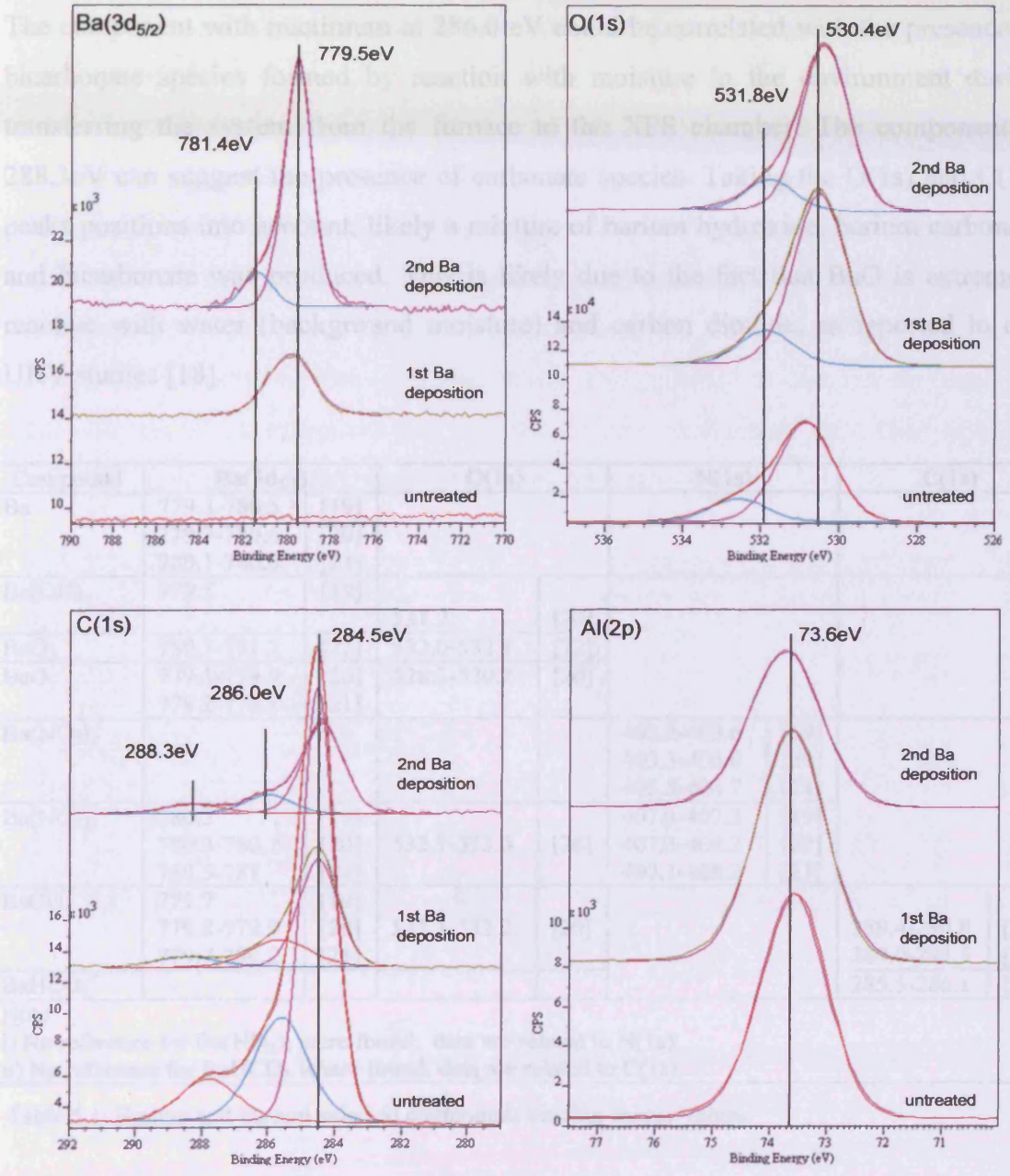

Fig 5.8: XP spectra showing the evolution of the features in the $Ba(3d_{5/2})$, O(1s), C(1s) and Al(2p) regions during the preparation of the BaO*/α-Al_2O_3(0001) system. Spectra are offset for clarity and peaks fittings are also shown.

The O(1s) recorded on the untreated alumina had a maximum at 530.7 eV. The main component of the O(1s) XP peak after the first barium deposition, was recorded at

530.4 eV, and could still be considered the one correlated with the alumina substrate. However, a general increase in the peak area was recorded, as well as the presence of a different oxygen species was detected and fitted with a peak having a maximum at 531.8 eV. The C(1s) could reasonably be fitted with three Gaussian peaks, the main one being at 284.5 eV and identified as carbonaceous contamination on the crystal. The component with maximum at 286.0 eV could be correlated with the presence of bicarbonate species formed by reaction with moisture in the environment during transferring the system from the furnace to the XPS chamber. The component at 288.3eV can suggest the presence of carbonate species. Taking the O(1s) and C(1s) peaks positions into account, likely a mixture of barium hydroxide, barium carbonate and bicarbonate was produced. This is likely due to the fact that BaO is extremely reactive with water (background moisture) and carbon dioxide, as reported in our UHV studies [18].

Compound	$Ba(3d_{5/2})$		O(1s)		N(1s)		C(1s)	
Ba	779.3-780.5 779.3-780.6 780.1-780.6	[19] [20] [21]						
$Ba(OH)_2$	779.5	[19]	531.2	[20]				
BaO_2	780.3-781.2	[22]	532.0-532.7	[22]				
BaO	779.1-779.9 779.2-779.8	[20] [21]	528.3-530.2	[20]				
$Ba(NO_2)_2$[i]					403.2-403.6 403.3-405.0 403.8-404.7	[19] [20] [21]		
$Ba(NO_3)_2$	780.5 780.3-780.7 780.5-781	[19] [20] [21]	532.9-533.0	[20]	407.1-407.3 407.3-408.2 407.1-408.2	[19] [20] [21]		
$BaCO_3$	779.7 779.8-779.9 779.7-780.2	[19] [20] [21]	531.1-532.2	[20]			289.4-290.8 289.0-291.5	[20] [21]
$BaHCO_3$[ii]							285.5-286.1	[23]

Note
i) No reference for $Ba(NO_2)_2$ were found, data are related to N(1s).
ii) No reference for $BaHCO_3$ where found, data are related to C(1s).

Table 5.1: Barium and barium selected compounds binding energy values.

The Al(2p) showed a maximum at ~73.6 eV, as expected for aluminium in Al_2O_3 [20]. The fractional signal of the Al(2p) peak was calculated as 0.585. Assuming that only BaO was prepared and an IMFP [24] of 2.88 nm for the photoelectron at a kinetic energy of 1413 eV (Al Kα, 1486.6 eV, minus Al(2p) binding energy, 73.6 eV) a theoretical film thickness of 1.54 nm, corresponding to 2.8 MLe, under the

approximation of uniform film growth, was obtained (since no information on the orientation of the structures prepared was available, the monolayer thickness has been taken as the unit cell size of BaO 0.552 nm). However, this information is pure speculation, since a high level of contamination, that could have attenuated the reference value for the Al(2p) XP peak, was recorded on the bare crystal before starting the preparation and the overlayer grows in form of particles in the way that will be shown later.

TM-AFM measurements (figure 5.9) showed that after adding the barium, the surface was covered in small particles, 1603 on a 10.9 μm^2, occupying ~23.3% of the area; this means 147 particles/μm^2, therefore ~1.5×10^{14} particles/m^2. The volume represented by the particles was evaluated as 2.5×10^5 nm^3 and the first neighbour distance in 55.3 nm. These values were determined via software [15], evaluating the surface area covered by the particles. It was still possible to observe the scratches characteristic of the untreated alumina; this feature runs across the whole image in figure 5.9 b), in the direction indicated by the blue arrow.

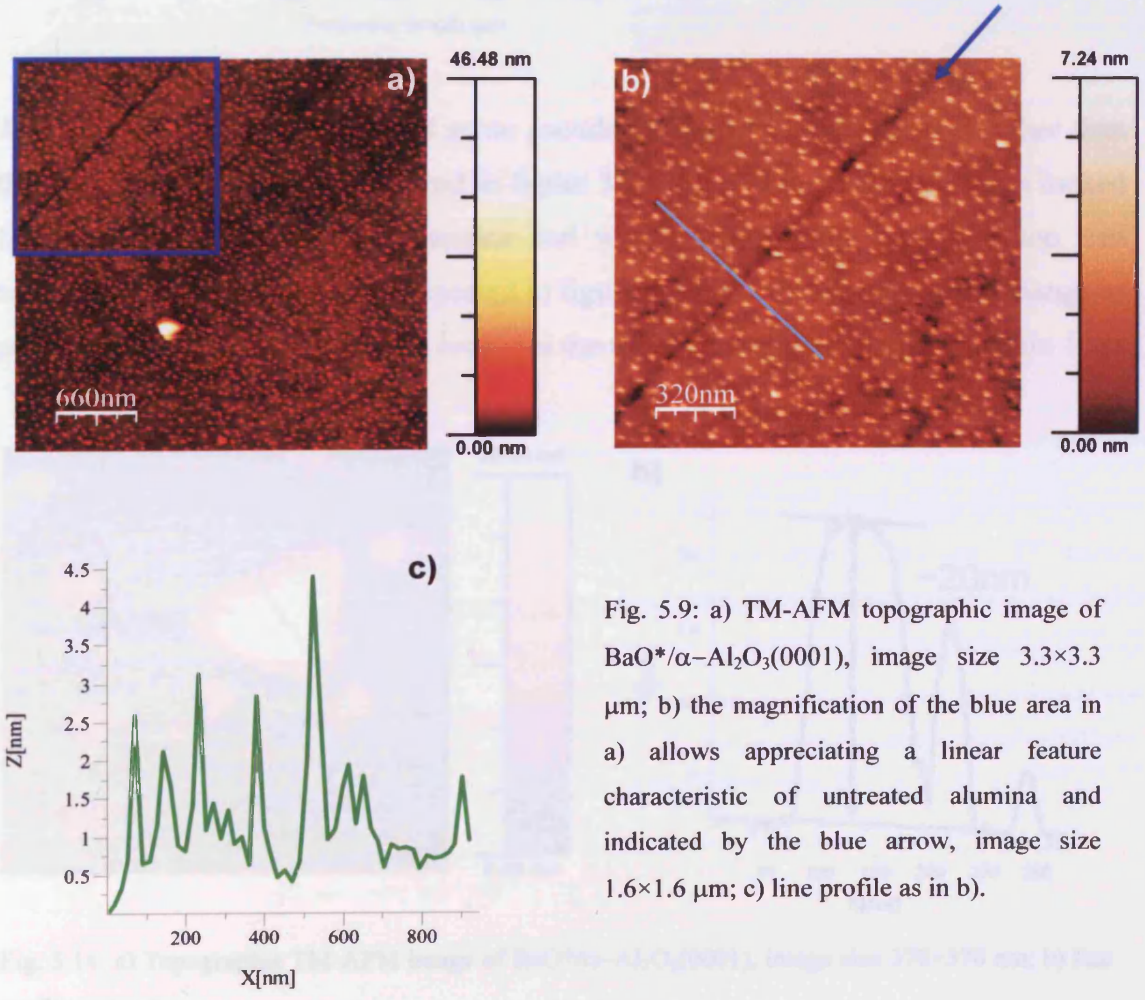

Fig. 5.9: a) TM-AFM topographic image of BaO*/α–Al_2O_3(0001), image size 3.3×3.3 μm; b) the magnification of the blue area in a) allows appreciating a linear feature characteristic of untreated alumina and indicated by the blue arrow, image size 1.6×1.6 μm; c) line profile as in b).

A PSD (Particle Size Distribution) analysis (figure 5.10), performed on figure 5.9 a), showed that the particle sizes were normal distributed with an average perimeter of 93±1 nm. In the approximation of circular particle shape, this would correspond to an average diameter of ~29.6 nm; however, when it is difficult to recognize the particle shape, an evaluation of the perimeter length appear more appropriate.

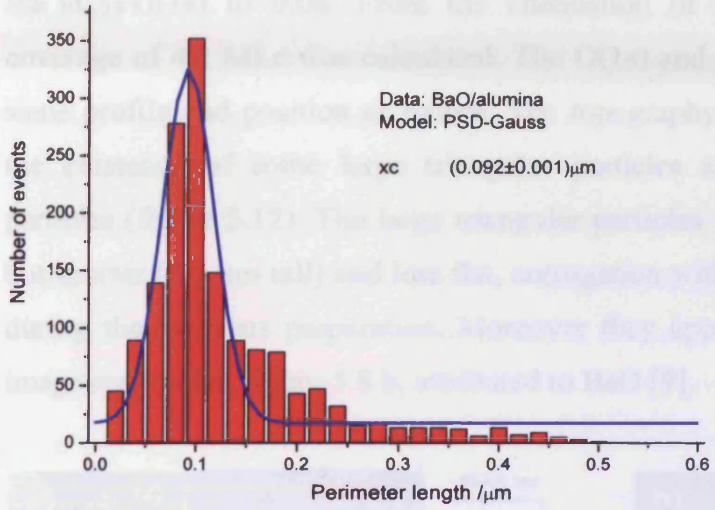

Fig. 5.10: PSD (Particle Size Distribution) analysis of the particles in figure 5.9 a). The average particle perimeter is 93±1 nm.

AFM imaging revealed also that some pseudo triangular shaped particles other than the irregularly shaped ones showed in figure 5.9 were present. These particles looked like equilateral or isosceles triangles and were ~20 nm high and their top was reasonably flat. An example is reported in figure 5.11: the three sides of the triangular particle are 134, 137 and 130 nm long and the roughness of the top part is within 1 nm.

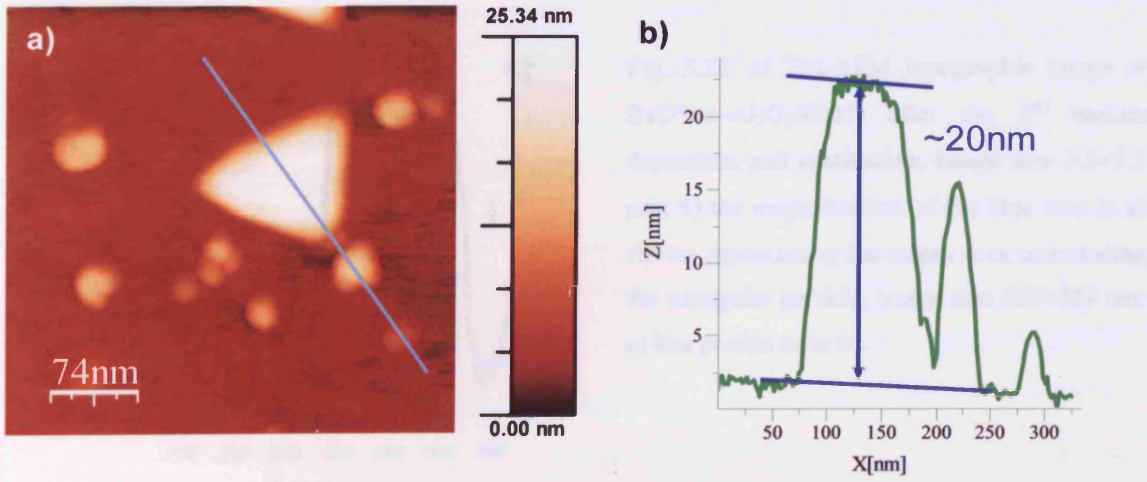

Fig. 5.11: a) Topographic TM-AFM image of BaO*/α–Al_2O_3(0001), image size 370×370 nm; b) line profile as in a).

To increase the coverage in barium compounds, another drop of barium nitrate solution was put on the surface and the system dried and calcined another time in the same way. The Ba($3d_{5/2}$) XP spectrum showed a maximum at 779.5 eV and an asymmetry at higher binding energy that could be fitted with a peak with maximum at 781.4 eV (figure 5.8). This could indicate that two different barium states were present. The Ba($3d_{5/2}$)/Al(2p) XP integral ratio went up to 0.65 and the Ba($3d_{5/2}$)/O(1s) to 0.08. From the attenuation of the Al(2p) peak, a theoretical coverage of 4.2 MLe was calculated. The O(1s) and C(1s) peaks showed exactly the same profile and position as before. The topography revealed by TM-AFM showed the existence of some large triangular particles surrounded by smaller rounded particles (figure 5.12). The large triangular particles were average three times wider, but shorter (6-7 nm tall) and less flat, corrugation within 3nm, than the ones observed during the previous preparation. Moreover they appeared very similar to the TEM image reported in figure 5.8 b, attributed to BaO [9].

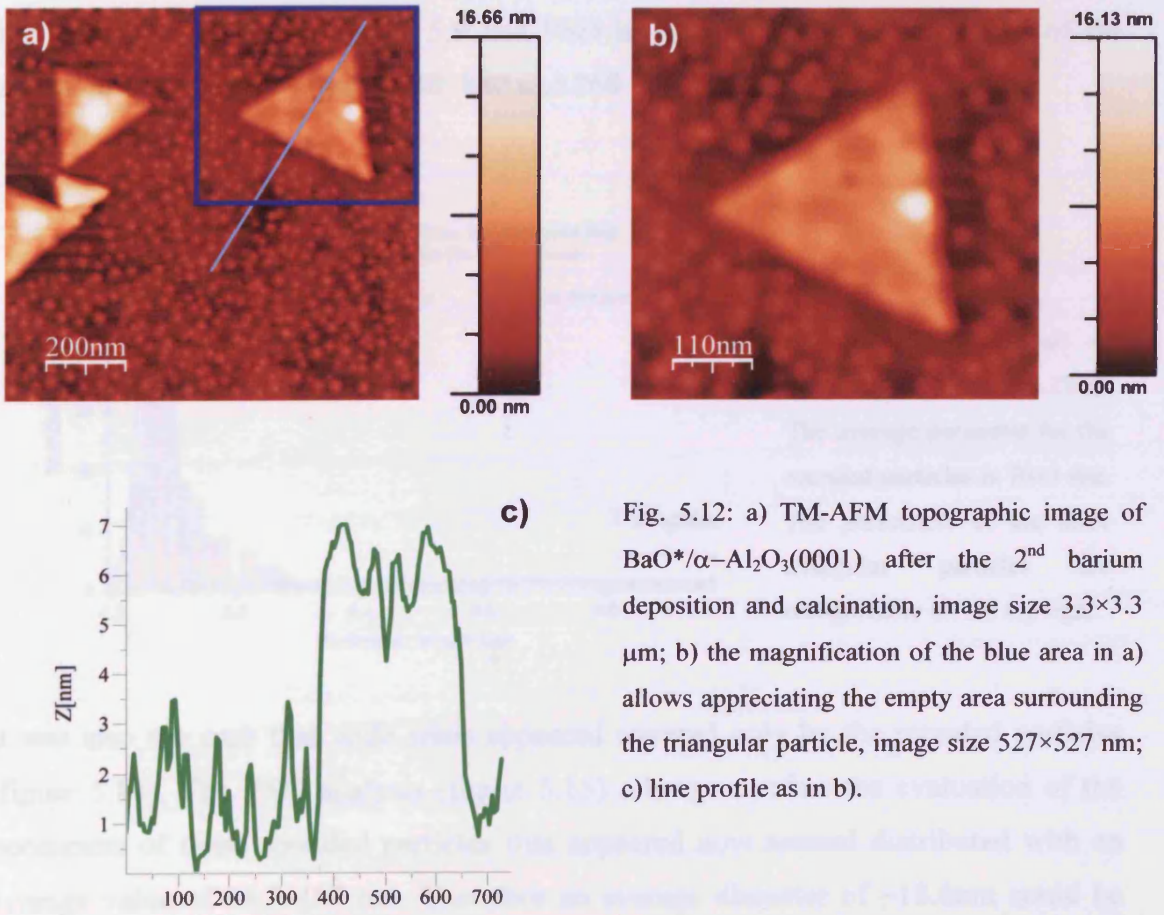

Fig. 5.12: a) TM-AFM topographic image of BaO*/α–Al_2O_3(0001) after the 2nd barium deposition and calcination, image size 3.3×3.3 μm; b) the magnification of the blue area in a) allows appreciating the empty area surrounding the triangular particle, image size 527×527 nm; c) line profile as in b).

Mainly because of their peculiar shape, also the particles prepared during this work are attributed to barium oxide. Looking at the area immediately surrounding the triangular particles edges, it can be observed that there is a gap between the triangular particles and the rounded ones. This could indicate that the smaller rounded particles have sintered to form the bigger triangular, due to the calcination process.

The PSD analysis performed on figure 5.12 a), showed that on a 1 μm^2 area 260 particles were present, therefore 2.6×10^{14} particles/m^2, covering the 37.8% of the surface. The bigger triangular particles covered the 11.4% of the surface, approximately a third of the total area covered by the barium oxide ad-layer. The volume occupied by the particles was evaluated as 9.4×10^5 nm^3 in total, 4.3×10^5 nm^3 by the triangular features, and the first neighbour distance in 42.7 nm. In the present case, two different shape are present, triangular and rounded. The perimeters of the rounded particles are Gaussian distributed, with an average value of 70±1 nm (figure 5.13), average diameter of 22.3 nm. They are therefore just slightly smaller than the previously prepared (see figure 5.9 and PSD in figure 2.10). The perimeters of the triangular particles are around 840, 880 and 960 nm.

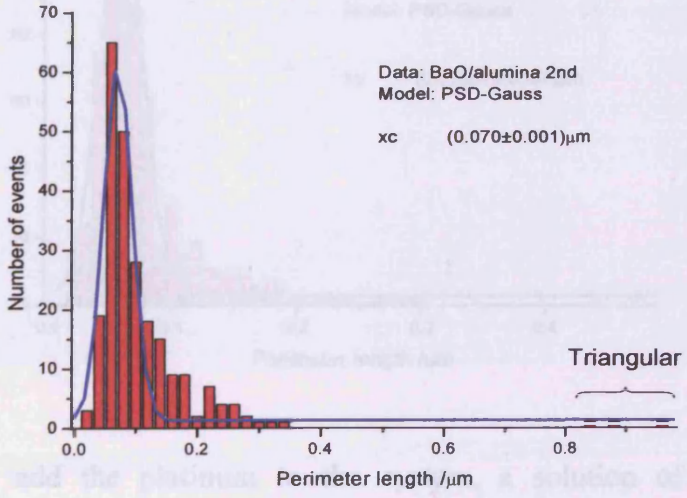

Fig. 5.13: PSD analysis of the particles in figure 5.12 a). The average perimeter for the rounded particles is 70±1 nm. The perimeters of the three triangular particles are recognizable on the top right.

It was also the case that wide areas appeared covered only by the rounded particles (figure 5.14). The PSD analysis (figure 5.15) allows to refine the evaluation of the perimeters of these rounded particles that appeared now normal distributed with an average value of 58.5±0.7 nm. Therefore an average diameter of ~18.6nm could be calculated. In picture 5.14, 652 particles could be counted, giving a density of

6.5×10^{14} particels/m^2, covering approximately 28.4% of the surface, having a first neighbour distance of 28.4 nm and occupying a volume of 2.3×10^5 nm^3.

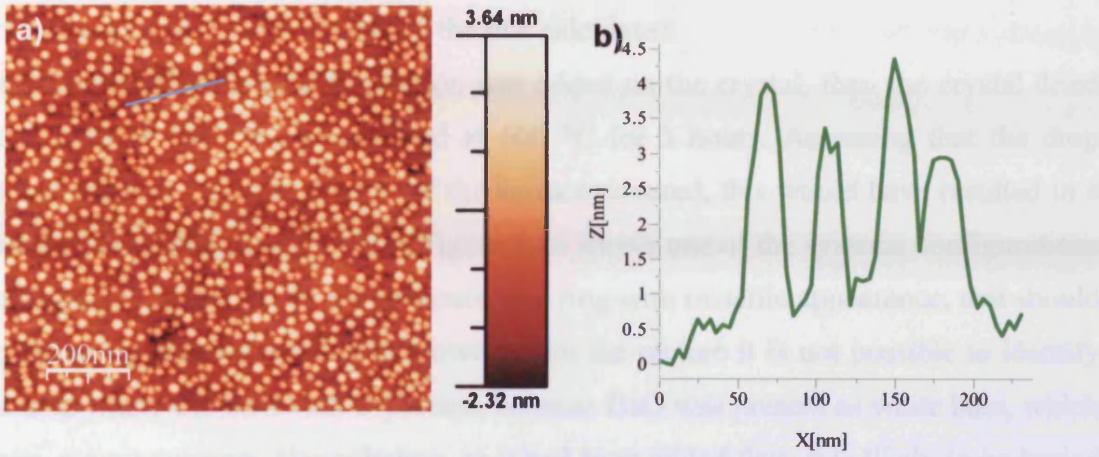

Fig. 5.14: a) Topographic TM-AFM image of BaO*/α–Al_2O_3(0001) showing only small rounded particles, image size 1×1μm; b) line profile as in a).

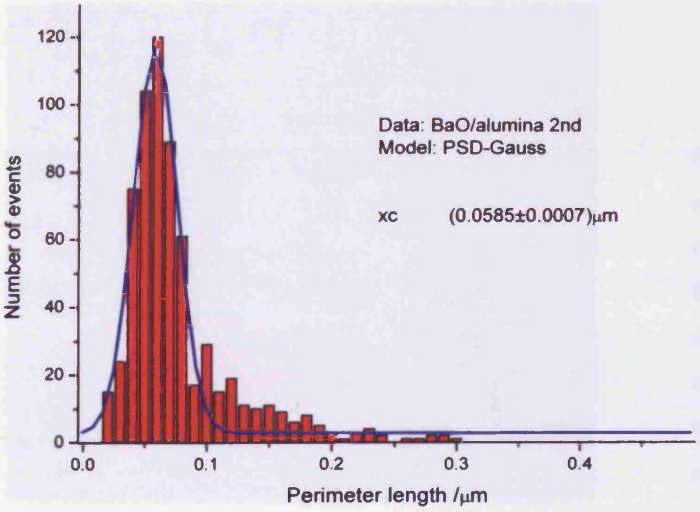

Fig. 5.15: PSD of particles in figure 5.14 a). The average particle perimeter is 58.5±0.7 nm, the average diameter 18.6nm.

To add the platinum to the system, a solution of $H_2PtCl_6{\cdot}6H_2O$ was prepared dissolving 0.251 g of hexahydro chloroplatinic acid in 250 ml of deionised water. 25 ml were transferred on a volumetric flask and diluted to 250 ml with deionised water, obtaining a 20mg/l solution (~3.8×10^{-5} mol/l). This concentration was determined taking into consideration that the footprint of one platinum atom was calculated as 0.098 nm^2, being its atomic radius 0.177 nm [25], therefore, ~1×10^{15} atoms are needed to prepare a 1 ML thick film on a 1×10^{14} nm^2 surface. Dividing by Avogadro's

number, this corresponds to 1.7×10^{-9} mol, which will be present in 0.033 ml, the volume of a drop of solution obtained adding the solution using a Pasteur pipette. This, in turns, corresponds to a concentration of $\sim5.1\times10^{-5}$ mol/l. The concentration prepared appeared close enough to the one calculated.

One drop (0.033 ml) of this solution was added on the crystal, then the crystal dried for 1 hour at 100 °C and calcined at 600 °C for 3 hours. Assuming that the drop spread uniformly on the quarter of the surface covered, this would have resulted in a platinum coverage of ~ 2.9 MLe. Figure 5.16 shows one of the systems configurations obtained, characterized by the presence of a ring with metallic appearance, that should represent the metallic platinum. However, on the picture it is not possible to identify the area where the BaO was deposited, because BaO was present as white halo, which gives a poor contrast. Nevertheless, as it had been added first, it is likely to be buried under the platinum, where a large amount of platinum is present. Where less platinum is present, BaO particles could be either in intimate contact with the platinum, or isolated.

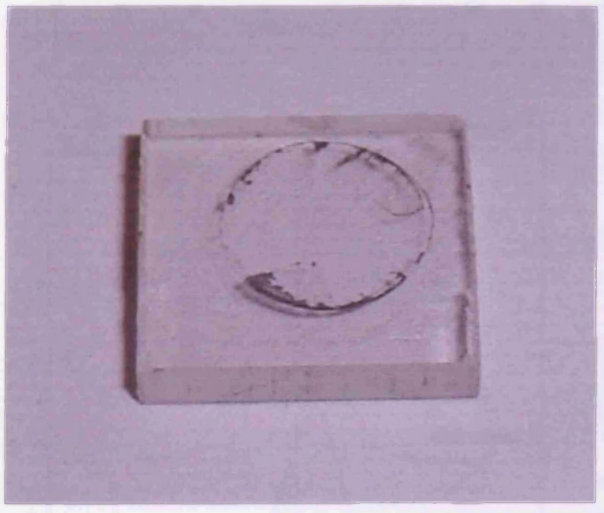

Fig. 5.16: The Pt/BaO*/Al_2O_3(0001) after Pt addition and calcination. A ring is visible on the surface. Since barium compounds are white and difficult to discriminate for contrast reasons, this ring should represent the platinum. The alumina crystal size is 1×1 cm.

XPS collected after calcination, revealed that a second peak appeared to the lower binding energy side of the Al(2p) peak (figure 5.17). This peak is in the right position (70.9 eV) for the Pt($4f_{7/2}$) peak and the presence of platinum was confirmed by the appearance of the Pt(4d) doublet at around 314eV on the survey spectrum (not shown). By fitting the Al(2p) region it was possible to appreciate the Pt(4f) doublet. The maximum of the Al(2p) resulted in 73.6 eV, value in agreement with the presence of Al^{3+}. The position of the Pt(4f) is compatible with the presence of platinum in the

metallic state. From the attenuation of the Al(2p), using an IMFP of 1.53 nm for the photoelectrons at the energy of the Al(2p) [24] and a monolayer thickness of 0.28 nm for the platinum [25], a theoretical platinum coverage of 0.5 MLe was obtained.

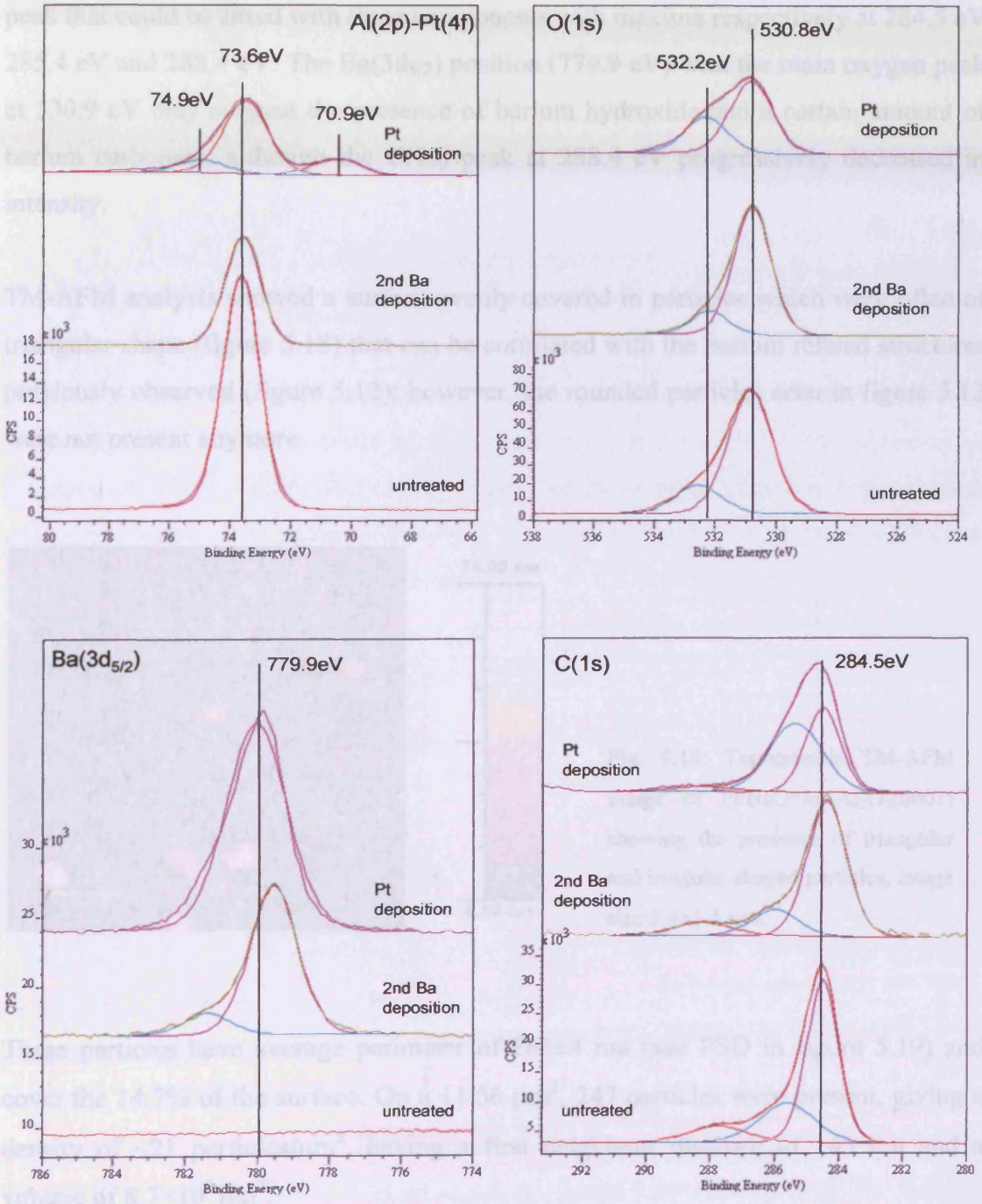

Fig. 5.17: XP spectra showing the evolution of the features in the Al(2p)-Pt(4f), O(1s), Ba($3d_{5/2}$) and C(1s) regions during the preparation of the Pt/BaO*/α-Al_2O_3(0001) system. Peak fittings are also shown and spectra are offset for clarity.

The O(1s) peak changed shape in the way that the shoulder at higher binding energy, fitted with a peak with maximum at 532.2 eV, was now more evident. After adding platinum, the Ba($3d_{5/2}$) shifted to 779.9 eV and its component formerly at 781.4 eV disappeared, meaning only one barium species was present. The C(1s) still showed a peak that could be fitted with three components with maxima respectively at 284.5 eV, 285.4 eV and 288.4 eV. The Ba($3d_{5/2}$) position (779.9 eV) with the main oxygen peak at 530.9 eV may suggest the presence of barium hydroxide and a certain amount of barium carbonate, although the C(1s) peak at 288.4 eV progressively decreased in intensity.

TM-AFM analysis showed a surface evenly covered in particles which were often of triangular shape (figure 5.18) that can be correlated with the barium related structures previously observed (figure 5.12); however, the rounded particles seen in figure 5.12 were not present anymore.

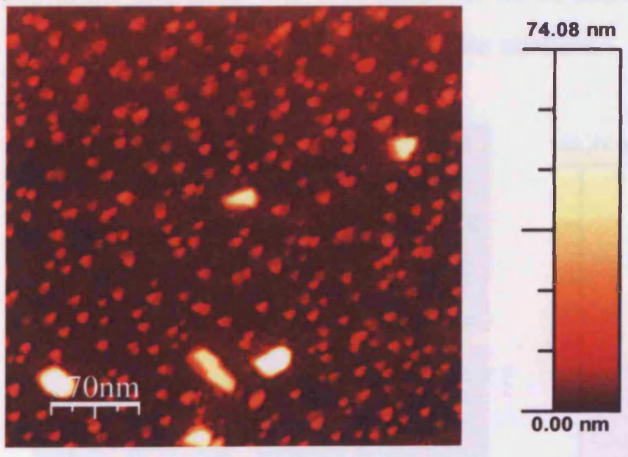

Fig. 5.18: Topographic TM-AFM image of Pt/BaO*/α–Al_2O_3(0001) showing the presence of triangular and irregular shaped particles, image size 3.4×3.4 μm.

These particles have average perimeter of 263±4 nm (see PSD in figure 5.19) and cover the 14.7% of the surface. On a 11.56 μm^2, 247 particles were present, giving a density of ~21 particles/μm^2, having a first neighbour distance of 145 nm and a volume of 8.7×10^5 nm^3.

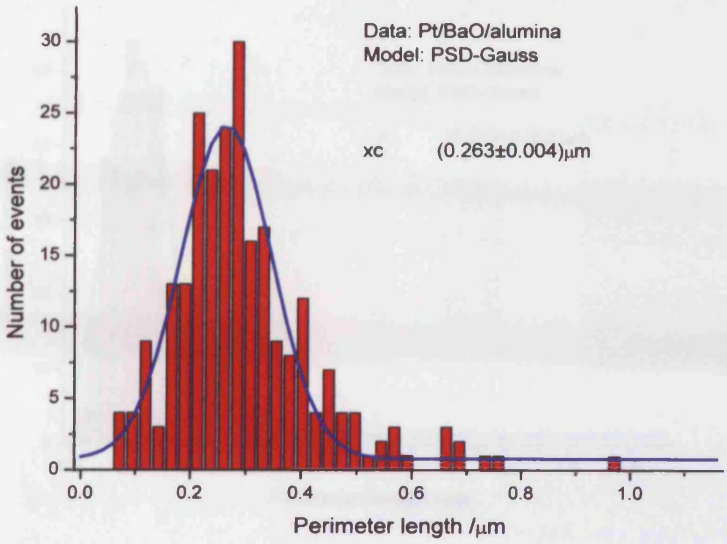

Fig. 5.19: PSD of particles in figure 5.18. The average perimeter length is 263±4 nm.

Worth to notice that at this stage, even scanning several areas inside the metal ring (figure 5.20 is another example), there was no way to identify the presence of particles of different shape that could suggest the presence of platinum. Nevertheless, platinum presence was recorded via XPS, therefore it should have been concentrated into the ring and not dispersed on the surface.

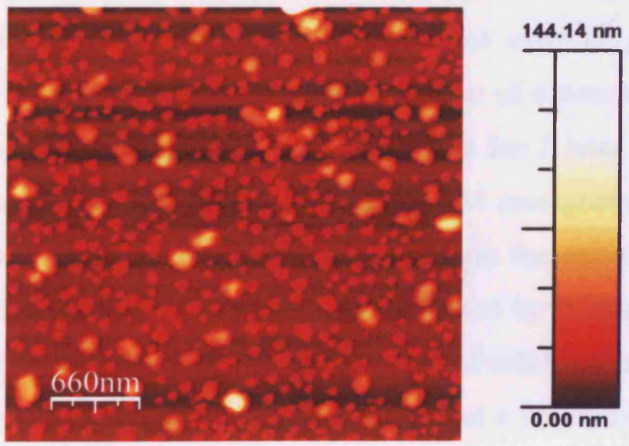

Fig. 5.20: Topographic TM-AFM image of another area of the same Pt/BaO*/α–Al_2O_3(0001) preparation as in figure 5.18, showing the presence of triangular and irregular shaped particles, image size 3.3×3.3 μm.

The PSD analysis (figure 5.21) performed on figure 5.20 showed consistent results with the one performed in figure 5.18, giving an average perimeter length of 216±5 nm, with a density of 36 particles/μm^2. However, the particles in this area covered the 26.7% of the surface with a first neighbour distance of 118nm and a volume of 3.3×10^6 nm^3.

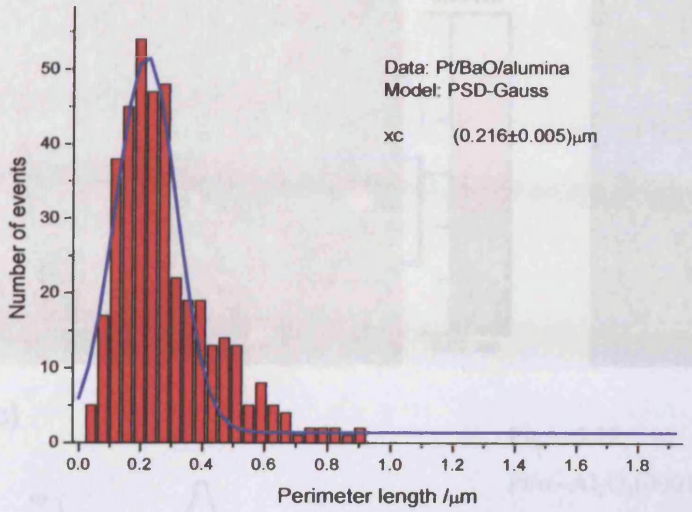

Fig. 5.21: PSD for the particles in figure 5.20. The average perimeter length is 216±5 nm.

The system prepared in the way just described was also tested for reactivity towards NO and NO/O_2. This will be illustrated in section 5.5.

5.3.1.3. BaO*/Pt/α-Al_2O_3(0001)

The BaO*/Pt/α-Al_2O_3(0001) was prepared using the same barium nitrate 100mg/l and chloroplatinic acid 20 mg/l solutions used to prepare the Pt/BaO*/α-Al_2O_3(0001) system. A drop of a 20 mg/l solution of chloroplatinic acid was put on an untreated alumina crystal and the system dried for 1 hour at 100 °C and calcined in air for 3 hours at 600 °C. After XPS and AFM measurements were collected, one drop of the barium nitrate 100 mg/l was added on the substrate obtained. The system was then dried for 1 hour at 100 °C and calcined for 3 hours at 600 °C. TM-AFM (figure 5.22 b) showed that after Pt deposition and calcination, a total of 185 particles, with a first neighbouring distance of 48.6 nm and a volume of 1.2×10^6 nm^3, were present on a 1 μm^2 surface. Among some smaller (average perimeter 58.4±0.6 nm, from the PSD analysis reported in figure 5.23) and irregularly shaped particles, which covered approximately 15.3% of the surface, few much bigger ones appeared. Some of them had a regular hexagonal shape. The one shown in figure 5.22 b) has a total perimeter of ~ 890 nm, covers approximately 4% of the surface and has a volume of 9.6×10^5 nm^3. The distribution of the smaller particles did not appear uniform, as some areas on the surface appeared empty.

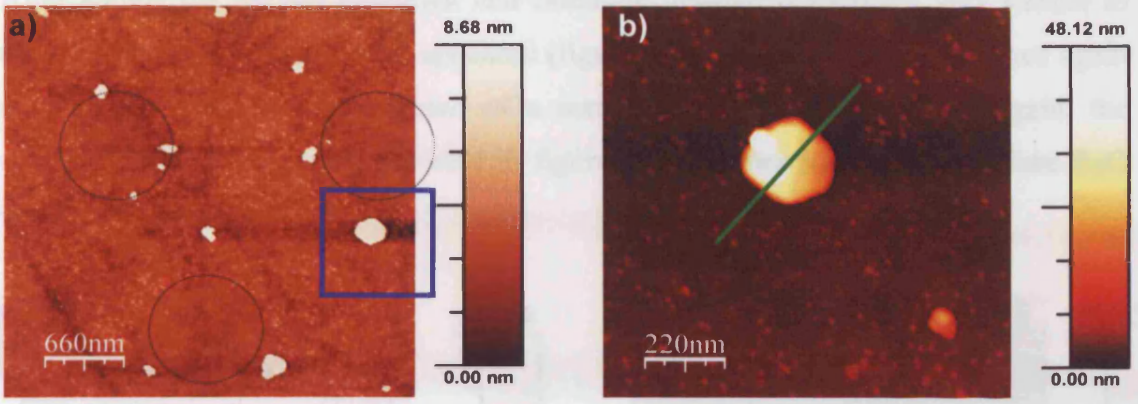

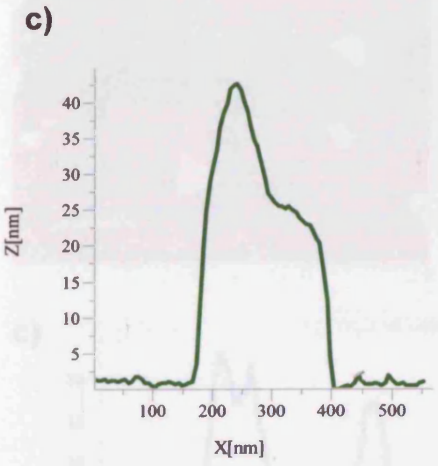

Fig. 5.22: a) Topographic TM-AFM image of Pt/α–Al_2O_3(0001) showing the presence of irregular shaped and hexagonal particles, image size 3.3×3.3 μm; the image was equalised in order to make more evident the areas covered by particles and the areas free of particles (dotted areas); b) close up of the area in the blue square in a): the area on the top of the hexagonal particle appeared free; image size 1×1μm; c) line profile as in b).

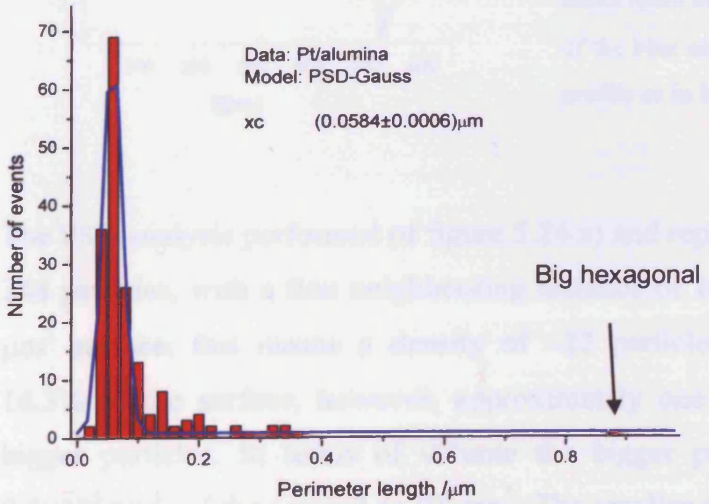

Fig. 5.23: PSD of particles in figure 5.22 b). The average perimeter length is 58.4±0.6 nm.

After adding the barium precursor and calcining, triangular particles very similar to the ones showed in figure 5.12 appeared (figure 5.24). These particles are once again not flat and they look comprised of a series of other particles. Once again, the similarity with the features reported in figure 5.3 b) appears evident, therefore BaO was likely prepared.

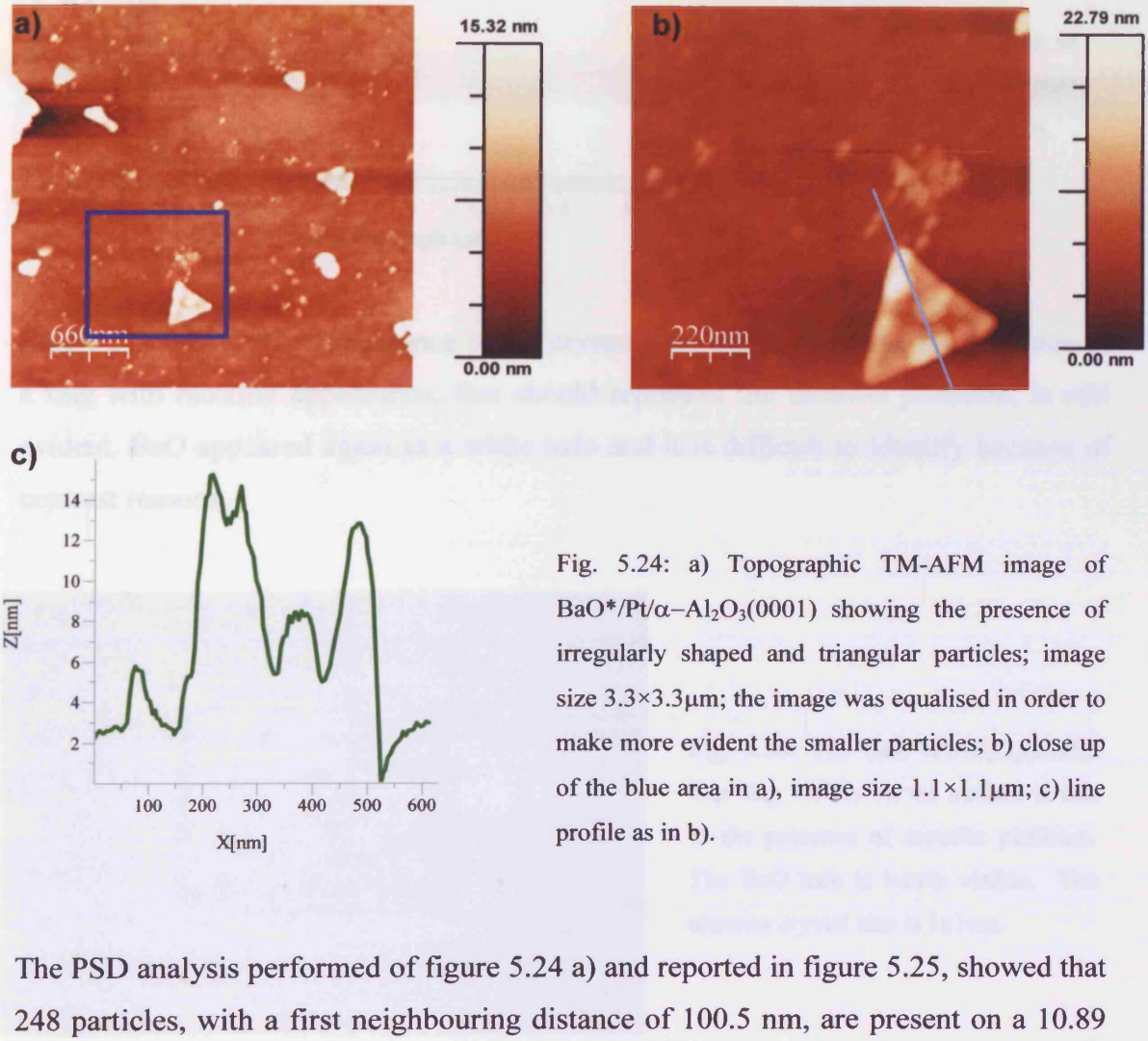

Fig. 5.24: a) Topographic TM-AFM image of BaO*/Pt/α–Al_2O_3(0001) showing the presence of irregularly shaped and triangular particles; image size 3.3×3.3μm; the image was equalised in order to make more evident the smaller particles; b) close up of the blue area in a), image size 1.1×1.1μm; c) line profile as in b).

The PSD analysis performed of figure 5.24 a) and reported in figure 5.25, showed that 248 particles, with a first neighbouring distance of 100.5 nm, are present on a 10.89 μm^2 surface; this means a density of ~22 particles/μm^2. These particles covered 16.3% of the surface, however, approximately one third is represented by the 24 bigger particles. In terms of volume the bigger particles represent roughly half, 9.4×10^5 nm^3, of the total, 2.4×10^6 nm^3. The smaller particles have average perimeter length of 120±1 nm, a value nearly double than the one showed by the system before adding the barium precursor.

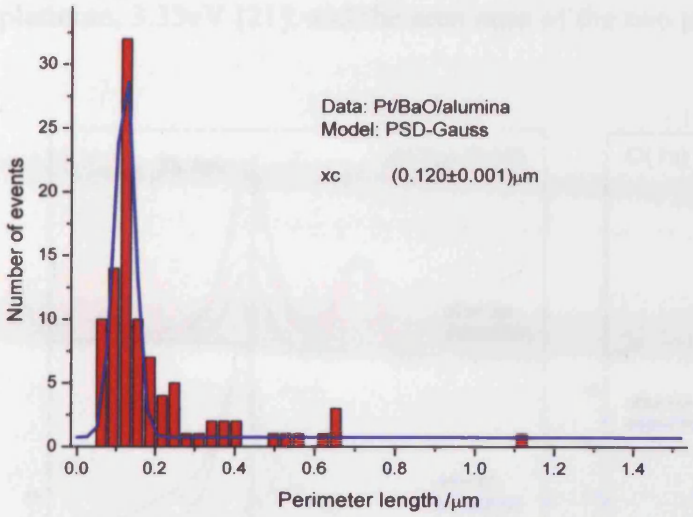

Fig. 5.25: PSD of particles in figure 5.24 a). The average perimeter length is 120±1 nm.

Figure 5.26 shows the appearance of the crystal after the preparation. the presence of a ring with metallic appearance, that should represent the metallic platinum, is still evident. BaO appeared again as a white halo and it is difficult to identify because of contrast reasons.

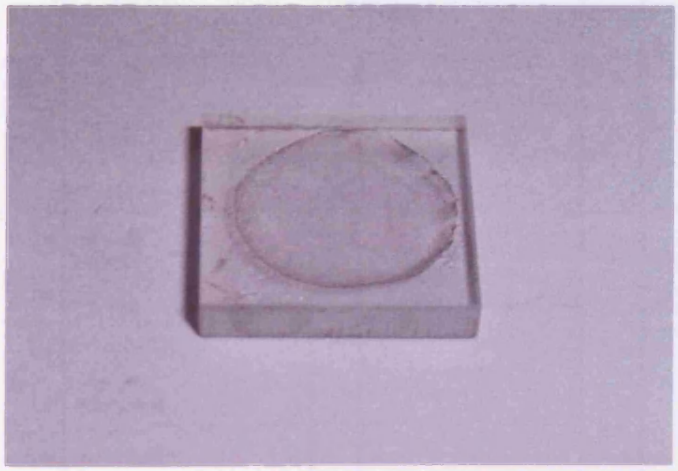

Fig. 5.26: The BaO*/Pt/Al_2O_3(0001). The ring visible on the surface is due to the presence of metallic platinum. The BaO halo is barely visible. The alumina crystal size is 1x1cm.

Figure 5.27 shows the XP spectra collected before and after platinum deposition but not calcination and after barium deposition and calcination. After platinum deposition, but before calcination, the Al(2p) XP spectrum appeared broader and the area under the curve could be fitted with three peaks. Subtracting the more intense peak at ~73.7 eV, a doublet appeared evident (figure 5.28 a). This doublet corresponds to the 4f XP spectrum of platinum, being the positions for the two peaks 72.7eV and 75.9eV, the

difference in energy between the two maxima 3.2eV, value in agreement with ΔJ for platinum, 3.33eV [21], and the area ratio of the two peaks ~1.23.

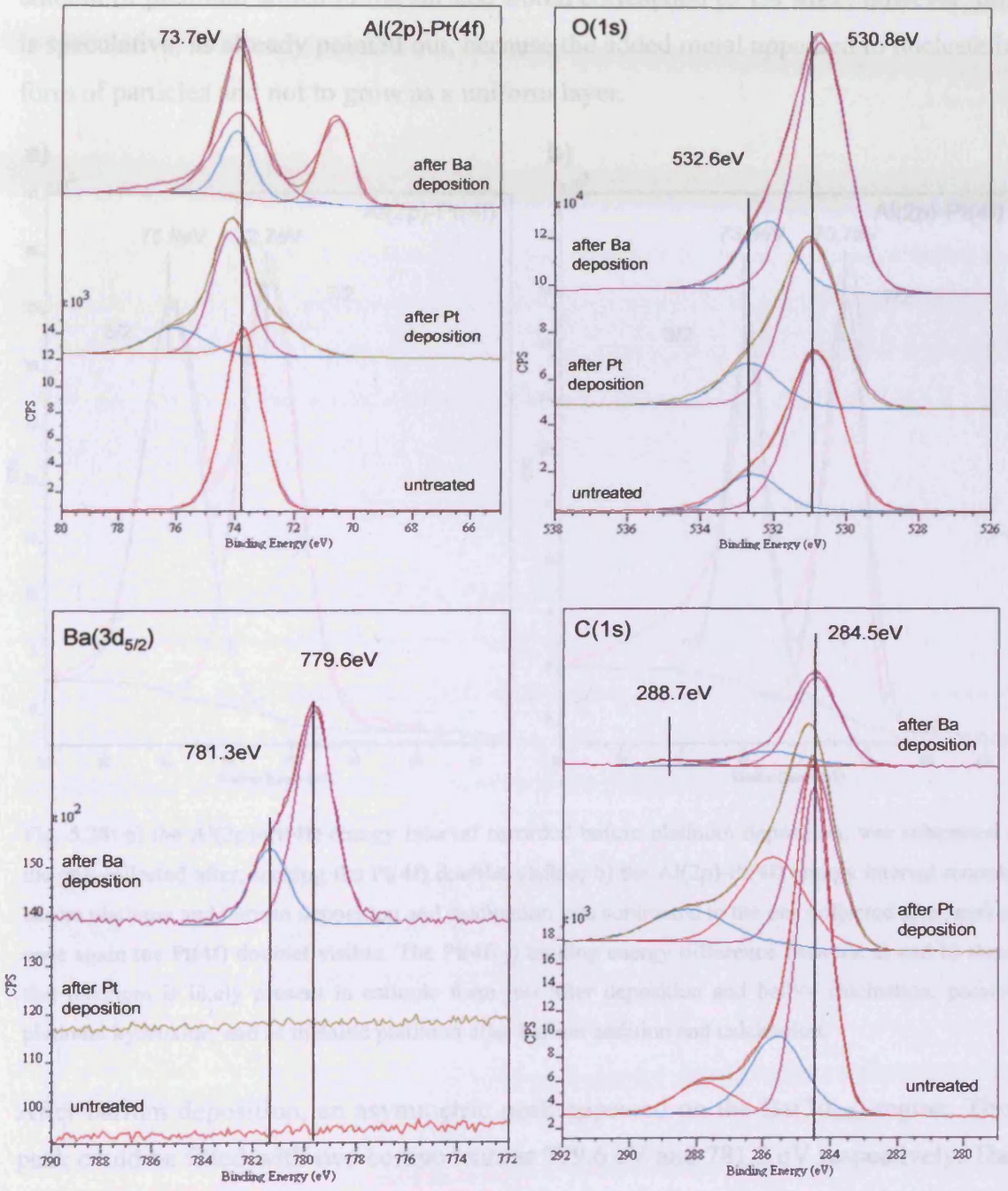

Fig. 5.27: XP spectra showing the evolution of the features in the Al(2p)-Pt(4f), O(1s), Ba($3d_{5/2}$) and C(1s) regions, during the preparation of the BaO*/Pt/α-Al_2O_3(0001) system. Spectra are offset for clarity and peak fittings are shown.

The binding energy value suggests that platinum was present in cationic form, maybe in form of platinum hydroxide, since the O(1s) shows a little increased asymmetry towards higher binding energy. From the attenuation of the Al(2p) XP peak, the amount of platinum added to the surface would correspond to 1.8 MLe; however, this is speculative, as already pointed out, because the added metal appeared to nucleate in form of particles and not to grow as a uniform layer.

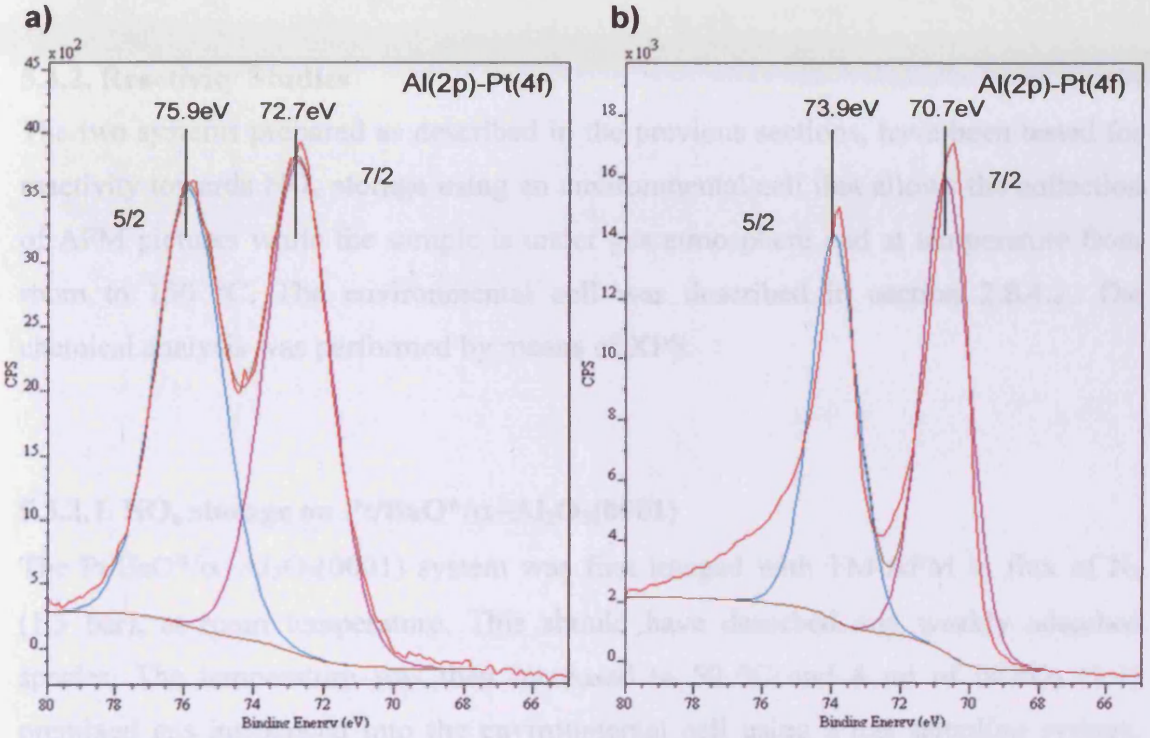

Fig. 5.28: a) the Al(2p)-Pt(4f) energy interval recorded before platinum deposition, was subtracted to the one collected after, making the Pt(4f) doublet visible; b) the Al(2p)-Pt(4f) energy interval recorded before platinum and barium deposition and calcination was subtracted to the one collected after, making once again the Pt(4f) doublet visible. The $Pt(4f_{7/2})$ binding energy difference between a) and b) shows that platinum is likely present in cationic form just after deposition and before calcination, possibly platinum hydroxide, and as metallic platinum after barium addition and calcination.

After barium deposition, an asymmetric peak appeared on the $Ba(3d_{5/2})$ region. This peak could be fitted with two components at 779.6 eV and 781.3 eV respectively. The peak at 779.6 eV is in agreement with the presence of BaO, whereas the shoulder fitted with a maximum at 781.3 eV, along with the presence of a C(1s) component at 288.8 eV might suggest the presence of a certain amount of barium carbonate. The Al(2p) region showed a different profile. A second peak appeared to the lower binding energy side of the Al(2p). Subtracting the Al(2p) peak, a doublet could again

be revealed, as shown in figure 5.21 b. This time the energy positions were 70.7 eV and 73.9 eV, ΔJ 3.2 eV and the area ratio ~1.23. If we assume that the component at 70.7 eV corresponds to Pt($4f_{7/2}$), then platinum has now to be regarded as metallic. From the attenuation of the Al(2p) peak, a BaO coverage of 0.6 MLe could be estimated.

5.3.2. Reactivity Studies

The two systems prepared as described in the previous sections, have been tested for reactivity towards NO_x storage using an environmental cell that allows the collection of AFM pictures while the sample is under gas atmosphere and at temperature from room to 150 °C. The environmental cell was described in section 2.8.4.2. The chemical analysis was performed by means of XPS.

5.3.2.1. NO_x storage on Pt/BaO*/α–Al_2O_3(0001)

The Pt/BaO*/α–Al_2O_3(0001) system was first imaged with TM-AFM in flux of N_2 (1.5 bar), at room temperature. This should have desorbed any weakly adsorbed species. The temperature was then increased to 50 °C and 4 ml of NO/O_2 (1:1) premixed gas introduced into the environmental cell using a gas sampling syringe. The topography initially showed the same features as in figures 5.18 and 5.20 and appeared unchanged while scanning in these conditions. The temperature was then increased to 100 °C and another 6ml of the same gas mixture were introduced. Although the topography appeared unchanged once again, XPS showed a change in the barium character with the appearance of a shoulder towards higher binding energy (781.4 eV) and the appearance of a double peak on the N(1s) region with maxima at 400.0 eV and 407.2 eV respectively (figure 5.29). The peak at 407.2 eV may suggest nitrate groups were produced during exposure of the system to NO/O_2. A N(1s) peak at around 400 eV is usually attributed to nitrogen in an organic matrix, however, these kind of species are difficult to form in the present conditions, because no organic compound were used. Another possibility could be due to CN^- group-like structures. Ozensoy and co-workers [25], investigating the adsorption of NO_2 on θ-Al_2O_3 thin films prepared on NiAl(110), proposed the formation of a nitrosonium-nitrate ionic

pairs ($NO^+NO_3^-$) where the N(1s) feature originating from the nitrosonium ion (NO^+) should have a binding energy in the 398-402eV range. No changes were observed in the O(1s), Al(2p)-Pt(4f) and C(1s) regions.

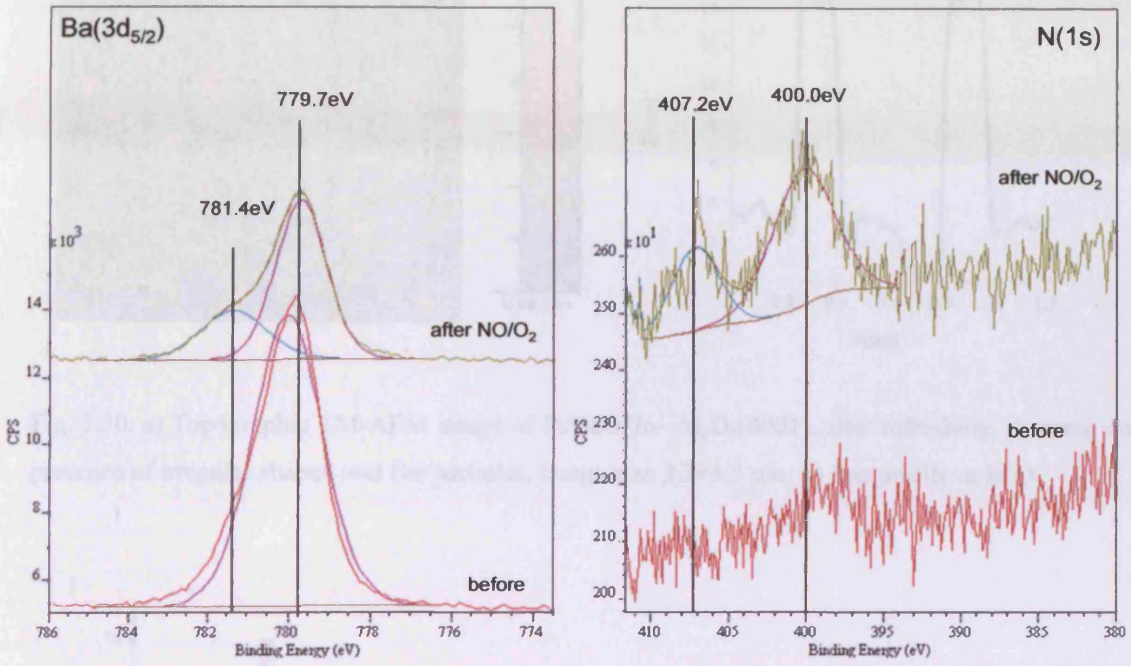

Fig. 5.29: XP spectra showing the Ba($3d_{5/2}$) and N(1s) regions of Pt/BaO*/α–Al_2O_3(0001) before and after NO/O_2 exposure (peaks fittings are also shown). Spectra are offset for clarity.

The sample was refreshed by annealing it for 3 hours at 500 °C; in this way the nitrate groups, and other contaminants such as hydroxides, should have been removed. XP spectroscopy showed that the system indeed reversed to the same chemical state as before the reaction, since the N(1s) peaks disappeared and the Ba($3d_{5/2}$) presented a single peak. TM-AFM images showed that the topography had changed: some flat and irregular islands were now present and covered ~18.5% of the surface (figure 5.30). Some pseudo triangular particles were also present, as showed by the circled area. On a 10.89 μm^2 surface, 91 particles are present, giving a density of approximately 8 particles/μm^2, with a first neighbouring distance of 217 nm. The particles cover 13.7% of the surface and occupy a volume of ~ 1.2×10^7 μm^3. The perimeter distribution is shown in figure 5.31. Although a Gaussian fitting would give

an average perimeter of 330 nm, few particles with perimeters greater than 1 μm are present.

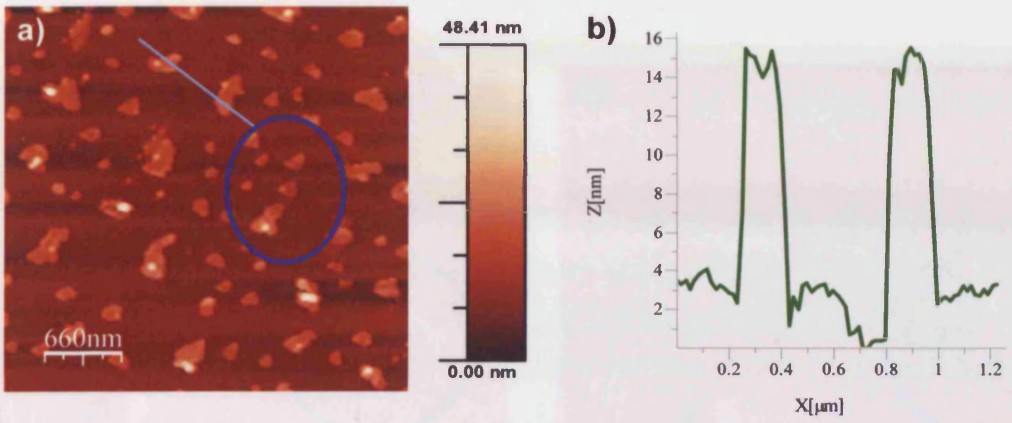

Fig. 5.30: a) Topographic TM-AFM image of Pt/BaO*/α–Al_2O_3(0001), after refreshing, showing the presence of irregular shaped and flat particles, image size 3.3×3.3 μm; b) line profile as in a).

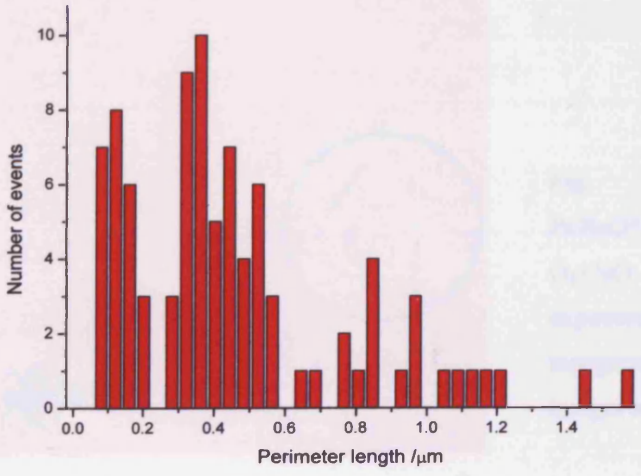

Fig. 5.31: PSD of particles in figure 5.30 a). The average perimeter length is 330 nm.

The reactivity of this refreshed sample was tested. The sample was initially scanned in flux of N_2 (1.5 bar) at room temperature. Then, using two different gas sampling syringes, 1 ml of O_2 and 1 ml of NO were added while scanning; the topography did not appear to change. The temperature was increased to 50 °C and 2 ml of O_2 and 2 ml of NO added. At this stage some feature appeared during scanning. Figure 5.32 shows a sequence of three pictures; the first was taken before increasing the temperature, the second just after the insertion of the 2 ml of NO and the third

approximately 30 minutes after O_2 and NO were added to the system. A new feature appears on the top of the particle in the blue circle in figure 5.32. Because of its shape, pseudo triangular in the top part, this particle is likely BaO.

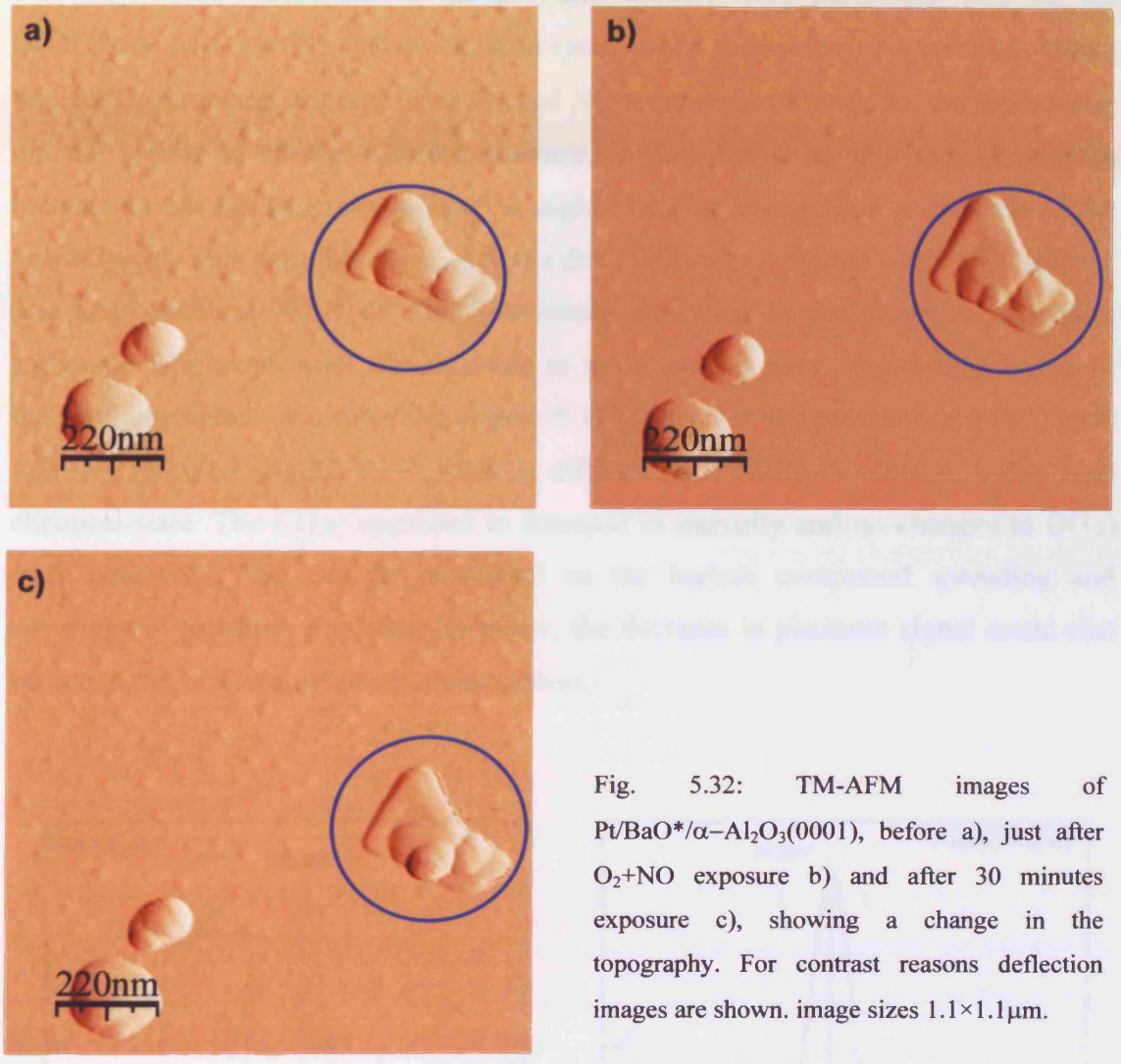

Fig. 5.32: TM-AFM images of Pt/BaO*/α–Al_2O_3(0001), before a), just after O_2+NO exposure b) and after 30 minutes exposure c), showing a change in the topography. For contrast reasons deflection images are shown. image sizes 1.1×1.1μm.

Although this could be because of the production of barium nitrate, another and maybe more realistic possibility, which has to be taken into account, is the accumulation on the top of the particle of loose debris physically moved by the tip while scanning. XP spectroscopy revealed once again the appearance of a component to the higher binding energy side of the Ba($3d_{5/2}$) peak and the presence of a double peak with maxima at around 407 eV, typical of nitrate groups, and 400 eV in the

N(1s) region. The N(1s) feature at 400eV is once again tentatively attributed to NO^+-like structures.

5.3.2.2. NO_x storage on BaO*/Pt/α–Al_2O_3(0001)

The experiments described in the previous section were performed also on the BaO*/Pt/α–Al_2O_3(0001) system. In both cases, when the system was scanned adding the NO/O_2 premixed gas and when O_2 and NO were separately added, the topography did not appear to change. On the contrary, in both the cases the XPS showed an increase in the Ba($3d_{5/2}$) component at higher binding energy and a decrease of the one at lower. This can, therefore, indicate that BaO was converted to another species. The component at 781.4 eV was previously attributed to the presence of barium carbonate. Moreover, after the exposure to the premixed gases, the disappearance of the platinum signals was recorded (figure 5.33). However, the presence of a N(1) peak was not observed (figure 5.34), making difficult to attribute the change in the BaO chemical state. The C(1s) appeared to increase in intensity and no changes to O(1s) were observed. This can be explained as the barium compound spreading and covering the platinum particles. However, the decrease in platinum signal could also be due to the increase in adventitious carbon.

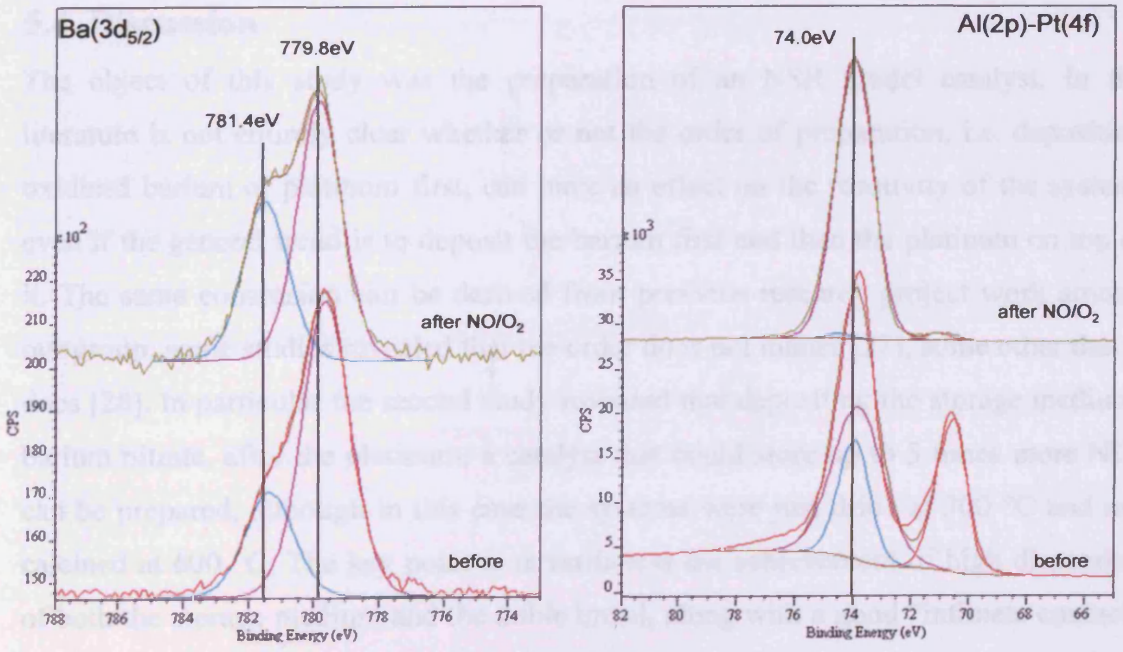

Fig. 5.33: XP spectra showing the Ba($3d_{5/2}$) and Al(2p)-Pt(4f) regions of BaO*/Pt/α–Al_2O_3(0001) before and after NO/O_2 exposure. Two Ba states are present. Peaks fittings are also shown. Spectra are offset for clarity.

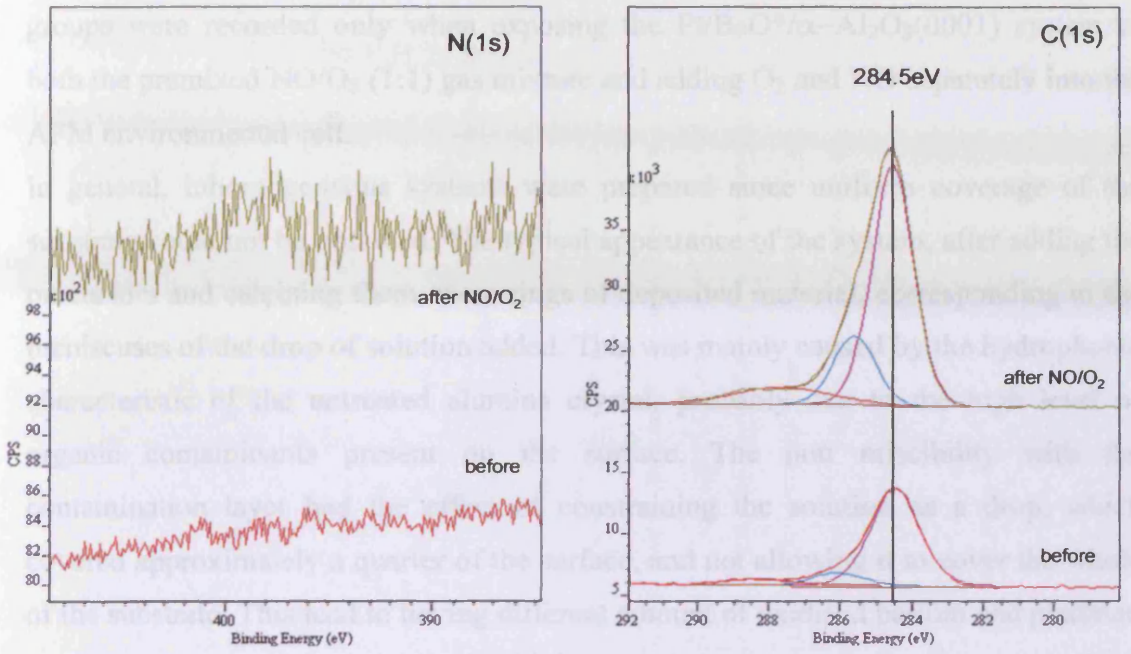

Fig. 5.34: XP spectra showing the N(1s) and C(1s) regions of BaO*/Pt/α–Al_2O_3(0001) before and after NO/O_2 exposure. Peaks fittings are also shown. Spectra are offset for clarity.

5.4. Discussion

The object of this study was the preparation of an NSR model catalyst. In the literature is not entirely clear whether or not the order of preparation, i.e. depositing oxidised barium or platinum first, can have an effect on the reactivity of the system, even if the general trend is to deposit the barium first and then the platinum on top of it. The same conclusion can be derived from previous research project work among our group: some studies revealed that the order does not matter [27], some other that it does [28]. In particular the second study revealed that depositing the storage medium, barium nitrate, after the platinum, a catalyst that could store up to 5 times more NO_x can be prepared, although in this case the systems were just dried at 300 °C and not calcined at 600 °C. The key point is nevertheless the achievement of high dispersion of both the storage medium and the noble metal, along with a good "intimate contact" between them, as already pointed out in section 4.2. Also in the present case, it was

found that the preparation sequence influenced the reactivity, and the more active system was the one in which the barium precursor was added as first. In fact, nitrate groups were recorded only when exposing the Pt/BaO*/α–Al_2O_3(0001) system to both the premixed NO/O_2 (1:1) gas mixture and adding O_2 and NO separately into the AFM environmental cell.

In general, inhomogeneous systems were prepared since uniform coverage of the substrate could not be obtained. The typical appearance of the system, after adding the precursors and calcining them, were rings of deposited material, corresponding to the meniscuses of the drop of solution added. This was mainly caused by the hydrophobic characteristic of the untreated alumina crystal, probably due to the high level of organic contaminants present on the surface. The non miscibility with the contamination layer had the effect of constraining the solution as a drop, which covered approximately a quarter of the surface, and not allowing it to cover the whole of the substrate. This lead to having different amount of oxidised barium and platinum on different areas of the crystals: the higher concentration on the meniscuses, nothing outside the meniscuses and a well dispersed array of particles inside the meniscuses. Because of this, particular care had to be taken when positioning the samples into the XPS in order to minimise the differences on the amount of material due to the preparation Nevertheless some differences in concentration were observed and where attribute to a not exact sample positioning more than to real differences due to change in morphology (as an effect of sintering) or reactivity. Since the coverage was not uniform and the deposited materials were nucleating as particles rather than growing as uniform layers, the coverage values given before have to be considered as a rough estimation only. Another source of error is the estimation of the area of the crystal (a quarter of the total area) covered by a drop of solution.

Particle Size Distribution (PSD) analysis, were systematically performed. The results obtained, in correlation with the different preparation steps and the coverages obtained, are summarised in table 5.2. As previously pointed out, the coverage evaluated via XPS is only speculative for a series of reasons, first of all because a substrate considered cleaned as received form the manufacturer was used to prepare to model systems.

Nr	System prepared	Description	Coverage XPS /ML	Coverage AFM /%	Particle density /particles m^{-2}	Average perimeter /nm	FND /nm	Volume /nm^3	Figure ref
1	BaO^*/Al_2O_3	Ba precursor first adding	2.8	23.3	1.5×10^{14}	93±1	55.3	2.5×10^{5}	5.9
2	BaO^*/Al_2O_3	Ba precursor second adding	4.2	37.8	2.6×10^{14}	70±1	42.7	9.4×10^{5}	5.12
3	BaO^*/Al_2O_3	As above, PSD on different area	4.2	28.4	6.5×10^{14}	58.5±0.7	28.4	2.3×10^{5}	5.14
4	$Pt/BaO^*/Al_2O_3$	Pt precursor adding	0.5 (4.7)	14.7	2.1×10^{13}	263±4	145	8.7×10^{5}	5.18
5	$Pt/BaO^*/Al_2O_3$	As above, PSD on different area	0.5 (4.7)	26.7	3.6×10^{13}	216±5	118	3.3×10^{6}	5.20
6	Pt/Al_2O_3	Pt precursor adding	1.8	15.3	1.8×10^{14}	58.4±0.6	48.6	1.2×10^{6}	5.22 b
7	$BaO^*/Pt/Al_2O_3$	Ba precursor adding	0.6 (2.4)	16.3	2.2×10^{13}	120±1	100.5	2.4×10^{6}	5.24 a

Table 5.2: Summary of PSD analysis done during systems preparation. BaO* indicates that the oxidised barium compound is a mixture of BaO, $BaCO_3$ and probably $BaHCO_3$, as described in the text. The coverage, after Ba precursor addition and evaluated via XPS, is based on the assumption that 1 ML of BaO (supposed pure) was taken as 0.552 nm, unit cell of cubic BaO; after Pt precursor addition, it is based on a 1ML thickness of 0.28nm, unit cell of Pt(111). The coverage is however relative to the untreated Al(2p) signal, which is less intense than the clean Al(2p) signal, because of the presence of carbon containing species contamination. AFM coverage was determined evaluated the portion of surface covered by the overlayer (particles). The value in bracket is the total coverage. The average perimeter was preferred to the diameter because the particles were not always circular. FND stands for First Neighbouring Distance.

In this case, a certain amount of carbonaceous contamination was always present, making impossible to obtain a reference value for the Al(2p) according to the attenuation of which the coverage was evaluated. The presence of carbon is likely one of the causes of the inhomogeneous dispersion of the particles obtained. The AFM coverage determination was made evaluating the portion of surface covered by the particles prepared. In figure 5.9, particles attributed to BaO and the bare alumina substrate could be imaged on the same time, thus the coverage should be less than 1ML. However, the coverage obtained via XPS was 2.8 ML. A particles density of 10^{13} – 10^{14} particles/m^2 was generally recorded. Nevertheless, it appears to be different analysing different area of the same preparation; as an example PSD 2 and 3 differ for more than one order of magnitude, but 4 and 5 give approximately the same value. This is correlated once again with the inhomogeneous character of the samples. The particles average perimeter, preferred to the average particle diameter because of the irregular shape of the particles, appeared to increase when both the components are present. This could be due to the sintering effect caused by calcining the crystal after the precursors solutions were added. This is in a way confirmed by the FND: the more calcined the sample, the longer inter distance between the particles. The volume occupied by the particles is in the 10^5 -10^6 nm^3 range and appeared to be as variable as the other parameters recorded.

The C(1s) peak presented always the same profile that did not appear to change during the preparation and the evaluation of the reactivity. It could be fitted with three peaks. Two of them could be easily assigned to graphitic carbon (284.5 eV) and carbonate species (~288.4 eV); the third one, with a binding energy of ~286.0 eV could describe a carbon which has oxygen and hydrogen in its chemical environment, such as a bicarbonate group. These species were therefore present on the untreated crystals as contamination derived mainly from exposure to air. Since this peak shape was always recorded, they represented the vast majority of the carbon species during all the experimental sessions. For this reason, the presence of barium carbonate or bicarbonate could be postulated, because of the high reactivity of the alkaline metal. Nevertheless, the triangular features observed after depositing the barium precursor and showed in figure 5.12 and figure 5.24 can tentatively be attributed to BaO as a comparison with images present in the literature (figure 5.3 b) [10]) and other experiments we performed in UHV. In that case we observed via STM similar triangular structures prepared by co-dosing of barium and oxygen on a Cu(111)

crystal. Other than the triangular shape, the not flat top surface of the particles, shown by the line profiles in figures 5.12 c) and 5.24 c), agrees with the hypothesis that barium oxide forms in form of clusters from the decomposition of a highly crystalline barium nitrate precursor, keeping the overall shape of its precursor. As for the metallic platinum particles, they have already been observed to assume hexagonal shape when platinum is deposited on α–Al_2O_3 and treated in oxidising atmosphere at 800 °C [7].
The reactivity studies were only a preliminary attempt to induce reaction on the systems prepared. Only when exposing the Pt/BaO*/Al_2O_3(0001) system to either premixed NO/O_2 or when NO and O_2 were separately added, XPS showed evidence of the formation of nitrate groups, but no AFM evidence was observed.

5.5. Conclusions and future work

This work was the first attempt to prepare a model of NSR catalyst, *ex vacuo*, via wet chemistry methods using an untreated alumina single crystal as substrate. Two different systems Pt/BaO*/α–Al_2O_3(0001) and BaO*/Pt/α–Al_2O_3(0001) were synthesised and tested for reactivity.
The preparation did not result in an evenly covered substrate, mainly because of the intrinsic or induced weak alumina hydrophilic behaviour. A way to obtain a more homogeneous ad-layer could be represented by the use of surfactants that should lower the surface tension of the solution used and allow obtaining uniform coverage. The surfactants, organic compounds such as soaps, could then be removed during the calcination process, leaving only the desired species on the surface. The side effect could be an increase in the presence of carbonaceous contamination deriving from the non complete surfactant removal. Another way could be pre-wash the bare alumina with methanol to remove contamination such as residual organic compounds and treat it with a strong base such as NaOH, in the attempt to anchor some -OH groups to the surface. Sodium contamination can be removed washing with deionised water, although this could also remove the hydroxide groups just added to the surface. The activation of the alumina surface in order to obtain a more homogeneous ad-layer is one of the aspects investigated at present in our group.

Of the two system prepared, the Pt/BaO*/α–Al_2O_3(0001) system appeared to be more active towards NO_x storage, since a N(1s) peak at the typical binding energy for nitrate groups, ~407 eV, was recorded after exposing this system to both premixed NO/O_2 and $NO + O_2$ mixed in situ atmospheres. Although this is in contrast with what previously concluded [27], it also means that the topic is still far away form being totally understood.

5.6. References

1. T. Tsirilin, J. Zhu, J. Grunes, G.A. Somorjai, *Topics Catal*, 19 (2), 2002, 165
2. Y. sakamoto, K. Okumura, Y. Kizaki, S. Matsunaga, N. Takahashi, H. Shinjoh, *J. Cat*, 238, 2006, 361.
3. J. Godin and J. P. Lafemina, *Phys. Rev. B*, 49, 1994, 7691.
4. Th. Bertrams, F. Winkelmann, Th. Uttich, H.-J. Freund, H. Neddermeyer, *Surf Sc.i*, 331-333, 1995, 1515
5. S.D. Sartale, H.W. Shiu, M.H. Ten, J.Y. Huang, M.F. Luo, *Surf. Sci.* 600, 2006, 4978
6. C. Sella, M. Mâaza, B. Pardo, F. Dunsteter, J.C. Martin, M.C. Sainte Catherine, A. Kaba, *Surf. Coat. Techn.*, 97, 1997, 603
7. K. Okumura, S. Hyodo, S. Noda, *J. Phys. Chem. B*, 105, 2001, 8345
8. K. Okumura, S. Hyodo, S. Noda, Y. Maruyama, *J. Phys. Chem. B*, 102, 1998, 2350
9. J. Szanyi, J.H. Kwak, J. Hanson, C. Wang, T. Szailer, C.H.F. Peden, *J. Phys. Chem. B*, 109, 2005, 7339
10. C.M. Wang, J.H. Kwak, D.H. Kim, J. Szanyi, R. Sharma, S. Thevuthasan, C.H.F. Peden, *J. Phys. Chem. B*, 110, 2006, 11878
11. Z.L. Wang, *Adv. Mater.*, 10, 1998, 13
12. P. Grütter, W. Zimmermann-Edling, D. Brodbeck, *Appl. Phys. Lett.*, 60, 1992, 2741
13. P. Markiewicz, M. C. Goh, *Langmuir*, 10, 1994, 5
14. Casa XPS software: free demo version at www.casaxps.com
15. WSxM software: free software downloadable at http://www.nanotec.es

16. M. Broughton, *The Fabrication of Gold Nanoparticles*, MChem Project Report, Cardiff University, 2007
17. D. James, E. Fourré, M. Ishii, M. Bowker, *App. Cat. B: Environmental*, 45 (2), 2003, 147
18. A. Tsami, F. Grillo, M. Bowker, R.M. Nix, *Surf. Sci.*, 600, 2006, 3403
19. www.lasurface.com, web-based XPS database.
20. X-ray Photoelectron Spectroscopy Database 20, Version 3.0, National Institute of Standards and Technology, Gaithersburg, MD, srdata.nist.gov/xps/
21. J.F. Moulder, W.F. Stickle, P.E. Sobol, K.D. Bomben in: J. Chastain (Ed.), *Handbook of X-ray Photoelectron Spectroscopy*, Physical Electronics, Eden Prairie, MN, 1992.
22. P. Morrall, M. Cristofolini, M. Bowker, unpublished data
23. K. Tanaka, K. Miyahara, and I. Toyoshima, *J. Phys. Chem.*, 88, 1984, 3504
24. See Appendix A; IMFP calculated using the TPP-2M model in: S. Tanuma, C.J. Powell, D.R. Penn, *Surf. Interf. Anal.*, 21, 1994, 165
25. Chemistry database in www.webelements.com
26. E. Ozensoy, C.H.F. Peden, J. Szanyi, *J. Phys. Chem. B*, 109, 2005, 15977
27. K. Hudson, *NOx Storage-Reduction Catalysis*, MChem Project Report, University of Reading, 2003
28. E. McCormack, *NOx Storage-Reduction Catalysis*, MChem Project Report, Cardiff University, 2005

Chapter 6

Conclusions

This research work focussed on the preparation of model systems related to automotive exhaust catalysis. The aim was to prepare these model systems, characterize their structure and quantify their reactivity. This was done mainly via a traditional surface science approach, using UHV conditions. Preliminary work regarding oxygen exposures was undertaken on a $CeO_2(111)$ single crystal. The Metal Vapour Deposition (MVD) technique was used to prepare the $CeO_{2-x}/Cu(111)$, $BaO_x/Pt(111)$ and $BaO_x/Cu(111)$ systems. Those systems were characterised and tested for reactivity via XPS, LEED and STM. This thesis also includes the first attempt among our group to obtain information about a model catalyst from a non-traditional surface science point of view, i.e. using non UHV techniques. NSR model catalyst, $Pt/BaO^*/Al_2O_3(0001)$ and $BaO^*/Pt/Al_2O_3(0001)$, were prepared by wet chemistry methods, their topography was studied via atmospheric pressure AFM and their chemical composition via XPS.

In Chapter 1 the relevance of surface science studies and the cross links with heterogeneous catalysis were highlighted. Metals and metal oxides are widely used in catalytic reactions either as catalysts, in a massive, polycrystalline form, or in a finely divided form, as for supported metal catalysts. However, they can be regarded as a collection of small single crystal, at the microscopic level. Understanding the surface properties of any single crystal particle can integrate the information acquired via heterogeneous catalysis method, helping to understand catalytic processes at atomic scale and in particular at surfaces. The knowledge of a process at atomic scale can help to improve catalyst design and performances. This is where surface science becomes essential, providing the right tool to gain information at atomic level. The advantage of using single crystals is the limited number of variables to be taken into account, since single crystals are one plane surfaces with a limited number of well

defined sites and a smaller surface area than powdered catalysts. Nevertheless, the transfer of knowledge from surface science to heterogeneous catalysis is complex because of the different condition in which heterogeneous catalysis and surface science work. Real catalytic processes are carried out at high temperatures and high pressures and with a mixture of crystallites, which can present a variety of morphological differences, as catalyst. Although the high temperature condition can be reproduced in a surface science equipment, the high pressure condition is not achievable because of the necessity of using UHV conditions in order to keep clean for a certain period of time, typically the time of one experiment, the surface of the crystal to be studied. At high pressure, reactions that would not occur in UHV conditions may take place, however they may not be noticed by the analytical methods used in UHV environment. Another limiting factor is the lost of homogeneity in the catalyst, due to the use of a single crystal instead of a mixture of crystallites; this could be partially amended using polycrystalline metal films instead of single crystals. Although this will give a more realistic system, the number of variables to be taken into account will be considerably higher. In fact this will introduce a different kind of surface with peculiar surface structure, area and sites.

The fundamental aspects of the techniques used during the experimental work were illustrated in Chapter 2.

Chapter 3 was addressed to the study of oxygen adsorption on ceria based systems; the first part gave an overview of the topic highlighting the complexity of the photoelectron spectroscopy data interpretation and the intrinsic difficulties in creating conductivity in such insulating material (~6 eV band gap), condition necessary to be able to use techniques like STM. The second part was related to experiments undertaken using a ceria(111) single crystal, therefore having only cerium and oxygen as subject of investigation. The CeO_2(111) single crystal has revealed to be of very hard to work with, mainly because of the difficulty of obtaining a smooth and clean surface. The interaction between oxygen and the ceria crystal was mainly studied via XPS. Reference spectra for the mostly reduced and mostly oxidised ceria surface were obtained. The mostly reduced surface, obtained by annealing the crystal in vacuum

several times at high temperatures, showed a content of Ce(III) ~74.4% and O/Ce integral ratio 1.62. The mostly oxidised surface had a typical amount of Ce(IV) ~ 92% and O/Ce integral ratio ~1.96; it was obtained by mild annealing the crystal in oxygen pressure. A configuration rich in Ce(IV) was characterised by a O(1s) peak at around 529.4 - 529.8 eV while the peak was observed at 530.8 - 531.2 eV for a Ce(III) rich configuration. These two configurations, however, did not correspond to fully oxidised i.e. O/Ce = 2 and fully reduced O/Ce = 1.5 stoichiometries, therefore a complete transition between CeO_2 and Ce_2O_3 could not be induced. Nevertheless, by exposure of the crystal to oxidation / reaction condition, a certain extent of oxidation / reduction of the surface was achieved (figure 6.1).

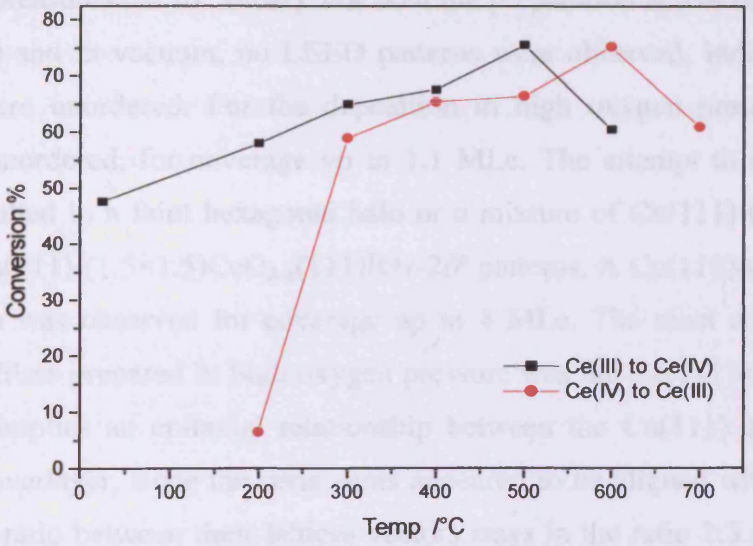

Fig. 6.1: Degree of oxidation of Ce(III) to Ce(IV) and degree of reduction of Ce(IV) to Ce(III) vs Temperature at which the experiments have been undertaken. Starting from a mostly reduced surface, oxidation was induced by annealing in oxygen (1×10^{-7} mbar, 30 minutes) at temperature T, then reduction was induced by annealing in vacuum for 30 minutes at temperature T + 100°.

Between 200 and 600 °C, the average increase of the O(1s) peak was evaluated in +25.5% and the average decrease as -23.8%. This could be explained as storage and de-storage of oxygen into the ceria crystal. However, if the increase of the O(1s) is sufficient to prove the storage process, a definitive proof of de-storage was not obtained since there was no possibility of performing TPD experiments which could have revealed possible desorption of oxygen from the crystal. Moreover, desorption of

oxygen from a ceria single crystal is reported not to happen below 1030 °C. The decrease in the amount of oxygen detected can be explained as migration of oxygen from the top layers of the crystal, into the bulk. In this latter case, the surface will result indeed reduced, therefore an increase of the amount of Ce(III) and a decrease of the oxygen recorded via XPS; however, this is not desorption of oxygen from the crystal, i.e. not de-storage.

The preparation and behaviour of thin ceria films deposited on Cu(111) were studied in the third part of the chapter. Depending upon the preparation conditions, the ceria layer resulted characterised by different oxidation states. Dosing cerium in vacuum, the main oxidation state for the cerium cations was 0, a larger amount of cerium 3+ was obtained dosing in low oxygen pressure (5×10^{-8} mbar) and mainly cerium 4+ at high oxygen pressures (5×10^{-7} mbar). For both the preparation at low oxygen pressure (5×10^{-8} mbar) and in vacuum, no LEED patterns were observed, indicating that the overlayers were unordered. For the deposition in high oxygen pressure the CeO_x layers were unordered, for coverage up to 1.1 MLe. The attempt to order the ceria overlayer resulted in a faint hexagonal halo or a mixture of Cu(111)-(1.5×1.5)CeO_{2-x}(111) and Cu(111)-(1.5×1.5)CeO_{2-x}(111)R+/-26° patterns. A Cu(111)-(1.5×1.5)CeO_{2-x}(111) pattern was observed for coverage up to 4 MLe. The most common pattern observed for films prepared in high oxygen pressure was the Cu(111)-(1.5×1.5)CeO_{2-x}(111). This implies an epitaxial relationship between the Cu(111) crystal and the CeO_{2-x}(111) overlayer, since the ceria spots appeared to be aligned with the Cu(111) spots and the ratio between their lattices vectors stays in the ratio 2:3 ratio. A model of this surface was proposed and it is shown in figure 6.2.

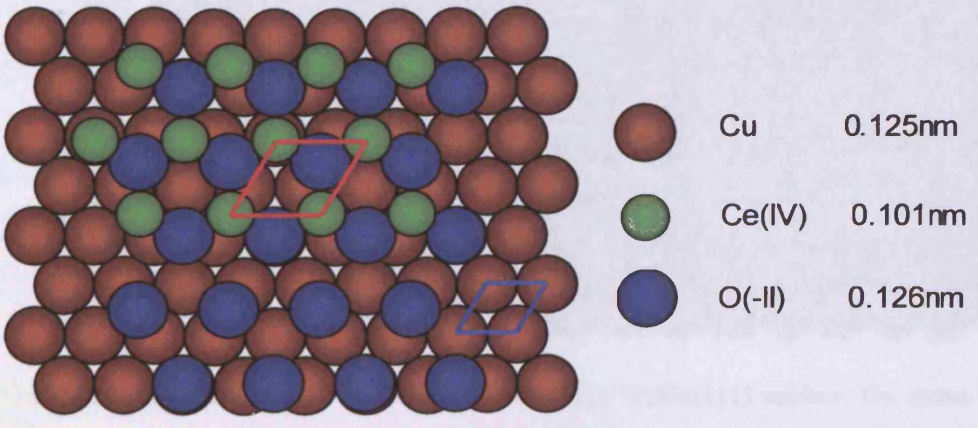

Fig. 6.2: A model of the aligned CeO_2(111)/Cu(111) surface. In blue the Cu(111) unit cell, in red the CeO_2(111) unit cell. One layer of oxygen atoms has been put between the copper and the cerium layers. 2/3 of oxygen atoms sit in 2-fold sites and the remaining 1/3 is directly on the top of a copper atom.

Figure 6.3 shows a model of the CeO_x domains rotated by +/-26° in respect of the Cu(111) main directions. In this case the spots related to the aligned (1.5×1.5) overlayer are sharper and better defined than the one belonging to the (1.5×1.5)R+/-26° structures, meaning that the domains with a rotated structure are probably less extended and less ordered than the aligned ones. In the film characterised by an aligned structures (high coverage), 2/3 (66%) of the oxygen layer between cerium and copper sits on 2-fold sites and the remaining 1/3 (33%) is directly on top of the copper atoms. At low coverage, when the +/-26° rotation is observed, the 15% of the oxygen atoms are on 3-fold sites, the 55% in 2-fold sites and the remaining 30% directly on top of a copper atom. The intrinsic stability of the sites goes as 3-fold > 2-fold > a-top. In terms of surface energy minimisation, the a-top atoms count for the same extent in both the structures, since their ratio is approximately the same in both cases. Because of the increase in 3-fold sites, the rotated lattice should be more stable than the aligned one. However, since at high coverage only the aligned lattice is observed, it appears to be the more stable structure.

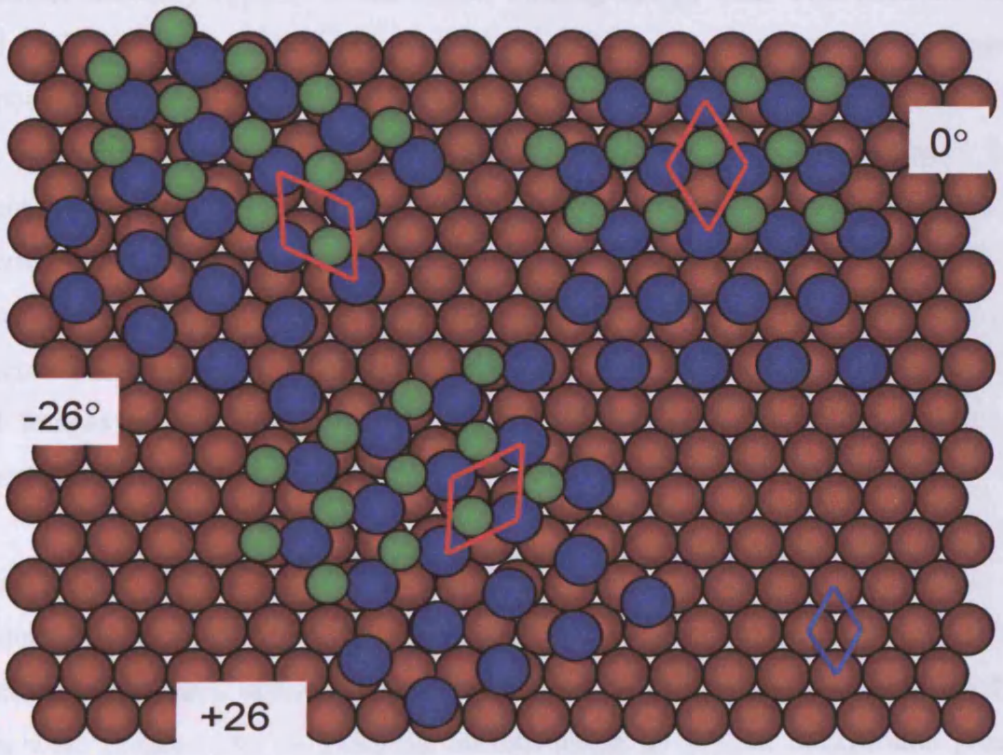

Fig. 6.3: A model of the +/- 26° rotated CeO_{2-x}(111)/Cu(111) surface. Cu atoms are brown, O atoms are blue, Ce atoms are green. In blue the Cu(111) unit cell, in red the CeO_2(111) unit cell. One layer of oxygen atoms has been put between the copper and the cerium layers. 15% of oxygen atoms sit in 3-fold sites, 55% in 2-fold sites and the remaining 30% is directly on the top of a copper atom.

Oxygen exposure experiments showed that below a film thickness of 2.6MLe, the films tend to exchange a larger amount of oxygen, often more than the theoretical 25% expected to convert CeO_2 to Ce_2O_3. Over 3.21MLe the films appear more difficult to oxidise/reduce, since the oxygen variation recorded is only few percent. This is in agreement with the TPD experiments reporting that oxygen does not desorb from CeO_2 below ~1030°C, being the thicker films a more bulk like configuration. The larger oxygen exchange occurs when a Cu(111)-(1.5×1.5)CeO_{2-x}(111) is present, and even more when the structure is Cu(111)-(1.5×1.5)CeO_{2-x}(111)R+/-26°. The higher oxygen mobility recorded at low coverage could depend upon the intrinsically lower stability of the rotated lattice. More grain boundaries between the crystal phases should be present in the rotated structure; these could represent more reactive, low coordination sites at which oxygen can be easier exchanged with the surroundings. Analogously on what observed during the single crystal investigations, the O(1s) XP peak occurs at ~529.6 – 529.7 eV for a film containing the majority of the cerium cations in 4+ oxidation state. When the amount of cerium 3+ cations became relevant, a shoulder normally appears to the higher binding energy side. This shoulder can be fitted with a maximum typically at 530.6 – 531.6 eV. However, in few cases a component at around 532 eV was observed. The interpretation of this peak is a hot topic on the ceria chemistry and different interpretations have been proposed. In the present case the attribution to hydroxides or carbonates could be ruled out. Nevertheless, since the presence of this peak is normally linked Ce 3+ cations and to a degradation in the LEED pattern, it appears adequate to identify it with a defective oxygen site localised on the very top layers, likely on the grain boundaries. Some STM images were collected. They showed that the ceria overlayer sinters upon thermal annealing.

Barium oxide studies related to NSR catalysis are presented in Chapter 4. An introduction to the topic is firstly given. The second part relates to the preparation and the structure of BaO_x layers gown on Pt(111). Carbonate free fully oxidised BaO_x layers were prepared by evaporating barium metal in oxygen background pressure (1×10^{-7} mbar), keeping the Pt(111) substrate at 300 °C, followed by an annealing treatment in oxygen (1×10^{-7} mbar) for 10 minutes at 500 °C. After preparation, XPS analysis showed the Ba($3d_{5/2}$) at 779.8 eV and the O(1s) peak at around 531.0 eV. Under annealing the barium peak stays usually constant in intensity and position,

although became narrower, whereas the O(1s) peak broadens. Two components can be reasonably fitted under its spectrum one with maximum at ~ 532.2 eV, attributed to the presence of barium peroxide species and one at lower binding energies, 530.2 eV, assigned to oxide species. The LEED pattern showed initially only faint hexagonal spots due to the platinum substrate, however a hexagonal 2x2 pattern appeared under annealing in vacuum at 500 °C when the XPS detected a layer comprised of ~80% BaO and the remaining BaO_2. Although very noisy, a 2×2 structure could be observed via STM. This configuration could correspond to either oxygen adsorbed on the platinum crystal, or to the oxidised barium layer as show in the model in figure 6.4.

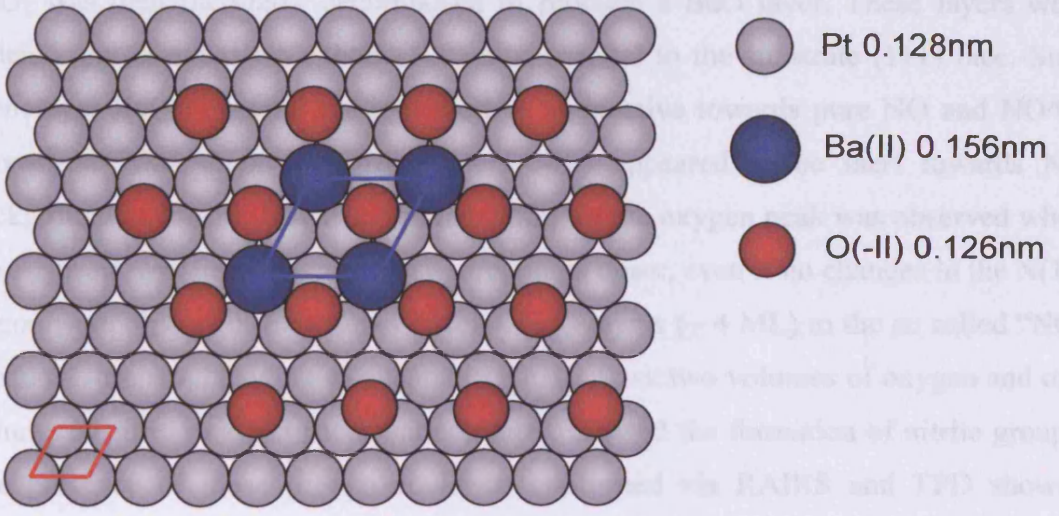

Fig. 6.4: Model proposed to describe the (2×2) overlayer on Pt(111) due to the presence of a mixed BaO/BaO_2 layer. In red the Pt(111) unit cell, in blue the unit cell due to the BaO_x overlayer.

Flash annealing up to 700 °C produced a $(2\sqrt{3}\times2\sqrt{3})R30°$ LEED pattern. Since the unit cell of Pt(111) is ~ 0.27 nm, the overlayer has a unit cell of ~ 0.93 nm. This value is higher than the one expected for a BaO(111) (2×2) reconstruction of 0.79 nm, but agrees with the one observed in the past by our group for an unordered barium overlayer on Pt(111) which started to order upon annealing.

Also when barium and oxygen (1×10^{-7} mbar) were co-dosed, keeping the platinum crystal at 200 °C, followed by annealing at 300 °C in vacuum for 30 minutes, the LEED pattern showed only the substrate diffraction spots, however, annealing at 400 °C in vacuum gave rise to a reconstruction formed by three (2×8) domains rotated 30°

with respect to each other but aligned with the substrate azimuthal directions. In this case the overlayer appeared to move under the influence of the STM tip. These data confirm previous STM investigations carried out within the group, when a number of different structures attributed to oxidised barium were observed. Exposure to NO and NO/O_2 did not show any effect, at least at the conditions in which the experiments were preformed.

The third part of Chapter 4 was related to the preparation and NO_x storage reactivity of BaO(100) layers prepared on a Cu(111) single crystal. The films were prepared dosing barium in vacuum and oxidising it to produce a mixture of BaO and BaO_2. BaO_2 was then thermally decomposed to produce a BaO layer. These layers were ordered and oriented with their (100) face parallel to the substrate (111) face. Sub-monolayer BaO films did not appeared to be reactive towards pure NO and NO/O_2 exposures. Also thick BaO films (~ 4 ML) appeared to be inert towards NO background exposure. However, a broadening of the oxygen peak was observed when the exposure was undertaken using a directional doser, even if no changes in the N(1s) region were observed. Exposures of thick BaO layers (~ 4 ML) to the so called "NO_x mixture" (prepared leaving to expand in a glass flask two volumes of oxygen and one volume of nitric oxide at room temperature), showed the formation of nitrite groups. The presence of these groups could be confirmed via RAIRS and TPD showed desorption of mass 30, likely due to NO^+ desorbing from the surface.

Chapter 5 was the first attempt among our group to prepare model catalysts via traditional wet chemistry methods. A brief description of similar experiments introduced the chapter. The second part was related to the preparation of the systems $Pt/BaO^*/\alpha-Al_2O_3(0001)$ and $BaO^*/Pt/\alpha-Al_2O_3(0001)$. The presence of metallic platinum was verified via XPS and confirmed via recording hexagonal particles with AFM (figure 6.5). XPS revealed that the storage medium, the barium compound prepared by decomposition of barium nitrate, resulted in a mixture of barium oxide, carbonate and probably hydroxide. The presence of barium oxide could however be confirmed because of the peculiar triangular shape of the particles recorded via AFM (figure 6.6). By comparison with the literature it appeared that this particles represent clusters of barium oxide that retained the shape of their barium nitrate parent particle.

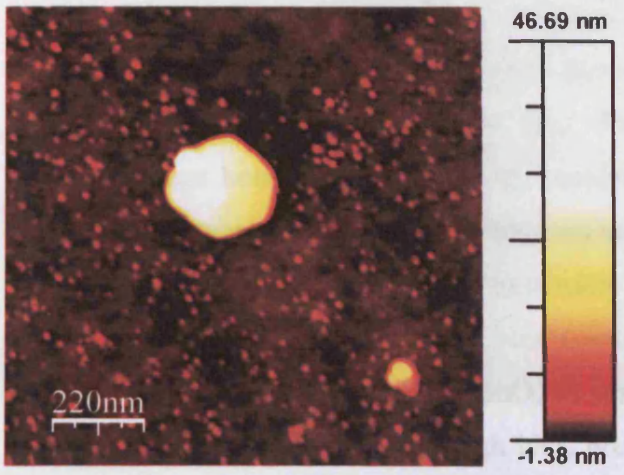

Fig. 6.5: Topographic TM-AFM image of Pt/α–Al_2O_3(0001) showing the presence of irregular shaped and hexagonal particles, image size 1×1μm.

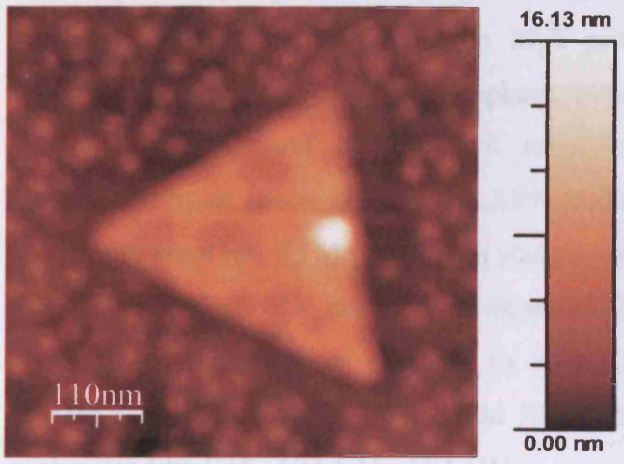

Fig. 6.6: Topographic TM-AFM image of BaO*/α–Al_2O_3(0001) showing the presence of irregular shaped and triangular particles, image size 527×527nm.

Since uniform coverage of the substrate could not be obtained while dropping the solution on it, inhomogeneous systems were prepared. The reactivity studies were an attempt to induce reaction on the systems prepared and image the process with in situ atmospheric pressure AFM. At present, although XPS showed evidence of the formation of nitrate groups when the systems were exposed to a mixed NO and O_2 flux of gas, no significant change in morphology was observed by AFM..

This research work leaves some open questions that can represent further routes of investigation.

A natural continuation of the ceria-based system study is to verify whether or not oxygen is destored or rather migrates into the bulk. This could be done performing oxygen experiments in a wider temperature interval, up to 1100 °C, and setting up a suitable TPD apparatus. A further development could be the preparation of NM/CeO_2 and NM/CeO_{2-x}(111)/Cu(111) systems, where NM stands for noble metal

nanoparticles in the 1 – 10 nm range. Suitable metals that could be added to the ceria in order to affect the gas-phase oxygen dissociation are the noble metals currently used in exhaust technology (Pt, Pd, Rh). This, in turn, would result in different oxygen storage behaviours. Ultimately, resolving the surface structure via STM and image the oxygen storage/destorage process would be the goal to be achieved. Since electron tunnelling appeared to be extremely difficult when using the ceria single crystal, in order to study this system, Non Contact AFM could be used.

In the literature NO_x storage on BaO_x/Pt supported systems is reported to occur mainly for bulk-like BaO and at high NO_x pressures. In order to reproduce this step, model systems comprised of few %BaO and of thick BaO layers on Pt(111) could be prepared in vacuum, transfer to a high pressure cell without exposing them to atmosphere, expose to a NO_x atmosphere, evacuate the gas, transfer them back to the analysis chamber and collect XPS measurements. A different option could be represented by *in situ* high-pressure XPS studies. The further step would be obtaining atomically resolved STM pictures in static conditions (after NO_x exposure). Providing the condition for UHV compatible experiments can be found, another step could be image the NO_x storage process in dynamic conditions. Finally, move to the destorage/reduction step. This could likely be induced using H_2 or small organic molecules like CH_4, CH_3CH_3, CH_3OH.

The preparation of NSR model catalysts via wet chemistry methods revealed to be very promising. However, the main issue encountered was the reparation of a homogeneous system comprised of BaO and Pt nanosized (1 -10 nm) particles. This is an ongoing research topic within the group and it is addressed in particular to the activation of the alumina substrate. This will allow to study a more suitable system. Ideally image the NO_x storage process in real time would be the goal to achieve. The use of high aspect ratio tips could help; however, this will improve mainly the vertical resolution. The use of the video rate AFM (allowing recording pictures at a rate of ~25 Hz), could open up the possibility of imaging fast reactions occurring on the surface. This however requires using very small alumina substrates (1.8×1.8×0.2 mm), therefore a fine preparation procedure is necessary, and the design of a state of the art instrumental setup.

Appendix A

IMFP calculation of selected cerium and barium compounds

A.1. Introduction

Surface sensitivity in XPS was described in section 2.4.5.1. The soft X-rays employed in XPS can penetrate several micrometers through the sample. Thus this method of excitation is not specific to the sample surface. When the excitation energy is bigger than the binding energy of the electrons, electrons are emitted from the sample (photoelectric effect). Because of inelastic collisions of the electrons inside the sample, only electrons generated within a certain depth will be able to be ejected form the sample. The surface sensitivity arises from the detection of these ejected electrons, the so called photoelectrons. The electrons emerging from this certain depth into the sample are described by three different properties defined as escape depth, attenuation length and inelastic mean free path.

The escape depth (for surface analysis techniques) is described as "The distance into the sample measured from the physical surface from which all but a fraction $1/e$ of the particles or radiation detected have originated" [1].

The electron attenuation length (AL) is defined as the thickness of material through which electrons may pass with a probability e^{-1} that they survive without inelastic scattering and depends on both the material and electron energy. An empirical and approximate formula to calculate AL (in nm) was derived by Seah and Dench in 1979 [2] for single elements:

$$AL = 538aE^{-2} + 0.41a^{3/2}E^{1/2} \qquad \ldots(A.1)$$

where E is the electron kinetic energy (eV). a^3 is the volume of one atom of the element in the solid state (nm^3), defined as:

$$a^3 = \frac{A}{\rho N_A} \times 10^{24} \qquad \ldots(A.2)$$

where A is the atomic weight, ρ the density of the bulk material expressed in kg m^{-3} and N_A Avogadro's number.

The attenuation length gives an estimation of the average net distance travelled by the photoelectrons, whereas the inelastic mean free path, IMFP, λ, is the average distance that the electrons travel between two inelastic scattering events. The AL is around 20% less than the IMFP due to the elastic scatterings which deflect the electron trajectories.

Penn developed a formalism that uses optical data to determine the IMFP of a material [3]. Fitting Penn's data with Bethe's equation for inelastic electron scattering in matter [4] (equation A.3, to be referred to as TPP-1), Tanuma and co-workers have calculated the IMFPs for a large number of elements and compounds for kinetic energies up to 2000eV [5, 6]:

$$\lambda = \frac{E}{E_P^2 \beta \ln(\gamma E)} \qquad \ldots(A.3)$$

where λ is the IMFP (Å), E is the electron kinetic energy (eV), $E_P = 28.8\ (N_V \rho / M)^{1/2}$ is the free-electron plasmon energy (eV), ρ is the bulk density (g cm^{-3}), N_V is the number of valence electrons per atom or molecule, M is the atomic or molecular weight and β and γ are parameters. To better fit further data for a wider range of materials, Tanuma and co-workers modified their TPP-1 model and derived TPP-2 [7–8], equation A.4 – A.9:

$$\lambda = \frac{E}{E_P^2 \left[\beta \ln(\gamma E) - \frac{C}{E} + \frac{D}{E^2} \right]} \qquad \ldots(A.4)$$

where the coefficients β, γ, C and D are defined as:

$$\beta = -0.1 + \frac{0.944}{\left(E_P^2 + E_G^2\right)^{1/2}} + 7.4\times10^{-4}\rho \qquad \ldots(A.5)$$

$$\gamma = 0.191\rho^{-0.5} \qquad \ldots(A.6)$$

$$C = 1.97 - 0.91U \qquad \ldots(A.7)$$

$$D = 53.4 - 20.8U \qquad \ldots(A.8)$$

$$\text{and } U = (N_V\rho/M) \qquad \ldots(A.9)$$

where E_P, N_V, ρ, M are defined as above and E_G is the band-gap energy (eV) for non conductive materials. Later they modified the β parameter (equation A.10) [9]. Equations A.4 and A6 –A.10 represent the TPP-2M model.

$$\beta = -0.1 + \frac{0.944}{\left(E_P^2 + E_G^2\right)^{1/2}} + 0.069\rho^{0.1} \qquad \ldots(A.10)$$

Based on this formula and on other previous models, Powell and Jablonsky published a database with several IMFPs already calculated and allowing to calculate IMFP values for unknown compounds [10]. Based on the TPP-2M formula only, a free software is also available for download from the net [11].

A.2. IMFP calculation for Ce and cerium oxides

The IMFP for cerium and cerium oxides was calculated using the NIST database 71 [10] using the parameters reported in table A.1:

Sample	M	ρ /g cm^{-3}	N_v	E_G /eV
Ce	140.11	6.77	9	--
CeO_2	172.11	7.10	21	3.4 [12]
Ce_2O_3	328.23	6.86	36	3.0 [12]

Table A.1: Parameters used to calculate IMFP values for cerium and cerium oxides.

Figure A.1 shows IMFPs vs kinetic energy values for cerium and cerium oxides. The values calculated using the QUASES software [11] are within 1% of error. This is probably due to a different level of precision when writing the computing code.

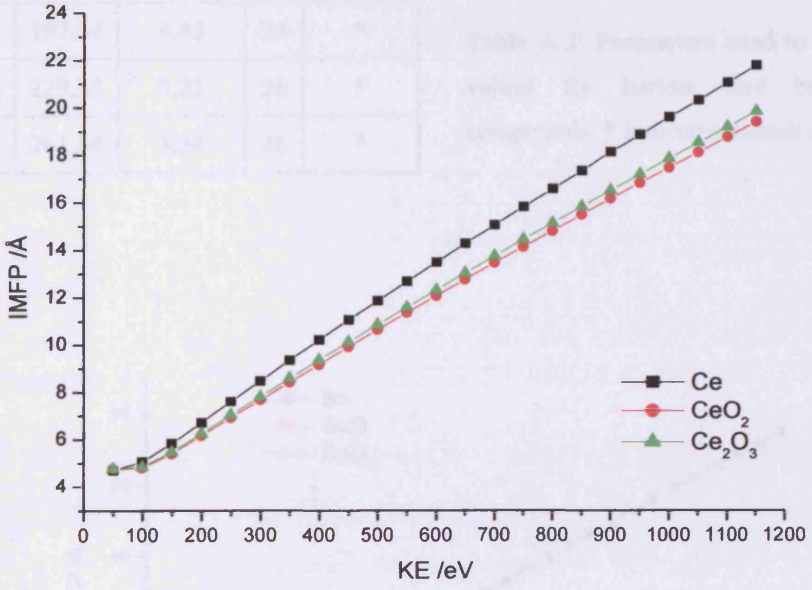

Fig. A.1: IMFP vs KE for cerium and selected cerium oxides.

A.3. IMFP calculation for Ba and selected barium compounds

In a similar way as for cerium and cerium compounds, barium and barium selected compounds IMFPs values were calculated using the QUASES software [11]. This second option was chosen because less time consuming. Unfortunately, for barium compounds several bandgap values were not found. However, for the correct

application of the TPP-2M model, if a value for the bandgap energy cannot be found, it is satisfactory to estimate this parameter because the IMFP is not a sensitive function of E_G [10]; in this case default values already present in the database were used. The parameters used are collected in table A.2. IMFP values for barium and barium oxide and peroxide are shown in figure A.2; IMFP for the other barium compounds are shown in figure A.3.

Sample	M	ρ /g cm^{-3}	N_v	E_G /eV
Ba	137.34	3.50	2	3.9
BaO	153.33	5.70	8	4.6 [13]
BaO_2	169.33	4.96	14	4.4 [13]
$Ba(OH)_2$	171.35	4.50	16	*
$BaCO_3$	197.34	4.43	24	*
$Ba(NO_2)_2$	229.35	3.23	36	*
$Ba(NO_3)_2$	261.34	3.24	48	*

Table A.2: Parameters used to calculate IMFP values for barium and barium selected compounds. * indicates default database value.

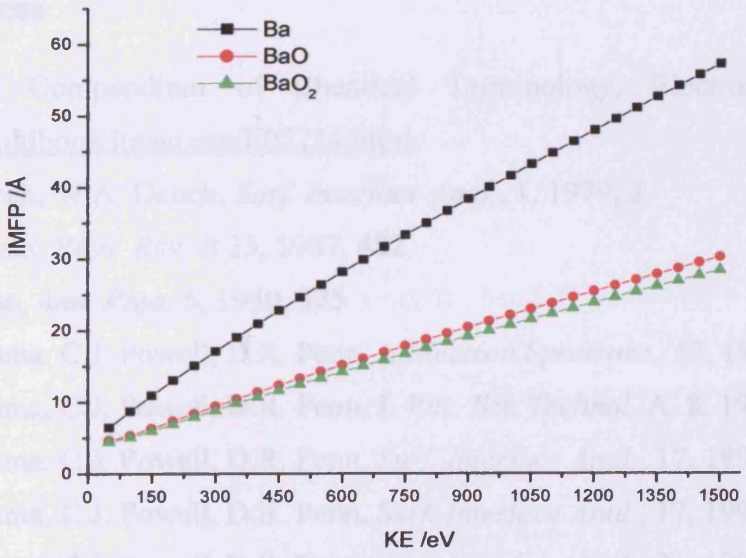

Fig. A.2: IMFP vs KE graph for barium, barium oxide and barium peroxide.

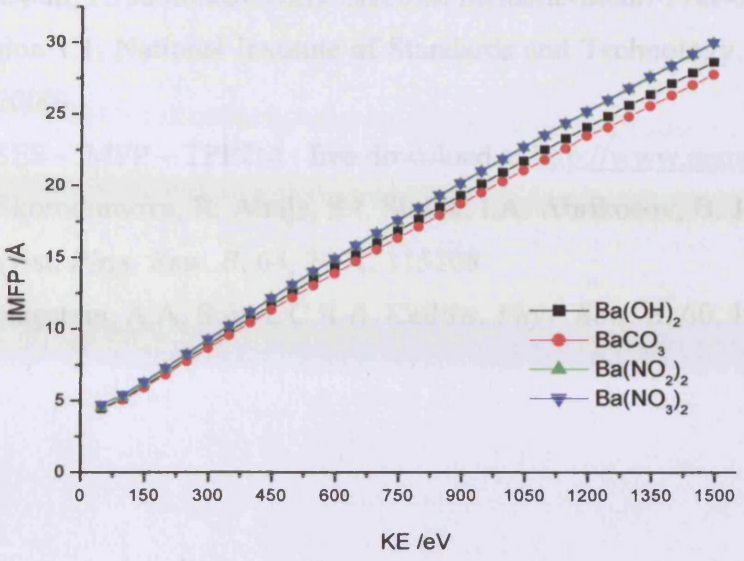

Fig. A.3: IMFP vs KE graph for other selected barium compounds. The curves for barium nitrite and nitrate are super imposable.

A.4. References

1. IUPAC Compendium of Chemical Terminology, Electronic version, http://goldbook.iupac.org/E02214.html.
2. M.P. Seah, W.A. Dench, *Surf. Interface Anal.*, 1, 1979, 2.
3. D.R. Penn, *Phys. Rev. B* 35, 1987, 482
4. H. Bethe, *Ann. Phys.* 5, 1930, 325
5. S. Tanuma, C.J. Powell, D.R. Penn, J. *Electron Spectrosc.,* 52, 1990, 285
6. S. Tanuma, C.J. Powell, D.R. Penn, J. *Vac. Sci. Technol.* A, 8, 1990, 2213
7. S. Tanuma, C.J. Powell, D.R. Penn, *Surf. Interface Anal.*, 17, 1991, 911
8. S. Tanuma, C.J. Powell, D.R. Penn, *Surf. Interface Anal.*, 17, 1991, 927
9. S. Tanuma, C.J. Powell, D.R. Penn, *Surf. Interface Anal.*, 21, 1991, 165

10. C.J. Powell, A. Jablonski, *NIST Electron Inelastic-Mean-Free-Path Database - Version 1.1*, National Institute of Standards and Technology, Gaithersburg, MD (2000).
11. QUASES - IMFP – TPP2M : free download at http://www.quases.com/
12. N.V. Skorodumova, R. Ahuja, S.I. Simak, I.A. Abrikosov, B. Johansson, B.I. Lundqvist, *Phys. Rew. B*, 64, 2001, 115108
13. M. Königstein, A.A. Sokol, C.R.A. Catlow, *Phys. Rew. B*, 60, 1999, 4594